The Ionospheric Continuous-wave E-region Bistatic Experimental Auroral Radar (ICEBEAR)

A Thesis Submitted to the
College of Graduate and Postdoctoral Studies
in Partial Fulfillment of the Requirements
for the degree of Doctor of Philosophy
in the Department of Physics and Engineering Physics
University of Saskatchewan
Saskatoon

By
D. Huyghebaert

Permission to Use

In presenting this thesis in partial fulfilment of the requirements for a Postgraduate degree from the University of Saskatchewan, I agree that the Libraries of this University may make it freely available for inspection. I further agree that permission for copying of this thesis in any manner, in whole or in part, for scholarly purposes may be granted by the professor or professors who supervised my thesis work or, in their absence, by the Head of the Department or the Dean of the College in which my thesis work was done. It is understood that any copying or publication or use of this thesis or parts thereof for financial gain shall not be allowed without my written permission. It is also understood that due recognition shall be given to me and to the University of Saskatchewan in any scholarly use which may be made of any material in my thesis.

Requests for permission to copy or to make other use of material in this thesis in whole or part should be addressed to:

Head of the Department of Physics and Engineering Physics
University of Saskatchewan
116 Science Place, Rm 163
Saskatoon, Saskatchewan S7N 5E2 Canada

OR

Dean
College of Graduate and Postdoctoral Studies
University of Saskatchewan
116 Thorvaldson Building, 110 Science Place
Saskatoon, Saskatchewan S7N 5C9 Canada

Abstract

The Sun drives many atmospheric processes on Earth through solar electromagnetic radiation, the solar wind, and the solar magnetic field. These solar phenomena interact with a region around the Earth where plasma can be formed, the ionosphere. This region is located 60–1000 km above the surface of the Earth, and is of interest to many scientists and engineers due to the interaction between radio waves and plasma. Variations in the ionospheric plasma density can cause disruptions to GPS signals and radio communications. Attempts have been made to measure the ionospheric plasma properties through the use of rockets, satellites, and remote sensing instrumentation.

One of the issues with measuring the ionosphere, specifically the lower altitudes of the ionosphere, is that it is expensive to do in situ. Rockets are required for in situ measurements at altitudes of 90–150 km (the E-region of the ionosphere). Rocket launches are expensive, so more efficient remote methods of measuring the E-region are typically used. This includes radars utilizing radio waves to scatter from the ionospheric plasma. From the scattered signal, plasma properties can be derived to provide insight into the physical processes occurring.

The Ionospheric Continuous-wave E-region Bistatic Experimental Auroral Radar (ICEBEAR) was developed to probe the E-region of the ionosphere using this mechanism. Through the use of modern radar hardware and techniques, it was possible to obtain simultaneously high temporal (down to 0.1 s) and spatial ($\approx$ 1.5 km) resolution images of ionospheric plasma density perturbations over a 600 km $\times$ 600 km field of view. The radar operates at 49.5 MHz and transmits a continuous-wave, pseudo random noise, phase modulated code to obtain these images. The radar is bistatic, with both transmitter and receiver being located in Saskatchewan, Canada, and operated by the University of Saskatchewan. The radar was designed with future improvements in mind, where each transmitter and receiver antenna are individually controlled/sampled. This Ph.D. dissertation describes the dynamics of the ionosphere, the design and construction of ICEBEAR, and presents some preliminary results, exhibiting the exciting modern capabilities of the system.

Acknowledgements

First, I would like to thank my supervisor, Dr. Glenn Hussey. Dr. Hussey has provided excellent guidance and support through all aspects of the design, construction, and operation of ICEBEAR. It has been a tremendously exciting and ambitious project, and I am grateful for having the opportunity to see it to completion.

I would also like to thank the co-principal investigators for the ICEBEAR project, Dr. Kathryn McWilliams and Dr. J.P. St.-Maurice. Without them, the project would not have been possible. Dr. Juha Vierinen is someone I would also like to thank as a co-author on the ICEBEAR publication.

I can not thank the SuperDARN engineering group enough for their time and effort in helping with the construction of ICEBEAR. The SuperDARN group has evolved over the years, and my thanks extends to Kevin Krieger, Marci Detwiller, Keith Kotyk, Jan Wiid, Naas van Rensberg, Bill Marshall, Marina Schmidt, and Randi Strunk. Those who spent a week constructing the ICEBEAR transmitter site in blistering heat I would especially like to thank. These people include Kevin, Marci, Keith, David Fairbairn, and Fraser Hird.

Cindy Jelinski is a member of the ISAS department that has been a huge aid in dealing with the administrative overhead of ICEBEAR. I thank her for always being willing to help and providing beneficial advice and guidance with many of the administrative duties. Also, to the other members of ISAS and the University of Saskatchewan physics department, thank you. This includes the graduate students, postdocs, professors, and administrative assistants. Dr. Ashton Reimer, Dr. Gareth Perry, Dr. Neil Johnson, Michael Patterson, Dr. Pasha Ponamarenko, Dr. George Sofko, Dr. Sasha Koustov, Debbie Gjertsen, and Marj Granrude are a few of the people I would specifically like to thank. I also thank my Ph.D. committee of Dr. Adam Bourassa, Dr. Michael Bradley, and Dr. David Klymyshyn for performing the time consuming duties associated with being on a Ph.D. committee.

Mike McKibben and the staff at Scientific Instrumentation Ltd. are also thanked for providing the facilities for constructing the multiple power amplifiers for ICEBEAR.

Last, but not least, I would like to thank my loving family and friends. They have encouraged me in every endeavour I have undertaken, and I am thankful for their support.

Contents

List of Tables

List of Figures

Partial List of Abbreviations

AC	Alternating Current
ADC	Analog to Digital Converter
BJT	Bipolar Junction Transistor
BPF	Band Pass Filter
BW	Bandwidth
CW	Continuous-Wave
DAC	Digital to Analog Converter
DC	Direct Current
DDC	Digital Down Converter
DDS	Direct Digital Synthesis
DSP	Digital Signal Processing
DUC	Digital Up Converter
EM	Electromagnetic
ERP	Effective Radiated Power
FET	Field Effect Transistor
FFT	Fast Fourier Transform
FM	Frequency Modulation
FOV	Field of View
FPGA	Field Programmable Gate Array
GPIO	General Purpose Input/Output
GPS	Global Positioning System
HDD	Hard Disk Drive
HF	High Frequency
IMF	Interplanetary Magnetic Field
IQ	In-phase and Quadrature
ISR	Incoherent Scatter Radar
LFM	Linear Frequency Modulation
LNA	Low Noise Amplifier
MHD	Magnetohydrodynamic
NTP	Network Time Protocol
PCB	Printed Circuit Board
PDU	Power Distribution Unit
PPS	Pulse Per Second
PRN	Pseudo Random Noise
PSK	Phase Shift Keying
PWM	Pulse Width Modulation
RF	Radio Frequency
SDR	Software Defined Radio
SNR	Signal to Noise Ratio
SWR	Standing Wave Ratio
VHF	Very High Frequency

Chapter 1

Introduction

Before delving into this Ph.D. dissertation, something must be noted. Portions of this dissertation have been published in Huyghebaert, D., G. Hussey, J. Vierinen, K. McWilliams, and J.-P. St-Maurice (2019), ICEBEAR: An all-digital bistatic coded continuous-wave radar for studies of the E region of the ionosphere, *Radio Science*, *54*(4), 349–364, doi: 10.1029/2018RS006747. ICEBEAR is an acronym for Ionospheric Continuous-wave E-region Bistatic Experimental Auroral Radar. The radar system described in the referenced publication is the culmination of my Ph.D. dissertation research and the radar was designed, constructed, implemented, and operated by myself, with the co-authors providing valued infrastructure, guidance, and discussion. As with the radar design and implementation, I wrote and lead the publication *Huyghebaert et al.* [2019]. Each chapter will include which figures and sections were originally published in this publication. In this introduction section, portions of Section 1.1 were originally published in *Huyghebaert et al.* [2019]. A footnote on the first page of each chapter will also include this information, such as shown at the bottom of this page.

1.1 Background and Motivation

It is not uncommon for people in many places across Canada to witness the aurora borealis, also known as the northern lights, on a regular basis. These dancing lights in the sky are created from energetic charged particles precipitating from space and interacting with the atmosphere of the Earth. The energetic particles excite different atmospheric species, such as

---

Portions of Section 1.1 were originally published in *Huyghebaert et al.* [2019].

molecular oxygen, to generate photons at certain wavelengths, producing the different colors of the aurora. The excitation of the atmospheric species can generate plasma, where plasma is a highly energized gas with the electrons stripped from the ions, in this case occurring from the excitation of the neutral atmosphere of the Earth. The photons in the aurora borealis are therefore evidence of atmospheric plasma phenomena occurring. From observations of the aurora, it is evident that there are many dynamical atmospheric and plasma processes occurring in the atmosphere of the Earth.

The aurora borealis occurs in a region known as the ionosphere. This region extends from approximately 60 km to 1000 km above the surface of the Earth, and is defined as the altitudes at which plasma persists in the near-Earth environment [*Kelley*, 2009]. The ionosphere is of great interest to scientists and engineers due to the interaction between radio waves and plasma, and also due to its potential influence on lower atmospheric weather. The ionospheric plasma is able to affect the characteristics of radio waves propagating through it, as well as reflect and scatter the radio waves. This can allow extended communication range from the reflection, but also can introduce errors into global positioning system (GPS) signals from the changes to the signal. Due to its effects on radio waves, scientists and engineers have attempted to measure and study the ionosphere since the invention of radio.

The ionosphere, especially the lower altitude regions, is difficult to measure due to its location. The minimum altitude of sustained orbit for satellites is $\approx$ 200 km, while planes typically fly at heights of up to 20 km. The region of interest of the ionosphere for this Ph.D. dissertation is the E-region, which is defined as 90–150 km in altitude above the surface of the Earth. For in situ measurements of this E-region, rocket experiments are required. These experiments are relatively expensive, and can only be performed occasionally. To remotely measure the ionosphere, radars, optical imagers, and magnetometers are therefore used. With advances in electronics hardware, these remote measurements are able to be performed continuously, rather than on a campaign basis. The ionosphere is able to be probed remotely using radars, such as ICEBEAR, due to the interaction between radio waves and plasma.

Radars initially used primarily analog circuits to generate radio signals to scatter off objects and be received post-scattering. The received scattered signal contained information about the object it scattered from, such as its relative velocity. The receiver also used many

front end analog circuits, where the data could then be recorded using paper, or was displayed on a screen. Advances in digital media storage and radio hardware provided opportunities to improve the design of radar systems [*Mitola*, 1995; *Richards et al.*, 2010]. These design improvements included the ability to record the radio signal digitally, the ability to create the transmission signal through digital circuits, and the ability to directly sample the incoming radio signal with minimal analog circuity.

Digital radar electronics are able to improve and expand upon many operations that previously analog radar electronics performed. This includes improvements to the control of the modulation of the RF signal, implementation of complex digital processing algorithms, and simply recording the signal. Using digital hardware and techniques it is possible to record the raw voltage samples of large bandwidth signals digitally, without the need to significantly process and/or filter the signal before storage. Some of the advances that made this possible include improvements to analog to digital converters and the ability to accurately synchronize multiple separately located system clocks. This allows multiple signal processing methods to be used on the data, providing flexibility and the ability to implement future advanced processing methods that increase the data quality [*Grydeland et al.*, 2005]. The improved digital storage in conjunction with advanced signal modulations has allowed digital processing to be used to obtain higher temporal and spatial resolutions for radars at non-prohibitive costs. These digital radio hardware and techniques have been recently applied to radars that measure the ionosphere, including the ICEBEAR radar described in this dissertation. ICEBEAR is an ionospheric coherent scatter radar, which is a category of ionospheric radars characterized by the ionospheric scattering physics utilized by the radar.

Coherent scatter radars observe echoes from the ionosphere through the scattering of radio waves from large amplitude plasma density perturbations generated by plasma instabilities. These perturbations are oriented along the magnetic field lines of the Earth, requiring the incident radio signal for a monostatic system to be approximately perpendicular to the geomagnetic field for radar scatter to occur (e.g., see the review by *Fejer and Kelley* [1980]). For a bistatic radar system, such as ICEBEAR, it is the bisector between the incident and scattered wave vectors that must be perpendicular to the background magnetic field. From the spectrum of the received signal one typically extracts a mean Doppler shift, a Doppler

width and a power level from the scattering region. Different types of coherent scatter radars have been used over the years to probe the plasma density irregularities in the E-region, each radar having its own unique characteristics (e.g., *Riggin et al.* [1986]; *Haldoupis and Schlegel* [1993]; *Koehler et al.* [1995]; *Greenwald et al.* [1995]; *Sahr and Lind* [1997]; *Hysell et al.* [2012]).

The enhanced accuracy and resolution provided by recent radio/radar advances, and implemented in ICEBEAR, are critical as there are still many unanswered questions regarding E-region plasma density irregularity scattering physics. Further investigations into the altitude dependence of E-region radar measurement spectra, and how the measurements of E-region plasma density irregularities vary with radar signal wavelength are needed. Reviews of the development of the understanding of E-region radar measurements and attempts at answering some outstanding questions can be found in *Fejer and Kelley* [1980], *Haldoupis* [1989], *Sahr and Fejer* [1996], *Schlegel* [1996], *Moorcroft* [2002], *Makarevich* [2009], and *Hysell* [2016]. These publications describe and characterize the different types of radar echoes received from the ionospheric E-region of the Earth and the technical progress that has taken place over the years. Many of the interesting and unresolved E-region irregularity spectra measured by previous radars occurred in the auroral region of the Earth. Through the design and implementation of a modern ionospheric radar system, such as ICEBEAR, it is possible to revisit, verify, and significantly expand upon this previous work.

1.2 Objectives

The objective of this Ph.D. dissertation was to design and construct a novel ionospheric coherent scatter radar using modern radio hardware and techniques to make simultaneously high spatial and temporal resolution measurements of E-region plasma density irregularities. A secondary objective was to have as large a field of view as possible. All this is needed to advance the understanding of plasma density instabilities and magnetospheric waves in the near Earth space plasma environment. I designed, constructed, implemented, and operated the radar system created to accomplish these objectives, which was named ICEBEAR. This involved the selection of components, creation of printed circuit board (PCB) and me-

chanical schematics, implementation and modification of various electronics designs, and the integration of all the different components to create a fully functional novel radar system. While members of the Institute of Space and Atmospheric Studies radar physics group at the University of Saskatchewan helped with the implementation of the ICEBEAR large antenna arrays at the radar sites, the other electronic systems related to ICEBEAR were fully implemented by myself. This included the design, prototyping and construction of all the ICEBEAR power amplifiers, where Scientific Instrumentation Ltd. (SIL) aided in the amplifier enclosure design. The amplifiers were designed with CW operation in mind, and a goal of 1 kW power output with remote monitoring capability implemented and minimal harmonics on the output signal. Previous radars had measured coherent E-region irregularity scatter with output powers of 150 W, so the amplifier output power of 1 kW was a very acceptable increase.

An objective of the ICEBEAR system was to significantly improve upon the results from previous ionospheric coherent scatter radars. One of these aspects was increasing the temporal and spatial resolution when compared to previous radars. Improvements to the resolution of radar measurements over previous systems is essential to further understand and characterize the plasma dynamics occurring in the ionosphere, as these processes can occur on time scales of < 1 s and spatial scales of < 1 km [*Kelley*, 2009]. Other radar systems have/had resolutions approaching these scales, but included drawbacks in their operation and interpretation of the signal recorded, such as aliasing in the range and/or frequency domains, and the inability to achieve both resolutions simultaneously. With these spatial and temporal scales in mind, an objective for ICEBEAR included obtaining temporal resolutions on the order of 100 ms and spatial resolutions on the order of 1 km, simultaneously. The radar waveform selected for the radar system is very important to achieving these resolution objectives, and therefore it was decided to make the ICEBEAR system adaptable to transmitting different waveforms. One of the radar waveforms analyzed utilized binary phase modulation, and was ultimately selected to achieve the simultaneous high spatial and temporal resolution.

Another objective with ICEBEAR was to remove the aliasing that plagued many previous radar systems. This aliasing created measurement ambiguity in the results. As well, the angle of arrival information (interferometry) for the ionospheric scatter was planned to be measured

using a linear receiving array, allowing the mapping of the scatter over a large field of view in 2-D (2-dimensional) space (latitude and longitude). The implementation of a digital design was decided upon so that it would be possible to reconfigure the linear receiving array at a future date to determine the location of the scatter in 3-D space. The location of the field of view in the auroral zone of the Earth is very important to further investigate many unresolved hypotheses surrounding the characteristics of certain E-region irregularity radar spectra, and was chosen as the location of the field of view for this reason.

By increasing the resolution of E-region plasma density perturbation measurements, ICEBEAR will advance the work that has been previously done on E-region plasma density instabilities, primarily the Farley-Buneman instability [*Farley*, 1963a; *Buneman*, 1963]. It will also be able to investigate Alfvén wave [*Alfvén*, 1942] propagation in the magnetosphere of the Earth, where Alfvén wave propagation studies require the time resolution of measurements to be on the order of 100 ms (10 Hz waves) [*Stasiewicz et al.*, 2000]. The advancement of understanding in these areas will provide a significantly better comprehension on the plasma physics occurring in the ionosphere of the Earth and their associated magnetosphere-ionosphere coupling processes.

As the design and construction of a radar system is an ambitious project, the data collected from the ICEBEAR system will not be interpreted in this thesis. Results are presented to exhibit the modern and improved capabilities of ICEBEAR, but further analysis of the measurements is left for future researchers.

The next section provides an overview of the different chapters of the thesis, with Chapters 2 and 3 discussing the magnetospheric and ionospheric processes of the Earth, Chapters 4 and 5 discussing radio wave propagation through a magnetized plasma and radar equations, Chapter 6 discussing digital radar hardware concepts and components, Chapter 7 reviewing previous E-region radar systems, Chapter 8 explaining the design and construction of the ICEBEAR system, Chapter 9 providing results from this novel system, and Chapter 10 presenting conclusions and future research directions for ICEBEAR E-region science.

1.3 Thesis Outline

The Sun is the primary driver for many atmospheric processes on Earth. This includes the creation of the ionosphere of the Earth. The interactions between the Sun and Earth are complex, involving electromagnetic (EM) radiation, magnetic fields, electric fields, charged particles, and neutral particles. Through interactions between these different physical phenomena, neutral gases in the atmosphere of the Earth can acquire enough energy to transition to what is considered the fourth state of matter, known as plasma. The plasma state of matter occurs when electrons and ions are separate species within a medium, where the electron is not bound to the ion. Due to the low particle density at high altitudes, the ions and electrons do not collide often, resulting in a low recombination rate of the disassociated atoms/molecules. With the electrons and ions as separate species, EM forces can influence the plasma medium, resulting in interesting physical effects. Chapter 2 provides an introduction to the Sun-Earth interaction as it relates to the magnetosphere of the Earth. The Sun-Earth interactions are a driving force in many ionospheric processes, where plasma density perturbations in the lower part of the ionosphere are what the new ICEBEAR system developed for this Ph.D. dissertation will be measuring.

Chapter 3 investigates the ionosphere of the Earth, which is a region located approximately 60 km to 1000 km in altitude above the surface of the planet. This region has been of interest to people for hundreds of years due to the aurora borealis, also known as the northern lights. The northern lights are generated from charged particle precipitation exciting different atoms/molecules in the upper atmosphere, where the depth of penetration of the charged particles corresponds to the initiated chemical process that produces the photon emissions. The different chemical processes result in different wavelengths of light being generated and observed. These particle precipitation events can create localized electric fields in the ionosphere, exerting forces on the plasma. There are also large scale electric fields generated from the magnetosphere of the Earth interacting with the interplanetary magnetic field, which produce a convection pattern of the plasma in the ionosphere. Through particle precipitation and convection, gradients and flows in the ionospheric plasma density can be generated, producing the potential for plasma density instabilities. The radio waves gener-

ated by the ICEBEAR system described in this dissertation scatter from the plasma density irregularities produced from these instabilities. There are still many unanswered questions about the coherent scatter spectra measured by previous researchers and their ionospheric coherent scatter radar systems, and ICEBEAR will greatly aid in answering these questions.

The ionosphere of the Earth affects EM wave propagation in complex ways, providing increased propagation distance of radio signals at certain frequencies due to scattering and reflection, and affecting radio signal characteristics through processes such as Faraday rotation and radio wave absorption. These effects can impact GPS location determination, FM radios, AM radios, and satellite communications. Chapter 4 describes many of the ways the ionosphere affects radio wave propagation, providing details on how radio waves scatter from plasma density irregularities and how different frequencies of radio waves are affected by plasmas with a background magnetic field, such as the ionosphere. An understanding of radar wave propagation is required to interpret the radar measurements made by the ICEBEAR system.

Chapter 5 presents and discusses the equations used to determine the range and Doppler shift of scattered radio waves used for radar. It describes how over-spread and under-spread targets (soft targets), defined as multiple scattering targets within a volume, are different from hard targets (e.g., planes), defined as a single large cross-section target, and examines the range and Doppler resolution of different radar waveforms. This includes a waveform similar to that used by ICEBEAR. The chapter closes with a discussion of the noise sources related to the ICEBEAR system.

After the background ionospheric physics is explained, the basics of the generation and reception of the radar signal is discussed in Chapter 6. ICEBEAR requires both radio signal generation and reception to operate successfully. The generation and reception of radio waves requires complex electronics, with impedance matching circuits and cables connecting different radio frequency (RF) devices. A simple digital radar system is described, starting with how RF systems are matched and filtered. A description of radio signal creation, including modulation, follows. From there an overview of amplifier design and operation is described for field effect transistor (FET) devices. The ICEBEAR power amplifier design and construction was a large portion of this Ph.D. dissertation, and a review of the different

amplifier types is provided as it relates to the radar design. After amplifiers, antennas are discussed, including different types of antennas, antenna arrays, and the effects of a ground plane and signal polarization. The antenna radiation pattern is extremely important for a radar system, as this defines where the radar signal will be transmitted from and received from. ICEBEAR utilizes horizontally polarized Yagi antennas, of which an overview is provided. This is followed by a review of digital receivers, and how a signal is digitized. The chapter closes with a discussion on the different types of clocks used to synchronize devices and geographically separate systems, such as ICEBEAR with its transmitter and receiver separated by ≈ 240 km.

With the background material covered, Chapter 7 describes previous ionospheric coherent scatter radars. Previous E-region radars separated the coherent scatter measurements into four different types, aptly named Type I, Type II, Type III, and Type IV. The radar systems obtained measurements of the E-region through pulsed and CW measurements, each radar with their own constraints. The ICEBEAR radar minimizes many of these constraints through the use of modern radio hardware and novel radar signal techniques paired with enhanced computing power to improve the radar measurements. The previously labelled Type III and Type IV coherent scatter spectra are especially of interest to ICEBEAR, as there are still many unresolved questions about the physics of these types of spectra.

The design choices made for the ICEBEAR system, and the construction of this new E-region coherent scatter radar are described in Chapter 8. The selection and construction of the ICEBEAR transmitter site is first described, followed by an introduction to the radar system. The electronics common to both the transmitter and receiver sites are discussed, including the transceiver selected, the antenna arrays, and how the measurements made at both sites are synchronized. The hardware specific to the transmitter follows, with the design of a very important component for the ICEBEAR transmitter, the power amplifier, described. The chapter concludes with hardware specific to the ICEBEAR receiver, and the processing performed on the received signal to obtain useful coherent scatter measurements of the E-region of the ionosphere.

Chapter 9 provides some initial results from the ICEBEAR system. A description of the initial operating characteristics is provided, along with ionospheric coherent scatter spectra

obtained from an event on 10 March, 2018. The horizontal angle of arrival of the scatter is calculated so that the scatter can be plotted to a map. Multiple plots can be sequentially combined to display the time evolution of coherent scatter structures in the ionosphere. Some preliminary results from multi-instrument studies are also provided, giving insight into the many collaborative studies that are possible with ICEBEAR in the future.

The Ph.D. dissertation closes with Chapter 10, where the ICEBEAR system is summarized and future directions for ICEBEAR studies are provided.

Along with the body of the dissertation, there are many appendices provided as supplemental material. The appendices include derivations of different ionospheric processes, and the Python programs used to operate the ICEBEAR transmitters and receivers. These appendices will be referenced where relevant.

The project set out to measure the E-region of the ionosphere using new radar measurement techniques to provide enhanced spatiotemporal resolution images of plasma density irregularities, and succeeded in accomplishing this. The ICEBEAR system provides a basis by which CW phase modulated transmitters can be utilized to provide coherent scatter measurements of the ionospheric plasma medium. The measurements from the ICEBEAR system will allow researchers to better understand the dynamics of the ionospheric E-region plasma medium and how the magnetosphere of the Earth couples to the ionosphere.

Chapter 2

The Space Environment of the Earth

The Sun provides energy to the atmosphere of the Earth through many different processes, but it can all be related back to EM radiation emissions from the Sun, the magnetic field of the Sun, and the charged particle emissions from the Sun that create the "solar wind". These physical phenomena interact with the magnetosphere and atmosphere of the Earth to cause different physical phenomena, such as the aurora borealis. The ICEBEAR system measures plasma density irregularities in the ionosphere of the Earth, where the ionosphere is described in detail in Chapter 3. Signatures of magnetospheric phenomena can appear in the plasma density irregularities that the ICEBEAR system measures. Before the ionosphere can be described, a discussion on what drives the many physical processes occurring in the ionosphere must be provided. This chapter is an overview of the Sun-Earth interactions providing a basic understanding of how the Sun is able to drive processes that occur in the ionosphere of the Earth.

2.1 The Solar System

The solar system we live in is located in the Milky Way Galaxy, the Sun being one of billions of stars in it. The Sun orbits the center of the galaxy approximately every 240 million years [*Sparke and Gallagher III*, 2007] and is located on the Orion arm [*NASA*, 2012], where an "arm" is an area with a larger density of stars extending in a spiral outward from the center of the galaxy. The boundary of the solar system is considered to be at the heliopause, which is where the solar wind pressure and the interstellar medium pressure balance, and is located approximately 18 billion km from the Sun [*Gurnett et al.*, 2013]. Beyond this distance the solar magnetic field deflects much less cosmic radiation, resulting in more high energy cosmic

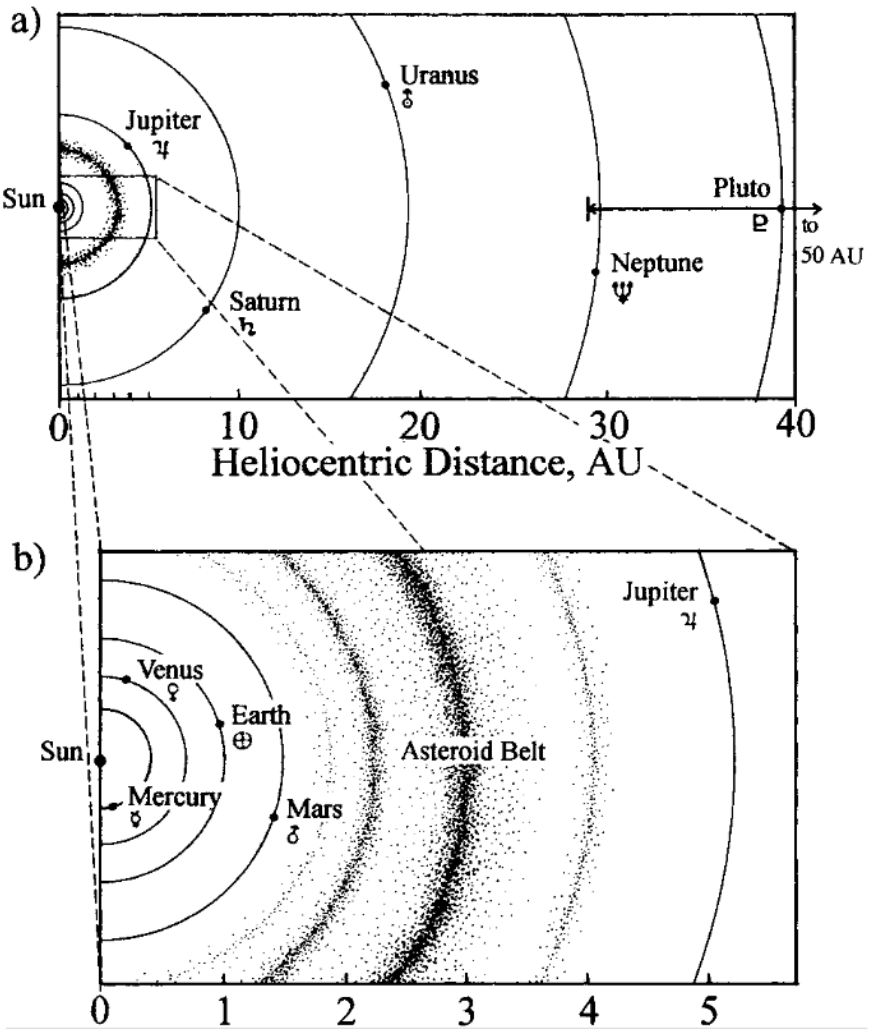

Figure 2.1: The orbits of the planets in the solar system. The Earth orbits at a distance of 1 AU, which is equivalent to 149,597,870 km. [*Lewis*, 2012]

radiation outside the solar system.

The solar system has 8 planets orbiting the Sun, the Earth being the third closest. The other planets are Mercury, Venus, Mars, Jupiter, Saturn, Uranus and Neptune, listed from closest to furthest. The orbits are shown in Figure 2.1, with the asteroid belt and Pluto included. These planets all orbit the Sun with varying periodicities and ellipsoids, and the distance between each planet is vast. The planet of interest for this dissertation, the Earth, has an orbit that takes approximately 365.256 days to complete, with an average distance of 149.60 million km from the Sun [*Lewis*, 2012].

Before discussing the Sun, the fourth state of matter, known as plasma [*Chen*, 2006],

must be described. The Sun, as well as much of the interstellar space medium, consists of plasma. The plasma state of matter is discussed and described in the next section.

2.2 Space Plasmas

Plasma is the state of matter where a neutral molecule or atom has an electron stripped from it due to an energetic process, and they do not immediately recombine [*Chen*, 2006]. Plasma is a super heated gas, in which the temperature of the gas causes the electrons to be separated from the ions. For a plasma to persist, the electrons are stripped from the atom or molecule at a rate greater than the recombination rate until an equilibrium is reached. In the solar system, an example of a dense high temperature plasma is the Sun, and an example of a weakly ionized low temperature plasma is the ionosphere of the Earth.

To be considered a plasma, the electrons and ions of the medium must act as separate species and be affected by EM forces. A weakly ionized medium can be considered a plasma, as long as the electrons and ions persist and act as separate particle species. The ionization ratio of a plasma is the portion of the medium that is ionized over the portion that is neutral. Weakly ionized plasmas typically have a large recombination rate and require a constant source of ionization energy to maintain their plasma state.

Due to the fact that plasmas are governed by both fluid mechanics and EM forces with complicated boundary conditions, they are complex to model and understand. An introduction to the basic electrodynamics equations used to model plasma physics is provided in Appendix A. The complex nature of plasmas can lead to interesting physical phenomena and applications. Ion propulsion, gas lasers, and controlled fusion are just a few of the applications of plasmas. Plasmas can also exhibit complicated plasma density instabilities from the distributions and motions of the different ion and electron species, especially in the presence of an external magnetic field. More information on some of the instabilities that are observed in the ionosphere of the Earth is provided in Chapter 3. The ICEBEAR signal scatters from large scale perturbations in the ionospheric plasma density which are generated from these instabilities.

The Sun is the dominant source of plasma generation in the solar system, and therefore

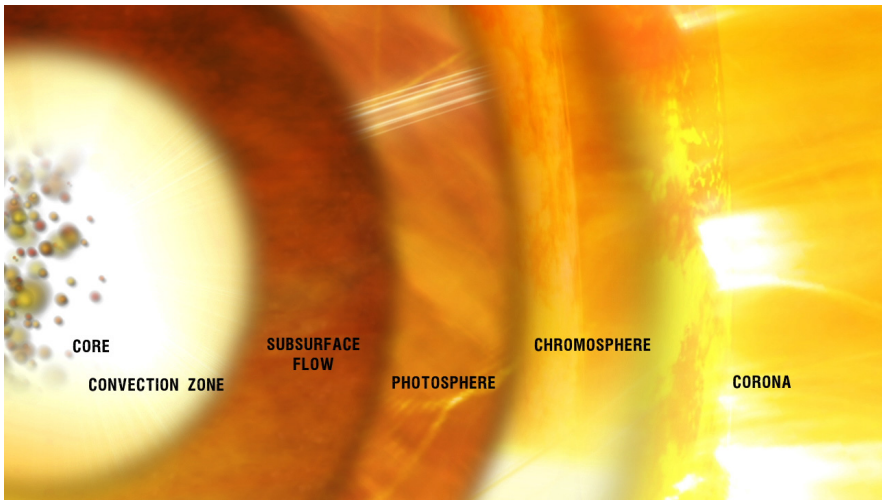

Figure 2.2: A depiction of the layers of the Sun. [*Fox*, 2014]

will be discussed next.

2.3 The Sun

The Sun is located at the center of the solar system and is approximately 1.3×10^6 times larger than the Earth [*Lewis*, 2012]. It creates energy through fusion processes and the energy is then radiated out as EM radiation, charged particles and neutral particles. The Sun is considered a medium sized star with an age of approximately 4.44×10^9 years.

The Sun consists of multiple layers: the core, the radiative zone, the convection zone, the photosphere, the chromosphere, the transition region and the corona [*Cravens*, 1997]. These layers are shown in Figure 2.2, where the transition region is located between the chromosphere and the corona. The corona is the region that supplies the solar wind with energetic particles that ultimately can interact with the atmosphere of the Earth. Although not a direct driver of E-region phenomena measured by ICEBEAR, the corona is of interest for this this Ph.D. dissertation due to its coupling to the solar wind.

The corona has a lower boundary approximately 2,000 km above the solar surface (the photosphere) and extends to approximately 1.4×10^6 km [*Marsch*, 2006]. It consists of a very hot plasma and is the upper atmospheric layer of the Sun, while the lower layer is the chromosphere [*Lewis*, 2012]. The corona has a temperature of 1×10^6 to 4×10^6 K , which is much hotter than the lower regions of the Sun that are closer to $5,800$ K [*Cravens*, 1997].

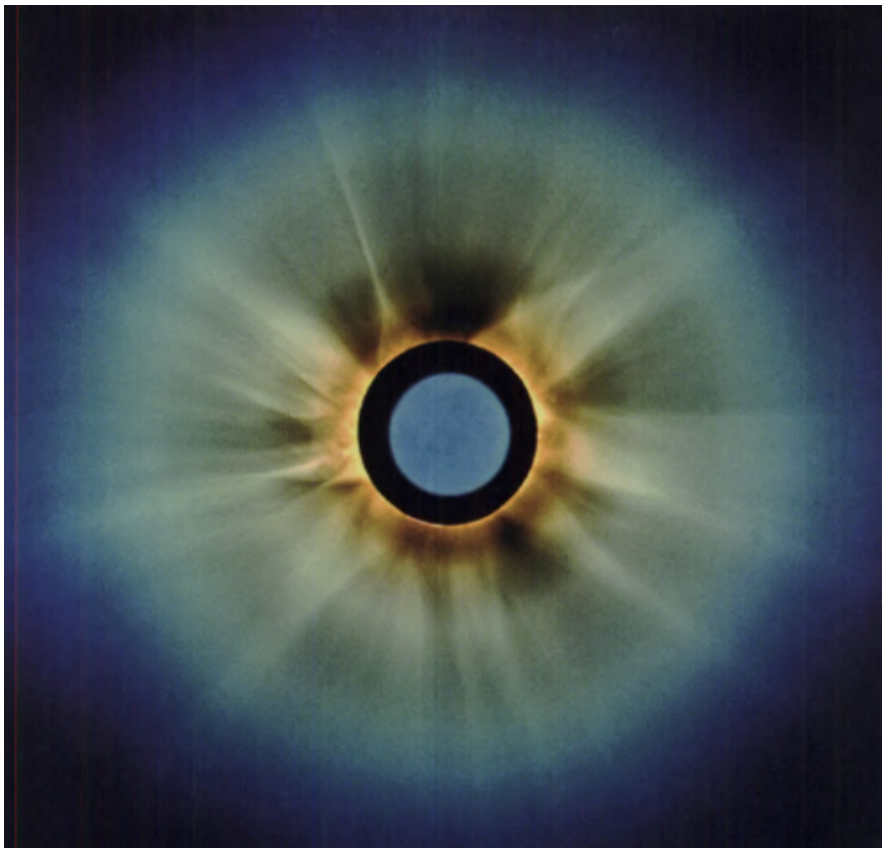

Figure 2.3: The solar corona in the visible spectrum during an eclipse. [*Prölss*, 2012]

A picture of the corona can be seen in Figure 2.3, with emissions from this region evident.

The reason for the drastic increase in temperature from the photosphere to the corona has yet to be determined, though there are some competing hypotheses. One hypothesis is that the increase in temperature is due to energies imparted during reconnection of the solar magnetic field [*Browning*, 1991]. When magnetic fields reconnect, they can accelerate the charged particles trapped on the magnetic field lines, effectively increasing the temperature of the particles. Magnetic reconnection will be described further in section 2.4.1 as it relates to the magnetosphere of the Earth, but for further insights into the hypothesis of coronal heating through reconnection see, for example, *Sturrock* [1999] and *Klimchuk* [2006]. Another hypothesis to explain the coronal heating phenomena has to do with magnetohydrodynamic (MHD) waves [*Browning*, 1991]. These waves accelerate the particles, providing an increase in kinetic energy, and thereby temperature, in the corona. For details on this hypothesis, see, for example, *Tu and Marsch* [1997], *van Ballegooijen et al.* [2011], and *Hahn and Savin*

[2014].

Whatever the reason for the extremely high temperatures in the corona, the temperatures have been shown to exist from measurements [*Withbroe*, 1988; *Warren and Brooks*, 2009]. Along with the much higher temperatures than the photosphere, the corona is much less dense than that of the solar surface, which can be thought of as similar to the difference between density of the surface and the atmosphere of the Earth. The corona has been referred to as part of the solar atmosphere [*Lewis*, 2012]. The high temperature, tenuous plasma radiates outward from the Sun, gyrating around the solar magnetic field, also known as the interplanetary magnetic field (IMF), as it travels. At a distance of a few solar radii ($\approx 1.4 \times 10^6$ km) the corona transitions into what is known as the solar wind [*Marsch*, 2006]. Before discussing the solar wind, the solar EM flux is discussed.

2.3.1 Solar Electromagnetic Flux

The Sun has a black body temperature of approximately 6000 K, where the spectrum radiated is presented in Figure 2.4. The photons observable at the Earth mostly originate from the photosphere of the Sun, but there are some contributions from the chromosphere and the corona. The atmosphere of the Earth absorbs different wavelengths of this light, where the inner spectrum (bottom curve) in Figure 2.4 shows the light that reaches the surface of the Earth.

The equation for the radiation produced by a black body radiator is given by Planck's Law [*Planck*, 2013], which states that the spectral radiance as a function of radiation frequency and black body temperature is given by,

$$B_\nu(\nu, T) = \frac{2h\nu^3}{c^2}\left(e^{(\frac{h\nu}{k_B T})} - 1\right)^{-1} \tag{2.1}$$

where ν is the frequency of the radiation in Hz, h is the Planck constant (6.626×10^{-34} J s), c is the speed of light (2.998×10^8 m/s), k_B is the Boltzmann constant (1.381×10^{-23} J K^{-1}), and T is the temperature of the body in K. The units for $B_\nu(\nu, T)$ are W sr^{-1} m^{-2} Hz^{-1}. The resulting spectrum as a function of wavelength for a 6000 K blackbody is the top curve in Figure 2.4.

The largest irradiance from the Sun is in the visible spectrum, with wavelengths from

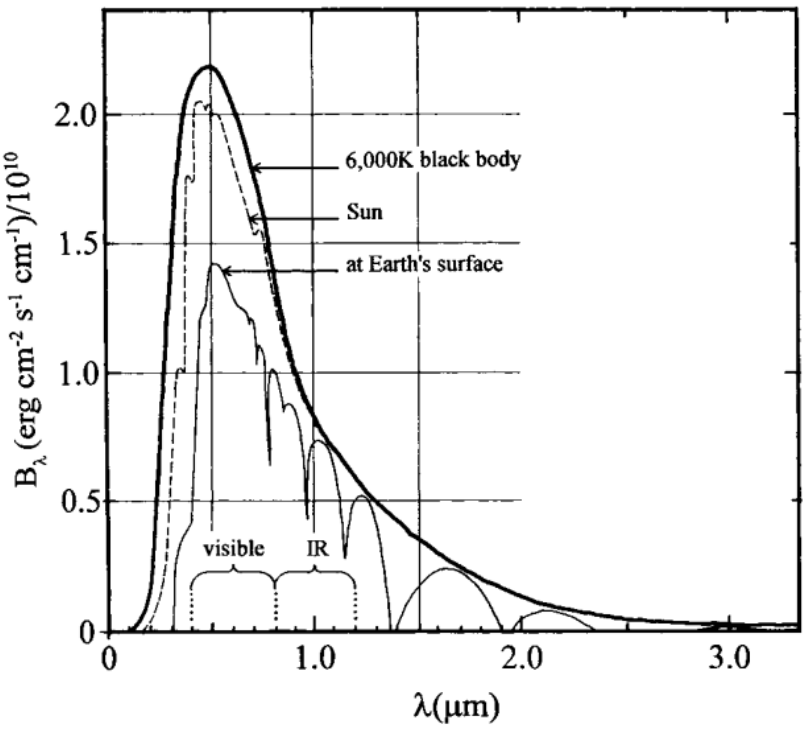

Figure 2.4: The solar emission spectrum plotted with a black body radiator at 6000 K and the measured emission spectrum at sea level. [*Lewis*, 2012]

390 nm to 700 nm. The solar irradiance is the power per unit area (i.e. W/m^2) of the light hitting a surface. This means that planets closer to the Sun than the Earth have a much larger solar irradiance than that of the Earth. The difference in solar irradiance between the planets contributes to their difference in temperatures.

Along with the solar irradiance, the solar magnetic field and charged solar particles can also transfer energy from the Sun to the planets.

2.3.2 The Solar Magnetic Field and The Solar Wind

The Sun has a magnetic field that is generated due to charge moving between the core and the convection zone [*Durney et al.*, 1993]. This solar magnetic field, also known as the interplanetary magnetic field (IMF), extends outward into the solar system, where electrons and ions are "bound" to the solar magnetic field lines. This effectively couples the solar wind and the IMF. As the corona expands and the charged particles escape the gravity of the Sun, the solar magnetic field is carried with them. This is known as the frozen-in condition, the

derivation of which is provided in Appendix A.

The result from the derivation is that the magnetic flux does not change over time as long as the conductivity of the plasma approaches infinity. This is a valid approximation as long as the ion and electron cyclotron frequencies (ω_{ci}, ω_{ce}) are much greater than the ion and electron collision frequencies (ν_i, ν_e), i.e. $\omega_{ci} \gg \nu_i$, $\omega_{ce} \gg \nu_e$. The cyclotron frequency is given by the equation [*Chen*, 2006],

$$\omega_{ci,ce} = \frac{q_{i,e}B}{m_{i,e}} \tag{2.2}$$

where $\omega_{ci,ce}$ is the ion or electron cyclotron frequency, $q_{i,e}$ is the charge of the ion or electron, B is the magnetic field, and $m_{i,e}$ is the mass of the ion or electron.

The solar wind characteristics originate from conditions on the Sun. These conditions are dependent on the solar corona, which can be affected by the layers closer to the solar core. As well, different solar latitudes produce different solar wind characteristics. This is presented in Figure 2.5, where it can be observed that along the solar equator the solar wind speed is low, but at higher solar latitudes the solar wind speed increases. The position of the Earth with respect to the Sun thereby determines the solar wind properties it experiences.

Also from Figure 2.5 it can be observed that the northern solar hemisphere had a magnetic field directed away from the Sun during the measurements, whereas the southern solar hemisphere had a magnetic field directed toward the Sun. During quiet solar conditions the solar magnetic field has a tilt and is reasonably constant and well defined, whereas during active solar conditions both the solar wind speed and the magnetic field are not so well defined, which can cause chaotic regions in the solar wind where the properties of the solar wind and magnetic field polarity can vary drastically [*McComas et al.*, 2003]. The magnetic polarity of the Sun reverses every 11 years, following that of the sun spot cycle which is discussed in the next section [*DeRosa et al.*, 2012].

In regions where there are oppositely directed magnetic fields, current flows between the magnetic fields. If the region extends over a large area, then large current sheets form. This occurs in the solar system due to the solar magnetic field and is depicted in Figure 2.6. The figure also shows the orbit of the Earth around the Sun with it passing through the heliospheric current sheet multiple times throughout its orbit. In the top right of Figure 2.6

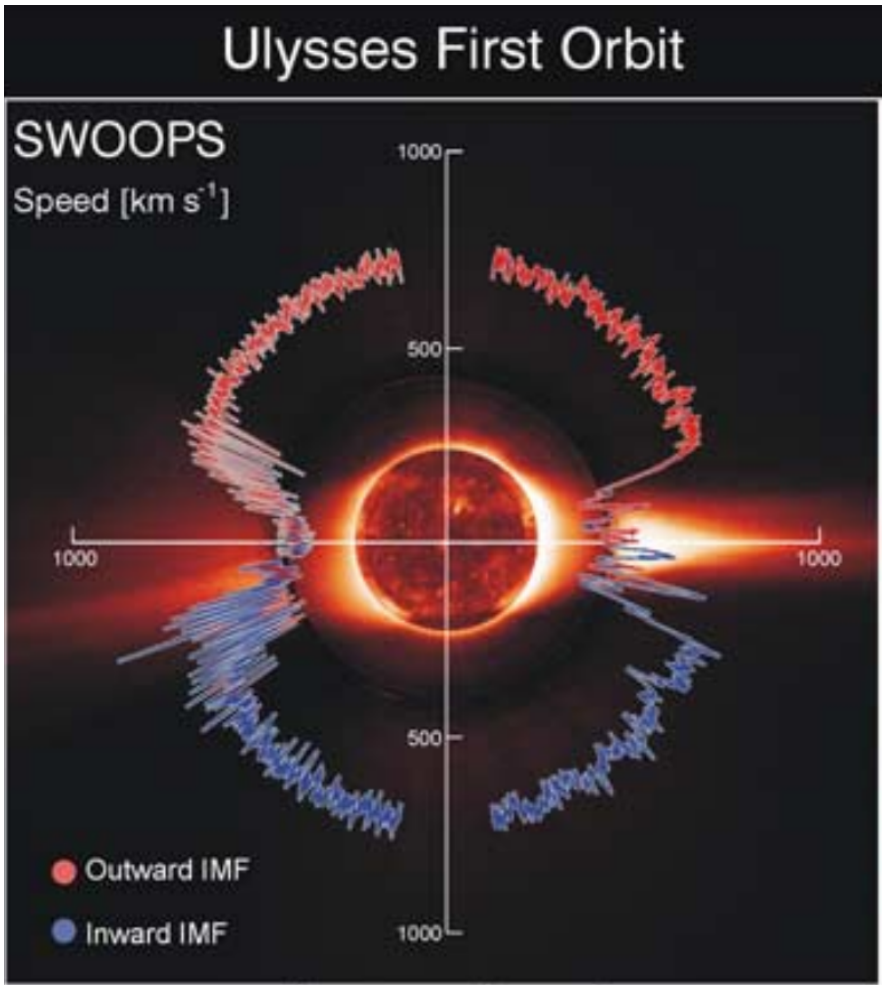

Figure 2.5: The solar wind velocity and magnetic polarity dependent on solar latitude. [*McComas et al.*, 2003]

there is also a depiction of the solar magnetic field geometry perpendicular to the orbit of the Earth. In the case of this insert, the Earth is in a region where the solar magnetic field is pointed towards the Sun.

The solar EM spectrum, as well as the solar wind and solar magnetic field properties vary with changing solar conditions. The solar conditions are governed by processes such as the solar cycle and solar flares. The changing solar conditions have periodicities and cycles that have been measured and can be approximately predicted. The ability to predict solar activity is important for predicting ionospheric conditions on Earth, where the solar wind and IMF influence the magnetosphere and ionosphere of the Earth. The next section describes the solar periodicities and cycles, and some of the previous studies performed to measure them.

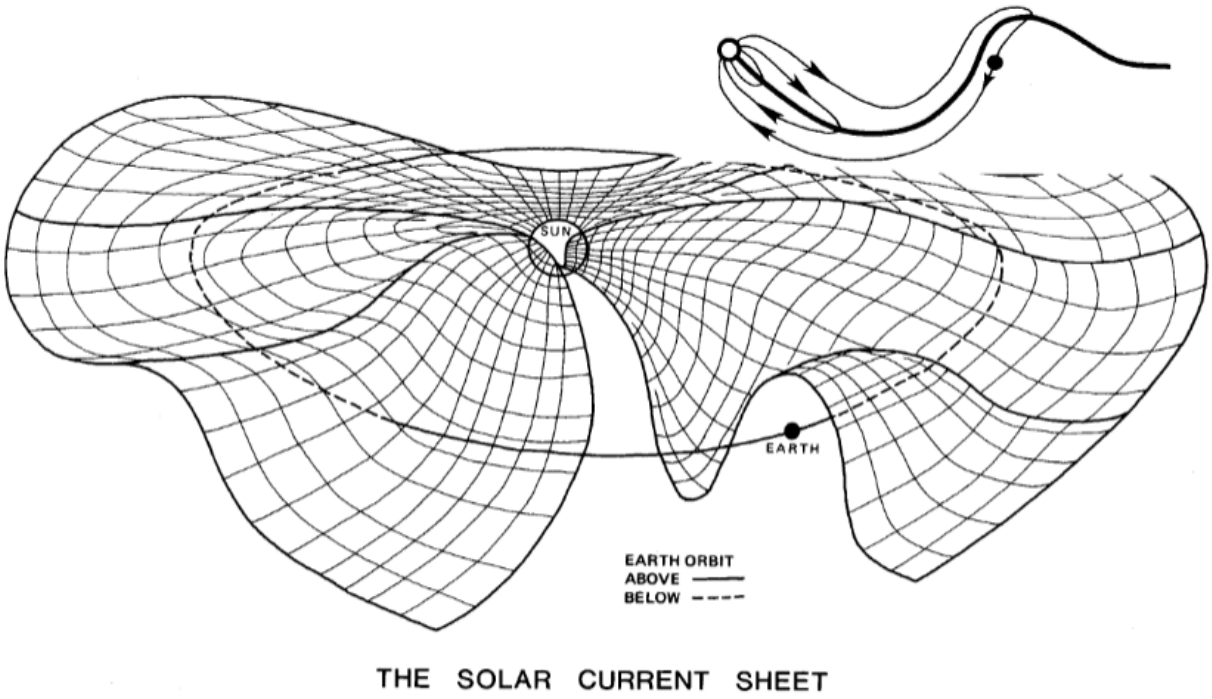

Figure 2.6: The heliospheric current sheet with a depiction of the orbit of the Earth. [*Akasofu*, 1981]

2.3.3 Sun Spots, Solar Cycles and the Solar Rotation

The conditions of the ionosphere are driven by the Sun, and can be occasionally predicted. Through solar activity predictions, it is possible to determine the most opportune times to operate the ICEBEAR system and search for ionospheric scatter in the measurements. The predictions of solar activity are driven by different factors and periodicities, some of which are described here.

The Sun will, from time to time, generate sunspots that appear on the photosphere [*Hathaway*, 2010]. The sunspots are darker and have a lower temperature than the surrounding region due to reduced convection from strong localized magnetic fields. Sunspots typically appear in pairs, with the magnetic field oriented into one and out of the other [*Cowling*, 1933]. There is a strong correlation between sunspots and increased solar activity, including increased coronal mass ejections, solar flares and prominences [*Hathaway*, 2010]. Coronal mass ejections are large scale ejections of particles and magnetic flux from the Sun outward into space, solar flares are an increase in EM radiation from an active area on the Sun, and

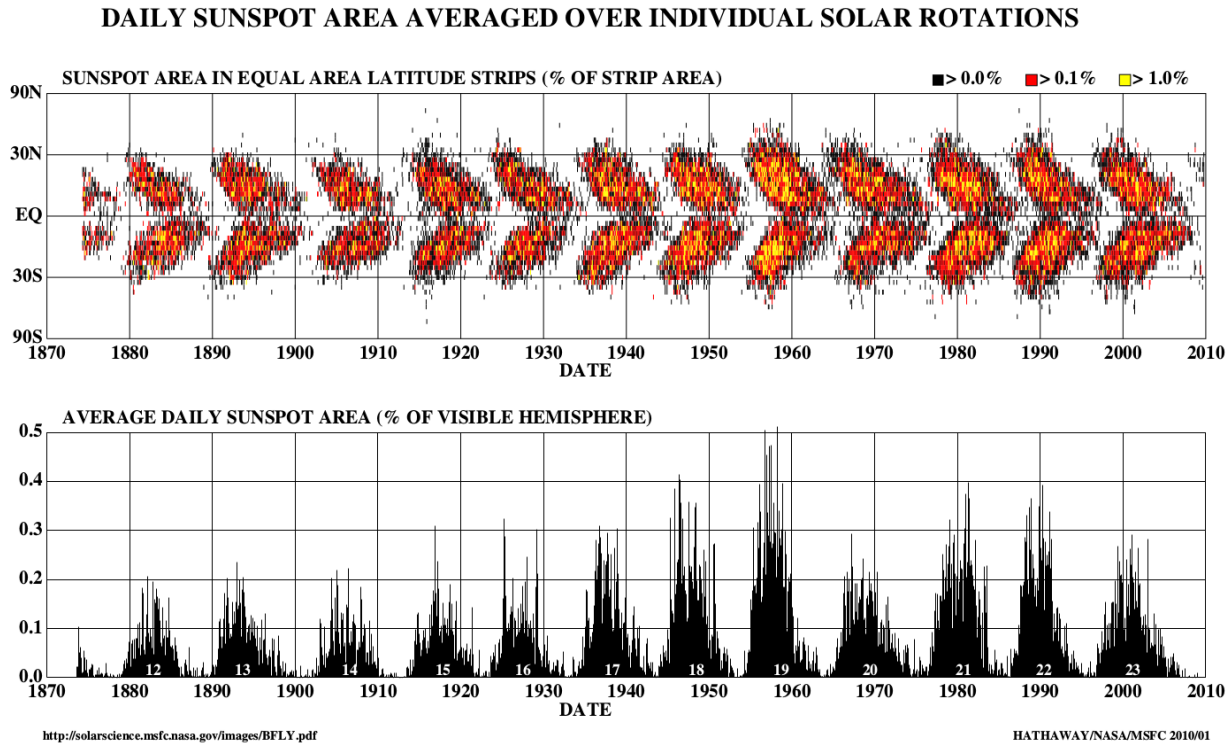

Figure 2.7: Plots depicting how sunspots vary with the 11 year solar cycle. [*Hathaway*, 2010]

prominences are extended active plasma loops that are still magnetically connected to the Sun [*Forbes*, 2000].

Sunspots typically follow an 11-year cycle, where there is an increase in the frequency of sunspots to a peak occurrence rate, which then decreases to a minimum [*Hathaway*, 2010]. The peak is known as solar maximum and the trough is known as solar minimum. A depiction of this 11-year cycle is presented in Figure 2.7. From the figure it can also be seen that the sunspots occur and propagate closer to the equator as the cycle progresses (top panel) and that not all cycles have the same coverage area of sunspots (bottom panel).

Along with the 11-year solar cycle, there is another periodicity from solar sources that is seen by the Earth. This is a 27-day periodicity due to a combination of the solar rotation and the orbit of the Earth. The Sun rotates once every 24.47 days at the solar equator, while the Carrington rotation, which takes the orbit of the Earth into consideration, is 27.2753 days [*Carrington*, 1863]. This is approximately how long it takes the Earth to see the same feature on the Sun twice, though it must be considered that different latitudes on the Sun rotate at

different rates. For predicting space weather this rotation period is very useful as the Earth will typically observe the same active region for multiple rotations of the Sun at a frequency of approximately the Carrington rotation. This 27-day periodicity has been observed in many solar wind properties [*Bame et al.*, 1993; *de Toma*, 2011; *Modzelewska and Alania*, 2013], as well as atmospheric measurements [*Lei et al.*, 2008; *Fioletov*, 2009; *Takahashi et al.*, 2010]. Knowing this information helped in the early stages of ICEBEAR operations to determine the most opportune times to search for interesting data.

Some of the planets have magnetic fields that can interact with the solar magnetic field and the solar wind. This interaction can result in interesting physical phenomena to occur, such as charged particle precipitation generating the the northern lights, or aurora borealis, on Earth.

2.4 The Magnetic Field of the Earth

The magnetic field of the Earth is generated from moving charge in the outer core region of the interior of the Earth [*Weiss*, 2002]. This magnetic field protects life on Earth from many energetic charged particles by deflecting them. The magnetic field strength at the surface of the Earth is on the order of 0.5 Gauss (0.5×10^{-4} T) and is relatively dipolar. In comparison, the magnetic field of the Sun at the Earth is approximately 10^{-9} T. The magnetic field of the Earth is tilted approximately 9.5 degrees from the rotation axis of the Earth, though it varies slightly over time [*Thébault et al.*, 2015]. The magnetic field is directed towards the Earth in the northern hemisphere and away from the Earth in the southern hemisphere. The northern magnetic pole of the Earth is therefore actually a "south" magnetic pole by definition and the southern magnetic pole of the Earth is actually a "north" magnetic pole.

The large scale plasma density perturbations that ICEBEAR measures are aligned parallel with the magnetic field of the Earth, and therefore the shape of the geomagnetic field is important for this dissertation. A description of the instabilities that produce these parallel plasma density irregularities is provided in Section 3.4. The solar wind and the solar magnetic field exert pressure on the magnetic field of the Earth, causing a deformation in the dipolar shape of the magnetic field of the Earth and a process called magnetic reconnection to occur.

2.4.1 Magnetic Reconnection

When two magnetic fields that are oppositely directed converge, a process called magnetic reconnection occurs. For reconnection to occur the frozen-in condition is broken and plasma is no longer bound by the magnetic field lines in the region of reconnection [*Treumann*, 2001]. In the case of the magnetic field of the Sun, this occurs commonly in the form of solar flares [*Masuda et al.*, 1994]. The solar magnetic field and the geomagnetic field can also exhibit reconnection, which commonly occurs at the magnetopause (dayside) [*Sonnerup et al.*, 1981] and at the magnetotail (nightside) [*Sergeev et al.*, 1995] in the geospace environment. The process of reconnection provides a mechanism by which the geomagnetic field is directly connected to the IMF, which can create particle precipitation and ionospheric convection in the ionosphere of the Earth. There are models that attempt to describe this reconnection process, but it is still not fully understood.

Magnetic reconnection is something extremely important in the phenomena that ICEBEAR measures. The effects on the ionospheric convection pattern and the electric fields generated from charged particle precipitation due to magnetic reconnection can be measured indirectly by ICEBEAR, where ICEBEAR measures plasma density perturbations generated from these phenomena. A further description of the ionospheric convection and plasma density perturbations is provided in Chapter 3.

One of the first models of reconnection was the Sweet-Parker model [*Parker*, 1957]. The model considers that the plasma is non-turbulent and that there is a steady state solution described by MHD equations. The Sweet-Parker model is generally realized in 2 dimensions (2-D), with the configuration of the system as shown in Figure 2.8.

In the figure, B is the magnetic field, V_{in} is the inflowing plasma velocity, V_{out} is the outflowing plasma velocity, δ is the half width of the current sheet, and L is the half length of the current sheet. Following *Kulsrud* [2001], one can derive the reconnection rate. Only a brief overview of the Sweet-Parker reconnection model is provided here.

V_{out} in Figure 2.8 is given by,

$$V_{out} \approx \frac{B}{\sqrt{\mu_0 \rho}} \tag{2.3}$$

where B is the magnetic field, μ_0 is the magnetic permittivity, and ρ is the density of the

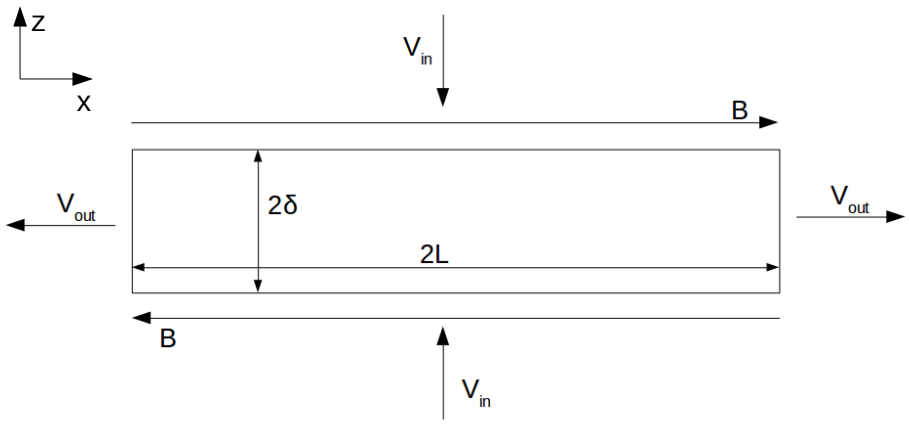

Figure 2.8: A 2-D system configuration for the Sweet-Parker magnetic reconnection model.

plasma. The value of V_{out} is also known as the Alfvén velocity (v_a).

Magnetic diffusivity, η [*Chen*, 2006], is also introduced as,

$$\eta = \frac{1}{\mu_0 \sigma} = \frac{1}{\mu_0} \frac{m_e \nu_e}{n_e e^2} \tag{2.4}$$

where m_e is the mass of an electron, ν_e is the collision rate of the electrons with the ions, n_e is the plasma density, and e is the fundamental charge.

A parameter that corresponds to the conductivity of a plasma, which is called the Lundquist number [*Loureiro and Uzdensky*, 2016], is given as,

$$S = \frac{L v_a}{\eta} \tag{2.5}$$

where L is the half-length of the reconnection region. Highly conductive plasmas have a large Lundquist number while highly resistive plasmas have a small Lundquist number. In the case of space plasmas, the Lundquist number is typically large ($> 10^{10}$).

The resulting reconnection rate for the Sweet-Parker model is given by,

$$R = \frac{V_{in}}{V_{out}} = \frac{\delta}{L} \approx \sqrt{\frac{\eta}{L v_a}} = \frac{1}{\sqrt{S}} \tag{2.6}$$

Through computer aided analysis, the Sweet-Parker magnetic reconnection model has been shown to be accurate for small Lundquist numbers, but does not accurately represent the speed of the reconnection process for plasmas with large Lundquist numbers [*Loureiro and*

Uzdensky, 2016]. As typical space plasmas have large Lundquist numbers, a better model must be used to accurately depict the reconnection process in the magnetosphere.

Petschek [1964] attempted to create faster reconnection rates for the Sweet-Parker model by considering a small localized portion of the current sheet that reconnects, rather than a large area. This model produces a reconnection rate of,

$$R = \frac{1}{\log(S)} \tag{2.7}$$

The reconnection rate of the Petschek model is much faster than the Sweet-Parker model, and occasionally is too fast [*Loureiro and Uzdensky*, 2016]. One issue with the Petschek model is that it uses shocks from a region to drive the reconnection process, without a mechanism by which these shocks are generated. As well, numerical solutions do not result in the Petschek solution with uniform or gradually changing resistivities over the region in consideration. If localized enhancements of resistivity in the numerical simulations are considered, the results do show some similarities to the Petschek model [*Loureiro and Uzdensky*, 2016]. These local enhancements in the resistivity fall within the effects of anomalous resistivity, which only occurs in plasmas when the charged particle cyclotron frequency is large compared to the collision frequency ($\omega_c \gg \nu$) [*Papadopoulos*, 1977]. Anomalous resistivity is the formation of localized enchancements in the plasma resistivity due to turbulence. It is likely that collisionless reconnection would occur before the Petschek model would be realized in nature [*Loureiro and Uzdensky*, 2016].

Presented here is a brief overview of magnetic reconnection, where research is still undergoing to understand this phenomena. What is known is that reconnection between the geomagnetic field and the IMF drives high latitude plasma convection in the ionosphere of the Earth and can produce particle precipitation at auroral latitudes [*Kelley*, 2009], which produce signatures detectable by E-region radars, such as ICEBEAR.

2.4.2 The Magnetosphere of the Earth

The dipolar magnetic field of the Earth, also known as the geomagnetic field, is compressed on the sunward side and elongated in the shadow of the Earth [*Sibeck et al.*, 1991; *Petrinec and Russell*, 1996]. This distortion is due to the solar wind exerting pressure on the magnetic field

of the Earth. Where equilibrium is reached between the dynamic pressure of the solar wind and the magnetic pressure of the magnetosphere of the Earth is the magnetopause. This is the boundary of the magnetosphere of the Earth. The dynamic pressure exerted by the solar wind on the magnetosphere varies, depending on the speed and density of the solar wind, and therefore the location of the magnetopause also changes [*Russell and Elphic*, 1978]. The magnetopause is located about 10 Earth radii upstream of the Earth during average solar wind conditions (density of 5 cm^{-3}, velocity of 400 km/s), and it can be located as close as about 5 Earth radii during extremely active solar wind conditions (density of 100 cm^{-3}, velocity of 1600 km/s) [*Otto*, 2005]. On the nightside of the Earth, the magnetopause location varies greatly, where it has been modelled to be in the range of 10 Earth radii to more than 100 Earth radii [*Wang et al.*, 2018].

The solar wind generates an electric field that is mapped into the magnetosphere of the Earth. This electric field is given by Equation A.33 in Appendix A,

$$E_{IMF} = -V_{sw} \times B_{IMF} \tag{2.8}$$

where V_{sw} is the velocity of the solar wind and B_{IMF} is the interplanetary magnetic field (IMF). This electric field creates a potential difference across the magnetosphere of the Earth. The potential is associated with the magnetic field lines, and can be mapped down to the surface of the Earth. The value of this potential difference is given by

$$V_{magnetosphere} = -E_{IMF} d_y \tag{2.9}$$

where d_y is the distance spanning the front of the ionosphere. The potential difference is typically in the range of 10–150 kV [*Boyle et al.*, 1997]. Notice that the polarity of the magnetic field will change the direction of the electric field in the magnetosphere of the Earth. This can change the orientation of the plasma convection in the poleward ionospheric regions [*Reiff*, 1982]. The convection of plasma in the polar caps of the Earth is a complex process, but this provides a basic understanding of how the convection flows occur.

The electric field that is mapped to the magnetosphere of the Earth is due to reconnection between the IMF and the geomagnetic field. When magnetic reconnection is suppressed due to the orientation of the IMF, the electric field is not able to be mapped down to the Earth,

as there are relatively few magnetic field lines from the Earth connected to the IMF. The reconnection rate can therefore affect plasma convection velocities [*Lockwood et al.*, 1990]. The electric field affects the strength and orientation of the ionospheric plasma convection, and the resulting cross polar cap potential may be measured by many different instruments including magnetometers [*Ridley and Kihn*, 2004], HF radars [*Shepherd et al.*, 2002] and satellites [*Reiff et al.*, 1981]. This is important for ICEBEAR as the electric fields mapped to the ionosphere drive ionospheric convection and can cause the growth of plasma density irregularities which the ICEBEAR signal scatters from.

A depiction of the magnetosphere of the Earth can be seen in Figure 2.9, where the IMF is also included. On the sunward side of the Earth reconnection can occur, where the oppositely directed magnetic fields merge. The post-reconnection magnetic field lines (the geomagnetic field lines that are connected to the magnetic field of the Sun) are carried across the polar cap to the nightside by the plasma. On the nightside the magnetic fields reconnect in the magnetotail, which is the region of elongated magnetic field lines on the night side of the Earth. Following magnetic reconnection in the magnetotail, the newly reconnected and highly distorted geomagnetic field attempts to return to a low-energy dipolar state. This transition accelerates plasma that is trapped along the magnetic field lines towards the Earth [*Paschmann et al.*, 1979], which can cause energetic charged particle precipitation in the auroral regions.

At the bottom of Figure 2.9 there is a zoomed in picture of the northern polar region of the Earth which shows the magnetospheric convection path mapped down to the Earth. It can be observed that the flows cross the polar cap from the sunward side to the anti-sunward side before traversing back to the sunward side at lower latitudes. This is the steady state convection pattern of the ionosphere of the Earth, which will be discussed further in Section 3.2. The ICEBEAR system has a field of view in the shaded "Auroral Zone" of the figure.

During magnetospheric reconnection the plasma associated with the reconnected magnetic field lines travels towards the Earth. As the plasma moves closer to the Earth it experiences a stronger magnetic field, effectively separating the ions and electrons along the dawn-dusk direction. This is due to the decreasing gyroradius with increasing magnetic field strength.

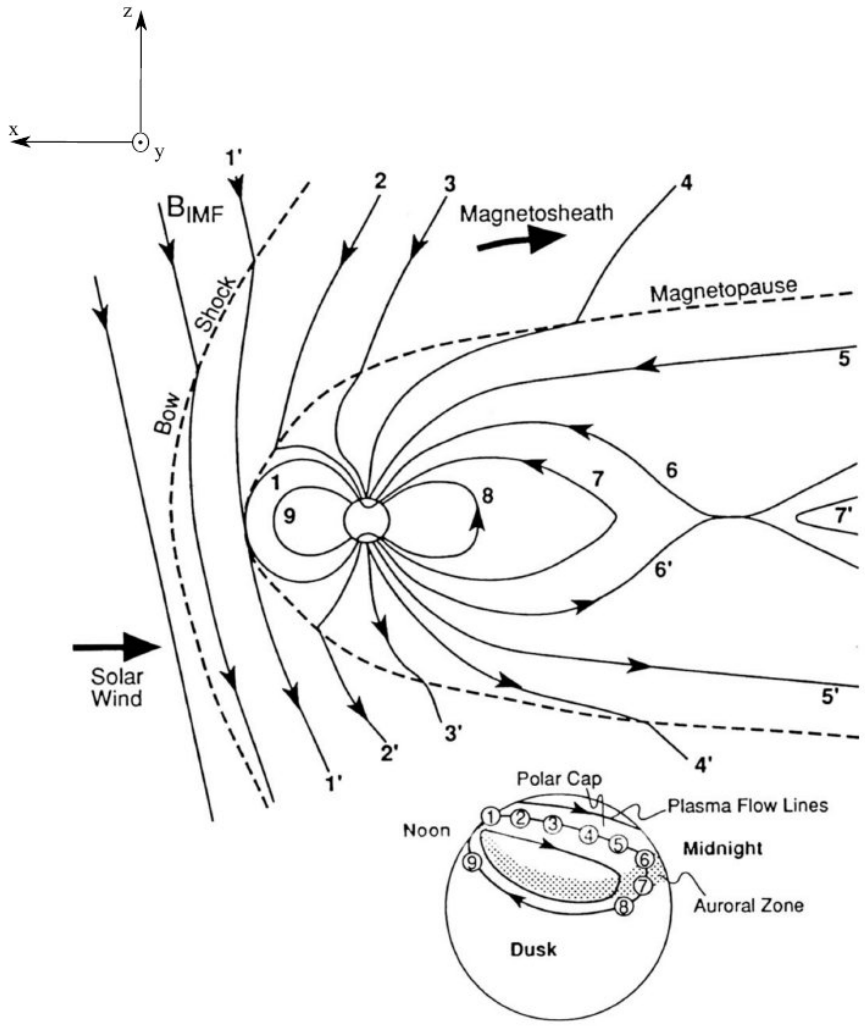

Figure 2.9: An example of magnetic reconnection in the geospace environment, where the insert shows the polar ionospheric convection pattern of the plasma. [From *Kivelson and Russell*, 1995]

A depiction of this process can be seen in Figure 2.10, where this figure shows the generation of the current across the magnetopause.

In the case of the dayside magnetopause of the Earth (Figure 2.10), the ions are deflected to the dusk side and the electrons are deflected to the dawn side [*Kelley*, 2009]. This results in currents flowing down the magnetic field lines on the dusk side and up the magnetic field lines on the dawn side. The currents generated from the dayside map to high auroral latitudes and are known as Region I currents. In the magnetotail of the Earth, the ions are deflected in the dawn direction and the electrons are deflected in the dusk direction. This results in

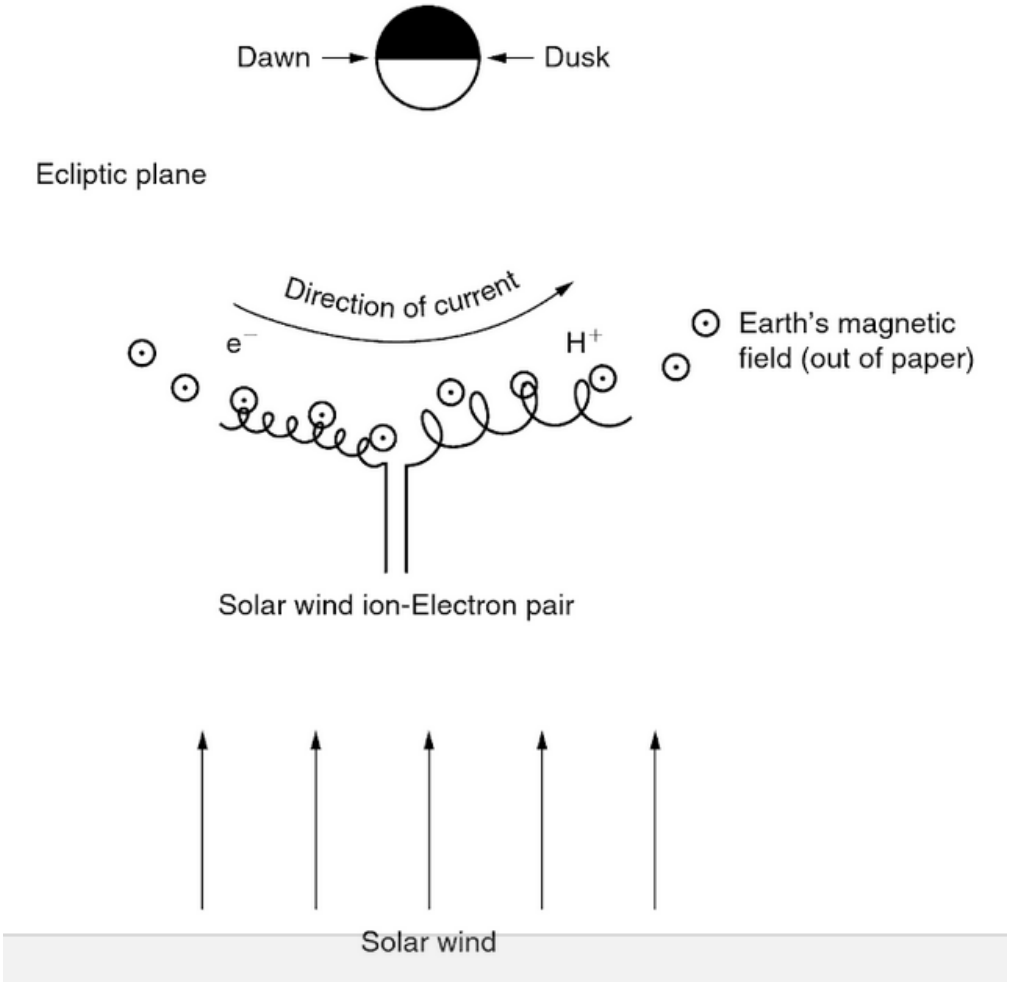

Figure 2.10: Depiction of the deflection of charged particles as they enter stronger magnetic field regions. This deflection generates a current across the magnetopause. [*Kelley*, 2009]

currents flowing downward, toward the Earth, on the dawn side and upward, away from the Earth, on the dusk side in the low latitude regions. These generated currents are known as Region II currents. This is why the Region I and II currents on the same side of the pole are of opposite polarity, which is shown in Figure 2.11. The region where these currents typically flow is known as the auroral region.

A depiction of the magnetospheric currents mapped to the northern hemisphere of the Earth is shown in Figure 2.11. There are three different labels for the currents in this region, the field-aligned currents, the Hall currents, and the Pederson currents. The field-aligned currents travel along the magnetic field lines, the Hall currents are directed perpendicular to

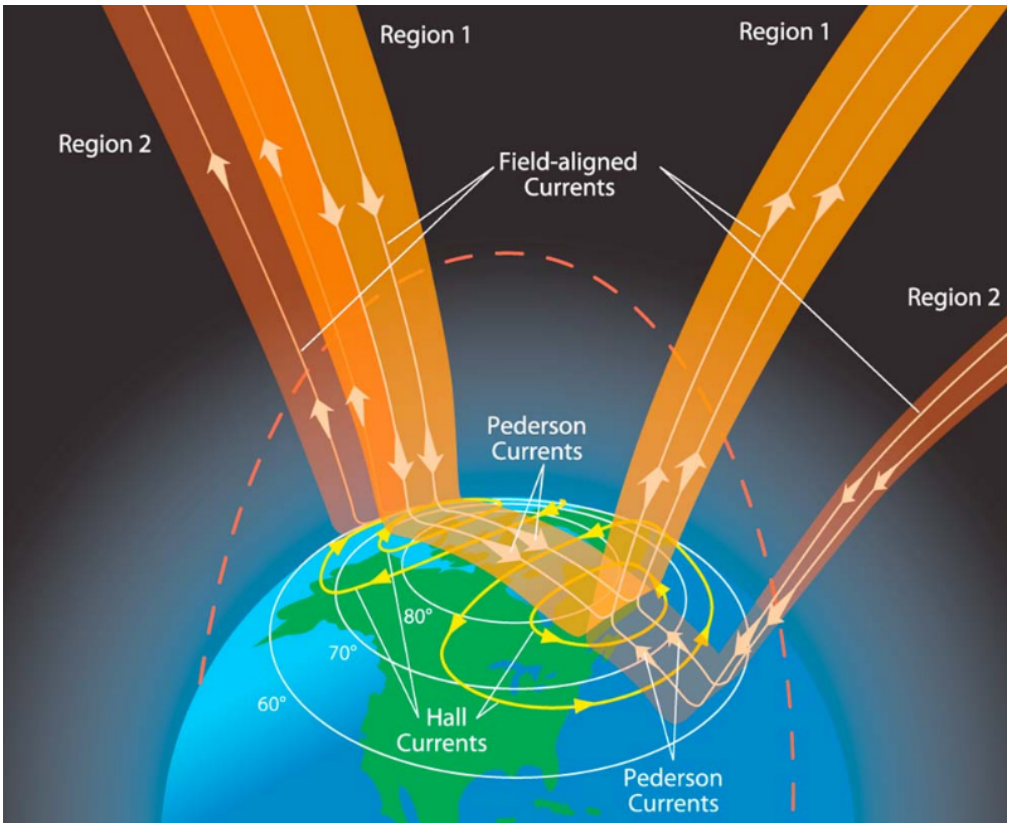

Figure 2.11: Magnetospheric currents mapped to the northern hemisphere of the Earth. The lighting of the Earth is not accurate, where the Sun would be opposite the direction of the flow over the polar cap (Figure 2.9). [*Le et al.*, 2010]

the magnetic field and the electric field, and the Pederson currents are directed parallel to the electric field and perpendicular to the magnetic field. A more in depth analysis of these currents in the ionosphere is provided in Section 3.2. What is important to know is that currents can flow down the magnetic field lines from the magnetosphere, depositing energy into the auroral and polar regions of the Earth. The ICEBEAR system makes measurements of plasma density irregularities in the auroral region of the Earth, where this energy is deposited.

The currents in the magnetosphere can be caused by either electrons or ions. A large scale view of the magnetospheric current system of the Earth is shown in Figure 2.12. Recall, for charged particles, a current is present between two oppositely directed magnetic fields. This means that there is a current sheet in the magnetotail of the Earth and there can be a current sheet at the magnetopause, depending on the IMF conditions. There can also be currents

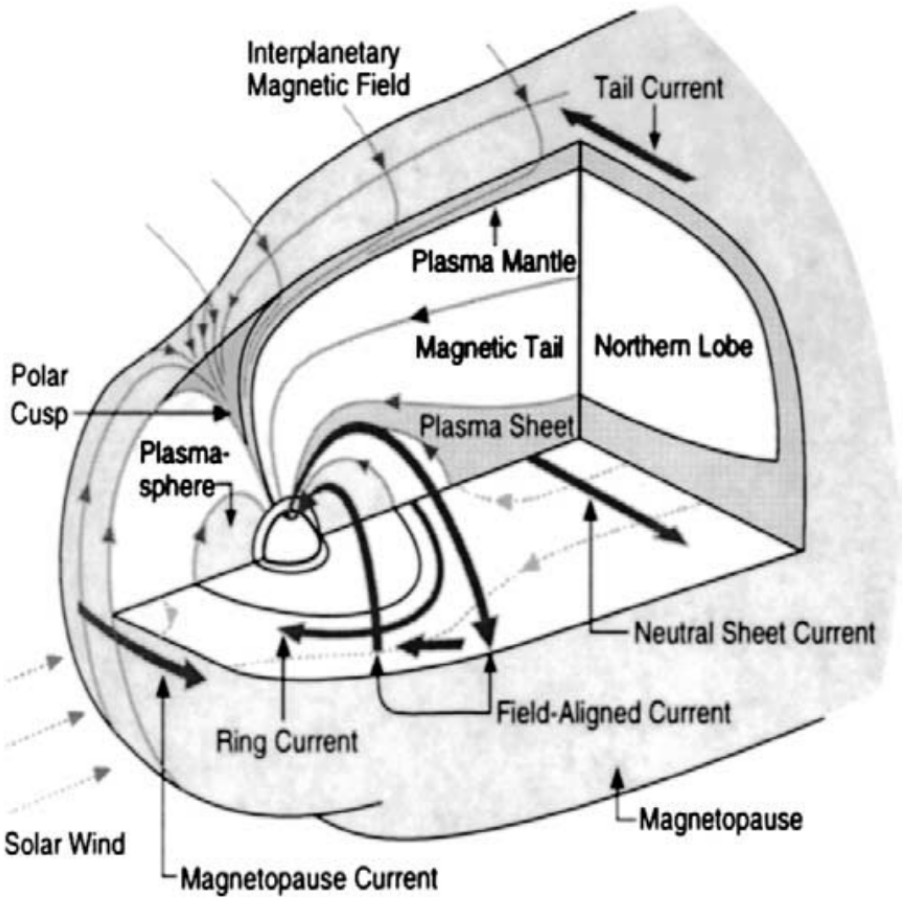

Figure 2.12: Magnetospheric current system of the Earth. [*Russell*, 2004]

that flow along magnetic field lines in the magnetosphere, which have been mentioned already as field-aligned currents. These currents are due to the fact that in the magnetosphere the conductivity parallel to magnetic field lines is typically much larger than the conductivity perpendicular to them.

In many instances, currents in the magnetosphere can be carried by waves. A type of wave that is common in the magnetosphere of the Earth is the Alfvén wave [*Alfvén*, 1942]. These Alfvén waves are MHD perturbations along magnetic field lines, and can create the field-aligned currents in the magnetosphere that connect to the ionosphere [*Chaston et al.*, 2007]. Section 2.4.3 discusses Alfvén waves and how they relate to the magnetosphere and ionosphere system of the Earth.

2.4.3 Magnetospheric Alfvén Waves

Alfvén waves [*Alfvén*, 1942] are MHD perturbations that can occur in systems with magnetic fields. These waves are relatively low frequency (0.1 – 10 Hz) in comparison to the cyclotron frequency of the charged particles. Alfvén waves and the associated field-aligned currents couple the magnetosphere and the ionosphere of the Earth. The ICEBEAR system is able to make measurements of ionospheric plasma density perturbations at high temporal resolutions that can be used to detect signatures of these waves.

An Alfvén wave is described by the equation,

$$\frac{\partial^2 \mathbf{B}'}{\partial z^2} = \frac{4\pi\rho}{B_0^2}\frac{\partial^2 \mathbf{B}'}{\partial t^2} \tag{2.10}$$

where B_0 is the homogenous background magnetic field, which in our case is the geomagnetic field, and the z-axis is setup to be parallel with it. $\mathbf{B}'$ is the magnetic field that varies with z and time (t), and ρ is the mass density of the plasma. This results in a velocity of,

$$V = \frac{B_0}{\sqrt{4\pi\rho}} \tag{2.11}$$

along the z direction. The velocity is therefore dependent on the strength of the magnetic field and the plasma density, and the wave propagates along the magnetic field direction.

Alfvén waves are generated in the magnetosphere from processes that perturb the plasma along the magnetic field lines, such as magnetic reconnection. Once the perturbation is generated the wave can propagate along the magnetic field line. In the case of the magnetosphere, this propagation is ultimately directed toward the Earth and is a mechanism by which the magnetosphere and ionosphere of the Earth are coupled. Some processes involved in this coupling include the ionospheric feedback instability and the ionospheric Alfvén resonator [*Lysak*, 1991; *Chaston et al.*, 2002].

The mass density of the atmosphere/thermosphere of the Earth decays exponentially with altitude [*Qian and Solomon*, 2012], while the magnetic field decays at a slower rate with altitude, resulting in an increase of the Alfvén wave speed with altitude ($V \propto \frac{B}{\sqrt{\rho}}$). The upper boundary of the ionospheric Alfvén resonator is where this velocity reaches a peak [*Lysak*, 1991]. The lower boundary is at the lower ionosphere of the Earth, where the Alfvén wave speed falls quickly due to a decrease in the density of the plasma. This results

in a region from the lower ionosphere to approximately 2-3 R_E where standing waves can be formed with periodicities of approximately 0.1–10 Hz. The standing waves can enhance and occur at the same time as the ionospheric feedback instability, which can further accelerate precipitating electrons and produce fine-scale auroral structures [*Lysak*, 1991].

The ionospheric feedback instability occurs due to precipitating energetic charged particles. These charged particles, upon reaching the ionosphere, ionize multiple neutral air molecules. This causes a large increase in the conductivity of the ionosphere. A positive feedback is created, where the increase in conductivity allows more charged particles to precipitate, further increasing the conductivity [*Lysak*, 1991]. The increase in particle precipitation can be detected by instruments measuring the ionosphere, such as magnetometers and auroral imagers [*Streltsov et al.*, 2010]. ICEBEAR will also be able to detect this increase in particle precipitation.

2.5 Overview of the Space Environment of the Earth

In summary, the Sun generates a magnetic field, charged particles, and EM flux that propagate outward from it. These fields and particles interact with the atmosphere and magnetosphere of the Earth to influence the ionosphere. The relationship between the magnetosphere and the solar wind/IMF can cause ionospheric particle precipitation and plasma convection in the auroral and polar regions of the Earth through magnetic reconnection. The field of view (FOV) of the ICEBEAR system is situated in the auroral region, allowing the measurement of ionospheric plasma density irregularities generated from these dynamic processes, and the signatures of magnetospheric waves that propagate down to the ionosphere. Signatures of this coupling between the ionosphere and magnetosphere will be observed in great temporal and spatial detail using the ICEBEAR system. Chapter 3 describes how the solar EM flux creates the ionosphere of the Earth, and the physics behind the plasma dynamics of the ionosphere, including the generation of plasma density irregularities through plasma instability processes.

Chapter 3

The Ionosphere of the Earth

Portions of Section 3.4.1 were originally published in Huyghebaert, D., G. Hussey, J. Vierinen, K. McWilliams, and J.-P. St-Maurice (2019), ICEBEAR: An all-digital bistatic coded continuous-wave radar for studies of the E region of the ionosphere, *Radio Science*, *54*(4), 349–364, doi: 10.1029/2018RS006747.

The ionosphere of the Earth is located from 60 km to 1000 km in altitude above the surface of the Earth [*Kelley*, 2009]. It is a region where plasma is generated and can persist over significant periods of time. The persistence of plasma in the ionosphere is due to the low particle density, resulting in a low recombination rate with neutral constituents, and the absorption of solar EM radiation during the day.

This generation and persistence of plasma in the ionosphere makes it a complex region. When trying to model the ionosphere, multiple species under the influence of EM forces can be considered. The neutrals, ions, and electrons are treated as different species in analysis, and, for more accurate results, the ions and neutrals can be sub-divided into different species of atoms and molecules, such as molecular oxygen (O_2) and nitric oxide (NO). Due to the multiple forces and particles to consider, along with not knowing exact particle densities, there are many difficulties in accurately analytically modelling the ionosphere, and in many instances assumptions and numerical solutions must be used to model and better understand the underlying physics.

The ionosphere is what the ICEBEAR radar measures, specifically the lower region of the ionosphere, the E-region. The radar signals scatter off perturbations in the plasma density (the physics of this scattering will be covered in the next chapter). This chapter investigates

---

Portions of Section 3.4.1 were originally published in *Huyghebaert et al.* [2019].

the physics behind the formation of the ionosphere, the steady state dynamics of the auroral ionosphere, and the generation of the gradient drift [*Linson and Workman*, 1970] and Farley-Buneman [*Farley*, 1963a; *Buneman*, 1963] instabilities which can cause perturbations in the ionospheric plasma density to grow.

3.1 Formation of the Ionosphere

Plasma is formed around the Earth at altitudes greater than 60 km. This plasma is created primarily through the absorption of solar EM radiation [*Bradbury*, 1938; *Nicolet and Aikin*, 1960] and does not rapidly recombine due to the low atmospheric density at these altitudes. Different species of atmospheric particles absorb different wavelengths of EM radiation and this, along with a decreasing recombination rate with altitude, creates multiple peaks in the plasma density [*Kelley*, 2009]. The altitudes these plasma density peaks occur at define the D-, E-, and F-regions of the ionosphere, which are discussed in Section 3.3. The depth of penetration of the solar EM radiation and the absorption rate of this radiation by an atmospheric species can be modelled using Chapman production functions [*Chapman*, 1931a,b].

The Chapman function is given by the equation [*Hunsucker and Hargreaves*, 2007],

$$q(z) = q(z_0) \exp\left(1 - \frac{e^{-z'}}{\cos\chi} - z'\right) \tag{3.1}$$

where $q(z)$ is the ionization rate for a given altitude, z, $q(z_0)$ is the peak ionization rate, z_0 is the altitude the peak ionization rate occurs at, χ is the zenith angle of the Sun, and z' is given by the equation,

$$z' = \frac{z - z_0}{H} \tag{3.2}$$

where H is the scale height, given by the equation,

$$H = \frac{k_B T}{mg} \tag{3.3}$$

where k_B is the Boltzmann constant, T is the temperature of the atmospheric species, m is the mass of the atmospheric species, and g is the gravity.

Some of the common plasma production curves in the ionosphere are shown in Figure 3.1, where it includes plasma production from both solar irradiance and photo electrons. Different atmospheric species have different Chapman curves, due to the different scale heights

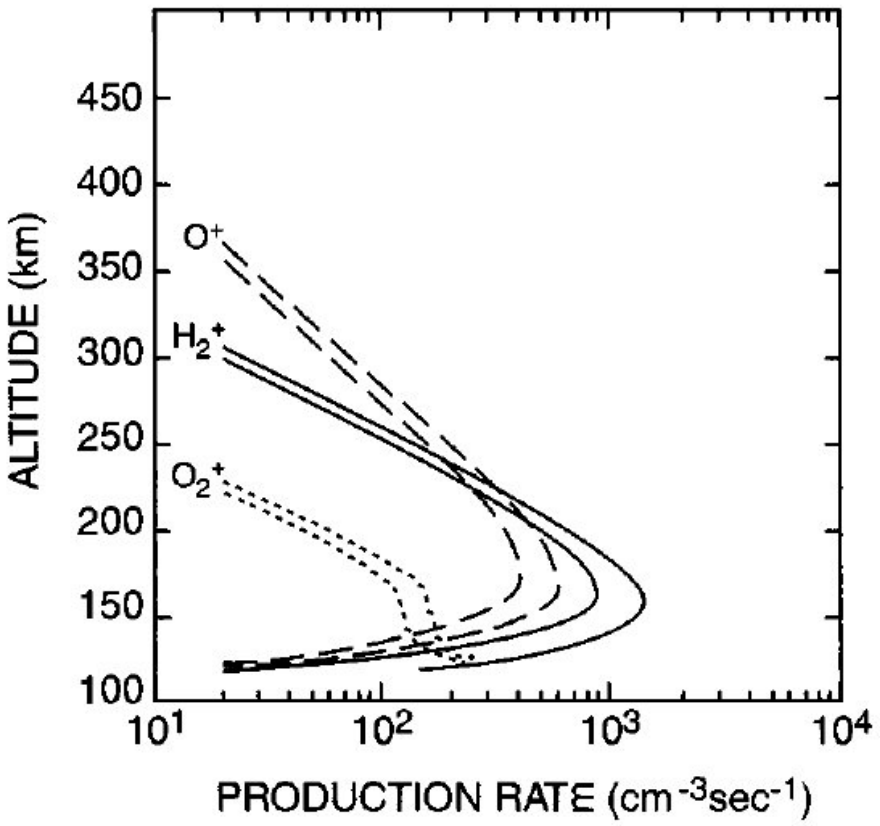

Figure 3.1: Production rates of plasma from the absorption of solar irradience in the ionosphere for different atmospheric species. The lesser production rate for each species does not include photo electrons. [From *Schunk and Nagy*, 2009]

associated with the species. The absorption spectrum for different atmospheric species is complicated, as there are multiple wavelengths of EM radiation that each species can absorb. The wavelengths of possible photon absorption are related to the absorption cross section of the different atmospheric species [*Nicolet and Aikin*, 1960]. This absorption of radiation can result in electron disassociation (creation of plasma), an enhanced energy state of the particle, and/or the disassociation of a molecule.

The steady state ionosphere will have a plasma density profile similar to that shown in Figure 3.2. The figure shows the densities of the multiple neutral and ion atmospheric species, as well as the electron density (e^-) which is the bulk plasma density. Clearly there is variance in the dominant ion species with altitude, which depends on the very complex atmospheric chemistry.

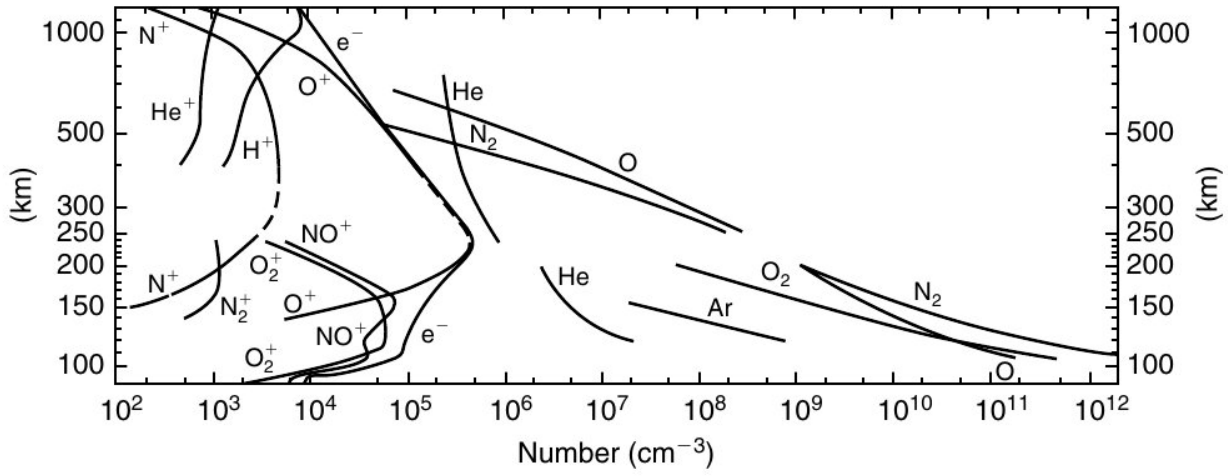

Figure 3.2: A vertical profile of the electron, ion and neutral densities in the ionosphere of the Earth. The bulk plasma density is considered equal to the electron density. [From *Johnson*, 1969]

Once the plasma is formed, the ions can transfer charge to different atmospheric species upon collisions in the lower ionosphere. Some of the processes for atomic oxygen are [*Kelley*, 2009; *Pfaff*, 2012],

$$O^+ + N_2 \rightarrow NO^+ + N \tag{3.4}$$

and,

$$O^+ + O_2 \rightarrow O_2^+ + O \tag{3.5}$$

where O is atomic oxygen, O_2 is molecular oxygen, N is atomic nitrogen, N_2 is molecular nitrogen, NO is nitric oxide, and the + exponent refers to a ion, where the species has a missing electron. At high altitudes, the densities of N_2 and O_2 are reduced, causing O to be the dominating ionized species, and these reactions to occur less frequently.

From *Kelley* [2009], the recombination rate of the plasma in the ionosphere varies with altitude. This variation is due to different dominant ion species at different altitudes and the collision rates between these ionic species and the electrons and background neutrals. At ionospheric E-region altitudes there are two dominant chemical processes that result in plasma recombination, which are,

$$NO^+ + e^- \rightarrow N + O \tag{3.6}$$

and,

$$O_2^+ + e^- \rightarrow O + O \tag{3.7}$$

where e refers to an electron. At F-region altitudes, the dominant recombination process is,

$$O^+ + e^- \rightarrow O + photon \tag{3.8}$$

Dissociative recombination (Equations 3.6 and 3.7) occurs more quickly than the radiative recombination (Equation 3.8) and, along with the increased collision rate of the atmospheric species at lower altitudes, causes the lower altitude plasma to recombine much more quickly than the higher altitude plasma, which mainly consists of $O+$ [*Kelley*, 2009; *Pfaff*, 2012].

One reason for the slow recombination rate in the high altitudes is that the faster recombination process for $O+$ ions is a two step process [*Kelley*, 2009]. The radiative recombination is a slow process, but the O^+ can transfer the charge to a O_2 or NO molecule when collisions occur. From there, the ionic molecule recombines with an electron and dissociative recombination can occur (Equations 3.6 and 3.7). These are some of the dominant chemical reactions in the ionosphere, but for a more comprehensive list, refer to *Ferguson* [1967].

Plasma in the ionosphere can also be created from charged particle precipitation [*Kelley*, 2009]. This process occurs at the high latitude regions of the Earth, where charged particles are able to follow magnetic field lines and precipitate into the atmosphere of the Earth. These charged particles collide with neutral particles, transferring energy to the neutral particles and resulting in excess energy being shed by emission of an electron. With a high energy charged particle this can create a cascade effect as the particle collides with multiple neutrals, generating a significant amount of ionization [*Kelley*, 2009]. The increase in ionization can also cause more particles to precipitate through the feedback mechanism discussed in Section 2.4.3. Some modelled precipitating electron penetration depths based on the electron energy and the pitch angle of the incoming electrons are shown in Figure 3.3. The pitch angle refers to the velocity distribution of the incoming charged particles with respect to the background geomagnetic field. The resulting figure provides evidence that precipitating charged particles with pitch angles greater than $\approx 67^\circ$ are reflected back into the magnetosphere. For a peak energy deposition of 100 km (E-region altitudes), the charged particles precipitating would have an energy < 100 keV according to this model. For rare

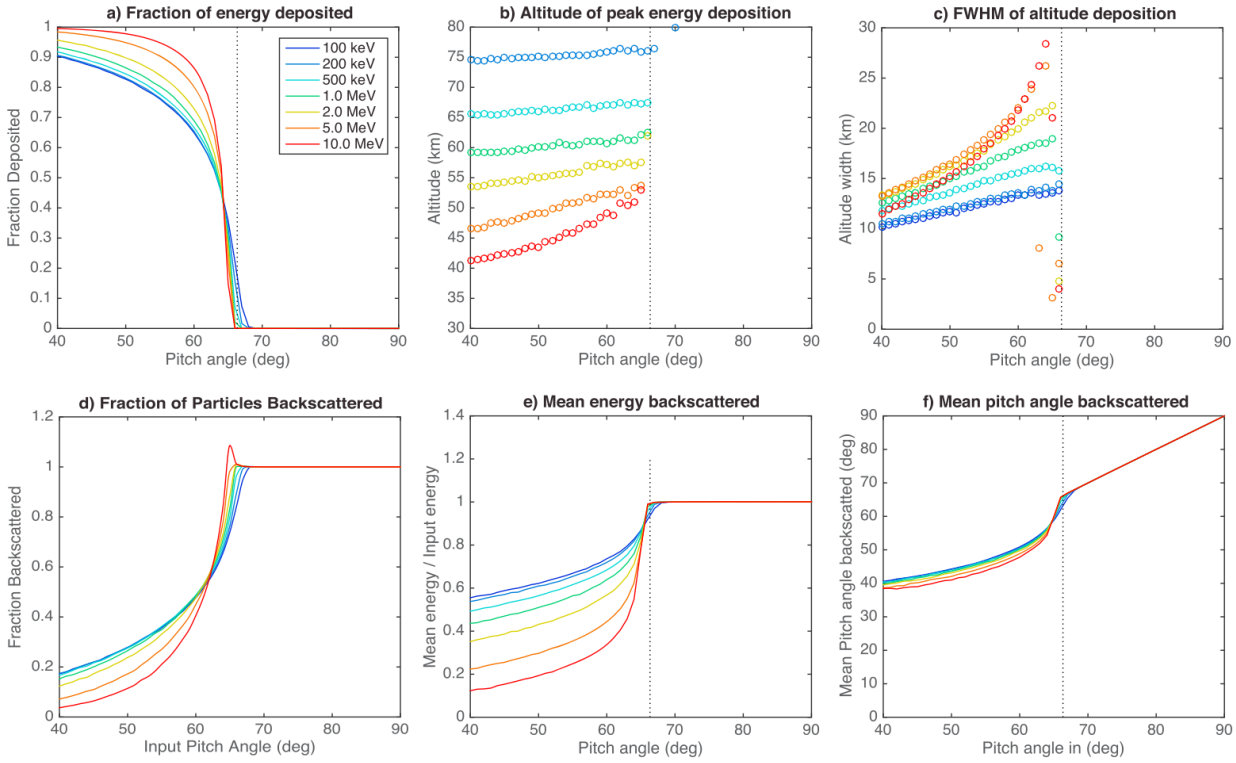

Figure 3.3: Electron energy deposition altitude based on electron energy and pitch angle using Monte Carlo simulations. [*Marshall and Bortnik*, 2018]

extremely energetic electron precipitation (> 10 MeV), the model shows that the particles can reach altitudes as low as 40 km. The possible penetration depth of these particles is important to note, as ICEBEAR measures plasma at altitudes of 90–120 km. The ICEBEAR radar can therefore measure plasma density perturbations at altitudes where charged particle precipitation energy deposition occurs.

During periods of energetic particle precipitation in the auroral zone, multiple different emission wavelengths of light can be observed. The wavelength of these emissions is related to the altitude at which the atmosphere is ionizing and recombining due to the chemical processes [*Banks et al.*, 1974]. This emission spectrum forms the aurora borealis. An example of the production rate of the red and green portion of the EM spectrum due to energetic particle precipitation is shown in Figure 3.4. While both emissions are due to energetic atomic oxygen, the atomic energy state transition is different (different wavelengths of light). The energy state transition of the red emission is slower than that of the green [*Rees and Jones*, 1973]. If the atomic oxygen collides with another atmospheric species before it transitions, it

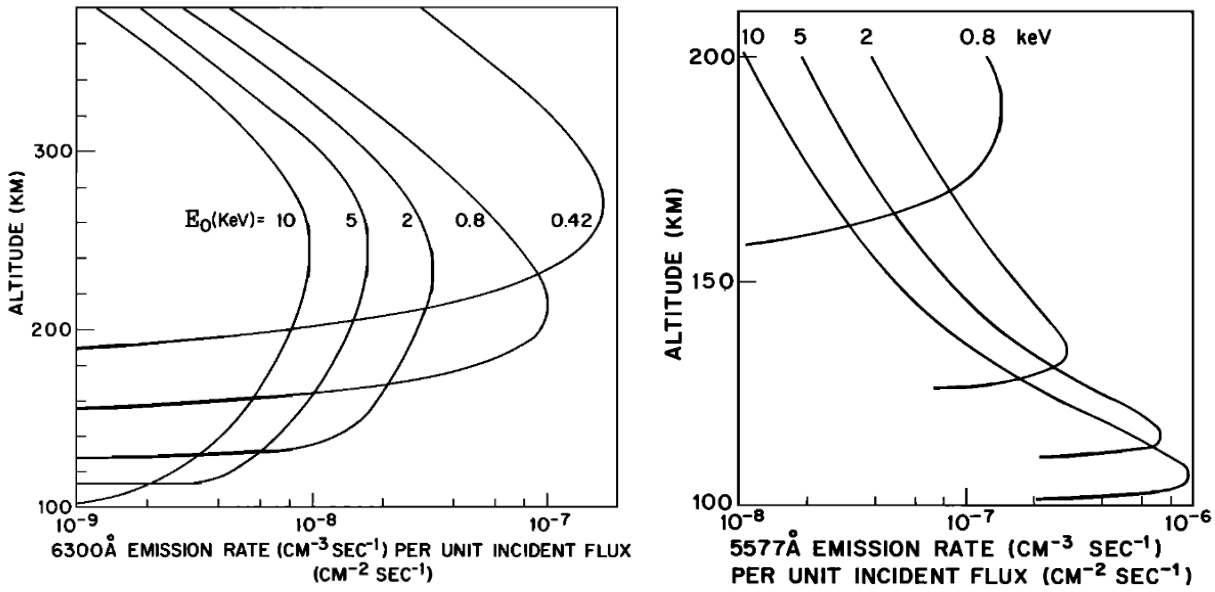

Figure 3.4: Energetic charged particle energy flux deposition and emission rate for red line (left) and green line (right) auroral emissions. [From *Banks et al.*, 1974]

will alter its energy state, interrupting the emission of a photon. This is what results in the different altitudes for the red and green emissions. The red emission requires a longer time for the transition to occur, and therefore requires a longer period of time between collisions. Red auroral emissions are therefore at higher altitudes, as there are less collisions due to the lesser atmospheric density.

Another source of ionization in the ionosphere of the Earth is meteors [*Skellett*, 1935]. The meteor trails can be ionized an order of magnitude greater than the background plasma density [*Dyrud et al.*, 2001]. These ionization trails quickly dissipate and have lifetimes on the order of seconds [*Greenhow and Neufeld*, 1955].

The meteor ionization and auroral particle precipitation can create localized plasma density enhancements in the ionosphere of the Earth, but the dominant source of ionization is still the solar EM flux. The varying EM spectrum absorption rates with altitude, along with varying recombination rates, creates multiple peaks in the background plasma density in the ionosphere, as was shown in Figure 3.2.

Once there is ionization in the atmosphere, the plasma then experience forces from EM sources. These EM forces cause the plasma to convect in the ionosphere of the Earth. The

next section describes the steady state motion of such a plasma.

3.2 Ionospheric Convection

It is important to understand the expected motions of the scatterer one measures with a radar. As ICEBEAR measures plasma density irregularities in the ionosphere, knowledge about the steady state motion of the plasma in the ionosphere is beneficial to understanding the measurements. This section investigates this steady state motion.

Ionospheric convection is the background bulk plasma movement in the ionosphere. For a derivation of the ionospheric plasma convection, one can refer to Appendix B. The resulting convection velocity of the electrons and the ions are [*Kelley*, 2009],

$$\mathbf{v}_i = \overleftrightarrow{\mathbf{k}}_i(q_i\mathbf{E} + m_i\nu_{in}\mathbf{u}) \tag{3.9}$$

and,

$$\mathbf{v}_e = -\overleftrightarrow{\mathbf{k}}_e(|q_e|\mathbf{E} - m_e\nu_{en}\mathbf{u}) \tag{3.10}$$

where q_i is the charge of the ions, q_e is the charge of the electrons, $\mathbf{E}$ is the electric field, m_i is the mass of the ions, m_e is the mass of the electrons, ν_{in} is the collision rate between ions and neutrals, ν_{en} is the collision rate between electrons and neutrals, and $\mathbf{u}$ is the velocity of the neutral particles. The tensors, $\overleftrightarrow{\mathbf{k}}_i$ and $\overleftrightarrow{\mathbf{k}}_e$, are provided as,

$$\overleftrightarrow{\mathbf{k}}_i = \frac{1}{m_i\nu_{in}} \begin{pmatrix} \frac{\nu_{in}^2}{\nu_{in}^2+\omega_{ci}^2} & \frac{\omega_{ci}\nu_{in}}{\nu_{in}^2+\omega_{ci}^2} & 0 \\ -\frac{\omega_{ci}\nu_{in}}{\nu_{in}^2+\omega_{ci}^2} & \frac{\nu_{in}^2}{\nu_{in}^2+\omega_{ci}^2} & 0 \\ 0 & 0 & 1 \end{pmatrix} \tag{3.11}$$

and,

$$\overleftrightarrow{\mathbf{k}}_e = \frac{1}{m_e\nu_{en}} \begin{pmatrix} \frac{\nu_{en}^2}{\nu_{en}^2+\omega_{ce}^2} & -\frac{|\omega_{ce}|\nu_{en}}{\nu_{en}^2+\omega_{ce}^2} & 0 \\ \frac{|\omega_{ce}|\nu_{en}}{\nu_{en}^2+\omega_{ce}^2} & \frac{\nu_{en}^2}{\nu_{en}^2+\omega_{ce}^2} & 0 \\ 0 & 0 & 1 \end{pmatrix} \tag{3.12}$$

where ω_{ci} is the ion cyclotron frequency (q_iB/m_i), and ω_{ce} is the electron cyclotron frequency (q_eB/m_e).

Current is defined as the movement of charge, where the particles that carry charge are ions or electrons. Current is therefore the movement of electrons and ions. From this we

can define the current density in a plasma as the density of plasma, n_e, where we assume quasi-neutrality, multiplied by the difference between the ion and electron velocities ($\mathbf{v}_i$-$\mathbf{v}_e$). Using equations 3.9 and 3.10 it is possible to determine the equation for the current in the plasma. The current in the plasma is then,

$$\mathbf{J} = \overleftrightarrow{\sigma}_E \mathbf{E} + \overleftrightarrow{\sigma}_u \mathbf{u} \tag{3.13}$$

where $\overleftrightarrow{\sigma}_E$ is the conductivity tensor, and the different terms in this tensor are labelled as the Pedersen (σ_P), Hall (σ_H), and Parallel ($\sigma_\parallel$) conductivities. $\overleftrightarrow{\sigma}_u$ is a tensor that provides the current of the plasma due to neutral winds.

The conductivity tensor is,

$$\overleftrightarrow{\sigma}_E = \begin{pmatrix} \sigma_P & \sigma_H & 0 \\ -\sigma_H & \sigma_P & 0 \\ 0 & 0 & \sigma_\parallel \end{pmatrix} \tag{3.14}$$

with the Pedersen conductivity,

$$\sigma_P = n_e |q_e|^2 \left(\frac{1}{m_i} \left[\frac{\nu_{in}}{\nu_{in}^2 + \omega_{ci}^2} \right] + \frac{1}{m_e} \left[\frac{\nu_{en}}{\nu_{en}^2 + \omega_{ce}^2} \right] \right) \tag{3.15}$$

the Hall conductivity,

$$\sigma_H = n_e |q_e|^2 \left(\frac{1}{m_i} \left[\frac{\omega_{ci}}{\nu_{in}^2 + \omega_{ci}^2} \right] - \frac{1}{m_e} \left[\frac{|\omega_{ce}|}{\nu_{en}^2 + \omega_{ce}^2} \right] \right) \tag{3.16}$$

and the parallel conductivity,

$$\sigma_\parallel = n_e |q_e|^2 \left(\frac{1}{m_i \nu_{in}} + \frac{1}{m_e \nu_{en}} \right) \tag{3.17}$$

The tensor for the currents due to neutral particle motion is given by,

$$\overleftrightarrow{\sigma}_u = n_e |q_e| \begin{pmatrix} \frac{\nu_{in}^2}{\nu_{in}^2+\omega_{ci}^2} - \frac{\nu_{en}^2}{\nu_{en}^2+\omega_{ce}^2} & \frac{\nu_{in}\omega_{ci}}{\nu_{in}^2+\omega_{ci}^2} + \frac{\nu_{en}|\omega_{ce}|}{\nu_{en}^2+\omega_{ce}^2} & 0 \\ -\frac{\nu_{in}\omega_{ci}}{\nu_{in}^2+\omega_{ci}^2} - \frac{\nu_{en}|\omega_{ce}|}{\nu_{en}^2+\omega_{ce}^2} & \frac{\nu_{in}^2}{\nu_{in}^2+\omega_{ci}^2} - \frac{\nu_{en}^2}{\nu_{en}^2+\omega_{ce}^2} & 0 \\ 0 & 0 & 0 \end{pmatrix} \tag{3.18}$$

The Pedersen conductivity is perpendicular to the magnetic field and parallel with the electric field, the Hall conductivity is perpendicular to both the electric and magnetic fields and the parallel conductivity is parallel with the magnetic field. Referring back to Figure 2.11, the Pedersen, Hall and parallel currents in the figure are given by Equation 3.13.

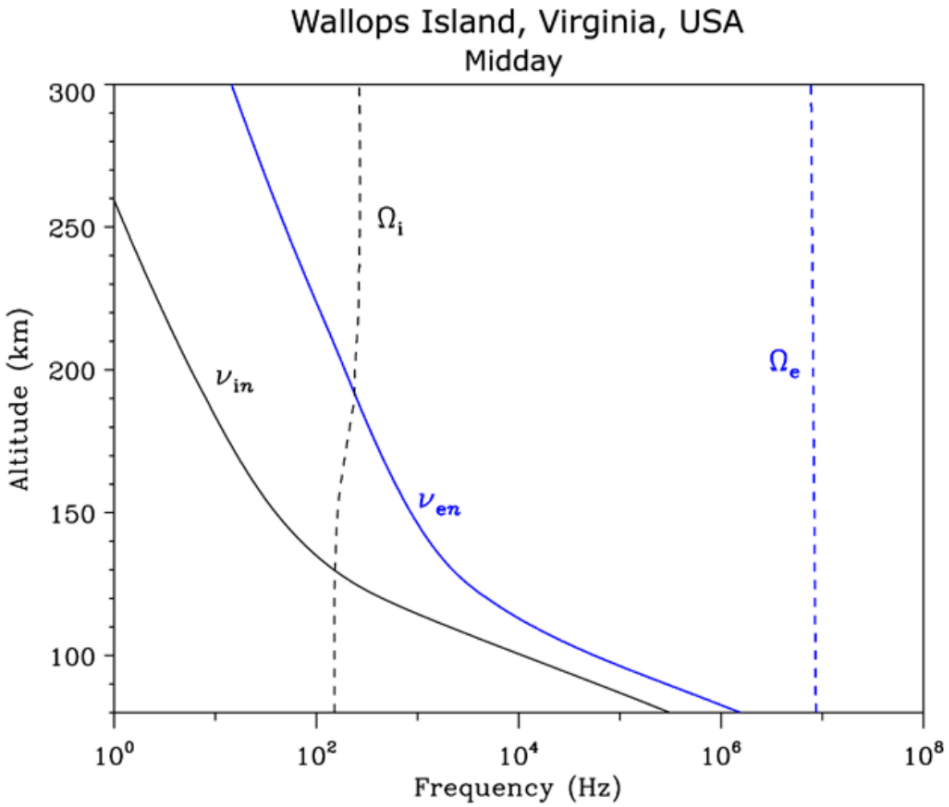

Figure 3.5: The typical electron and ion cyclotron frequencies and the electron and ion collision rates plotted ($\Omega_i \equiv \omega_{ci}$, $\Omega_e \equiv \omega_{ce}$) [*Pfaff*, 2012]

.

A significant factor at different altitudes of the ionosphere is the ratio between the ion or electron cyclotron frequencies and the respective collision rates with the neutral particles. Figure 3.5 shows the electron and ion collision rates and their respective cyclotron frequencies. At altitudes between 75 km and 125 km it can be seen that the electrons are magnetized ($\omega_{ce} > \nu_{en}$) while the ions collide enough with the neutrals to be unmagnetized ($\nu_{in} > \omega_{ci}$). This means that in this region the ions follow a combination of the neutrals and the electric field and the electrons follow the $\mathbf{E} \times \mathbf{B}$ drift. At altitudes above 150 km both the ions and electrons are magnetized and flow in approximately the same direction ($\omega_{ce,ci} > \nu_{en,in}$).

With the values of the cyclotron and collision frequencies approximated, the conductivities can be determined. These conductivities are shown in Figure 3.6. The plot shows that the conductivity of the ionosphere can significantly change depending on the time of day and on the altitude.

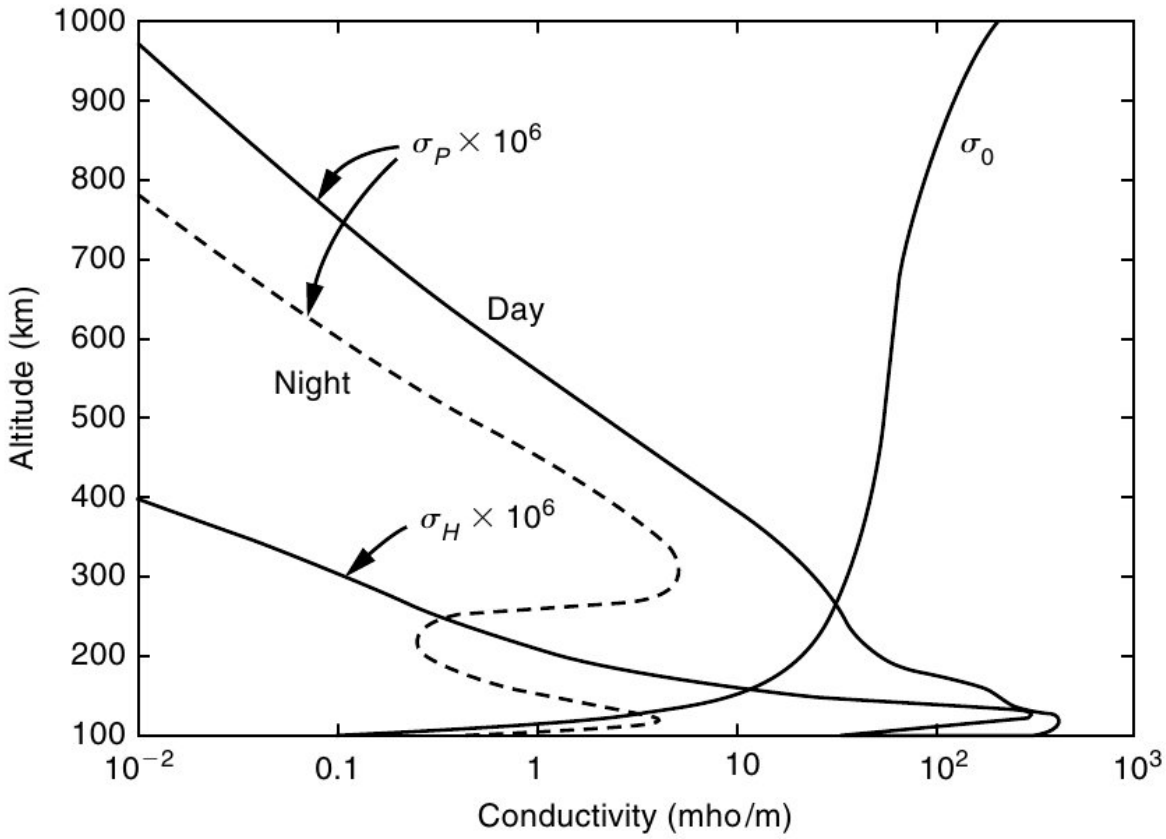

Figure 3.6: The Hall (σ_H) and Pedersen (σ_P) conductivities of the ionosphere. [*Kelley*, 2009]

From Chapter 2 we know that the interaction between the geomagnetic field and the IMF generates electric fields that are mapped down to ionospheric altitudes. From the electric field and the conductivity tensor, the flow of the plasma and the generated electric currents can be determined.

At equatorial and mid-latitudes there are different mechanisms by which electric fields are generated compared to auroral latitudes. The processes at mid-latitudes are beyond the scope of this thesis, but for more information on these processes, refer to *Kelley* [2009] and the references therein.

Now that the ionization profile and the plasma motion have been described, one can observe that both the plasma density and the dominant plasma motion vary with altitude. Different altitudes in the ionosphere were labelled by previous researchers as different regions. The regions were labelled based upon the reflection of radio waves from the plasma

density peaks, but have since been determined to have other defining characteristics. These characteristics will be described in the next section.

3.3 Regions of the Ionosphere

In Figure 3.7 it is shown that the plasma density profile can be categorized into three regions, the D-region, the E-region, and the F-region [*Kelley*, 2009]. These regions are separated by differing characteristics, such as different neutral particle densities, plasma densities, dominant ion species, and ion-to-neutral collision frequencies. The ICEBEAR system measures plasma density irregularities in the E-region, but an overview of all three regions is provided here as many times the regions are linked by physical processes.

The D-region plasma layer is formed from a multitude of atmospheric constituents absorbing solar EM radiation. The ionization of the D-region peaks between altitudes of 60 km and 90 km and, at these altitudes, there is a large collision rate between the plasma and the neutral atmospheric constituents [*Kelley*, 2009]. This collision frequency is much greater than the respective ion and electron cyclotron frequencies, resulting in the plasma drifting in the same direction as the neutral particles. There is also a large plasma recombination rate in this region, resulting in a quick decay of the plasma density when no ionization sources are present. The dominant ion in this region is NO^+, though many different ion species are present.

The E-region plasma layer is formed mainly from molecular oxygen and peaks at an altitude of approximately 105 km. The region extends from 90 km to 150 km [*Kelley*, 2009]. The ions are influenced by a combination of the electric field and the neutrals in this region, while the electrons $\mathbf{E} \times \mathbf{B}$ drift. This is due to the mean ion-to-neutral collision frequency being greater than the ion cyclotron frequency ($\nu_{in} > \omega_{ci}$) and the mean electron-to-neutral collision frequency being less than the electron cyclotron frequency ($\nu_{en} < \omega_{ce}$) at E-region altitudes. This different relative drift between the ions and electrons results in currents flowing in the E-region. The E-region plasma layer is reduced at night from the high recombination rate due to the high collision frequency between the ions, electrons and neutrals and from there being no photoionization source. Relatively large plasma densities

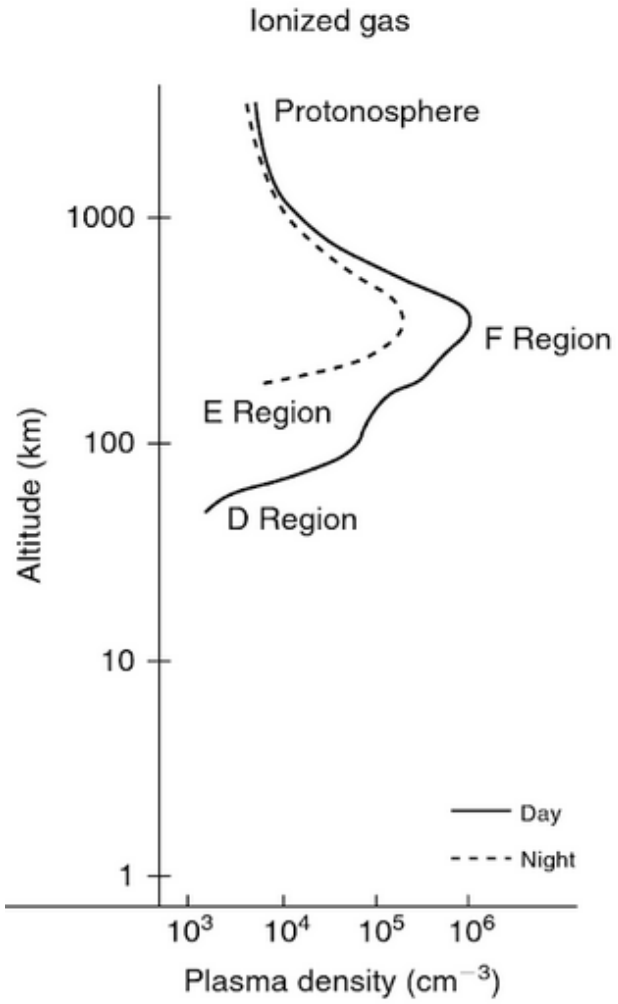

Figure 3.7: The ionization of the atmosphere with the different ionospheric layers labelled. [*Kelley*, 2009]

in the E-region on the night side of the Earth are therefore caused by particle precipitation effects or plasma transport processes from the dayside [*Kelley*, 2009]. The dominant ions in this region are O_2^+ and NO^+, as can be observed in Figure 3.2.

The F-region plasma layer is the highest labelled layer and is formed mainly from ionized atomic oxygen (O^+). It peaks at an altitude of $\approx$ 250 km, dependent on the time of day, and extends between altitudes of 150 km to 500 km, or higher [*Kelley*, 2009]. During the day there are actually two peaks in the plasma density, known as the F1 and F2 peaks. The F1 peak in plasma density, located between 160 km and 180 km, is caused by a peak in the atomic oxygen absorption of solar EM radiation and the F2 peak, located between 200 km

and 400 km, is caused by the ionization rate due to solar EM radiation being greater than the plasma recombination rate at this altitude. The F1 peak is diminished at night, while the F2 peak persists due to the relatively low plasma recombination rates at its corresponding altitudes. Both the electrons and ions follow the $\mathbf{E} \times \mathbf{B}$ drift in this region due to the collision frequency with the neutral species of the ionosphere being less than their respective cyclotron frequencies ($\nu_{in,en} < \omega_{ci,ce}$). This drift (the cross-product of the electric and magnetic fields) is derived in Appendix A. The large scale E-field, and therefore the $\mathbf{E} \times \mathbf{B}$ drift, is strongly influenced by the interactions between the magnetic fields of the Earth and Sun, as was discussed in Chapter 2.

Differing fluid characteristics, along with a forcing mechanism, can create separation of charge and density gradients in the plasma. This separation of charge can create small-scale electric fields within the plasma, which can cause density gradients to grow over time. The positive growth of these plasma density gradients is termed an instability, and can increase the amplitude of waves and turbulence in the plasma. The periodic plasma density structures are what is measured by ionospheric coherent scatter radars, such as ICEBEAR. The next section investigates some common types of instabilities and how plasma density perturbations grow in the auroral ionosphere of the Earth.

3.4 Ionospheric Plasma Instabilities

As mentioned in Chapter 2, the Sun is the primary driver of the ionosphere of the Earth. Plasma motion can result in separation of charge, which can then result in localized electric fields being generated. These electric fields can drive small-scale plasma convection and create localized instabilities in the plasma density.

The study of these ionospheric plasma instabilities is one of the major motivations for developing the ICEBEAR radar, so a short review is included here. Review papers and other associated publications will be referenced throughout, providing a library of references for those interested in a more in depth analysis of the topic. This review will focus on the ionospheric instabilities in the auroral E-region, though it will briefly touch on the auroral F-region gradient drift instability mechanism. There are many other mechanisms by

which ionospheric instabilities are produced, and they are discussed in *Kelley* [2009] and the references therein.

3.4.1 Previously Measured E-Region Coherent Scatter Spectra

The ICEBEAR system is a coherent scatter radar, which measures radar spectra similar to what are shown in this section. The scattering process of radar signals from ionospheric plasma density irregularities will be described in Chapter 4, with predecessor coherent scatter radars described in Chapter 7, and the ICEBEAR radar described in Chapter 8. Previously, VHF coherent scatter radars have measured Doppler spectra from the E-region, and these observations were separated into four different types (e.g., *Sahr and Fejer* [1996]). These types were classified by the spectral width and Doppler speed of the radar echoes. This section provides a brief overview of the types and a description of what is believed to cause the Doppler spectra measured. An idealized plot of the different types of spectra observed is provided in Figure 3.8, with the y-axis (normalized) indicating the returned power and the x-axis indicating the Doppler shift and width.

Type I echoes were observed to drift at approximately the ion-acoustic speed in a direction close to parallel with the electron $\mathbf{E} \times \mathbf{B}$ drift. Their spectral width was found to be measurably less than the mean Doppler shift of the echoes. Type I spectra were observed whenever the line of sight component of the electron drift exceeded the threshold speed of the Farley-Buneman instability [*Farley*, 1963b; *Buneman*, 1963]. An example Type I spectrum is shown in the top panel of Figure 3.8.

Type II echoes were observed to have a Doppler shift that is much smaller than the ion-acoustic speed and a spectral width on the order of the ion-acoustic speed. Based on equatorial electrojet observations, they were thought at first to be the bi-product of the gradient drift instability [*Knox*, 1964; *Tsuda et al.*, 1966; *Reid*, 1968; *Fejer and Kelley*, 1980]. However, it has become evident that these Type II echoes are actually a nonlinear manifestation of Farley-Buneman instabilities when the observations are from a direction close to perpendicular to the background electron flow direction (e.g., *Hamza and St.-Maurice*

Portions of Section 3.4.1 were originally published in *Huyghebaert et al.* [2019].

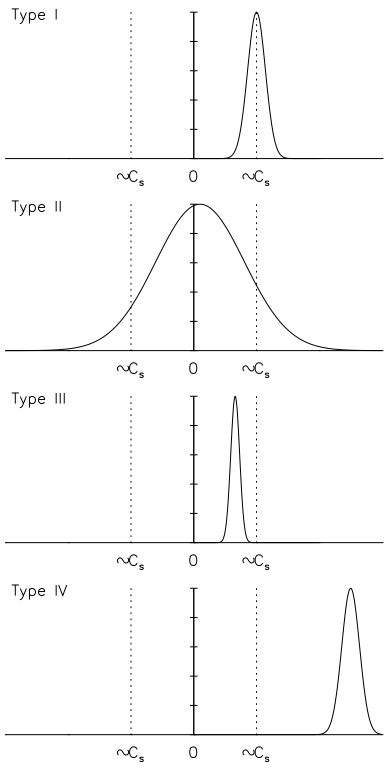

Figure 3.8: The different types of E-region radar spectra measured. [*Hussey*, 1995]

[1993]; *Otani and Oppenheim* [2006]). Type II echo spectra are similar to what is shown in the second panel of Figure 3.8.

The rarer Type III and Type IV echoes (third and fourth panels of Figure 3.8) were characterized by much smaller Doppler widths than Type I waves, to the point that they have been recently associated with weak turbulence [*St.-Maurice and Chau*, 2016]. Type III echoes were observed to have Doppler shifts less than one half the ion-acoustic speed and were observed under strong Farley-Buneman instability conditions. It was therefore concluded that they are associated with the Farley-Buneman instability. Their recent detection at altitudes below 100 km by *Chau and St.-Maurice* [2016] suggests they may be related with the existence of weakly growing modes associated with Modulated Electron Ohmic Heating by Waves (MEOHW) [*Dimant and Sudan*, 1997; *St.-Maurice and Chau*, 2016].

Type IV echoes were characterized by very narrow spectra and Doppler speeds significantly greater than (> 2) the ion-acoustic speed. They are therefore thought of as being weakly growing modes (weakly turbulent) due to the narrow spectra. Similar to Type III echoes, Type IV echoes were observed under strong Farley-Buneman instability conditions.

Various explanations for these spectra measurements have been suggested: Farley-Buneman waves growing in strongly unfavourable gradients [*St.-Maurice et al.*, 1994], Farley-Buneman waves in the presence of high electron temperatures [*Fejer et al.*, 1986], and weakly growing Farley-Buneman waves excited at the top of the E-region layer, where the contribution of the ion motion added to that of the plasma density waves moving at the threshold ion-acoustic speed relative to the ions produces a Doppler shift that is comparable to the electron $\mathbf{E} \times \mathbf{B}$ drift for a ground-based observer [*St.-Maurice and Chau*, 2016].

The next sections will discuss the theory behind the growth of the instabilities that generate these different types of spectra.

3.4.2 Ion Acoustic Waves

Before describing the physics behind plasma density instabilities, fluid waves are first discussed. An example of a propagating wave in a neutral medium is that of sound waves. These waves propagate through the atmosphere at a speed given by [*Wong*, 1986],

$$v_{sound} = \sqrt{\frac{\gamma_n k_B T_n}{m_n}} \tag{3.19}$$

where γ_n is the adiabatic index, k_B is the Boltzmann constant, T_n is the temperature of the neutrals, and m_n is the mass of the neutrals. The speed of sound is due to neutral particle density perturbations in the atmosphere.

Plasmas have a somewhat similar wave propagation mechanism due to the interactions between the ions and electrons. This is known as the ion-acoustic wave [*Chen*, 2006]. The speed of this wave is given by,

$$C_s = \sqrt{\frac{\gamma_e k_B T_e + \gamma_i k_B T_i}{m_i}} \tag{3.20}$$

where γ_e is the adiabatic invariant of the electrons, γ_i is the adiabatic invariant of the ions, k_B is the Boltzmann constant, T_e is the temperature of the electrons, T_i is the temperature of the ions, and m_i is the mass of the ions.

While this ion-acoustic speed is for a propagating wave, there are also plasma density perturbations oriented perpendicular to magnetic fields that have positive growth rates, where

the perturbation grows due to favorable growth conditions. This growth rate of the instabilities must overcome the plasma diffusion rate, which acts to remove plasma density gradients. A description of the ionospheric plasma diffusion rate is provided in Section 3.4.3. Once the diffusion rate is discussed, the two dominant types of plasma density instabilities in the ionosphere are described. These two types of instabilities are labelled as the interchange instabilities [*Tsunoda*, 1988] and the Farley-Buneman, or two-stream, instability [*Farley*, 1963a; *Buneman*, 1963]. The instabilities will be described in Section 3.4.4 and 3.4.5.

3.4.3 Cross-Field Diffusion

Perturbations in the plasma density in the ionosphere undergo diffusion, which attempts to cause a uniform plasma density. This diffusion happens at different rates parallel and perpendicular to the magnetic field of the Earth. A value for the diffusion parallel to the geomagnetic field is [*Kelley*, 2009],

$$D_{\parallel} = 2D_i \tag{3.21}$$

where D_i is the diffusion coefficient for the ions. The bulk parallel diffusion rate is double the ion rate due to the effect of the electrons also undergoing diffusion.

The equation for the diffusion coefficient of the ions is given by [*Kelley*, 2009],

$$D_j = \frac{k_B T_j}{M_J \nu_{jn}} \tag{3.22}$$

where k_B is the Boltzmann constant, T_j is the temperature of the atmospheric species, M_j is the mass of the atmospheric species, and ν_{jn} is the collision rate between the atmospheric species and the neutrals.

The plasma is also able to diffuse across the magnetic field lines. Without collisions, the plasma would be bound to the magnetic field, similar to the "frozen-in" solar wind discussed in Chapter 2. The diffusion value for cross-field diffusion in the ionosphere is given by [*Kelley*, 2009],

$$D_{j\perp} = \frac{k_B T_j}{M_j} \left(\frac{\nu_{jn}}{\nu_{jn}^2 + \omega_{cj}^2} \right) \tag{3.23}$$

where ω_{cj} is the cyclotron frequency of the given atmospheric species. This equation is valid for both the E-region and the F-region.

From Equation 3.23 it can be seen that the diffusion rate of the plasma is dependent on the temperature of the plasma and the collision rate with the neutrals. For the F-region, a typical cross-field plasma diffusion rate is on the order of 1-10 m^2/s [*Kelley*, 2009]. In the E-region the diffusion rate is greater than that of the F-region due to the increased collision frequencies. A cross-field diffusion coefficient of $\approx$ 10-30 m^2/s and a parallel diffusion coefficient of $\approx 90 m^2/s$ is given by *Oppenheim et al.* [2000] for an altitude of 105 km. The diffusion rates must be considered when determining whether an ionospheric plasma density perturbation will grow in amplitude or decay.

For the F-region, the diffusion rate is typically a value between the electron diffusion rate and the ion diffusion rate. This variation is due to a complex process where electric fields in the F-region can be mapped to the E-region. For more information on this, see *Vickrey and Kelley* [1982] and *Kelley* [2009].

If one considers the plasma density perturbation to be a wave that is $\propto \exp[j(\mathbf{k}\cdot\mathbf{r} - \omega t)]$, and ω consists of real and imaginary frequency components $(\omega_R + j\gamma)$, the growth rate of instabilities in the ionosphere is related to the rate of diffusion by,

$$\gamma = -k^2 D_\perp \tag{3.24}$$

where $\mathbf{k}$ is the wave vector of the density perturbation. This indicates that small wavelength instabilities diffuse much more quickly than large wavelength ones [*Kelley*, 2009]. The growth rate of an instability must overcome this value for the plasma density gradient to be enhanced.

With this diffusion mechanism in mind, we can now investigate the growth rate of instabilities in the ionosphere. The next section looks into the generation mechanism and the growth rate for the ionospheric gradient drift instability.

3.4.4 The Gradient Drift Instability

Significant gradients in the plasma density can be generated through the transport of plasma, or by localized plasma production. The transport of enhanced density plasma can be from the dayside ionosphere over the polar cap to the nightside ionosphere, where it begins to decay due to diffusion and a lack of plasma production. There can also be enhanced plasma production due to energetic particle precipitation or meteors, which will create localized

plasma density gradients. These plasma density enhancements can create instabilities along the interface between high density and low density plasma. One such instability is the gradient drift instability.

The gradient drift instability is created when there is a background electric field with a gradient in the plasma density perpendicular to the background magnetic field [*Tsunoda*, 1988]. It is considered a convective instability, and is similar to the more commonly known Rayleigh-Taylor instability. The Rayleigh-Taylor instability occurs between the interface of two fluids, an example being a more dense liquid resting on a less dense liquid. A small perturbation can set the instability in motion, where the more dense liquid will sink through the less dense liquid and the less dense liquid will rise through the more dense liquid. A model of this process is presented in Figure 3.9. From the figure it can be observed that the instabilities are generated along the interface of the fluids.

In the case of the ionospheric gradient drift instability, the interface occurs between a more dense plasma and a less dense plasma. An initial perturbation can grow along this interface due to EM forces on the plasma. The setup for ideal F-region gradient drift growth is presented in Figure 3.10. The background electric field is oriented perpendicular to the gradient in plasma density, and the background magnetic field is oriented perpendicular to both these vectors. Due to the polarized electric field developed from the separation of charge, this causes an initial perturbation along the fluid interface to grow. This perturbation will grow until secondary processes come into effect. The gradient drift instability is also known as the $\mathbf{E} \times \mathbf{B}$ drift instability [*Tsunoda*, 1988] due to the role the electric and magnetic fields play in the growth rate.

The growth rate and phase velocity of these instabilities in the F-region is given by [*Tsunoda*, 1988; *Kelley*, 2009],

$$\gamma = \frac{V_0}{L} \tag{3.25}$$

and,

$$\omega_R = \mathbf{k} \cdot \mathbf{V}_0 \tag{3.26}$$

where L is the gradient scale length, $\mathbf{V}_0 = (\mathbf{E} \times \mathbf{B})/B^2$ drift, and $\mathbf{k}$ is the wave vector. These equations are for values of $\omega \ll \nu_{in}$ and for $kL \gg 1$. The growth rate is therefore independent of the wave vector, k, though it is dependent on the scale length (L) of the two-fluid interface.

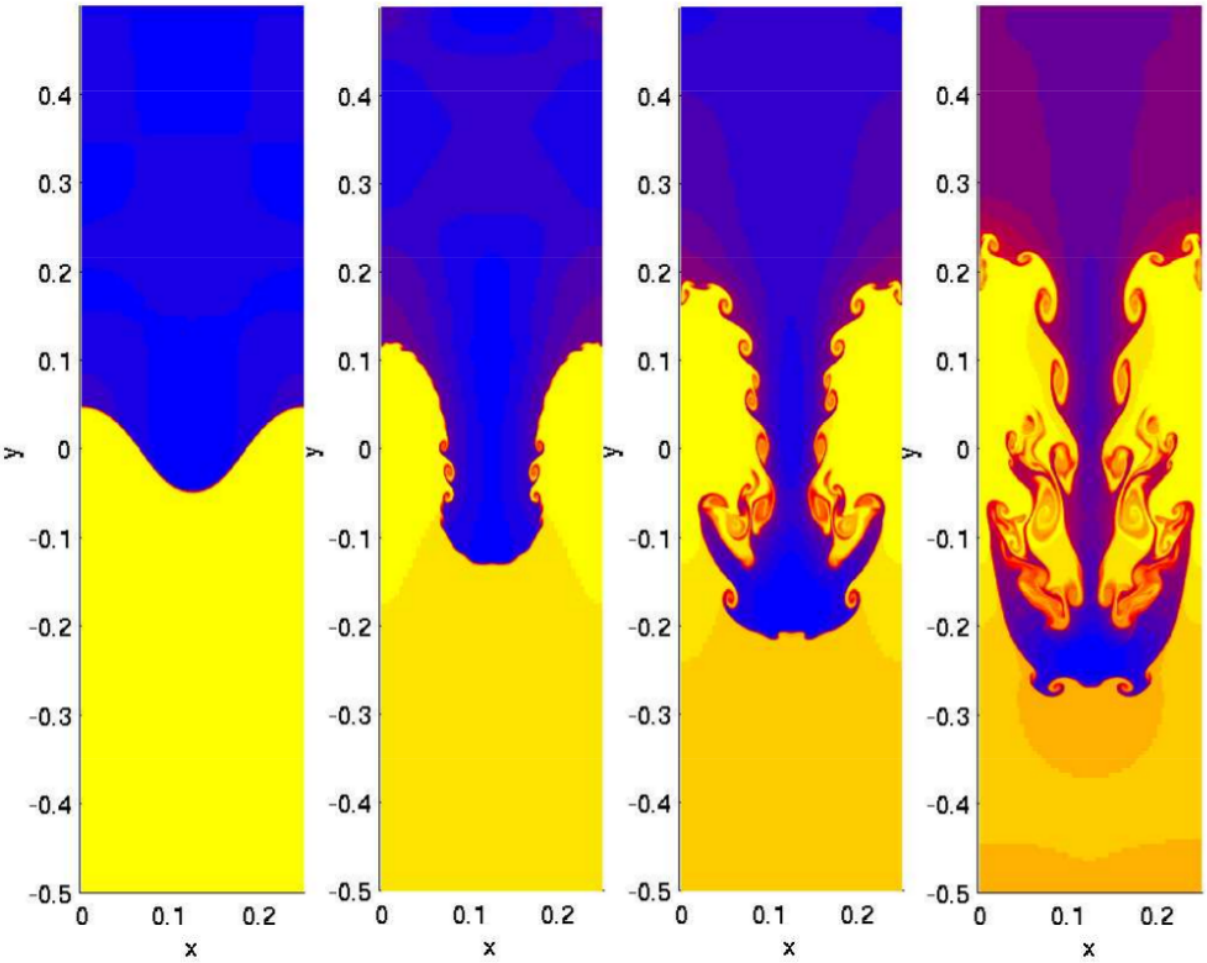

Figure 3.9: A modelled simulation of the Rayleigh Taylor Instability. [From *Li and Li*, 2006]

There have been attempts to model the gradient drift instability in the F-region of the ionosphere. Once such model is presented in Figure 3.11. In this model the plasma is moving to the left ($-x$-direction) and the observer is looking along the magnetic field line. The instability forms on the trailing edge of the plasma, and over time overtakes the plasma structure. It should be again mentioned that this is for the F-region of the ionosphere, and that the plasma density perturbation is a factor of 2 above the background for this model.

The gradient drift instability presents itself slightly differently in the E-region. At E-region altitudes, it can hypothetically occur with the plasma density gradient parallel with the background electric field [*Linson and Workman*, 1970]. While this produces a non-zero growth rate, the growth rates are too small in the E-region to produce a primary instability at

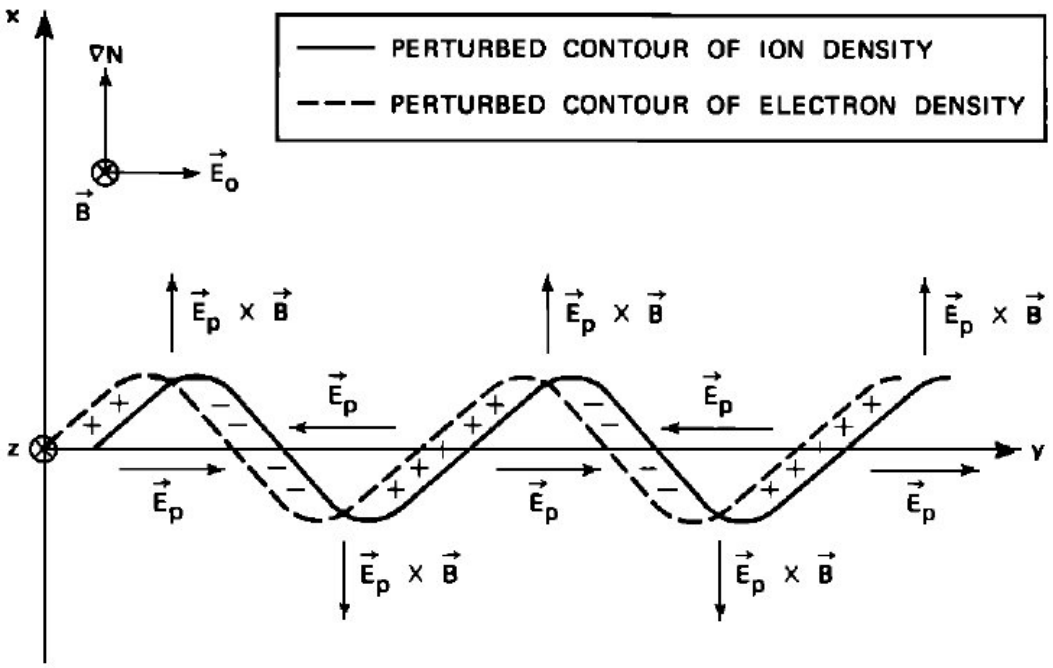

Figure 3.10: A depiction of the gradient drift instability in the F-region of the ionosphere. [From *Tsunoda*, 1988]

small perturbation wavelengths with the diffusion rates being too fast. This discussion is for sub deca-meter instability wavelength growths [*Sudan et al.*, 1973], as that is the instability wavelength detected by ICEBEAR ($\approx$ 3 m).

An exception is that there are times when extremely dense meteors create a very large gradient in the plasma density, which is generated due to the ablation of the meteor in the lower ionosphere [*Close et al.*, 2004]. An example of the gradient drift instability occurring in a meteor trail is provided in Figure 3.12. This modelled instability was generated with a 15:1 ratio between the background plasma density and the enhanced density. These large density gradients quickly dissipate in the lower ionosphere altitudes with the three snapshots of the model only being over a 40 ms time period.

Due to the lack of a physical mechanism by which the E-region gradient drift instability growth rate is greater than the diffusion rate at 3 m wavelengths, another hypothesis has been developed where the supposed E-region gradient drift instabilities (Type II measured spectra) at these wavelengths are due to secondary processes related to the Farley-Buneman instability mechanism. The next section introduces the Farley-Buneman instability, and

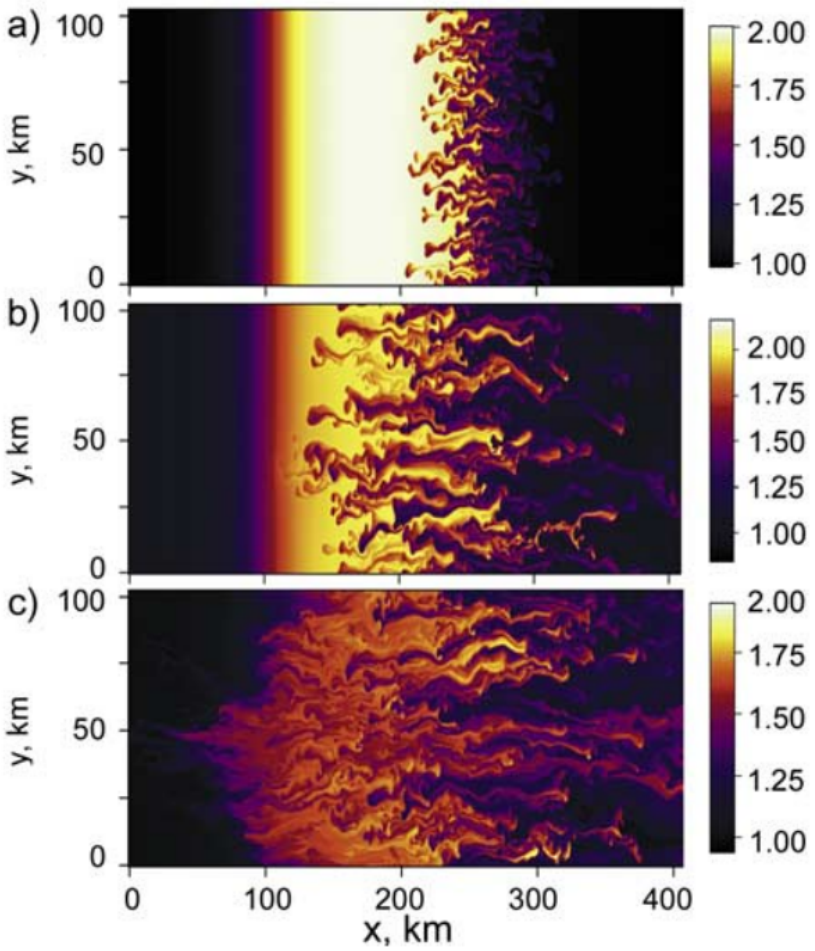

Figure 3.11: The modelled evolution of the F-region gradient drift instability. The time of the plots is: a) 0.44 hours, b) 0.9 hours and c) 1.8 hours. [From *Gondarenko and Guzdar*, 2004]

investigates the literature surrounding the secondary generation of "gradient drift" waves in the E-region.

3.4.5 The Farley-Buneman Instability

Many irregularities have been measured travelling at approximately the ion-acoustic speed in the E-region of the ionosphere (Type I measured spectra). Here we introduce the Farley-Buneman Instability [*Farley*, 1963a; *Buneman*, 1963], which occurs when the electron motion exceeds the ion motion by the ion-acoustic speed. This happens in the E-region of the ionosphere, as this is where the ions have a large collision frequency causing them to follow a

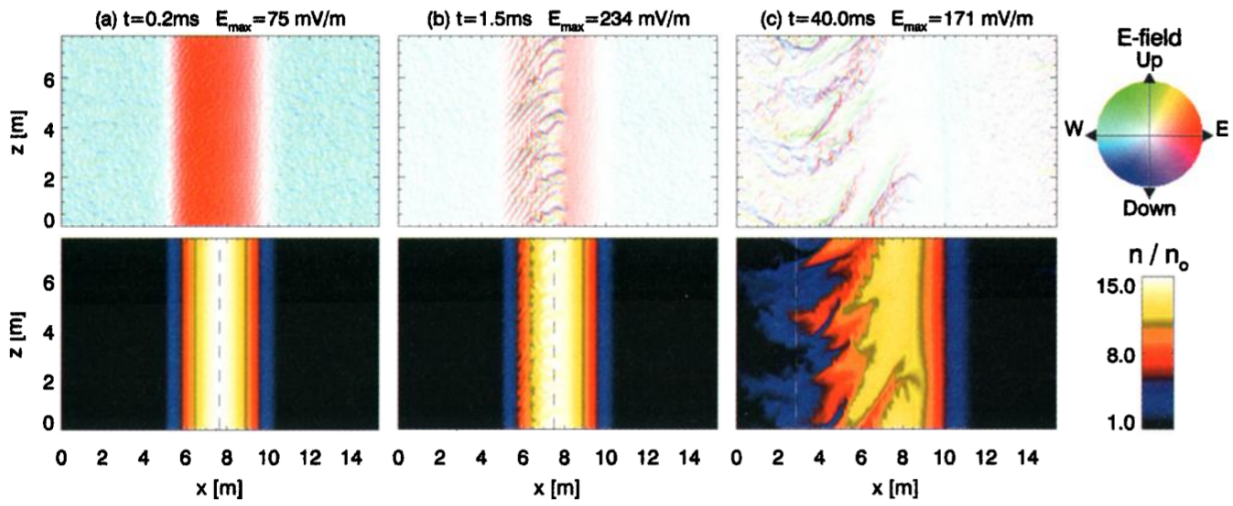

Figure 3.12: The modelled evolution of the gradient drift instability from a meteor trail. [From *Oppenheim et al.*, 2000]

combination of the neutrals and the electric field (unmagnetized) while the electrons follow the $\mathbf{E} \times \mathbf{B}$ drift (magnetized), allowing a difference in velocity between the two species. For a derivation of the 2-D Farley-Buneman instability, one can refer to Appendix C. The appendix loosely follows the derivation provided in *Kelley* [2009], with additional terms considered in the Fourier analysis of the MHD equations.

As mentioned previously, a plasma density wave can be modelled by the equation,

$$n = n_0 \exp j(\mathbf{k} \cdot \mathbf{r} - \omega t) \tag{3.27}$$

where n is the plasma density, ω is the frequency of the wave, which can be given as a complex value ($\omega = \omega_R + j\gamma$), resulting in positive growth for positive values of γ, and $\mathbf{k}$ is the wave vector of the plasma density perturbation.

The phase velocity of the Farley-Buneman instability derived in Appendix C is given by the equation,

$$\frac{\omega_R}{k} = v_{io}\cos\theta_i \pm \sqrt{\frac{\gamma_e k_B T_e + \gamma_i k_B T_i}{m_i} + \frac{\gamma^2}{k^2} + \frac{\gamma}{k^2}\frac{\omega_{ce}\omega_{ci}}{\nu_{en}} + \frac{\gamma}{k^2}\frac{m_i\nu_{in} + m_e\nu_{en}}{m_i}} \tag{3.28}$$

and the growth rate is given by,

$$\gamma = \frac{1}{2}\left(\frac{\omega_{ce}\omega_{ci}}{\nu_{en}} + \frac{m_e\nu_{en}}{m_i}\right)\left(\frac{kv_{e0}\cos\theta_e - \omega_R}{\omega_R - kv_{i0}\cos\theta_i}\right) - \frac{\nu_{in}}{2} \tag{3.29}$$

where k is the plasma density wave vector, ω_R is the frequency of the density perturbation, v_{io} is the background ion velocity, v_{eo} is the background electron velocity, θ_i is the angle between the background ion flow and the plasma density wave vector, θ_e is the angle between the background electron flow and the plasma density wave vector, C_s is the ion-acoustic speed, γ is the growth rate of the plasma density instability, ω_{ce} is the electron cyclotron frequency, ω_{ci} is the ion cyclotron frequency, ν_{en} is the collision rate between electrons and neutrals, ν_{in} is the collision rate between ions and neutrals, and m_i is the mass of the ions.

Equations 3.28 and 3.29 can be reduced to what is shown in the literature (e.g. *Kelley* [2009]). To reduce the equation, the ion velocity is taken to be stationary, and a term is introduced,

$$\psi = \frac{\nu_{en}\nu_{in}}{\omega_{ce}\omega_{ci}} \tag{3.30}$$

Utilizing this new ψ term, the Farley-Buneman growth rate and phase frequency are,

$$\gamma = \frac{\psi}{\nu_{in}(1+\psi)}(\omega_R^2 - k^2 C_s^2) \tag{3.31}$$

and,

$$\omega_R = \frac{k v_{e0} \cos\theta_e}{1+\psi} \tag{3.32}$$

These are similar to the forms of the Farley-Buneman instability growth rate and frequency equations that are typically shown in the literature. For a more in depth description of this conversion, refer to Appendix C.

From Equations 3.28 and 3.29, it can be seen that the Farley-Buneman instability can not grow in the F-region of the ionosphere due to the electrons and ions both following the $\mathbf{E}\times\mathbf{B}$ drift. The growth rate at these altitudes will not attain a value for which the plasma density perturbations will grow. For the instability to grow, it requires an electron velocity greater than the phase velocity of the density perturbation, which is the ion-acoustic speed for small growth rates. In other words, the electrons must have a velocity that is greater than the sum of the ion velocity and the ion-acoustic speed for the plasma density perturbation to grow due to the Farley-Buneman mechanism. For small growth rates, this perturbation will propagate at a velocity given by the sum of the ion velocity and ion-acoustic speed. These equations

were determined considering perpendicular propagation of the plasma density perturbation with respect to the background magnetic field.

A more rigorous derivation is provided by *Hysell et al.* [2014], where the growth rate and frequency are given as,

$$\omega_R = \frac{k_x(V_d + v_{e0} - v_{i0})}{1+\psi} + k_x v_{i0} \tag{3.33}$$

and,

$$\gamma = \frac{1}{1+\psi}\left[\frac{\psi}{\nu_{in}}(\omega_{ir}^2 - k_\perp C_s^2) - \frac{\omega_{ir}}{L}\frac{k_x}{k_\perp^2}\frac{\nu_{in}}{\Omega_i}\right] \tag{3.34}$$

where $\omega_{ce,ci} \equiv \Omega_{e,i}$, the x direction is the direction of the $\mathbf{E} \times \mathbf{B}$ drift, and ψ is given as,

$$\psi = \frac{\nu_{en}\nu_{in}}{\Omega_e\Omega_i}\left[1 + \frac{\Omega_e^2}{\nu_{en}^2}\frac{k_\parallel^2}{k_\perp^2}\right] \tag{3.35}$$

where $k_\parallel$ is the wave vector parallel with the background magnetic field, and $k_\perp$ is the wave vector perpendicular to the background magnetic field. There is also a more complex derivation that can be found in *St.-Maurice and Chau* [2016] involving ion heating due to the Farley-Buneman instability, though this is beyond the scope of this dissertation.

A companion paper of *St.-Maurice and Chau* [2016] by *Chau and St.-Maurice* [2016] presented results from 17 March, 2015, using a meteor radar. Though not optimized for ionospheric scatter, this radar was able to pick up E-region coherent echoes during a very magnetically active time. The publication by *St.-Maurice and Chau* [2016] presented that the phase speed and growth rates of the Farley-Buneman instabilities are altitude dependent, and provided a theoretical framework by which this is the case. Some modelled growth rates and altitudes based on this framework are provided in Figure 3.13. In the figure it can be observed that the growth rate of the Farley-Buneman instability varies with both flow angle and altitude. The growth rates plotted are for instability wavelengths of 4.5 m, which is similar to the ICEBEAR measurement wavelength of 3 m. The growth rates are also modelled for active conditions, with a background electron velocity of 2000 m/s. This model shows an asymmetry in the growth rates dependent on the wave propagation direction with respect to the background $\mathbf{E} \times \mathbf{B}$ drift. There are also more situations realized in the publication for different wavelengths and background plasma flows.

One of the issues with the derivation of the Farley-Buneman instability provided in Appendix C, and the growth rates from literature, is that they do not describe why or how the

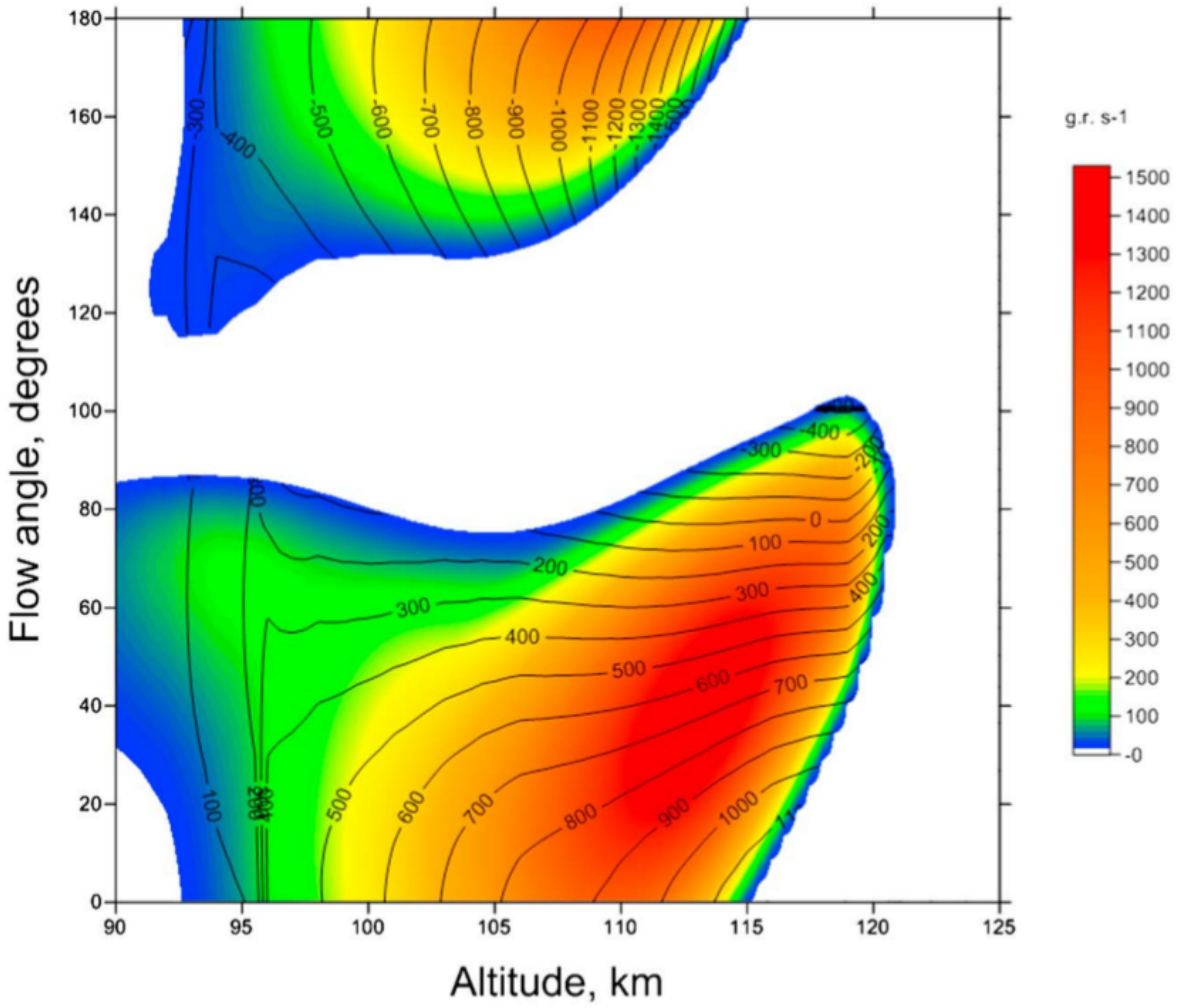

Figure 3.13: Growth rate of FB instabilities based on flow angle and altitude for 4.5 m wavelength and V_{e0} of 2000 m/s. [From *St.-Maurice and Chau*, 2016]

instabilities saturate and stop growing. The saturation of the Farley-Buneman instability has been argued to be due to secondary electrically polarized fields within the instability [*Oppenheim et al.*, 1996]. These polarized electric fields effectively create a rotation of the plasma density enhancement caused by the initial instability and slow down the plasma convection, thereby decreasing the growth rate.

The hypothesis of secondary waves being generated from large scale propagating waves was proposed by *Sudan et al.* [1973]. *Sudan et al.* [1973] stated that the gradient drift instability is able to produce large wavelength, but not small wavelength, density irregularities in the ionospheric E-region. They suggested that the saturation of the growth rate for large

scale instabilities could be due to the transfer of energy to the secondary waves. While this was not specifically for the Farley-Buneman instability, it provided a possible mechanism for the saturation of instabilities through secondary processes.

Oppenheim et al. [1996] modelled the process of the saturation of the Farley Buneman wave through secondary $\mathbf{E} \times \mathbf{B}$ drifts in 2-D using simulations. This included the rotation of plasma gradient structures within the FB primary waves. The modelled secondary waves were perpendicular to the background plasma convection, with the plasma density troughs moving one direction and the plasma density peaks moving the opposite direction. This study was then followed up by *Otani and Oppenheim* [1998] providing a theoretical framework for this type of saturation. The orientation of this system can be seen in Figure 3.14.

Another approach to the problem was suggested by *St.-Maurice and Hamza* [2001], where instead of Fourier analysis of the system they considered a plasma "blob" propagating in the E-region of the ionosphere. By neglecting Fourier analysis, it was possible to predict plasma dynamics for large density perturbations. The plasma density enhancement, or blob, becomes polarized and creates an interior electric field. This polarized electric field generates a secondary polarized electric field, effectively rotating the blob. The electric field generated within the blob eventually counteracts the external electric field, effectively slowing the blob down to the ion-acoustic velocity. This study provided an alternative theoretical framework for the derivation of the secondary electric field resulting in saturation of the growth rate of the Farley-Buneman instability.

Both mechanisms proposed by which the Farley-Buneman instability saturates involve polarization electric fields within the density enhancements or depletions causing the plasma density structures to rotate and decrease in velocity.

Years after these studies, *Oppenheim and Dimant* [2013] modelled the Farley-Buneman turbulence in 3-D. This provided enhanced results on the angular dependence of the magnitude of the waves with respect to the $\mathbf{E} \times \mathbf{B}$ drift. Figure 3.15 shows one of the results from this study. As the direction of the wave vector becomes off perpendicular to the background magnetic field, the scale of the density perturbation is reduced, and the peak velocity of its propagation is also reduced. These plots were generated for 3 m scale perturbations, which is similar to the scale of perturbations ICEBEAR will measure.

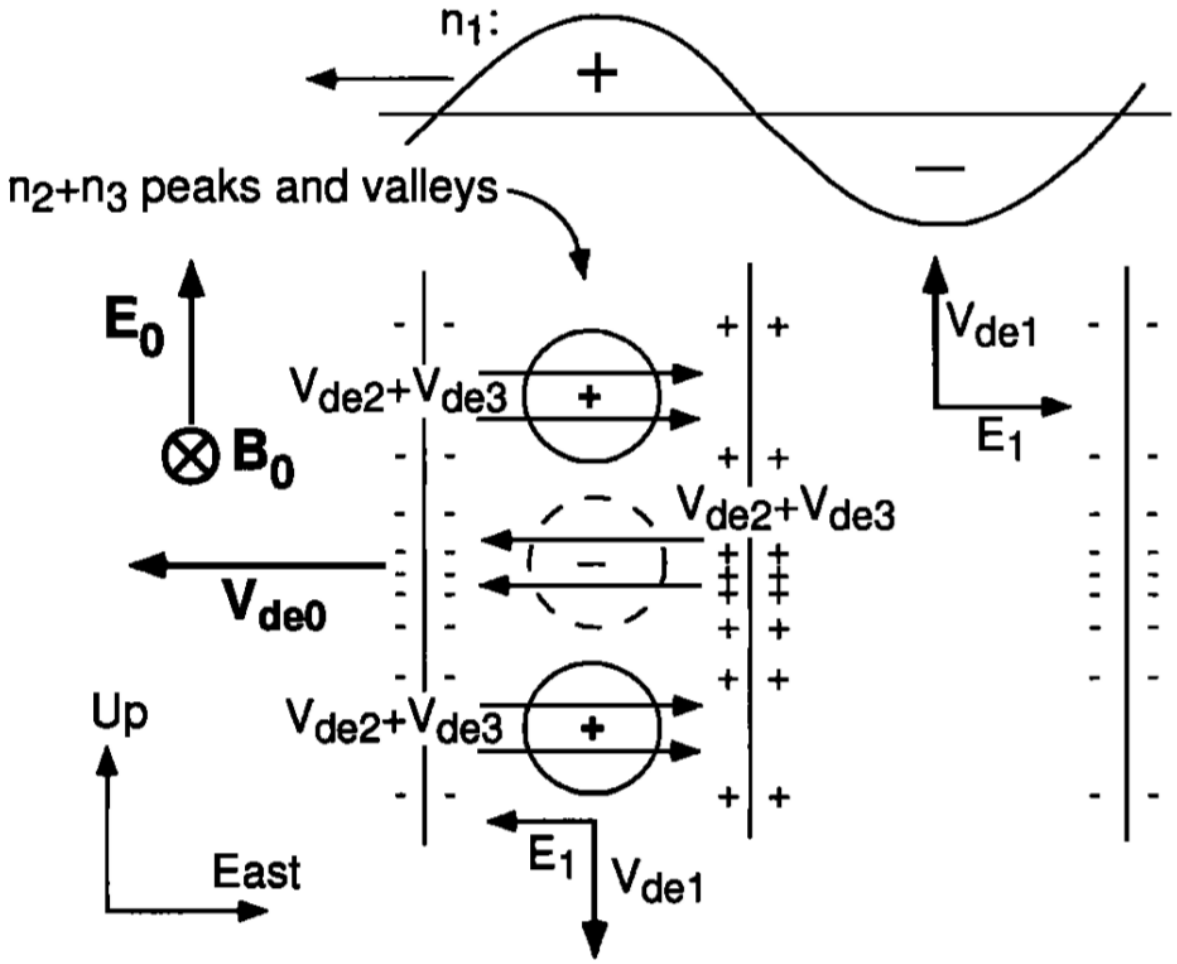

Figure 3.14: Schematic description of Farley-Buneman instability saturation through polarizing electric fields. [From *Otani and Oppenheim*, 1998]

There has been extensive research on the topic of the Farley-Buneman instability, much of which has been discussed here, and an understanding is beginning to take shape, though there are still some questions to be answered. These questions include, how does the theoretical work match with the radar spectra measured, specifically the Type III and Type IV spectra, and how does the Farley-Buneman instability growth rate saturate in the ionosphere? While there are secondary polarization fields presented as a possible mechanism for the growth rate saturation, this needs to be verified experimentally. Using the ICEBEAR radar, it will be possible to further investigate 3 m wavelength plasma density perturbations in high temporal and spatial resolution over a large FOV in order to answer these outstanding questions.

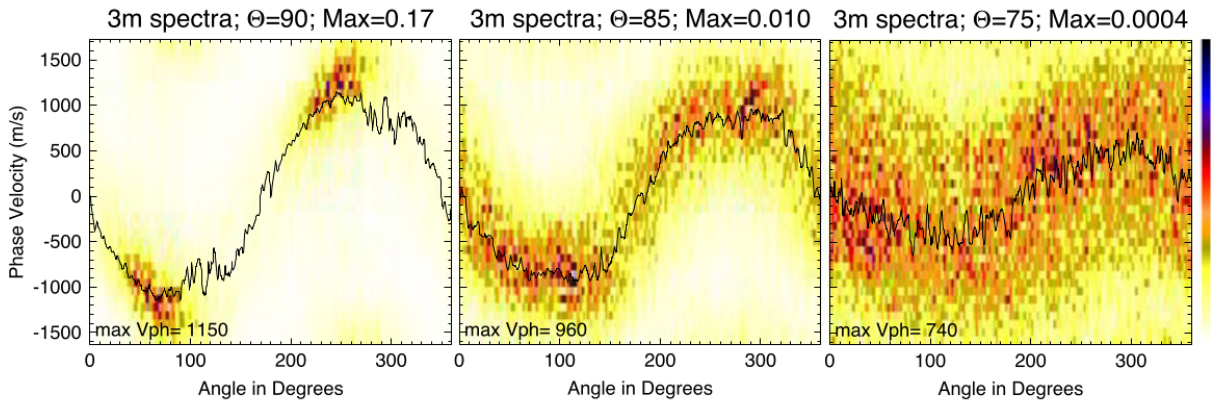

Figure 3.15: Expected phase velocities and growth rates of Farley-Buneman waves for varying flow angles. A flow angle of 0° is the direction of the background electric field. The separate panels correspond to different aspect angles. [From *Oppenheim and Dimant*, 2013]

3.5 Overview of Ionospheric Dynamics

The first few chapters of this Ph.D. dissertation have provided an overview of the interaction between the Sun and Earth as it relates to the ionosphere of the Earth. The Sun provides energy to ionize the atmosphere of the Earth, creating plasma and the region known as the ionosphere. The plasma is affected by the interaction between the magnetic fields of the Earth and Sun, where the plasma convects in the polar and auroral regions due to this interaction. It is important to have a basic understanding of the dynamics of this region as it is where the ICEBEAR FOV is located.

The convecting plasma, as well as energetic charged particle precipitation, can create plasma density gradients, which can grow due to plasma density instabilities if certain conditions are met, such as the difference between the electron and ion velocities in the plasma being above a threshold value. If the growth rate of these instabilities is larger than the diffusion rate of the plasma, the plasma density gradients grow. The ICEBEAR radar signal scatters off these plasma density perturbations at wavelengths of ≈ 3 m, and therefore the generation and decay process of density instabilities at these wavelengths is highly relevant. The physics behind the scattering from these ionospheric plasma density perturbations is covered in the next chapter, Chapter 4.

Chapter 4

Radio Physics of the Ionosphere

The ionosphere of the Earth affects radio wave propagation. Radio waves are a subset of EM waves in which the frequency of the wave is in the range of 3 kHz–300 GHz [*Silver*, 2012]. A further subset of this radio band is called the very-high frequency (VHF) band, which consists of radio waves with a frequency of 30–300 MHz. ICEBEAR operates at a frequency of 50 MHz, and is therefore operating in the VHF radio band. The electric and magnetic fields of radio waves interact with the ionospheric plasma, and this interaction can alter the properties of the radio waves and scatter them.

The ionosphere has been probed using radio instruments since 1924 [*Appleton and Barnett*, 1925]. It was quickly realized there are multiple plasma layers to the ionosphere, which were named the D-, E-, and F-regions [*Berkner*, 1937; *Watt et al.*, 1937]. The properties and formation of these layers were discussed in Chapter 3.

EM waves are governed by Maxwell's equations [*Griffiths*, 1999] which are included in Appendix A. The velocity of an EM wave in a vacuum is given by,

$$c = \frac{1}{\sqrt{\epsilon_0 \mu_0}} \tag{4.1}$$

where c is the speed of light in a vacuum, ϵ_0 is the constant of permittivity in free space and μ_0 is the constant of permeability in free space. In a medium, the speed of the EM wave becomes,

$$v_c = \frac{c}{\eta} \tag{4.2}$$

where η is the index of refraction. The index of refraction can be written as,

$$\eta = \frac{k}{\omega} c \tag{4.3}$$

where ω is the frequency of the EM wave and k is the wave vector of the EM wave. The index

of refraction can be used to predict the characteristics of EM waves in different mediums. The index of refraction for plasmas will be discussed in Section 4.2.

EM waves are generated from acceleration of charged particles creating perturbations in an electric and magnetic field. The equation for the energy flux density of the EM wave, also known as the Poynting vector, is given by,

$$\mathbf{S} = \frac{1}{\mu_0}(\mathbf{E} \times \mathbf{B}) \tag{4.4}$$

where $\mathbf{E}$ is the perturbation electric field and $\mathbf{B}$ is the perturbation magnetic field. The electric and magnetic field perturbations are given by the equations,

$$\nabla^2 \mathbf{E} = \mu_0 \epsilon_0 \frac{\partial^2 \mathbf{E}}{\partial t^2} \tag{4.5}$$

$$\nabla^2 \mathbf{B} = \mu_0 \epsilon_0 \frac{\partial^2 \mathbf{B}}{\partial t^2} \tag{4.6}$$

where the solutions to these equations are that of a propagating wave, proportional to $\exp[j(\mathbf{k} \cdot \mathbf{r} - \omega t)$. The fields associated with the wave therefore vary in space in time, where the propagation is in the direction of $\mathbf{E} \times \mathbf{B}$.

One of the reasons the ionosphere has been of interest to scientists and engineers is due to the effects it has on radio waves. Radio waves propagating through plasma undergo unique effects, which will be investigated in this chapter. A degradation on GPS accuracy [*Hernández-Pajares et al.*, 2011], and a variation in the maximum obtainable radio wave propagation distance from ground-based stations [*Appleton and Beynon*, 1940], are just a few consequences of these ionospheric effects. By utilizing the ionospheric effects on radio waves, it is possible to probe the plasma using radio waves to derive information about the dynamical processes occurring. The ICEBEAR radar investigates different ionospheric processes through this mechanism, specifically coherent scatter from ionospheric irregularities.

4.1 Snell's Law and RF Signal Refraction

The propagation of a radio wave across a boundary with a changing index of refraction is governed by Snell's law [*Griffiths*, 1999], given by the equation,

$$\eta_1 \sin\theta_I = \eta_2 \sin\theta_T \tag{4.7}$$

where η_1 is the index of refraction of the medium before the boundary, η_2 is the index of refraction of the medium after the boundary, θ_I is the angle between the incident radio wave and the boundary normal direction, and θ_T is the angle between the refracted radio wave and the boundary normal direction. If there is no physical solution to this equation, the radio wave is reflected at the boundary. The orientation of the system is presented in Figure 4.1.

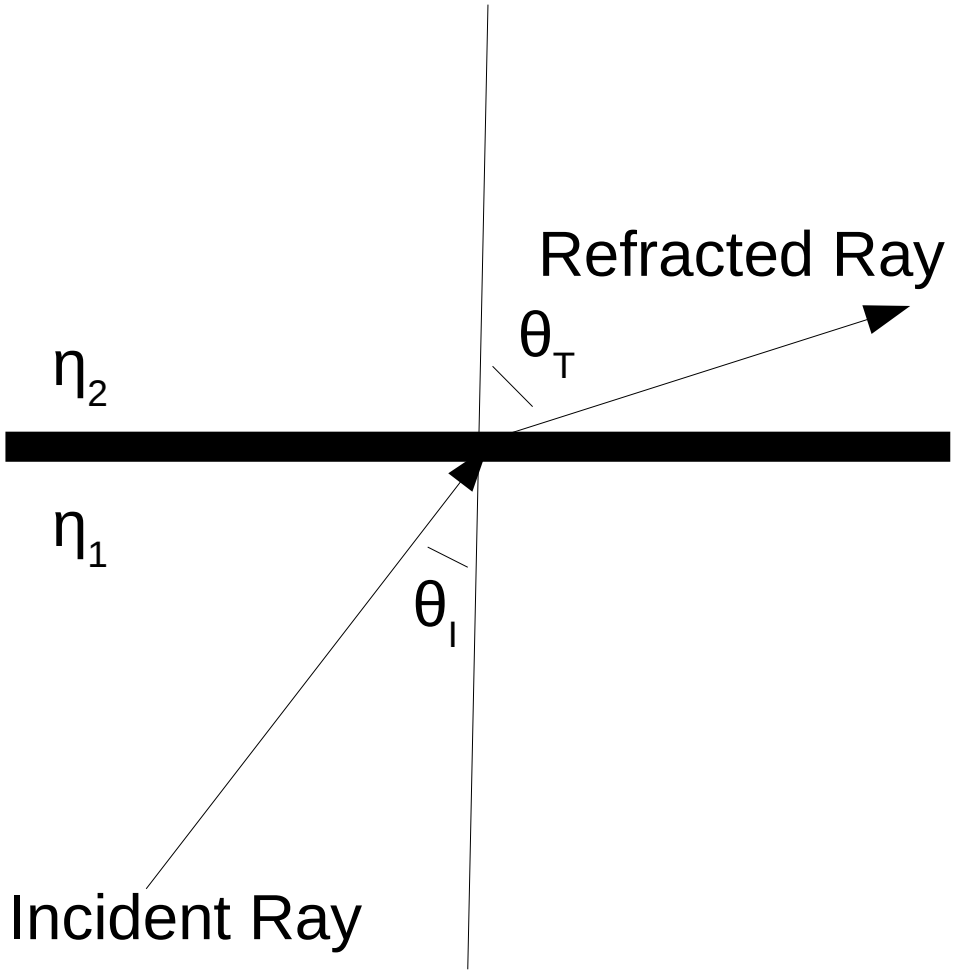

Figure 4.1: System configuration for Snell's Law. The RF ray refracting towards the boundary occurs when the index of refraction in the second medium is less than the first.

Snell's Law allows a radio wave propagation path to be modelled based on the index of refraction of different mediums. To use this equation, the index of refraction must first be determined. The next section provides the basis for the derivation of the index of refraction in the ionosphere.

4.2 The Appleton-Hartree Equation

The ionosphere can change the properties of propagating EM waves due to its varying plasma density and other plasma characteristics. Though the analysis of this system is complex, it is possible to model the ionosphere and predict the propagation of EM signals through this ionized medium. One model for determining the index of refraction in a plasma with a background, constant magnetic field is the Appleton-Hartree Equation [*Hartree*, 1931; *Budden*, 1961]. This equation can accurately predict the propagation of radio waves through the ionosphere.

The Appleton-Hartree equation is given by [*Budden*, 1961],

$$\eta^2 = 1 - \frac{X}{1 - iZ - \frac{Y_T^2}{2(1-X-iZ)} \pm [\frac{Y_T^4}{4(1-X-iZ)^2} + Y_L^2]^{1/2}} \tag{4.8}$$

with the terms given by,

$$X = \frac{\omega_{pe}^2}{\omega^2} = \frac{n_e e^2}{\epsilon_0 m_e \omega^2} \tag{4.9}$$

$$Z = \frac{\nu_{en}}{\omega} \tag{4.10}$$

$$Y_L = \frac{\omega_{ce}}{\omega} \cos\theta \tag{4.11}$$

and,

$$Y_T = \frac{\omega_{ce}}{\omega} \sin\theta \tag{4.12}$$

From the Appleton-Hartree equation, the index of refraction is dependent on the plasma density n_e, the collision frequency of the electrons with the neutrals ν_e, the frequency of the radio wave ω, the electron cyclotron frequency ω_{ce}, and the angle between the radio wave propagation path and the background magnetic field θ. Some constants are also involved in the calculation, namely the electron charge e, the permittivity of free space ϵ_0, and the mass of an electron m_e. It should be noted that ω_{pe} is the plasma frequency, the derivation of which is provided in Appendix A.

Without a magnetic field, Y_L and Y_T are 0, and without electron collisions, Z is 0. This results in an index of refraction of,

$$\eta^2 = 1 - X \tag{4.13}$$

where the index of refraction is therefore only related to the plasma density. In a collisionless, unmagnetized, plasma the index of refraction is therefore < 1. In the ionosphere, the electron density increases with increasing altitude from approximately 60 km to 250 km (Figure 3.7), resulting in a decreasing index of refraction with increasing altitude in this region. This causes the radio wave to refract towards the surface of the Earth (Equation 4.7), allowing radio waves to propagate much further through the ionosphere than would be possible without refraction. Significant refraction occurs for frequencies below 10 MHz [*Pocock and Luetzelschwab*, 2012], resulting in radio signals being directed back towards the surface of the Earth, allowing long distance over the horizon radio communications with radio receivers at these frequencies. The bending of the radio signal is also useful for obtaining radio wave propagation perpendicular to magnetic field lines [*Greenwald et al.*, 1995], providing favorable scattering conditions from ionospheric irregularities which are aligned along the magnetic field lines (Section 3.4). The reason for wanting the radar signal to be aligned perpendicular to the ionospheric plasma density irregularities is provided in Section 4.3. If the index of refraction is negative, reflection of the radio wave occurs. This negative index of refraction occurs when the radio frequency is less than the plasma frequency.

Now, if collisions are included in the calculation of the index of refraction, it becomes,

$$\eta^2 = 1 - \frac{X}{1 - iZ} \tag{4.14}$$

For this to be physical, ω must have an imaginary component. This imaginary component is the decay rate, or absorption rate, of the RF signal due to electron collisions. This is similar in concept to the growth rates previously presented for plasma instabilities in Section 3.4 (and derived in Appendix C). The absorption, or attenuation, of the radio signal is related to a combination of the electron density and the collision rate between electrons and neutrals in the plasma, where an increase in either of these quantities increases the absorption rate [*Dyson and Bennett*, 1979]. Highly ionized regions at low altitudes therefore exhibit the most absorption of the radio spectrum. As well, lower frequency waves typically experience more absorption than higher frequency waves [*Budden*, 1961].

When considering a background magnetic field B_0, the analytical solution to radio wave propagation becomes more complicated. There are multiple solutions due to the "±" in

the denominator of Equation 4.8. This means that multiple modes of the radio wave can propagate, and this has been verified by experiments [*Belrose and Burke*, 1964; *Vogler and Hoffmeyer*, 1993; *Gillies et al.*, 2010]. The different modes that propagate have been labelled the extraordinary (X-) and ordinary (O-) modes. The effects of this mode splitting are evident at HF and lower frequencies, but reduced at VHF and higher frequencies. Due to this, radio wave mode splitting is not currently considered for the ICEBEAR system.

Another phenomenon that plasma induces in radio waves is Faraday rotation. Faraday rotation is the rotation of the polarization of a radio wave due to magnetic field effects. To determine the amount of Faraday rotation a radio wave undergoes, a line integral over the radio wave path is taken. This is shown by the equation [*Titheridge*, 1972],

$$\Omega_{rot} = \frac{2.36\times10^4}{f^2}\int n(l)M(l)\,\mathrm{d}l \tag{4.15}$$

where Ω_{rot} is the amount of Faraday rotation in radians, f is the frequency of the wave, $n(l)$ is the plasma density as a function of the radio path, and $M(l)$ is the magnetic flux as a function of the radio path oriented parallel to the propagating radio wave. From Equation 4.15, it is observed that higher frequency radio waves undergo less Faraday rotation than lower frequency waves. From the Faraday rotation effect it is possible to obtain electron density profiles of the ionosphere using radio signals [*Titheridge*, 1972; *Meyer and Nicoll*, 2008]. ICEBEAR only measures the horizontal linear polarization of the incoming scattered signal, but future modifications could include polarization measurements of the radio wave to determine Faraday rotation effects on the signal.

A 50 MHz radio signal (ICEBEAR operating frequency) undergoes very little refraction as it travels through the ionosphere. At most the radar signal bends $< 5^\circ$ from the original propagation path during very active ionospheric conditions [*Watermann*, 1990]. The amount of refraction for varying amounts of ionospheric activity on a 50 MHz radio signal is shown in Figure 4.2. From the figure it can be seen that with only the E-region ionospheric plasma layer, the radio signal will refract just over 1.5° over ranges greater than 1200 km during quiet conditions (bottom curve). This provides an estimate for the amount of refraction a 50 MHz radio wave will undergo for ICEBEAR operations.

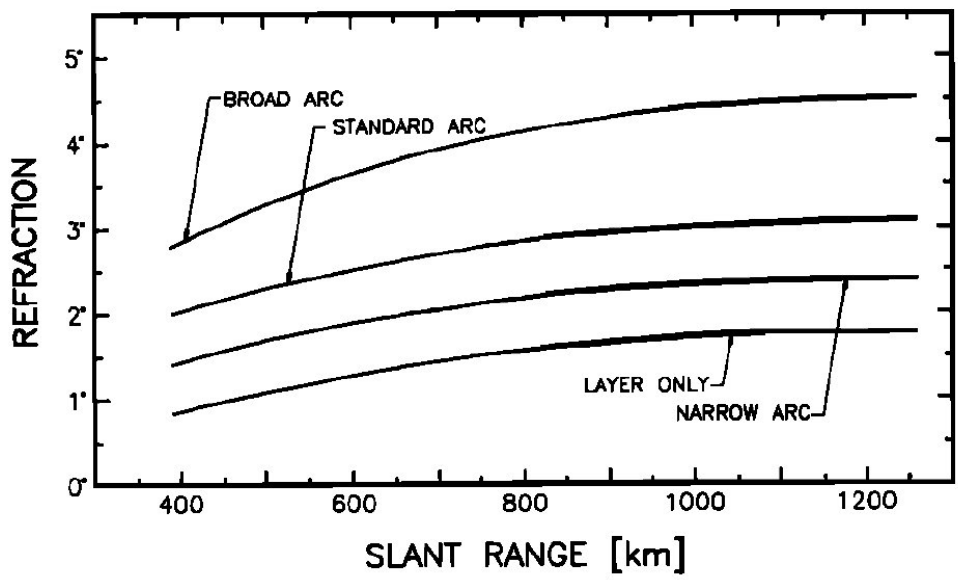

Figure 4.2: Amount of refraction experienced by a 50 MHz radio signal for varying levels of ionospheric activity. [*Watermann*, 1990]

4.3 Charged Particle Radio Wave Scattering

Due to the plasma in the ionosphere, radio waves can be reflected and scattered. A reflection occurs when a radio wave is incident upon a significant change in plasma density, and the radio wave is of sufficiently low frequency, resulting in a negative index of refraction. This was discussed in Section 4.2. The ICEBEAR radar is able to make use of both radio wave reflections and scatter from ionospheric plasma to obtain information about the ionosphere of the Earth.

Radio waves can reflect from meteor trails in the ionosphere [*Sugar*, 1964]. As a meteor dissintegrates in the atmosphere, it significantly ionizes the atmospheric constituents, creating a large gradient in the index of refraction. The ionization created by the meteor can be magnitudes higher than the background plasma density. The large gradient in the index of refraction can cause the reflection of radio waves which can be detected using radio receivers.

For RF frequencies above the plasma frequency, scattering can occur from the electrons in the plasma. For charged particles, the different types of scattering have been separated into Thomson Scattering [*Thomson*, 1906] and Compton Scattering [*Compton*, 1923]. The difference between these types of scattering is the wavelength of the incident EM radiation

with respect to the Compton wavelength, which is given by,

$$\lambda_C = \frac{h}{mc} \tag{4.16}$$

where h is the Planck constant, m is the mass of the particle and c is the speed of light. For Thomson scatter the wavelength of the EM radiation must be at least a couple orders of magnitude larger than the Compton wavelength [*Compton*, 1923]. This allows quantum theory to be neglected when deriving the effects from RF scattering due to charged particles.

For this analysis, it is also considered that the wavelength of the EM radiation is greater than the Debye length of the plasma. The equation for Debye length is given by [*Chen*, 2006],

$$\lambda_D = \sqrt{\frac{\epsilon_0 k_B T_e}{ne^2}} \tag{4.17}$$

where ϵ_0 is the constant of permittivity, k_B is the Boltzmann constant, T_e is the electron temperature, n is the electron density and e is the elementary charge. For typical E-region values of $T_e = 250$ K , and $n = 10^{10}/\mathrm{m}^3$, the Debye length is $\approx$ 10 cm.

The Debye length is the scale length at which EM radiation of larger wavelength are shielded from the ions of the plasma by the electrons. For ICEBEAR frequencies, which have wavelengths on the order of meters, the electrons are able to shield the electrostatic potential generated from the EM waves from the ions. The radio waves scatter from the electrons and the ions are not affected, nor are they directly measured. While the ions are not directly measured, due to the coupling between the electrons and the ions in the plasma, the characteristics of the ions affect the radio spectrum of the scattered RF signal.

The scattering process for radio waves scattering from the ionospheric plasma is derived in Appendix D. The derivation draws from *Griffiths* [1999], *Richards et al.* [2010], and *Perry* [2015] to determine the scattered signal that will be measured for a bistatic ionospheric scatter system.

From the derivation, the equation of the scattered electric field for a single electron is,

$$\mathbf{E}_{rad}(\mathbf{r}, t) = \frac{\mu_0 q^2}{4\pi m_e r_s r_t} \sqrt{\frac{P_t}{2\pi\epsilon_0 c}} \exp\left[j(((\mathbf{k_t}\cdot\mathbf{r_t} - \mathbf{k_s}\cdot\mathbf{r_t}) + \mathbf{k_s}\cdot\mathbf{r_r}) - \omega_r t)\right] \sin\theta_a \hat{\mathbf{r}}_{s\perp} \tag{4.18}$$

where μ_0 is the permeability constant, q is the charge of the electron, m_e is the mass of the electron, $\mathbf{r_s}$ is the vector from the electron to the receiver, $\mathbf{r_t}$ is the vector from the transmitter

to the electron, $\mathbf{r_r}$ is the vector from the transmitter to the receiver, P_t is the transmitted power, ϵ_0 is the constant of permittivity, c is the speed of light, $\mathbf{k_t}$ is the transmitted wave vector, $\mathbf{k_s}$ is the scattered wave vector, and θ_a is the angle between the particle acceleration due to the incident EM wave and the scattered EM wave. $\hat{\mathbf{r}}_{s\perp}$ refers to the fact that the scattered electric field is perpendicular to the direction of propagation. The geometry of the system is provided in Figure 4.3.

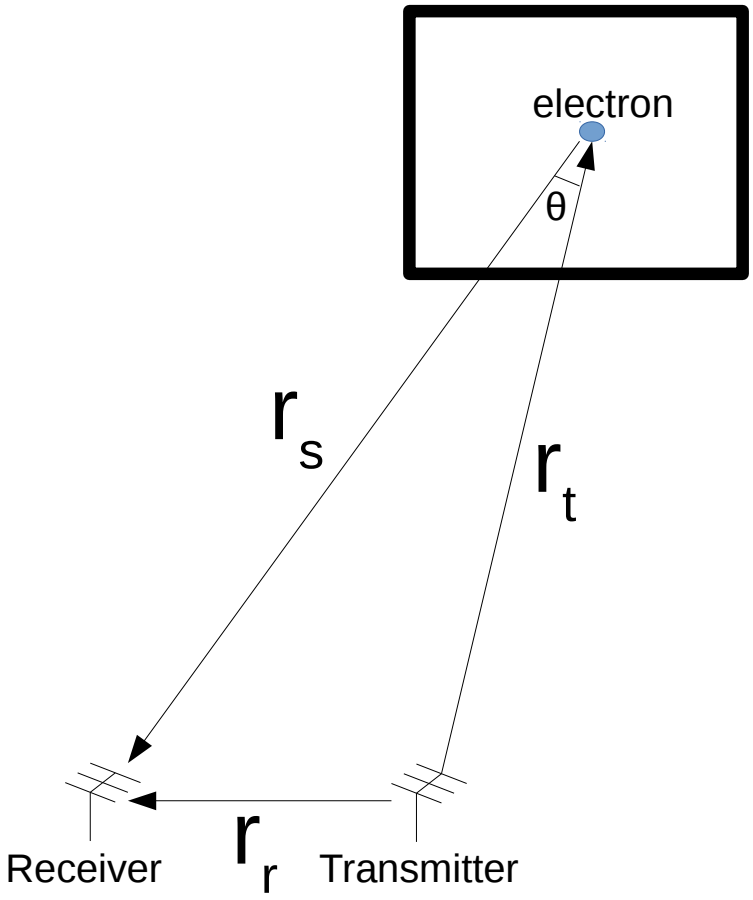

Figure 4.3: Scattering configuration for equations. Note that the changes in the range vectors will change only slightly for a given volume.

To determine the scattered signal from multiple electrons, a volume of the ionosphere is integrated over. The plasma density perturbations with wave vectors of $2\cos(\theta/2)k_t$ ($\lambda_t/2$ for monostatic radars) interfere constructively, while the other wavelengths cancel [*Haldoupis and Schlegel*, 1993; *Koehler et al.*, 1995]. After the integration, the power spectrum received

at the receiver is given as,

$$\langle P(\omega)\rangle = (P_t A_e)\left(\frac{\mu_0^2 q^4}{64\pi^3 m_e^2 r_s^2 {r_t}^2}\right) V^2 [\Delta n(k_{irr},\omega)]^2 \tag{4.19}$$

where V is the volume integrated over, and $\Delta n(k_{irr},\omega)$ is the plasma density perturbation spectrum for a irregularity wavelength based on the radar transmitter frequency and the angle between the incident and scattered signal.

Both incoherent scatter and coherent scatter radars use the same scattering mechanism, though the perturbations in the plasma density that the radio waves scatter from are generated differently. This can be confusing, as the "incoherent" scatter moniker refers to the plasma density perturbations, and not the scattering process. The coherence time of the plasma density perturbations is where the moniker originates from. The phase of the signal is still preserved post-scattering in both instances.

Coherent scatter radars scatter from large-scale plasma density perturbations that are generated from the instabilities discussed in Section 3.4. These include plasma density irregularities generated by the Farley-Buneman instability and the gradient drift instability. Incoherent scatter radars scatter from the thermal fluctuations of the plasma, which can be modeled using dispersion relations of the ions and electrons [*Perry*, 2015]. The thermal fluctuations of the plasma are much smaller in amplitude than those generated by instabilities, and are not aspect sensitive. Typically radars measuring incoherent scatter direct the radar beam away from the perpendicular condition, else the receiver is swamped with coherent scatter.

4.4 Ionospheric Radio Physics Overview

Chapter 3 provided evidence that the instabilities are typically aligned along the magnetic field lines due to their conditions for maximum growth. As mentioned, radio waves refract towards the Earth due to the index of refraction of the ionosphere, allowing the radio waves to become perpendicular with the magnetic field of the Earth. The coherent scattering conditions discussed in this chapter show that density perturbations at $\approx \lambda_t/2$ wavelengths along the radio wave path are required for constructive scattering of the signal. Combining

all these factors together is what allows for measurements using ionospheric coherent scatter radars, the ICEBEAR system included, where transmitted radio waves scatter from large scale plasma density perturbations aligned parallel to the magnetic field and are measured at a receiver.

Now that an approximate scattered power and spectrum has been determined, it is possible to discuss the radar physics behind obtaining these details. Chapter 5 describes the different equations related to extracting the radar spectra and the range of the ionospheric radar scatter, as well as some example radar waveforms that can be utilized.

Chapter 5

Radio/Radar Physics

Radar stands for radio detection and ranging [*Richards et al.*, 2010]. A radar system uses radio waves to detect the location and speed of remote objects, allowing one to obtain details about that object from a distance. The radio waves propagate at the speed of light, and thereby provide details much more quickly than would be possible with in-situ measurements, if in-situ measurements would even be possible. Radar makes it relatively inexpensive to monitor a large area from a centralized location.

Radar was first used for target detection and ranging, using rather primitive analog circuits [*Richards et al.*, 2010]. The initial radar systems produced radio waves that scattered off metallic objects with a large scattering cross section, producing a large EM wave reflection. The reflected wave was detected and measured to determine the range of the objects. Radars have also been used to measure multiple targets spread throughout a volume [*Richards et al.*, 2010]. Volume target ("soft" target) radar scattering is different than scattering from a large metallic object ("hard" target), as there are contributions to the radar scatter from multiple targets. This results in a spreading of the radar spectrum over range and Doppler, and is discussed in Section 5.3. The spreading of the radar spectrum due to contributions from multiple scatterers occurs for ionospheric radio wave scattering, where a derivation of the ionospheric scattering process is provided in Appendix D. Over time radar systems have become more advanced, where analog circuits have been replaced by digital ones, allowing more control over the transmitted signal, an increase in the signal processing power, a larger bandwidth digitization capability, and an increase in the quality of the received signal. These improvements result in an increase to the resolution of the measurements, as will be explored in Section 5.5.

This chapter explores the physics and analysis behind radar measurements. The theory

and equations describe how to calculate the return power, range and Doppler shift of the radar signal, and how these parameters can be used to describe a remote object. There is also a discussion on different radar waveforms, the processing performed on radar signals using a Fast Fourier Transform (FFT), and potential sources of noise in the radar measurements.

5.1 Radar Overview

Radar physics consists of the use of radio waves to scatter off remote objects to obtain details about these objects. Characteristics, such as the range and velocity of remote objects, can be determined through measuring the scattered signal. Using different radar waveforms makes it possible to change the resolution of the range-Doppler spectrum. The power of the signal received compared to the system noise determines whether or not the measurement is valid.

Radar systems can be monostatic or bistatic. This refers to whether the transmitter and receiver are in the same location (monostatic), or if they are located separately (bistatic). There are advantages and disadvantages to either setup, but since the ICEBEAR radar is bistatic, this dissertation focuses on bistatic radar configurations.

Depending on the wavelength and the distance from a radar/radio antenna to the area of interest, the signal transmitted and/or received is considered to be in the near- or far- field. Signals that are considered in the far-field can be treated in a simplified fashion compared to those in the near-field. In the far-field the radio signal is considered to be a plane wave, with a power dependence of $1/r^2$, where r is the range from the antenna to the point of interest. The location of the transition from the near-field to the far-field for radars is given by the condition [*Richards et al.*, 2010],

$$r > \frac{2D^2}{\lambda} \tag{5.1}$$

where r is the range from the antenna to the scatterer, D is the antenna aperture size, and λ is the wavelength of the EM wave. For a 50 MHz signal and a 60 m radar antenna array, the far field occurs at $\approx$ 1.2 km. The radar measurements for ICEBEAR are at ranges greater than 100 km, and therefore it is acceptable to consider the scattered signal to be in the far-field. In the near-field, the signal can no longer be considered a plane wave. This makes analysis much more complicated, but needs not be considered further in this dissertation.

With this condition covered, it is possible to investigate the equations associated with radars.

5.2 Essential Radar Equations

There are some radar equations that are common to all systems. These describe the power received from a scattered signal, the Doppler velocity of the object, and the range that the scatter occurred at.

The "radar equation" describes the power received for a given transmitted power, with certain terms simplified. The equation for a bistatic system is given by [*Richards et al.*, 2010],

$$P_r = \frac{P_t G_t G_r \lambda^2 \sigma_{bistatic}}{(4\pi)^3 r_t^2 r_r^2} \tag{5.2}$$

where P_t is the power transmitted, G_t is the gain of the transmitter antenna, G_r is the gain of the receiver antenna, λ is the EM wave wavelength, $\sigma_{bistatic}$ is the scattering cross section of the target for a bistatic system, r_r is the range from the receiver to the target, and r_t is the range from the transmitter to the target. From this equation the approximate returned power for a transmitted power can be predicted, as long as the radar cross section of the target and range to the target are known.

Within the received scattered signal is other information about the target. One of these parameters is the relative velocity oriented along the radio signal path. The Doppler shift for a monostatic system of the target is given by [*Richards et al.*, 2010],

$$\Delta f = -\frac{2v_t}{\lambda} \tag{5.3}$$

where Δf is the shift from the center frequency, v_t is the velocity of the target along the scattering path, and λ is the wavelength of the EM wave. The Doppler shift of a moving target is used in police radar to determine the speed at which vehicles are travelling. For bistatic radars, the equation is [*Willis*, 2005],

$$\Delta f = -\frac{1}{\lambda}\frac{\partial}{\partial t}\left(r_r + r_t\right) \tag{5.4}$$

This states that the change in the receiver-to-scatter range and the change in the transmitter-to-scatter range over time is what affects the Doppler shift of the signal. For a monostatic

system this reduces to Equation 5.3. The bistatic Doppler determination can be re-written as,

$$\Delta f = -\frac{2v_t}{\lambda}\cos\left(\theta/2\right) \tag{5.5}$$

where θ is the angle between the rays connecting the transmitter and target and the receiver and target, and v_t is the projection of the velocity of the target along the $\theta/2$ bisector.

As well as the velocity along the signal path and cross section of the target, the range of the target can be determined. The range is determined from the time delay between the radar transmission and the radar reception of the signal. This can be described for a monostatic system with the equation,

$$\Delta R = \frac{c\tau}{2} \tag{5.6}$$

where ΔR is the range resolution, c is the speed of light, and τ is the unmodulated pulse length. For bistatic systems this becomes more complicated, as the range is not the propagation distance of the radar signal divided by 2. For bistatic systems, the total propagation path is considered instead of the range. The total propagation distance is given by,

$$l_{path} = c\tau \tag{5.7}$$

To determine where the scatter occurred, more information than the radio path distance is required. If the radar has a large FOV, beamforming and interferometry can be used to further determine the location of the scatter, which is discussed in Section 6.5.

5.3 Single Target vs Volume Target

Radar targets are typically separated into two groups, single targets and volume targets [*Hysell*, 2018]. Single targets ("hard" targets) include aircraft, meteor trails, and satellites. Volume targets ("soft" targets) include targets with multiple scatterers within a volume contributing to the overall power returned to the radar. Some examples of this are weather radars measuring precipitation and ionospheric radars measuring plasma in the ionosphere.

The radar echoes received from single targets are typically point like, where there is little to no spreading of the Doppler shift and the range of the echoes are well defined. For the ICEBEAR radar, single target echoes are accepted to be meteor trails or aircraft, with a single

peak of high power at a single range and Doppler shift. This results in a power returned given by Equation 5.2, where the scattering cross section is for a single target.

Volume target echoes are complex, in that the radar measurements are from multiple scatters in the radar scattering volume. To determine the power returned from a volume target, one must consider how each of the scatterers contributes to the returned power. The difference in distance between the different scatterers must be considered, where the scattering process for ionospheric scatter is derived in Appendix D and discussed in Section 4.3.

For a volume target, there are commonly scatterers moving in multiple directions at different speeds in the medium, resulting in a central "bulk" speed of the medium, with a spread of Doppler shifts, or a spectral width, associated with it [*Richards et al.*, 2010]. The range spread is due to the measured medium being over a large area, though this is not always the case. Section 4.3 provided an overview of the scattering process for electrons in the ionosphere.

The next section considers what is actually being measured in a radar system. In the case of radio waves, it is the varying voltage received at an antenna, which is then sampled at a radio receiver.

5.4 Voltage Samples

To understand how the radar equations relate to the radar signal, an overview of what is actually being measured by a radar must be provided. The radar measures voltages at timed intervals, providing a discretely sampled time series. Section 5.5 uses idealized voltage samples to generate range-Doppler resolution plots for different waveforms. The voltage samples can be transformed to a power based on the characteristic impedance of the radar system, and related to a frequency through analysis of how the voltage samples vary over time. These parameters can be related to the radar cross section and the Doppler shift of the signal.

For a signal to be fully sampled, it must be sampled at double its bandwidth (Nyquist sampling theorem [*Richards et al.*, 2010]). This requirement applies to the average sampling rate of the signal. With both real and imaginary components measured, it is possible to fully

sample a signal with a bandwidth up to the sampling frequency [*Richards et al.*, 2010]. Radio signals are typically recorded as real and imaginary voltages that describe the amplitude and phase of the EM wave. The voltage samples are labelled as in-phase (real) and quadrature (imaginary) voltage samples (IQ). The reason the real voltages must be sampled at double the bandwidth, and not double the frequency, is because higher frequency signals can be aliased into the base measurement band. Figure 5.1 shows how a signal can alias into neighbouring Nyquist bands when only measuring the real component of the voltage. If a signal has a Doppler shift that is larger than the Nyquist band due to the sampling rate, the object will appear to be travelling at the wrong velocity. This is an important design consideration for a radar system.

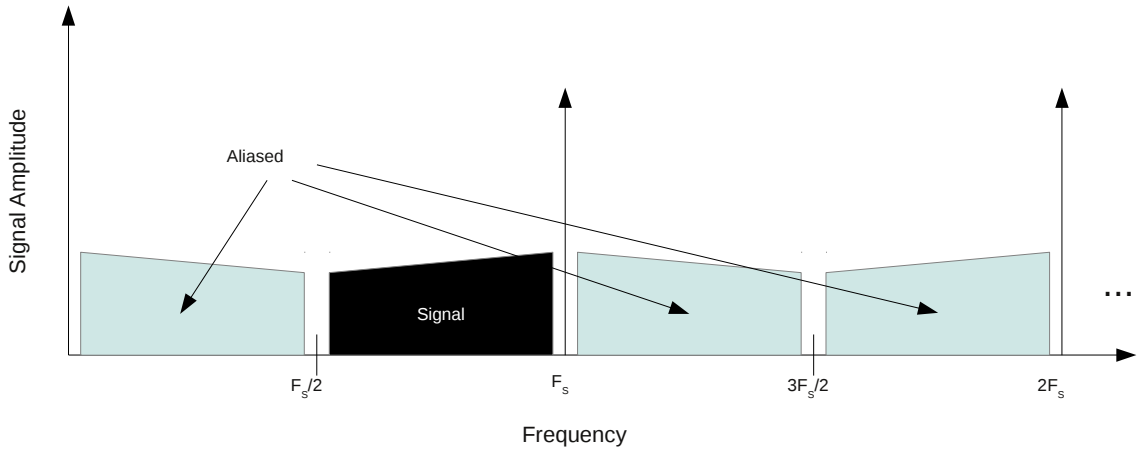

Figure 5.1: Example of Nyquist zone aliasing in the frequency space, where F_s is the sampling frequency.

Further studying Figure 5.1, there are a couple things that can be noticed. If a signal being sampled is located at a $F_s/2$ boundary and has a bandwidth spanning this boundary, it will be aliased with itself. Therefore it is recommended to have a sampling rate that is larger than twice the frequency you wish to sample. As well, one can use aliasing and/or mixing to effectively sample frequencies that are higher than the sampling rate, as the Nyquist sampling theorem only limits the bandwidth of a radio signal you are able to sample. Through the use of an RF filter on the radio front end, the Nyquist zone measured can become unambiguous.

Note that every second Nyquist zone is inverted when aliased to the baseband [*Kester*, 2009]. More information on mixing, filtering and sampling via analog to digital converters (ADCs) will be provided in Chapter 6.

An example of two waves propagating at different frequencies and their associated IQ voltage samples are shown in Figure 5.2. The left-side plots of the figure depict a sampling rate at the same rate as the frequency of the signal. The IQ samples are offset by 90 degrees, allowing the signal to be fully sampled. When the samples are plotted, they appear as a 0 Hz signal. In the plots on the right, the frequency of the wave is set to be 1000 Hz, while the sampling rate is set to 900 Hz. The resulting measurement shown has a frequency of 100 Hz, as is expected due to aliasing.

With a brief understanding of the measurements as complex voltages, we can model some waveforms and their performance in the Doppler-range space.

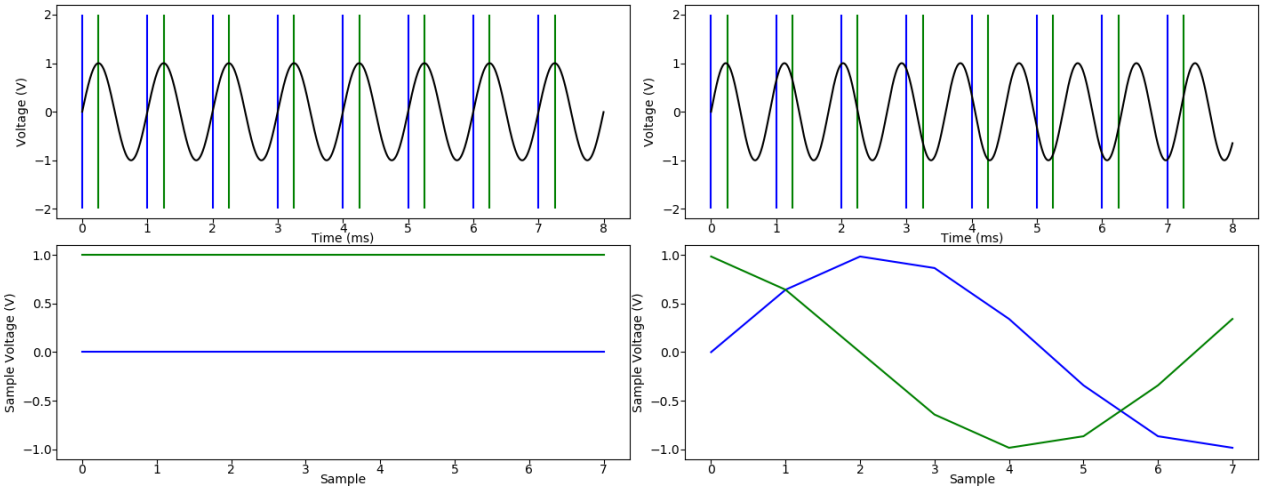

Figure 5.2: Real (blue) and imaginary (green) voltage sampling example. Details are in text.

5.5 Radar Waveforms

The radar waveform transmitted affects the resolution in range and Doppler shift of the signal received. There are two aspects to the radar waveform, the radar waveform modulation and the radar waveform coding. The radar waveform modulation refers to the type of modulation scheme transmitted with respect to the amplitude, phase and frequency of the carrier. This

can consist of a pulse, multiple pulses, a frequency varying in time or different phases between pulses, among other implementations. A further description of signal modulation is provided in Section 6.3.2. The radar waveform coding refers to the "code", or information, that is transmitted.

The radio bandwidth of a transmitted waveform relates to the total path length resolution from the equation [*Richards et al.*, 2010],

$$l_{path} = \frac{c}{BW} \tag{5.8}$$

where c is the speed of light, and BW is the bandwidth of the signal. The total path length refers to the distance the radio wave traverses to and from the target. For a system with a co-located transmitter and receiver (monostatic), the range resolution is the path length resolution divided by 2. The bandwidth is related to the pulse length through the expression,

$$BW = \frac{1}{\tau} \tag{5.9}$$

where τ is the length of the radar pulse. One issue with decreasing the pulse length to increase the range resolution is that, for a given transmit power, the average power of the waveform decreases. This can create issues when attempting to achieve a sufficient signal to noise ratio (SNR).

It is also possible to modulate a continuous-wave (CW) signal, effectively creating a continuous string of pulses with different phases. This provides a continuous sampling of a medium, while still obtaining range determination. The processing and analysis of a modulated CW signal was previously challenging, but with modern radio techniques and technology is now relatively straightforward. A CW modulation was implemented for ICEBEAR and is covered later in this section.

The Doppler resolution of a signal is based on the total time of the measurement. This is provided by the equation [*Richards et al.*, 2010],

$$\Delta f = \frac{1}{\Delta t_{meas}} \tag{5.10}$$

where Δf is the frequency resolution, and Δt_{meas} is the time length of the measurement. From this equation it is known that increasing the measurement time decreases the size of the Doppler bins in frequency space.

Before describing the different radar waveform properties, some terminology must be defined. This includes the terms convolution, cross-correlation, autocorrelation, coherent integration, and noncoherent integration.

The convolution of two data sets is the integral of the product between two data sets, where one data set is shifted and reversed (i.e. "shifted windowing"). The discretized version of this can be shown by the equation [*Richards et al.*, 2010],

$$y[n] = \sum_{m=-\infty}^{\infty} f[m]g[n-m] \tag{5.11}$$

where m is the sample offset, or shift, that is summed over to produce a value corresponding to sample n. Convolutions are commonly used in digital filters.

A cross-correlation compares two time series, determining where there is a peak correlation between the two by incrementing one time series in time and multiplying it by the other. This is shown by the equation [*Kapinchev et al.*, 2015],

$$(f \cdot g)(\tau) = \int_{-\infty}^{\infty} f^*(t)g(t+\tau_s)\,\mathrm{d}t \tag{5.12}$$

where $f^*(t)$ is the complex conjugate of the function, which is multiplied with the function $g(t)$ at an offset, or shift, of τ_s. Where the two function match there will be a peak in amplitude. For a discretized time series, this can be written as [*Richards et al.*, 2010],

$$c_{fg}[m] = \sum_{n=-\infty}^{\infty} f^*[n]g[n+m] \tag{5.13}$$

where m is the "lag", offset, or shift, and n is the sample number. The plots in this section are generated using a discretized time series. If $f[n] = g[n]$, the cross-correlation function is known as the autocorrelation function of $f[n]$ [*Richards et al.*, 2010].

There are two different types of integration methods to improve measurements for radars. These are coherent and noncoherent, also known as incoherent, integration [*Richards et al.*, 2010]. Coherent integration takes the phase of the signal into account, and increases the SNR as a factor of N, where N is the number of samples used. Noncoherent integration only considers the amplitude of the signal, and by averaging the samples, decreases the variance in the noise of the signal. Noncoherent integration effectively increases the SNR by a factor less than N ($\sqrt{N}$ for Gaussian processes) [*Yang et al.*, 2007]. The waveforms discussed here are

integrated coherently, but the ICEBEAR radar also makes use of noncoherent integration, by combining multiple coherently integrated measurements. The coherence time of E-region plasma density irregularity measurements is within an order of magnitude of 10 ms [*Schlegel*, 1996], which is why ICEBEAR uses a 100 ms coherent integration time before incoherently integrating the measurements.

If one knows the transmitted waveform, it is possible to search for this waveform in the received signal. This can be accomplished through the use of a cross-correlation, where the received signal is cross-correlated with the transmitted waveform. There will be a peak where the two waveforms match at some time delay. This process is achieved through matched filtering, which is a form of coherent integration. The time delay between the filter and the correlation peak is related to the range of the scattered signal. If we take a matched filter and multiply it by its conjugate, as well as the frequency of the wave, the matched filter equation is [*Hysell*, 2018],

$$m(\tau_s - t_0, \nu) = \int_{-\infty}^{\infty} u(t - t_0)u^*(t - \tau_s)e^{j2\pi\nu t}dt + noise \tag{5.14}$$

where we consider the target to be at a delay of t_0, τ_s is the time delay relative to t_0, ν is the Doppler shift as a frequency, $m(\tau_s - t_0, \nu)$ is the matched filter output as a function of the time delay and Doppler shift, $u(t-t_0)$ is the signal at a delay of t_0 (we are using the matched filter as the signal in this example), $u^*(t - \tau_s)$ is the conjugate of the matched filter, and t is the time. The ν term in $m(\tau_s - t_0, \nu)$ comes from the fact that $\int_{-\infty}^{\infty} u(t-t_0)u^*(t-\tau_s)e^{j2\pi\nu t}dt$ is a Fourier transform. This can be written as,

$$\chi(\tau_s, \nu) = \int_{-\infty}^{\infty} \chi(\tau_s, t)e^{j2\pi\nu t}dt \tag{5.15}$$

where $\chi(\tau_s, t) = u(t - t_0)u^*(t - \tau_s)$ and $m(\tau_s, \nu) = \chi(\tau_s, \nu) + noise$. The range-Doppler ambiguity of each waveform can be analyzed by taking the square of $\chi(\tau_s, \nu)$ and taking the target to be at $(0, 0)$. This provides the ambiguity function, and is given by the equation, *Hysell* [2018],

$$|\chi(\tau_s, \nu)|^2 = \left| \int_{-\infty}^{\infty} u(t)u^*(t - \tau_s)e^{j2\pi\nu t}dt \right|^2 \tag{5.16}$$

This then provides the Doppler shift and range ambiguity of a given waveform. While the equations above were a continuous spectrum, we must consider that in real measurements the

time series are discretized. The plots of the ambiguity functions shown later in this section are discretized, and show what is expected in real-world radar applications, neglecting noise.

An important property of the ambiguity function, or any transmitted waveform is given by the Schwartz inequality [*Hysell*, 2018], which states,

$$|\chi(\tau_s, \nu)|^2 \leq \left(\int_{-\infty}^{\infty} |u(t)|^2 dt \right)^2 \tag{5.17}$$

This means that the ambiguity function, or matched filter, power has a maximum that is proportional to $u(t)$, the signal transmitted. If $u(t)u^*(t)$ is normalized, so that $\int_{-\infty}^{\infty} u(t)u^*(t)dt = 1$, the maximum value of the ambiguity function is 1.

The properties of the ambiguity function include [*Mahafza*, 2002; *Hysell*, 2018]:

1. The maximum value occurs at $\chi(0, 0)$
2. The function is symmetric about $(0, 0)$
3. The volume under the ambiguity function is constant
4. The ambiguity function can also be found in Fourier space, where $U(f)$ is the Fourier transform of $u(t)$. This can be shown by,

$$|\chi(\tau_s, \nu)|^2 = \left| \int_{-\infty}^{\infty} U(f)U^*(f - \nu)e^{-j2\pi\tau_s f} df \right|^2 \tag{5.18}$$

From these characteristics, we know that the maximum value for the normalized matched filter is 1, which occurs at $(0, 0)$. Another important note is that the volume under the ambiguity function is constant, so for an ideal thumbtack ambiguity function response, the excess volume must be distributed somewhere in the range-Doppler space. The last point notes that the ambiguity function can be found in Fourier space, which can improve processing time for a given waveform.

5.5.1 Single Pulse Ambiguity Function

The discretized ambiguity functions for different waveforms have been plotted. These waveforms include the single pulse waveform, the multi-pulse waveform, the linear frequency

modulation (LFM) waveform, and the phase coded CW waveform. These waveforms were compared for use with ICEBEAR, though an early design decision was to make the radar CW. As will be observed, utilizing phase modulation on a CW signal can provide simultaneous high range and Doppler resolution, allowing E-region plasma density irregularities to be well sampled.

Figure 5.3 shows the discretized ambiguity function for a single pulse. From the plot it can be seen that the single pulse has very good range resolution, but sacrifices Doppler resolution to obtain this. The range resolution is based on the pulse length (τ) dependence. Using a sampling rate matching $1/\tau$, no Doppler information is obtainable (similar to taking the Fourier transform of a delta function, which corresponds to a constant value). If the signal is oversampled, the Doppler shift can be resolved, but only with a frequency resolution of $1/\tau$, where the Doppler ambiguity would appear as a sinc function. The τ dependence results in a trade off between range resolution and Doppler resolution when using a single pulse radar system. The τ used for the plots in this section is 10 μs, corresponding to a bandwidth of 100 kHz.

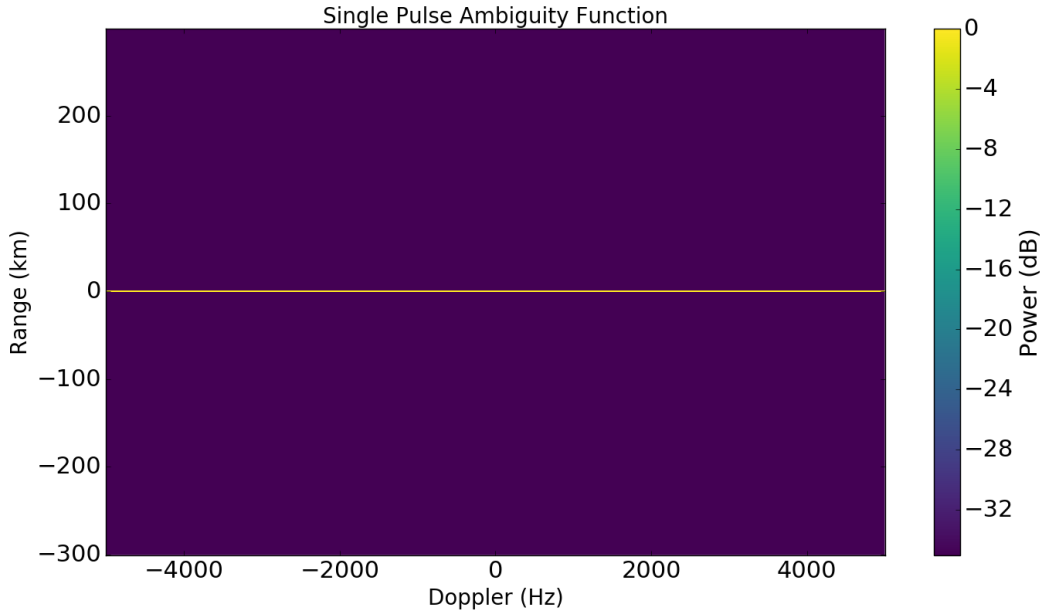

Figure 5.3: A plot of a single pulse ambiguity function with a τ of 10 μs.

The self clutter in the range domain is nonexistent using the single pulse. Self clutter refers to the interference of the signal transmitted with itself. How this affects the measurements

will become evident when discussing the other radar waveforms. There are methods to obtain simultaneous high Doppler and range resolutions, such as through pulse compression [*Richards et al.*, 2010], and these will be discussed later in the chapter.

5.5.2 Multi-Pulse Ambiguity Functions

Instead of using a single pulse, it is possible to string multiple pulses together with spacing between them. The ambiguity function of a multi-pulse sequence with equal spacing between the pulses is shown in Figure 5.4. In the figure it can be observed that instead of the lack of Doppler resolution and high range resolution, there is now range ambiguity and high Doppler resolution. The plot was created using a spacing of 40 μs between pulses, with 10 μs pulse lengths.

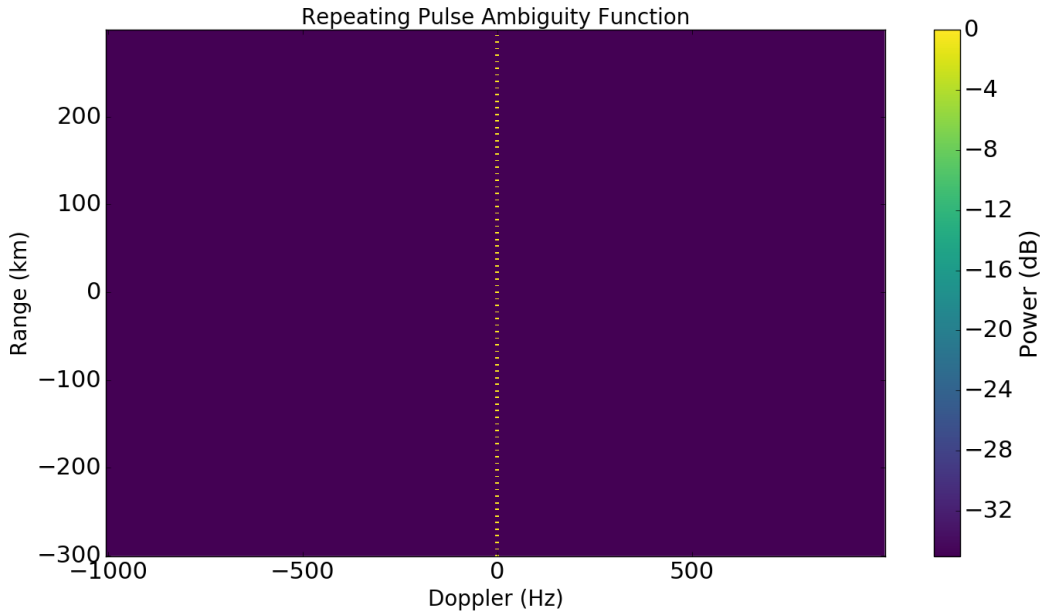

Figure 5.4: A plot of an ambiguity function for a repeating pulse sequence with equal spacing between pulses.

Figure 5.5 shows the ambiguity function for a multi-pulse sequence with different pulse spacing. Some Doppler details are now able to be obtained, but the multi-pulse sequence has introduced self-clutter in the range space. This makes the signal somewhat ambiguous in range.

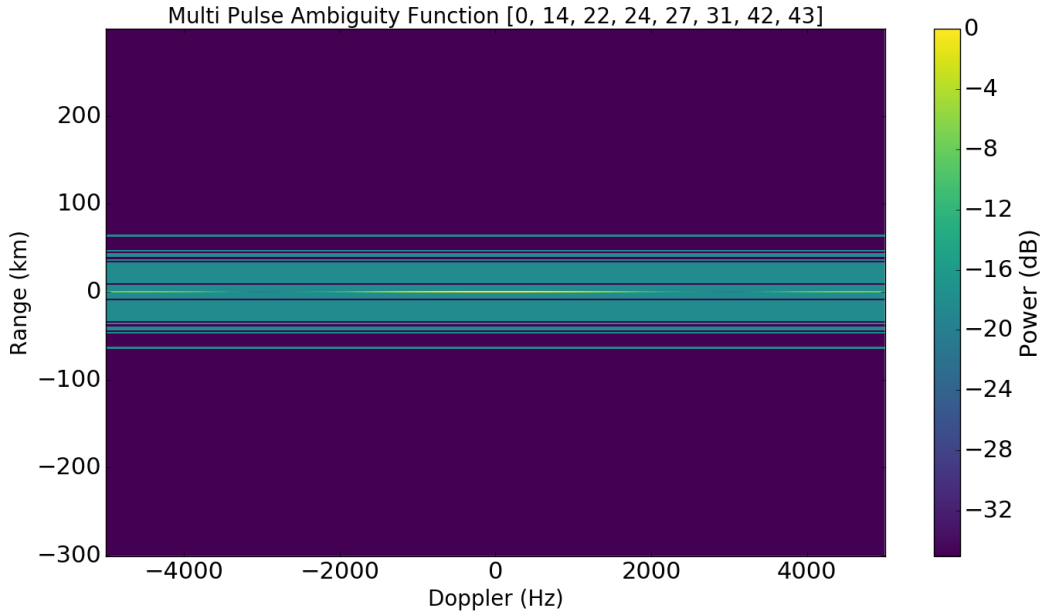

Figure 5.5: A plot of the ambiguity function for a multi-pulse sequence. The sequence of pulses is given by [0,14,22,24,27,31,42,43], which is a sequence called "katscan" used with SuperDARN.

To determine the Doppler speed of the scatter for multi-pulsed systems, typically the phase of each pulse is compared with the phase of other pulses in the same sequence. These can be combined to present the linear phase shift of the signal in time, which can be related to the Doppler shift of the scattered signal. This improves the Doppler resolution, but typically assumes there is a single scattering volume at a given range. The process of correlating multiple pulses with each other in a multi-pulse sequence is known as an auto-correlation function. A modelled spectral width and Doppler shift can be fitted to the measured auto-correlation function to obtain details about the scattering volume. This is what is done for SuperDARN, and is described thoroughly in the Ph.D. dissertation by *Reimer* [2018].

5.5.3 Linear Frequency Modulation Ambiguity Function

Another type of waveform commonly used in radars is the linear frequency modulation (LFM) waveform [*Richards et al.*, 2010; *Hysell*, 2018]. The ambiguity function for the LFM waveform is plotted in Figure 5.6. Over time the frequency of the radar signal is linearly changed. As the rate of change in the frequency is increased, the ambiguity function peak becomes more

and more tilted in the range-Doppler space. Using this waveform creates self-clutter in both the Doppler and range domains. There are also exponential frequency modulation schemes, and schemes where the frequency is ramped up and down. A frequency ramping up and down radar waveform was used by a previous University of Saskatchewan radar named the FMCW (Frequency Modulated Continuous Wave) radar [*Cooper*, 2006]. This radar is described in Section 7.8 and was a precursor to ICEBEAR.

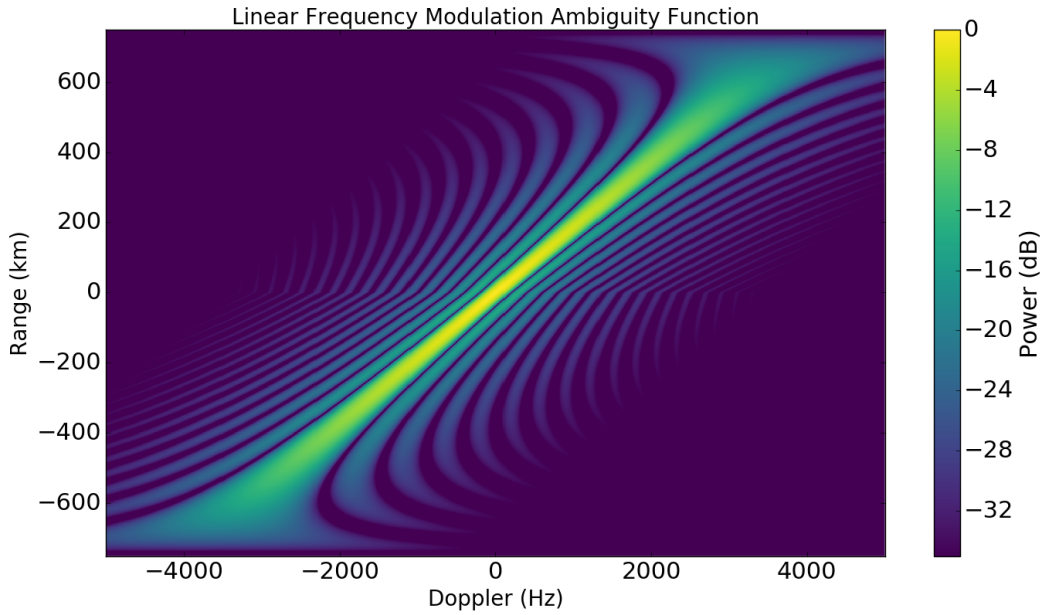

Figure 5.6: A plot of the linear frequency modulation ambiguity function.

5.5.4 Phase Modulation Ambiguity Function

The continuous-wave phase modulated signal is another type of modulation. The signal has a constant frequency, but a code is transmitted by changing the phase of the signal at defined intervals. This is similar to phase shift keying (PSK) in communications. In Figure 5.7 a binary pseudo-random noise (PRN) phase code was used to produce the ambiguity function. A 10 μs interval between binary phase changes and a 100 ms code length were used. These are the parameters that are currently in use by the ICEBEAR radar. A change to the interval between phase changes of the signal changes the range resolution, where a smaller interval results in a finer range resolution. A change to the code length changes the Doppler frequency

resolution of the waveform, where longer code lengths provide finer Doppler frequency resolution. The range resolution is not increased due to requiring a bandwidth outside the limits of the ICEBEAR Radio License, and the Doppler resolution is not increased due to the finite coherence time of the ionospheric coherent scatter.

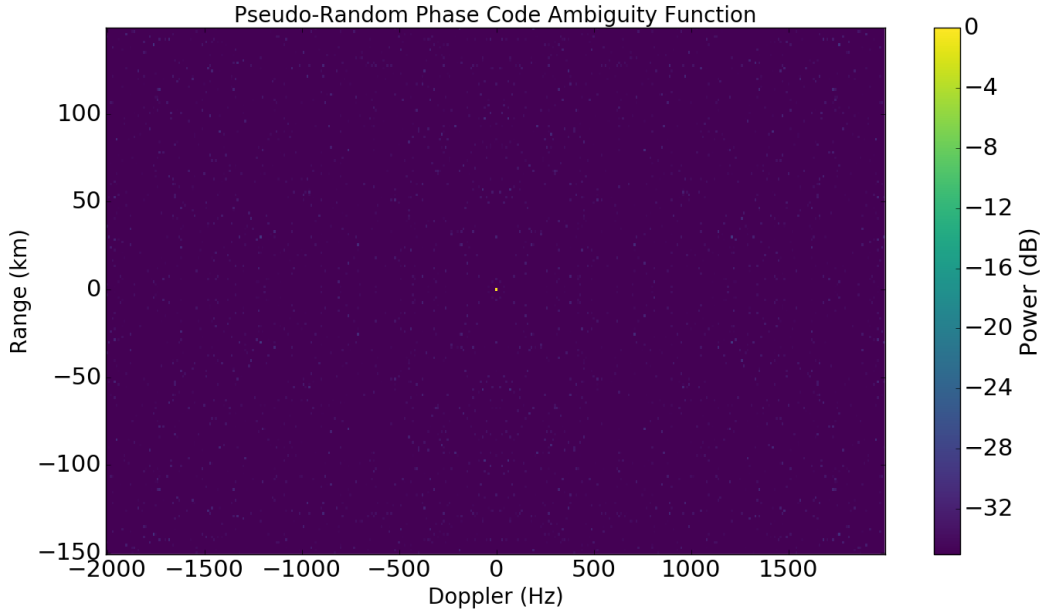

Figure 5.7: A plot of a pseudo random phase code ambiguity function.

The yellow point in the middle of Figure 5.7 is the resolution of the binary phase code in Doppler and range. This "thumbtack" response is what is desirable in an ambiguity function, as there is minimal ambiguity in Doppler and range. Self clutter does exist using a CW pseudo-random noise (PRN) phase code, where the signal return is $\approx$ 28 dB above the self-clutter floor. This means that the dynamic range of a radar system is 28 dB below that of the strongest signal return when operating with the PRN pseudo-random code used here. The 28 dB dynamic range can result in masking lower power ionospheric scatter if the radar scatter being observed has a power larger than this dynamic range, and must be kept in mind when analyzing the results.

A zoomed in view of the thumbtack in Figure 5.7 is presented in Figure 5.8. When zoomed in, it can be observed that the ambiguity function has a 1.5 km range resolution (monostatic) and a 10 Hz Doppler resolution, as expected from Equations 5.6 and 5.10.

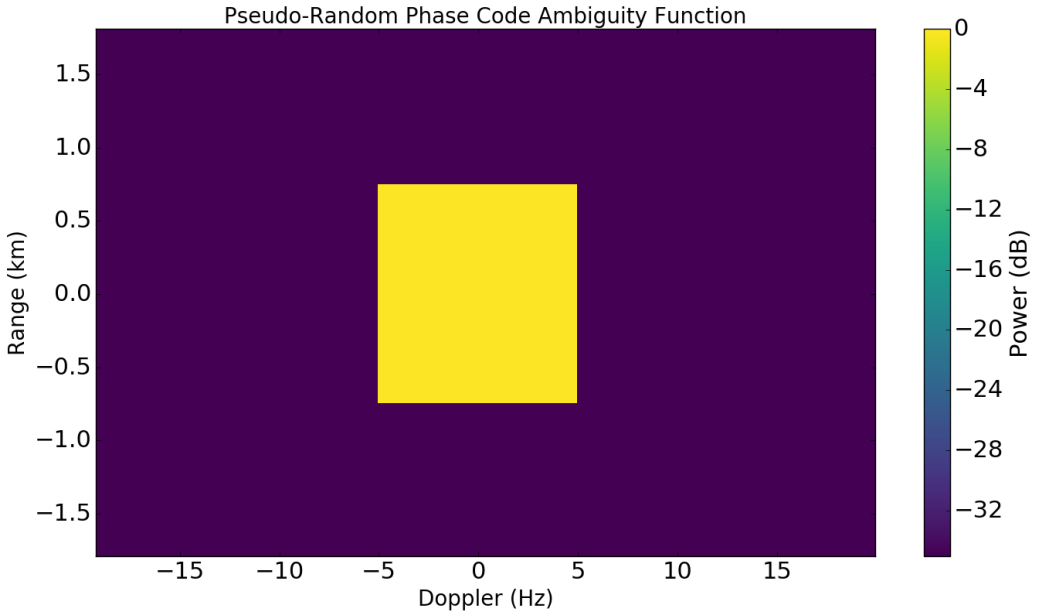

Figure 5.8: A zoomed in plot of Figure 5.7 with $\approx$ 28 dB isolation between the peak power and the self-clutter (interference of the waveform with itself). It can be observed from the figure that this type of radar waveform provides a thumbtack like response in the range-Doppler space, which is ideal for ICEBEAR operations. With the 10 μs symbol length and 100 ms code length used in the waveform, a 1.5 km range resolution and 10 Hz Doppler frequency resolution is evident.

5.5.5 Ambiguity Function Summary

As described, the ambiguity function is a method of determining the range and Doppler resolution of a radar waveform. The ambiguity functions of some of the more common waveforms have been plotted and shown, with the best "thumbtack" response being provided by the CW PRN phase modulated waveform (Figure 5.8). This concept of a waveform is what was used with the ICEBEAR radar, providing a 28 dB signal to clutter range from the strongest signal recorded by the radar. With the characteristics of the waveform used by ICEBEAR (further details in Sections 8.3.4 and 8.5.3), the range resolution was 1.5 km and the Doppler resolution was 10 Hz. These characteristics were determined through the use of a sampled time series, where a Fast Fourier Transform (FFT) was used in the analysis. The next section describes this analysis tool.

5.6 The Fast Fourier Transform

The plots in Section 5.5 were created using fast-Fourier transforms (FFTs), rather than analytical Fourier transforms. The fast-Fourier transform is a useful mathematical technique in analyzing radar spectra. This technique takes a discretized time series and converts it to frequency space, allowing the dominant frequencies in the data to be presented. This is the same as the discretized Fourier transform, where the fast-Fourier transform uses mathematical techniques to process the signal faster. The equation for a discretized Fourier transform is given by [*Brigham*, 1988],

$$G\left(\frac{n}{NT}\right) = \sum_{k=0}^{N-1} g(kT)e^{-j2\pi kn/N} \qquad n = 0, 1, ..., N-1 \tag{5.19}$$

where $G(\frac{n}{NT})$ is the power for a given wave number (or frequency), $g(kT)$ are the complex samples, k is the sample number, T is the time between samples, N is the total number of samples, and n/NT is the wave number, with n being an integer up to the total number of samples. If there are only real samples, the frequencies are only positive.

With a CW phase coded system, an FFT can be used to obtain the Doppler spectrum for a given range once the phase is decoded. This is what was done above when generating the ambiguity function. The FFT and phase decoding (matched filtering) create an intensive data processing requirement when analyzing the CW PRN phase modulated code.

The ambiguity functions plotted here were idealized, but in real-world applications there is noise added to the signal. A short discussion of where this noise comes from is covered in the next section.

5.7 Noise

Now that we know how the waveform can change the ambiguity function, including how the signal can interfere with itself through self-clutter, another thing that must be considered is system generated noise and external noise. Noise provides a lower detection bound for the signal, the level it has to be above once all factors have been considered for the measurement to be usable. Averaging multiple measurement samples reduces the variance in the noise, which

can improve the detection of actual ionospheric scatter measurements. The variance of the ionospheric scatter is also important to consider. The understanding of noise is important for ICEBEAR because it will determine whether or not the ionospheric scatter will be detectable by the receiver.

Noise is generated from multiple sources, including filters, feedlines, and amplifiers. For a given passive device at temperature T, the noise power generated is given by the equation [*Hysell*, 2018],

$$P_T = k_B T(BW) \tag{5.20}$$

where k_B is the Boltzmann constant, T is the temperature of the device in Kelvin and BW is the frequency bandwidth. At room temperature (290 K), the noise value is -174 dBm/Hz$\times(BW)$.

For amplifiers, the noise figure is typically given in the data sheet as an amplifier characteristic. When receiving a signal it is obviously desirable to have a lower noise figure on the amplifiers, or else the signal may not be detectable.

There are also external noise factors, such as other radio or radar stations broadcasting at the same or nearby frequencies, interstellar noise, and sky noise. These external "noise" signals can result in unusable measurements, and measures are taken to minimize their effects. Figure 5.9 presents the different sources of noise and their typical values over part of the radio frequency spectrum. At 50 MHz, galactic noise is significant and has an equivalent noise temperature of $\approx$ 9100 K, which corresponds to a noise value of -159 dBm/Hz$\times(BW)$, or -109 dBm for a 100 kHz bandwidth. This value is $\approx$ 15 dB above the noise level of an antenna at a temperature of 17°C. These values correspond to the values used with the ICEBEAR system, where the sky noise is expected to be 15 dB above the antenna noise value.

The SNR for a radar system is calculated in many different ways. It can be determined through expected values, taking the median of the spectra, taking "quiet" range-Doppler bins as the noise floor, or by some other means. The initial results for the ICEBEAR radar used the median of the spectra as the noise value, though different noise determination methods can be compared in the future due to the raw voltage samples being recorded and stored with ICEBEAR.

Once the noise of a measurement is determined, the SNR of the measurement is deter-

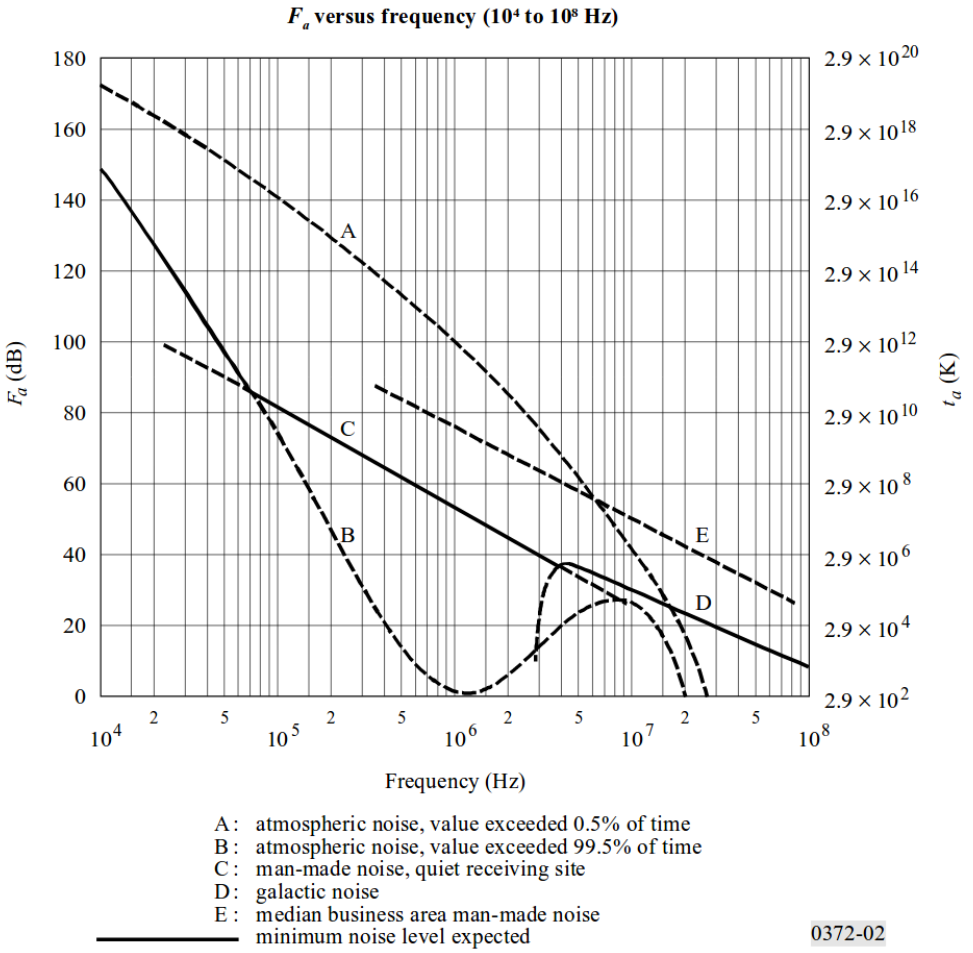

Figure 5.9: A plot of various noise sources and their typical values from 10 kHz to 100 MHz. F_a is the external noise factor with respect to the antenna noise (290 K) and t_a is the external noise equivalent temperature. Note that the scales are logarithmic. [*ITU-R*, 2016]

mined for ICEBEAR through the equation,

$$SNR = \frac{S - N}{N} \tag{5.21}$$

where S is the signal and N is the noise.

There are ways to reduce the noise in a radar system. One way is to reduce the temperature of the electronics. This then decreases the noise power, as shown from Equation 5.20 for passive components. Another method of reducing noise is to change the operating frequency of the system if possible. If there is an external noise source that is corrupting your measurements, changing the frequency may be the easiest method for reducing noise. A hardware radio filter is also an effective method of reducing noise. This can attenuate external noise

sources that can potentially saturate your receiver and/or amplifiers. It is also possible to remove noise through signal processing if the noise generated is a known signal. This is computationally intensive, but can work if other methods are unavailable.

5.8 Radar Signal Summary

The determination of the Range and Doppler shift of a radar target from the received scattered/reflected signal was discussed. The difference between a volume target and a single target was briefly reviewed, where the ionosphere is considered a volume target consisting of many individual scatterers of the radar signal. The ICEBEAR radar measures the ionosphere, and therefore volume targets must be considered when analyzing the data. The volume scatter for a ionospheric radar was examined in Section 4.3.

Different radar waveforms were examined by generating an ambiguity function for each of them. The ambiguity function provides the hypothetical range and Doppler resolution of the radar waveform neglecting external noise and nonlinear signal generation effects. The waveforms analyzed included the CW PRN phase modulated code to be used by the ICEBEAR system. This waveform has a point-like ambiguity function in range and Doppler resolution. The noise of a radio system was also examined, and a brief overview of methods to reduce noise were covered.

The background of what the ICEBEAR system is trying to measure, how a radio signal interacts with the ionosphere, and how a radar waveform results in range and Doppler measurements has been covered. The next section investigates how a radar waveform can be generated using a digital radar system, where the different components and concepts in electronics systems are discussed.

Chapter 6

Radar/Radio Signal Generation, Recording and Conditioning

This chapter describes the electronics required to generate and record the ICEBEAR signal. This includes radio frequency filters, digital to analog converters, frequency mixers, radio amplifiers, antennas, analog to digital converters, and synchronization hardware. The operation of all these devices will be described, as well as how they are used to obtain usable radar signal measurements. How antenna arrays can be used to map the location of radar scatter will also be described. The descriptions in this chapter provide a background on many of the devices used in the ICEBEAR system, though for finer details on the ICEBEAR system the reader is referred to Chapter 8.

Initial radar systems were based on analog electronics, where the signal would be displayed on an oscilloscope or some other analog device [*Brown*, 1999]. This changed with the invention of computers, and the ability to store information electronically. Even with this storage capability, the signal was required to be mixed in the analog domain to the center frequency of interest, and then a limited bandwidth around that center frequency could be stored due to large storage requirements for large bandwidths. Many times the signal would be processed in real time to reduce the data footprint. Advances in analog to digital converters, field programmable gate arrays, the rate of data transfer, and the storage capabilities of hard drives have allowed radars to be "fully" digital, with minimal analog electronics involved in the circuitry [*Wu and Li*, 1998]. The advancement of digital computing power has aided in the analysis of the large amounts of data resulting from the raw voltage samples being stored.

A basic diagram of a bistatic software radio radar system is shown in Figure 6.1, where ICEBEAR has a similar setup to this system as will be discussed in Chapter 8. A computer

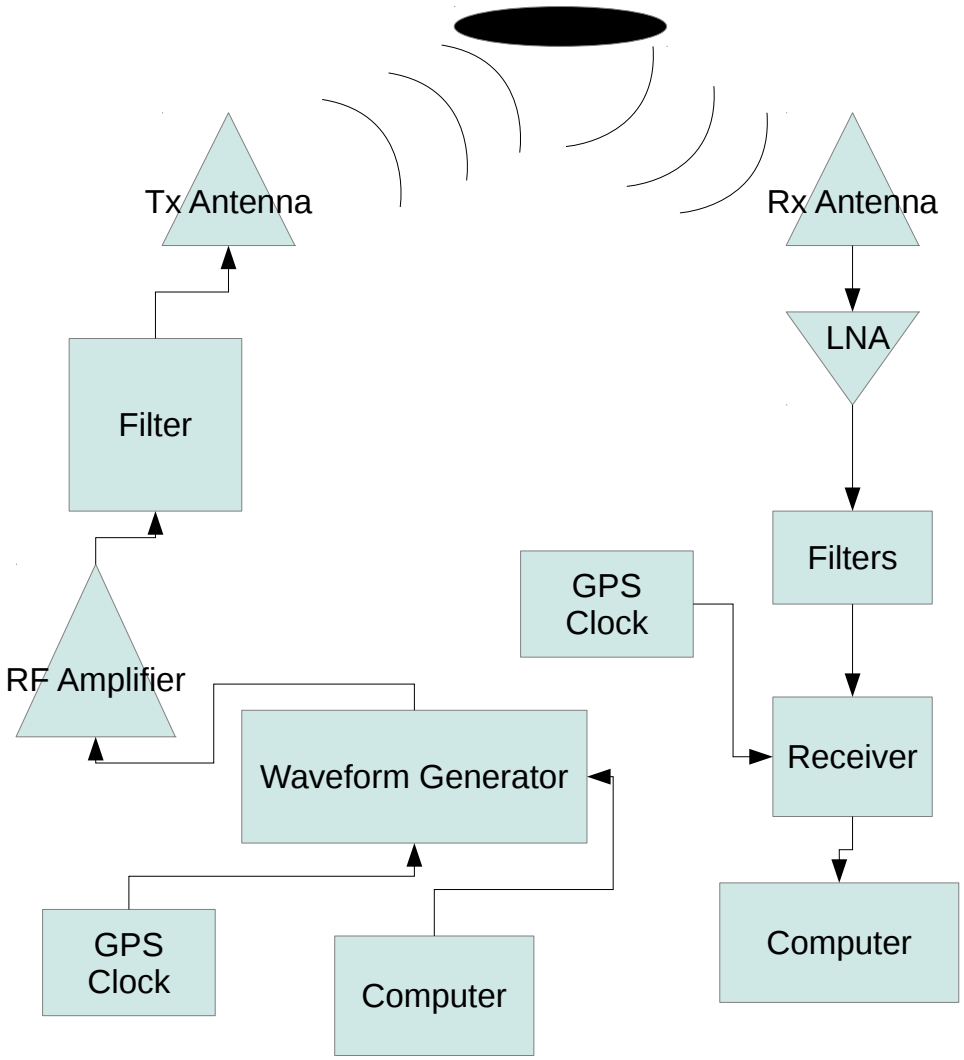

Figure 6.1: Block diagram of a digital radar system. Described in the text.

is used at both the receiver and transmitter sites to communicate with and control the radar. On the transmitter side, a clock synchronized transmission source, in this case a waveform generator, is used to produce the signal that will be transmitted. The signal is amplified to a sufficient power level, and filtered to fall within the Radio License limits. The amplified and filtered signal is then transmitted from a radio antenna. The radio signal scatters or reflects off an object and is measured at the receiver antenna. From here, it is amplified using a low noise amplifier (LNA), filtered to remove unwanted out of band signals, and recorded by a clock synchronized radio receiver. The signal can then be stored on a hard drive or processed to obtain usable radar measurements. The hardware integral in performing these operations

will be discussed in detail in this chapter.

6.1 Matching Networks

Matching networks are required in electrical systems to minimize reflected power and maximize power transfer at given frequencies. Many different systems, such as transistors, have an input and output impedance that is not at the characteristic system impedance. This creates a need for matching networks to be implemented to reduces losses in the system. For the ICEBEAR system, matching networks were required for the amplifier design and the other RF connections. This section will describe some methods available to improve the matching between different electronics systems.

When two systems are connected together, there is a transmitted and reflected portion of the signal. To optimize power or the reflection of the signal at a boundary, an impedance matching network can be used. The reflection coefficient for a single transmission line fed load is [*Silver et al.*, 2012],

$$|\Gamma_r| = \left| \frac{Z_L - Z_T}{Z_L + Z_T} \right| \tag{6.1}$$

where Γ_r is the reflection coefficient, Z_L is the complex load impedance and Z_T is the complex transmission line impedance. The reflection is therefore minimized when the transmission line and load have the same impedance.

Radio electronics systems all have an input and output impedance, which is typically given on the corresponding data sheet. For coaxial cables, the impedance is dependent on the dielectric material used between the core conductor and the conductor shield, the conductor material used, and the distance between the core and shield. If we consider the cable to be loss-less, this impedance can be calculated as [*Straw and Cutsogeorge*, 2012],

$$Z_T = \sqrt{\frac{L}{C}} \tag{6.2}$$

where L is the inductance, and C is the capacitance of the cable. Coaxial cables are used for the RF connections in the ICEBEAR system.

Transformers can be used as an impedance matching device. They are able to change the impedance of a system and change the ratio of voltage to current [*Silver et al.*, 2012].

Transformers consist of windings of conductors, where they are magnetically coupled to other conductor windings. The changing magnetic flux generated from the current in one of the coils generates a current in the other coil. These transformers can be used to change the impedance of a system, which is given as,

$$\frac{N_S}{N_L} = \sqrt{\frac{Z_S}{Z_L}} \tag{6.3}$$

where Z_L is the impedance of the load, Z_S is the impedance of the source, N_S is the number of turns for the transformer on the input, and N_L is the number of turns of the transformer on the output. Different ferro-magnetic materials can be used as the core in the transformer, which allows the transformer to work in a broader frequency band. Transformers are therefore critical as part of impedance matching circuits.

An example of when this is useful is for amplifier design. Typically the input impedance of a transistor is significantly lower than 50 ohms, requiring a method to match a large difference in impedance. This can be accomplished with a transformer, where designs implementing a 9:1 impedance transformation (3:1 coil ratio) are common, though the ratio can be changed by changing the ratio of coil windings. With a 9:1 impedance transformation, a 50 Ω input is now at $\approx$ 5.56 Ω on the output of the transformer. If a ferro-magnetic core is used, this matching can be accomplished for a broad range of input frequencies, where an inductor and capacitor matching solution would cause the impedance matching circuit to vary significantly over broad ranges of frequencies.

Impedance matching is also important in radio electronics in the connection between a transmission line and an antenna. The impedance of an antenna is not typically equal to the impedance of the transmission line. A balun is used to match these devices to the input transmission line, where balun stands for balanced to unbalanced. An example of a balanced system is a center fed dipole to be used as an antenna [*Straw and Cutsogeorge*, 2012]. This system is symmetrical with respect to the feed point, and the currents are balanced along each of the dipole directions. An example of an unbalanced line is a transmission line, where the center conductor carries the signal and the outside shield is grounded. The balun is used to change the transmission line unbalanced system to a balanced one to feed the antenna, and is typically integrated with an impedance matching circuit. The antennas used with ICEBEAR

include a balun device for matching the coaxial feedline to the antenna impedance.

6.2 RF Filters

Filtering is an essential part of radio systems, both in the digital and analog domains. Filtering can act to reduce interference between radio systems, reduce noise, and improve SNR [*Tonne et al.*, 2012]. An example of where this is important in ICEBEAR is to remove FM radio/TV station interference outside the frequency band of interest. Without the attenuation of the FM radio station signal the pre-amplifiers of ICEBEAR are saturated, creating nonlinearities in the received signal. These FM radio/TV ground stations are only a few km away, which is why filtering their signal is so important.

There are four characteristic filters, named with respect to the band of frequencies blocked and passed. These four filter types are the low pass filter (LPF), the band pass filter (BPF), the high pass filter (HPF) and the band stop, or notch, filter. This section investigates the different types of RF filters in both the analog and digital signal spaces, with discussions on the properties of different filter implementations.

6.2.1 Hardware RF Filters

The analog filter has many different realizations. Amplifiers can act as filters, as signals above or below certain frequency thresholds may not be amplified due to the characteristics of the amplifier. There are also passive analog RF filters, that use passive electronics components to remove unwanted harmonics and signals from outside the radio band of interest. These passive electronics components include resistors, inductors, capacitors, transformers, and crystals.

Before investigating the different filters and characteristics, the terminology must be described [*Tonne et al.*, 2012]. The pass band of a filter refers to the frequencies which undergo the least amount of attenuation from the filter. The cutoff frequency refers to the frequency at which the output has a gain of -3.0 dB compared to the pass band. The stop band of a filter refers to frequencies where the signal is attenuated to below a certain threshold. The value of attenuation for the stop band is based on the application of the device.

Some other characteristics to be concerned with for filters include the characteristic impedance of the filter, the pass band ripple, the insertion loss, and the power handling capabilities. The characteristic impedance of an RF circuit is designed typically to be 50 or 75 ohms, though for specialized operations this could be different. The pass band ripple refers to the variation in the gain over the pass band. For radio applications, it is optimal to reduce the pass band ripple to be as low as possible [*Tonne et al.*, 2012]. The insertion loss is the attenuation of the pass band with respect to the input signal. The power capability is important as, depending on where the filter is used, it may need to dissipate a large amount of power. This is especially true if used on the output of a power amplifier, for example, in order to minimize radio signal harmonics introduced from the amplifier.

Amplifiers have a band of operating frequencies where the amplifier is able to amplify an input signal. Signals outside this range may be amplified at a lower gain, attenuated, or not passed through the amplifier at all. This can effectively filter the signal outside the operating frequency band. The frequency band for an amplifier and/or transistor is provided on their respective datasheets. For ICEBEAR, the transmitted signal has a relatively narrow bandwidth, though harmonics of this signal are suppressed by the final stage amplifier. On the ICEBEAR receiver broadband low noise amplifiers are used on the front end of the system, resulting in minimal filtering from these amplifiers.

Passive filters are widely used in radio applications [*Das*, 2004; *Tonne et al.*, 2012]. These are inexpensive electronics filters and can be extremely useful when designed properly. The passive filter is a circuit of passive electronics components that acts to remove unwanted frequencies from the signal. This is possible due to the frequency dependence of different electronic components, such as capacitors and/or inductors. The RF band pass filter used on the ICEBEAR receiver front end is a passive filter with a center frequency of 49.5 MHz, and a pass band of 1 MHz.

There are also more niche filters, that are more expensive and have more defined uses. One of these is the crystal filter, where the resonant frequency of the crystal filter is determined by the cut of the crystal. The crystal filter has a very sharp transition from the pass to stop band, but typically has very narrow pass bandwidths [*Tonne et al.*, 2012]. This makes these filters excellent for narrow bandwidth radio applications, but inapplicable for broad

bandwidth applications. Crystal filters were investigated for use with ICEBEAR, but due to the cost and the narrow bandwidth were deemed unusable.

6.2.2 Digital Filters

With the modernization of radio technology, many electronics filtering processes are now performed in software rather than hardware [*Bloom*, 2012a]. This can involve a convolution between a filter and the recorded voltage samples, resulting in the filtered signal as an output. The incoming signal is measured with a broad bandwidth (high sampling rate), and once in the digital domain digital processes can be used to filter the signal. ICEBEAR performs decimation, low pass filtering, and matched filtering in the digital domain, which is discussed further in Section 8.5.3.

The advantage of digital filters over analog filters is that digital filters have less of a hardware footprint, and the digital filter is much more adaptable than a hardware filter. For example, if a radio listener wishes to change the radio station they are listening to, with a digital filter it consists simply of changing a digital value in the filter process. In the analog domain, a variable hardware filter would be required, or a different filter would need to be inserted in the signal chain. The drawback of digital filtering is that the processing power required for complex digital filter implementation can be immense, which can result in non-real time processing without additional analog filtering.

Some forms of filters are extremely difficult to implement in the analog domain, and require the digital domain to do so. This includes many radar matched filter waveforms (Chapter 5). There are also low pass, high pass, band pass and notch filters that can be implemented in the digital domain, many times with more accuracy and better control than a corresponding analog filter. The design of these different types of digital filters will not be covered here, but for more information one can refer to *Rorabaugh* [1997] and/or *Losada* [2004].

6.3 Signal Generation

The first thing that must be determined when creating a radio system is how the signal will be generated. This is done using analog and digital circuits, each with their benefits and drawbacks. From Chapter 5, a basic understanding of the resolution of different waveforms was presented. While it is relatively easy to model the waveform, the creation of such a waveform in the analog domain is no trivial task. The selection of a system that can generate complex radar waveforms was of extreme importance in the ICEBEAR system, with ICEBEAR transceivers described in Section 8.3.2. This section will investigate how a signal, or radar waveform, is generated using modern radio hardware.

Over the years advances have been made in the development and implementation of different signal generation techniques, both for radio and for radar. For radar systems, electronic oscillators were initially used to generate the radar signal. These devices take a direct current (DC) voltage and convert it to analog voltage oscillations with a defined frequency [*Stockton et al.*, 2012]. There are many different types of oscillator designs, for which details are beyond the scope of this dissertation. Nonetheless, it is sufficient to know that the initial implementations of signal generation would use an oscillator to convert a DC voltage to a AC electronic signal. This signal could then be used for communications and/or radar. As advances were made in the field of radio electronics it became possible to generate a modulated signal at baseband frequencies and use an oscillator and RF mixer to transform the signal to be centered at the oscillator (carrier) frequency [*Newkirk and Karlquist*, 2012]. This provided a modulated signal at the oscillator frequency. An overview of RF mixers follows.

6.3.1 RF Mixers

To increase the throughput of communication information, more and more advanced modulation was required on radio signals. To create a signal with modulation, a waveform was generated at baseband frequency and was mixed with an oscillator frequency using an analog mixer [*Newkirk and Karlquist*, 2012]. This then shifted that modulation to be centered on the oscillator frequency, which was typically the carrier frequency. This radio technique is

extremely useful for generating a modulated signal at the required frequency. Traditionally this mixing was performed in the analog domain, but advances in digital electronics and processing techniques now allow it to be done digitally. This makes maintaining phase and frequency coherence across multiple receive and transmit channels much easier, and allows digital control of the RF mixing system. ICEBEAR utilizes digital mixing methods at both the transmitter and receiver and makes use of these benefits. For ICEBEAR the transmitter signal is digitally mixed from baseband to a higher carrier frequency to be transmitted. At the receiver the scattered received signal is digitally mixed to baseband from the carrier frequency. Analog mixing is not performed in the ICEBEAR system, though an overview is provided here as it is an important technique in radar systems. A discussion of digital mixing follows the discussion on analog mixing.

The mixing frequency in an RF mixer can be generated using many different methods, though it typically involves an oscillator. One form of an oscillator is an amplifier and a filter in a feedback loop [*Stockton et al.*, 2012]. Using positive feedback, the initial signal is generated from the noise of the system, which is then filtered and passed back into the amplifier. The amplified noise signal is continually looped back and filtered until a stable signal power level is reached at the frequency determined by the filter. From this basic oscillator design, RF engineers have designed a multitude of methods to allow selection of a frequency. These are referred to as frequency synthesizers, and some details are given in *Stockton et al.* [2012].

An analog mixer works by combining two signals, typically a generated frequency and the modulation to be transmitted. The modulated signal is near baseband frequency and can include phase modulation, amplitude modulation, and/or frequency modulation. The mixers discussed here are multiplicative mixers. Note that additive mixers also exist, but are not used in the ICEBEAR system. Multiplicative mixers are complex circuits. For some examples of multiplicative mixer circuits the reader is directed to *Newkirk and Karlquist* [2012].

In circuit and block diagrams, a mixer is labelled as a circle with an "X" through it (Figure 6.2). A multiplicative mixer takes two signals and multiplies them together. The result is the signal shifted to the addition of the two frequencies and the difference of the two

frequencies [*Newkirk and Karlquist*, 2012]. This is given as $f_0 - f_i$ and $f_0 + f_i$, where f_0 is the frequency of the oscillator signal and f_i is the frequency of the input signal.

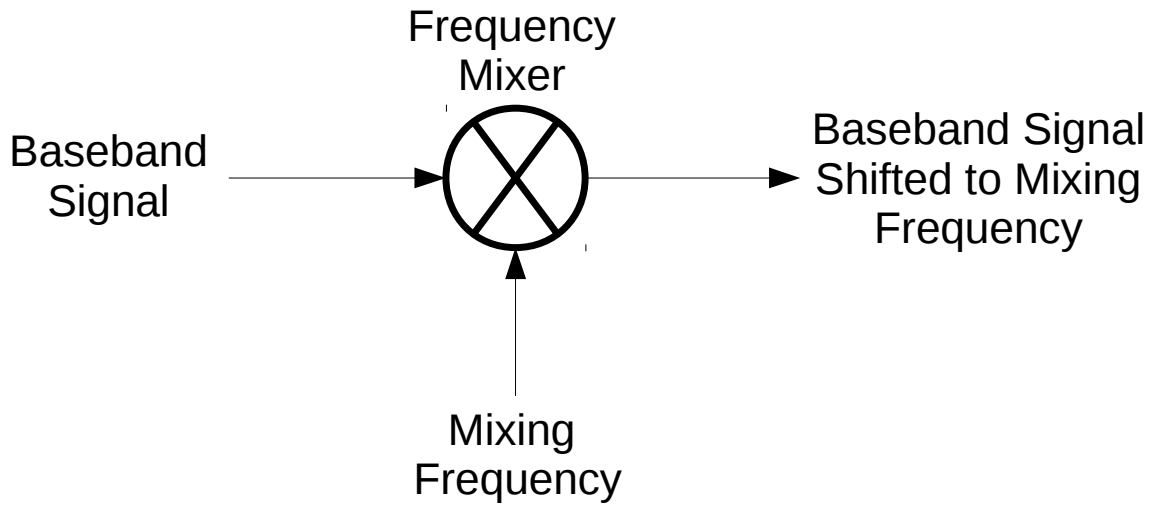

Figure 6.2: Block diagram of a frequency mixer.

An example of the frequency spectrum pre- and post- mixing is provided in Figure 6.3. As displayed by the figure, the input signal at 5 Hz is shifted by 50 Hz after being mixed with a 50 Hz carrier signal. The mixed signal now has a 50 Hz wave where the input signal had an amplitude of 1.0. This is a method of creating pulses and modulation for radio and radar systems, where an initial modulation is mixed with a carrier frequency to shift the signal to the transmission frequency wanted. The mixer can introduce harmonics into the signal so care must be taken when using these devices to be certain the output is what is wanted [*Newkirk and Karlquist*, 2012].

A signal can also be digitally mixed. This can be accomplished through field programmable gate arrays (FPGAs), specialized circuits, or in software, as was done for the example in Figure 6.3 [*Parsons et al.*, 2008; *Bloom*, 2012a]. Digital mixers mix the incoming digital signal with a digitally generated frequency, creating a shift of frequency to the sum and difference of the frequencies, same as an analog mixer. As with all digital methods, this can introduce nonlinearities into the signal due to quantization effects, however, the benefit is added signal control.

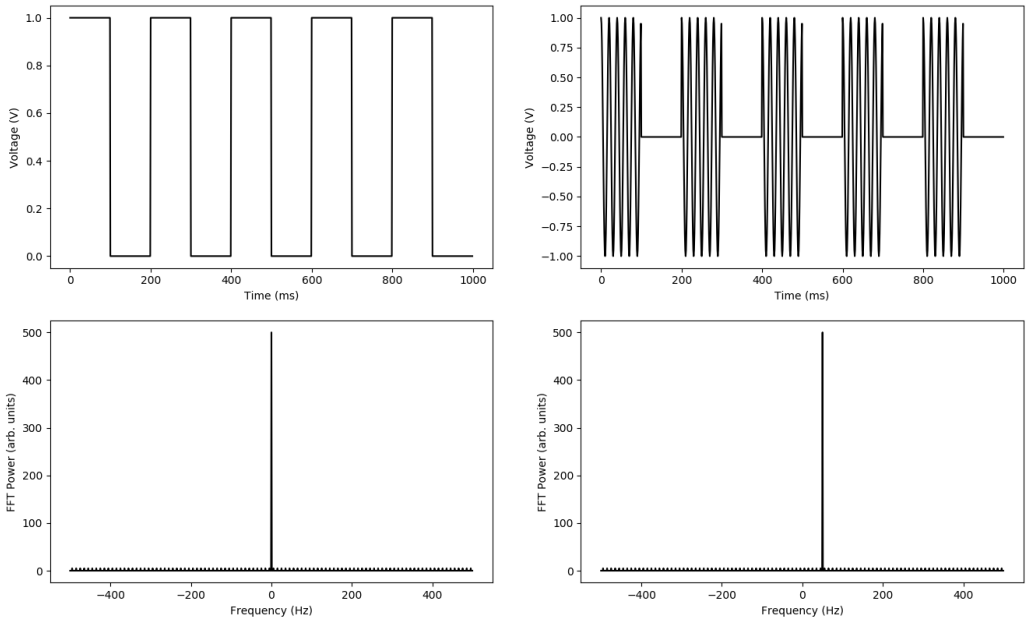

Figure 6.3: Mixing example of mixing a signal at baseband with a 50 Hz signal. It can be seen that the signal is shifted 50 Hz in frequency.

6.3.2 Signal Modulation

There are three types of radio modulation commonly used. These modulation types are amplitude modulation, phase modulation, and frequency modulation [*Bloom*, 2012b]. There are also modulations used which are a combination of these types to obtain the desired signal characteristics. Different modulation types were investigated for use with the ICEBEAR system, as utilizing modulation with a carrier signal can improve the range resolution of a radar [*Richards et al.*, 2010]. For the resolution of different modulation schemes (radar waveforms), the reader is referred to Section 5.5. The ICEBEAR system utilizes phase modulation to obtain simultaneous high spatial and temporal resolution with a CW signal. A discussion on the signal processing of this modulated signal is provided in Section 8.5.3.

The name of the modulation describes the method used for information transfer. Amplitude modulation works on the basis of varying of the amplitude of the carrier signal to transfer information, frequency modulation works on the basis of varying the carrier frequency to transfer information, and phase modulation works by varying the phase of the

carrier signal to transfer information. Many current radio communications systems use a combination of phase and amplitude modulation for data transfer, including the cellular networks, for example, quadrature amplitude modulation (QAM) [*Hanzo et al.*, 2004]. Systems can generate the modulation at baseband, and then use an analog or digital mixer to transmit the modulation at the carrier frequency. There are many different ways to produce these modulations, but only digital schemes are presented here, which is also known as digital signal processing (DSP) [*Bloom*, 2012a].

Digital signal generation is commonly achieved using a digital to analog converter (DAC). This device takes a digital signal and converts it to an analog voltage. Depending on the dynamic range and sampling rate of the DAC, it can introduce nonlinearities into the signal, such as harmonics [*Bloom*, 2012a]. This is due to the step-like voltage changes corresponding to changes in the digital voltage value, as the values are quantized. An example of this quantization effect is presented in Figure 6.4. The top panel of the figure is the wanted signal, the second panel is the digitized signal with quantization effects, and the bottom panel is the signal after being filtered. The bottom panel is similar to the wanted signal in the top panel, but quantization effects are still evident. By increasing the bit-resolution and sampling rate of the DAC these effects can be diminished, but still exist. To remove the nonlinearities, filters are used (Section 6.2). This is one of the drawbacks to using digital generation of radio signals, though the benefits of signal control and operation are significant. The ICEBEAR transmitter system uses digital signal generation techniques to produce the modulated transmission signal.

After the DAC, the signal can either be mixed to the carrier frequency or directly amplified if it is already at the RF frequency required. Recent advances in radio hardware have produced DACs with high bit-resolution (14-bit) and sampling rates in the GHz range (9 giga samples-per-second (GSPS)) [*Texas Instruments*, 2017]. With these advances the need for analog mixing is rapidly diminishing, and signals can be directly produced digitally up to GHz frequencies.

Along with the DAC and filtering, a clock reference is used for timing of the samples. The combination of the clock reference, DAC, and filtering associated with generating the radio signal is known as direct digital synthesis (DDS) [*Bloom*, 2012a].

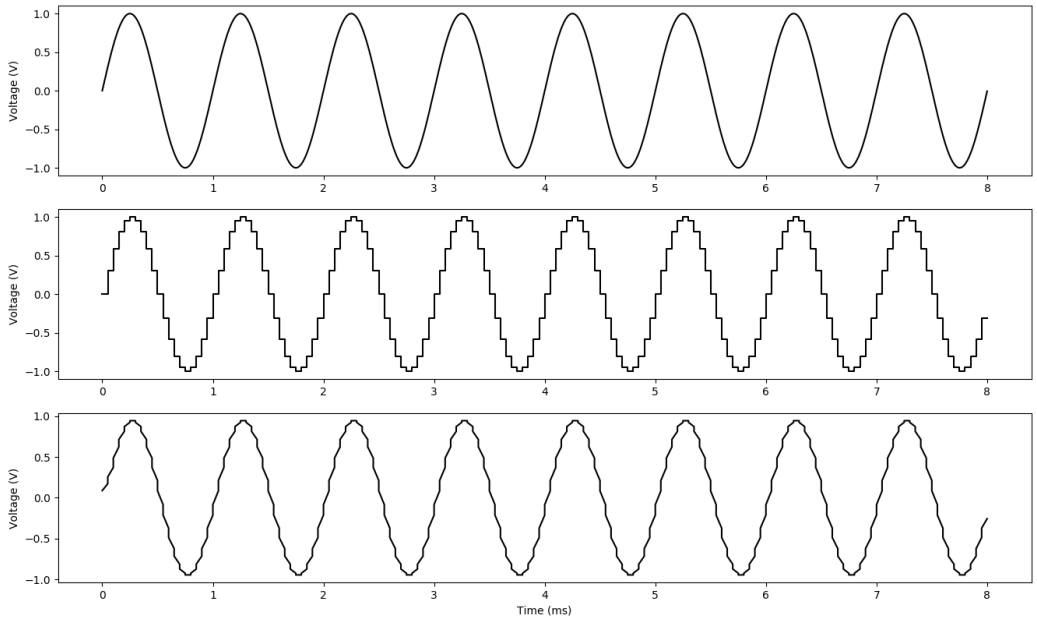

Figure 6.4: Example of how a voltage wave can be produced through digital to analog conversion. The top panel is the desired signal, the middle panel is the generated signal from a DAC and the bottom panel is the generated signal after using a simple digital low pass filter. In practice the low pass filter would be implemented in the analog domain. This figure simply provides an illustration of the signal generation process.

The signal may need to be sampled more frequently than the data is initially sampled at due to the DAC characteristics. This up conversion in sample rate can be accomplished using a digital up converter (DUC) [*Bloom*, 2012a]. This electronics device will repeat or interpolate samples to obtain a higher sampling rate so that the input sampling rate for the DAC matches the output rate.

Combining the devices and techniques described in this section provides a signal generation system, such as the one shown in Figure 6.5. The input digital signal is sampled at a certain rate, and then converted to a sampling rate that matches the digital to analog converter (up conversion). The DAC converts the digital value to an analog voltage, which is then filtered to diminish the effects of quantization. If the DAC has a sufficiently high sampling rate for the frequency desired, the analog mixing and second filtering stage are not required. This setup will allow the generation of a signal with a bandwidth of one half the

sampling rate of the DAC, shifted to a frequency determined from the analog mixing stage. The ICEBEAR signal generation utilizes the DUC, DAC, and filter stages of the system shown here, and does not require the analog mixing stages for the radio frequencies used.

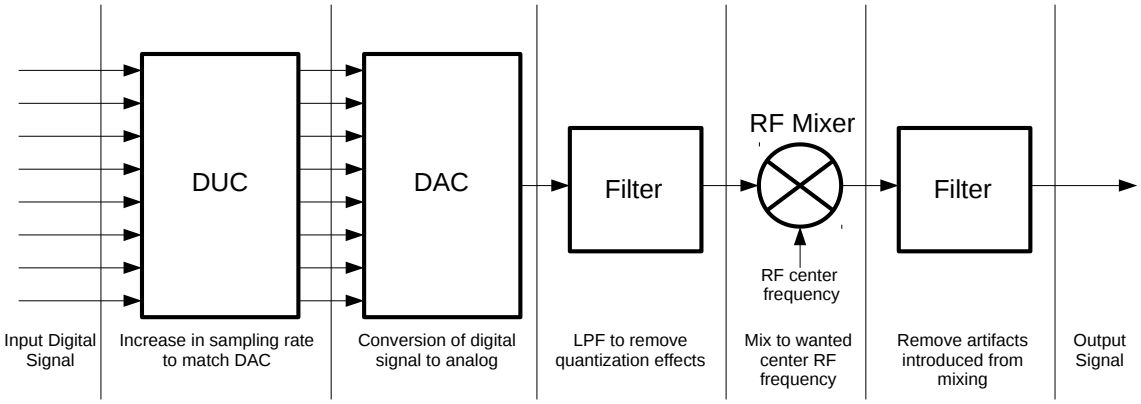

Figure 6.5: Block diagram of signal generation system.

Once the signal is generated, and set to the appropriate carrier frequency, it commonly needs to be amplified. To do this, a radio amplifier is used. The next section investigates the operation of different radio amplifiers.

6.4 Amplifiers

A typical signal generator will produce a radio signal with a maximum power on the order of 1–10 mW. A 10 mW signal corresponds to a peak voltage level of 1 V for a 50 Ω system (10 dBm). An amplifier is used to increase the power of such a signal before being transmitted at an antenna. Without this amplification, it is difficult to detect radio signals at a radio receiver over significant distances.

One of the key components in the ICEBEAR system are the transmitter amplifiers. The output of the ICEBEAR amplifiers is required to be at least 55 dBm, with a gain of 55 dB, so that the ionospheric scatter can be measured at a receiver. These were minimum values, where the objective was to obtain a larger power output and gain. Another design goal for the amplifier was to be efficient with linear 50 MHz signal amplification. This section provides background information on the general design and operation of amplifiers, with a detailed description of the ICEBEAR transmitter amplifiers provided later in Section 8.4.1.

As part of my dissertation project, I designed and built the ICEBEAR power amplifiers.

6.4.1 Amplifier Devices and Classes

There are two commonly used types of transistors in amplifiers, these are the metal oxide semiconductor field effect transistor (MOSFET), and the bipolar junction transistor (BJT) *Sedra and Smith* [2004]. The BJT will not be investigated here, as the ICEBEAR amplifiers use MOSFET components in their design. There are also other devices used for signal amplification, such as vacuum tubes and klystrons, which will be briefly explained later.

The design of a NMOS field effect transistor (FET) can be seen in Figure 6.6. When the gate voltage is driven high, it creates a channel for current to flow through the device. This is accomplished through doping the substrate. In this setup the "source" is connected to ground and a voltage is applied at the "drain". For an RF input signal on the gate, this then varies the current flow through the device, which can be used to amplify a signal.

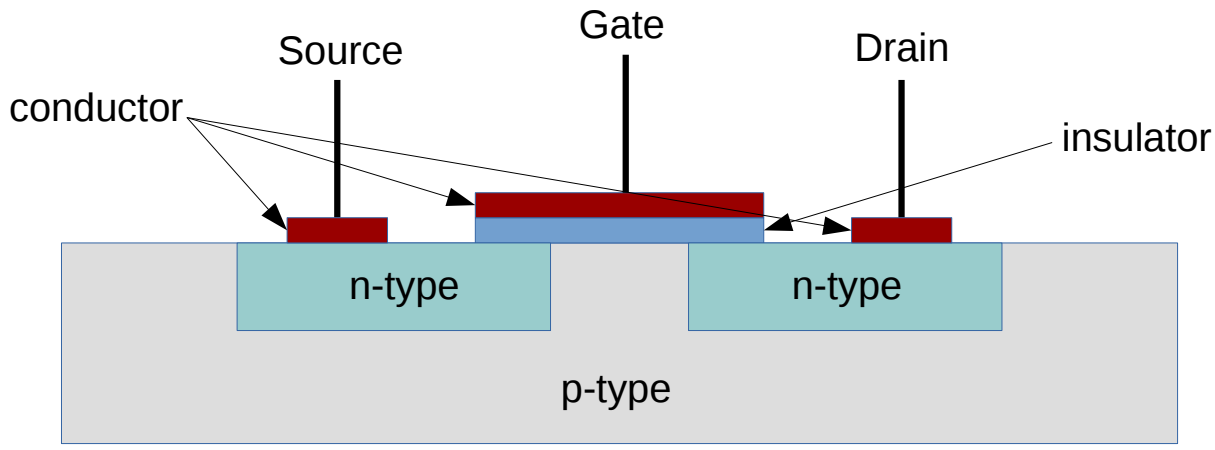

Figure 6.6: Basic npn MOSFET design. The n-type section is doped with excess electrons and the p-type substrate is doped with excess hole (positive charge). Adapted from [*Sedra and Smith*, 2004]

An example of multiple IV-curves for a MOSFET are shown in Figure 6.7. The IV curve refers to the current-voltage relationship of the amplifier, where the slope of a given point on the load-line is related to the impedance of the load. Each of the curves refers to a voltage on the gate, while the x-axis is the voltage drop from the drain to the source v_{DS}, and the y-axis

is the current from the drain to the source i_D. In the figure, Q is the DC bias point about which an AC signal will oscillate along the CBQA line. For linear amplification purposes, it is desired to be in the saturation region of the transistor.

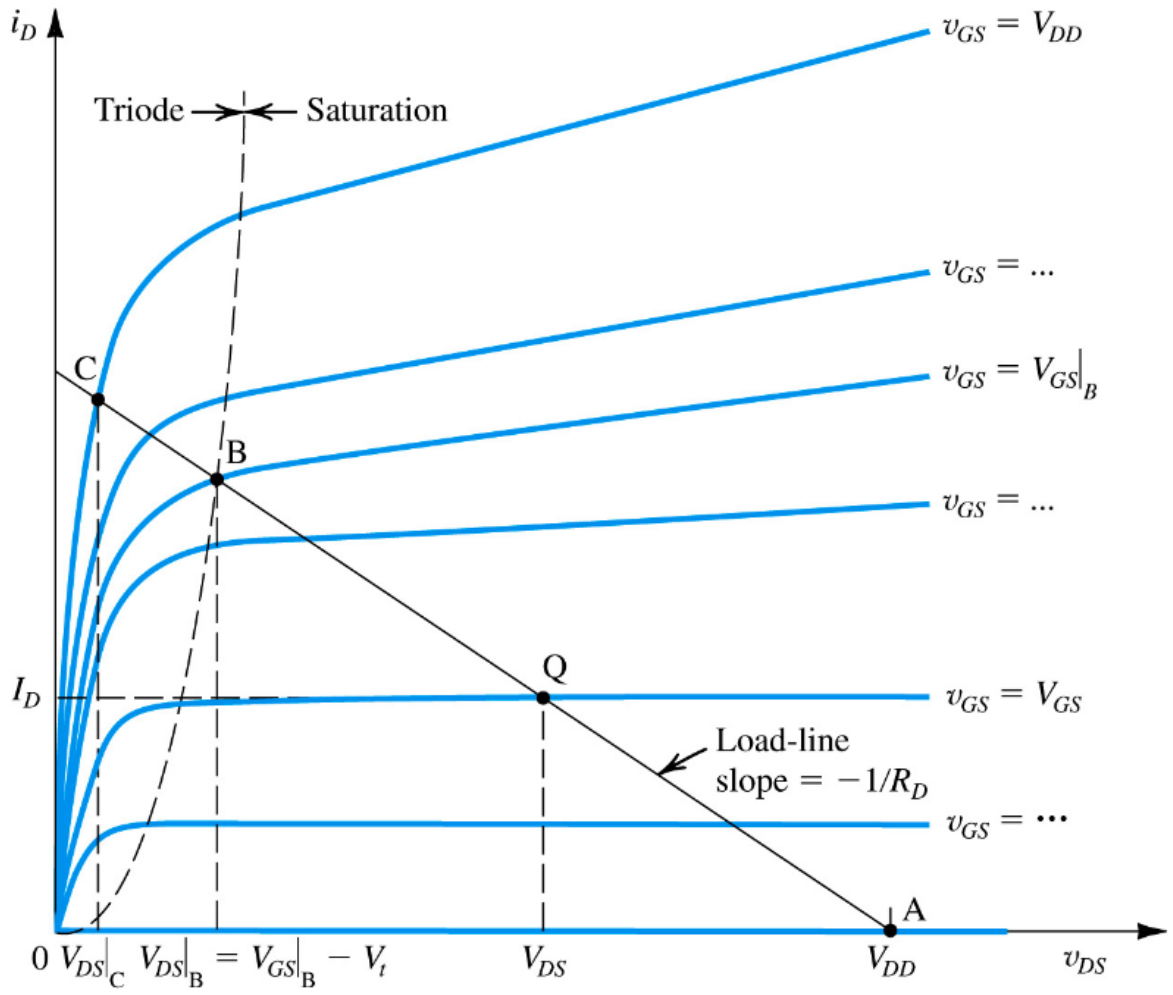

Figure 6.7: IV curves for an example MOSFET device [*Sedra and Smith*, 2010]

.

There are multiple types of amplifiers, each with advantages and disadvantages. These have been labelled as class A, B, C, and D [*Sedra and Smith*, 2004]. There can also be combinations of different classes of amplifiers to obtain improvements over the use of a single type. A survey of these different types was performed to determine which amplifier class would be ideal for the ICEBEAR system.

Class A amplifiers are the most linear of the amplifier classes, but also the least efficient.

An example of a class A amplifier is shown in Figure 6.8. The circuit diagram uses BJT devices, but a similar setup would be used for a class A MOSFET circuit. From the output voltage, it can be observed that there are no nonlinearities in the output signal. These class A amplifiers have a single transistor that is biased to its mid IV curve point (Q point in Figure 6.7). This allows the most amplification of the signal for the positive and negative transitions before saturating and creating nonlinearities. With the mid-point bias (Q point), this means that the amplifier is constantly drawing current, resulting in the low efficiency of this amplifier architecture. The class A amplifier is ideal for initial amplifier stages in a multi-stage amplifier due to the relative power draw being low and a highly linear signal being preferred so that signal nonlinearities do not propagate through the amplifier/signal chain.

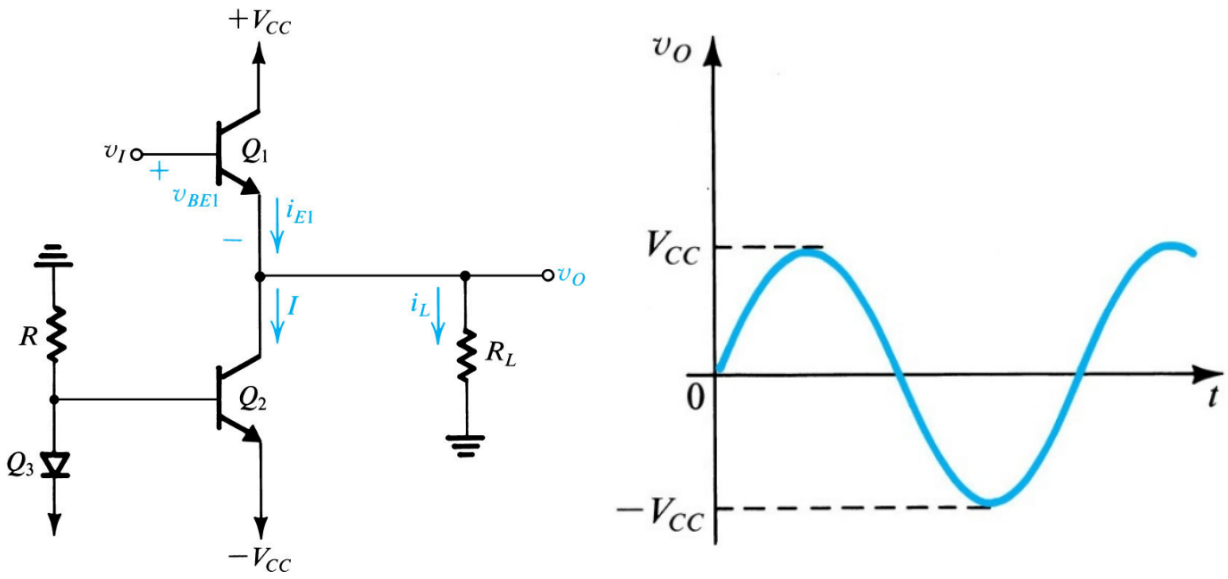

Figure 6.8: Class A circuit example with the output voltage [*Sedra and Smith*, 2010]

.

Class B amplifiers operate using two transistors, but with no input bias. Each transistor handles one polarity of the incoming signal, but since there is no bias, a discontinuity exists as the wave transitions from positive to negative and vice versa. An example of a class B amplifier using BJTs is shown in Figure 6.9. The discontinuity is due to the diode voltage required to overcome the base conduction band. From the figure, the discontinuity is evident

in the output voltage signal. This class B setup results in a much more efficient amplifier than a class A amplifier, but the nonlinearities created from the transition region create distortion in the output signal.

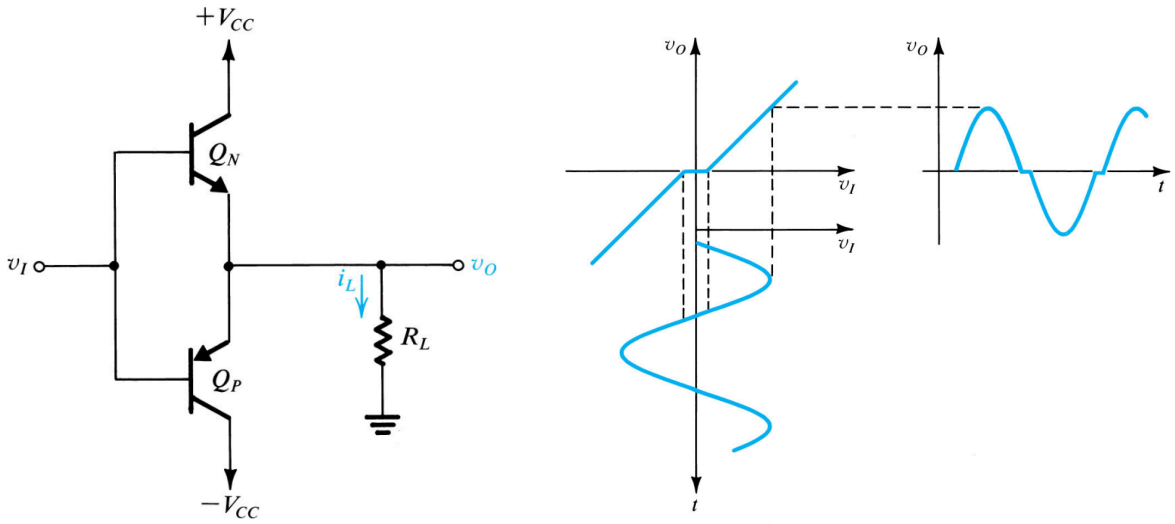

Figure 6.9: Class B circuit with input voltage (v_I) and output voltage (v_O) characteristics [*Sedra and Smith*, 2010]

.

Class AB amplifiers take the advantages of both class A and B amplifiers and attempt to minimize the disadvantages. These amplifiers are less linear than class A, and less efficient than class B, but attempt to reach a compromise between efficiency and linearity. The dual transistor setup from class B operation is used, now with a small bias applied to the transistors. This small bias reduces, or even eliminates, the non-conduction region experienced by class B amplifiers. An example of a class AB amplifier using BJTs is shown in Figure 6.10. The small bias means that the transistors are conducting when idle, but minimally. In the right panel of the figure, it can be observed that the discontinuity between the positive and negative portions of the signal is all but eliminated, and there is a linear relationship between in the input and output voltages.

A class C amplifier has similarities to a class A amplifier, but with only a minimal bias applied to the gate. This results in only half the waveform being amplified, and creates significant distortion of the signal. The benefit of this is that the amplifier is more efficient,

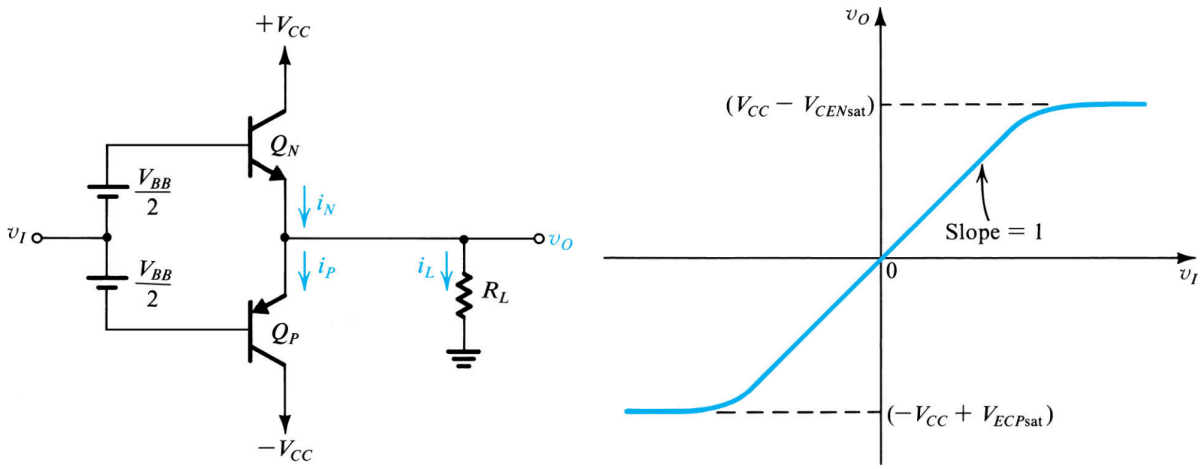

Figure 6.10: Class AB circuit with the voltage transfer function (v_O plotted against v_I) [*Sedra and Smith*, 2010]

.

and it is possible to filter out the distortion introduced to the signal.

The other classes of amplifiers are defined as switching amplifiers, as the output is either on or off [*Bloom*, 2012c]. The amplifier designations start at class D and continue through the alphabet. These amplifiers use nonlinear hardware and techniques to produce signals with extremely high efficiency ($\approx 95\%$).

As the best trade off between linearity and efficiency for radio applications is the class AB amplifier, many RF amplifier systems are designed around this architecture, including the ICEBEAR amplifiers. Typically FET transistors have efficiencies on the order of 50%, but recent developments have been improving greatly upon this efficiency. An example of a recent FET device with a 75% efficiency is the MRFX1K80H from NXP Semiconductors [*NXP Semiconductors*, 2018]. This dual transistor device is able to operate at frequencies of 1.8 MHz to 500 MHz, has a maximum power output of 1,800 W continuous, and has a gain of ≈ 27 dB. As many devices use the class AB amplifier architecture, there are a significant portion of dual transistor packages pre-made for this configuration. The ICEBEAR amplifiers did not make use of these new efficient transistors, but it is important to note that advances in transistor efficiency have been occurring since the design of ICEBEAR and will be worth exploring if the amplifiers are re-designed.

6.4.2 Broadband Amplifiers

Many radio applications require similar amplifier characteristics over large frequency ranges. There are different design decisions that can be made to accomplish this broadband amplification. The ICEBEAR amplifiers were designed with an industrial partner who desired broadband RF operation of the amplifier, and some methods to accomplish this are explored in this section. Some of these methods include using a transformer on the input and output, and using a feedback circuit.

It is typical for amplifier designers to sacrifice gain for broadband operations. An example of how this is accomplished is shown in Figure 6.11. When the voltage of the input signal is "high" at the gate, the voltage of the output signal at the drain is "low", and vice versa. With a proper feedback circuit, it is possible to attenuate the input at certain frequencies using this information. The feedback circuit provides less gain at the peak gain frequencies, but allows for the gain to be uniform over a broader range of frequencies. If more gain is required, it is possible to cascade multiple broadband amplifiers [*Silver et al.*, 2012]. A feedback circuit is used in both the stage 2 and stage 3 portions of the ICEBEAR amplifier design.

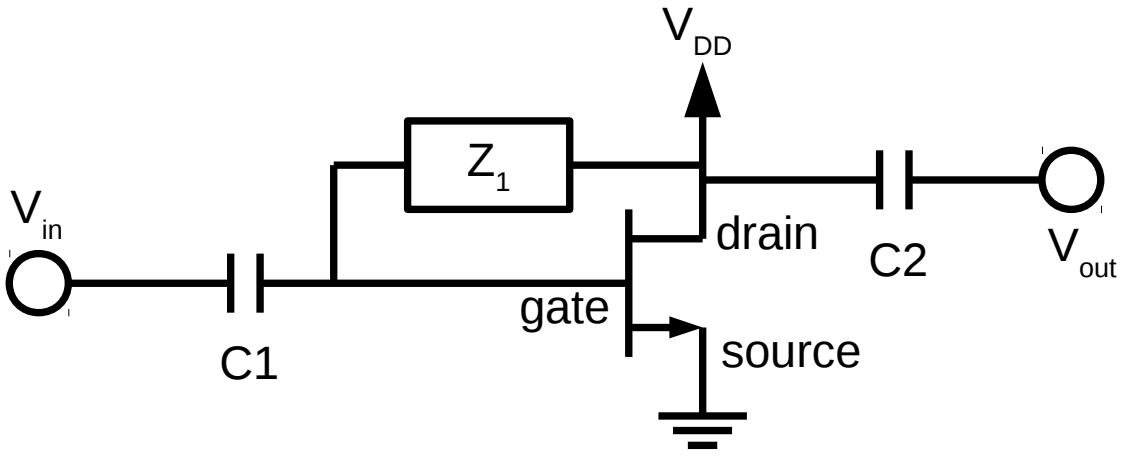

Figure 6.11: Example of one method to make an amplifier more broadband through using a feedback circuit to cause the gain to be uniform over a broader range of frequencies.

In Figure 6.11, the impedance of Z_1 is selected so as to reduce the highest gain of some fre-

quencies, providing a more uniform gain across the frequency band. The feedback impedance has a larger impedance at frequencies outside of that frequency band, reducing the amount of attenuation at these out of band frequencies.

Another method of creating broadband impedance matching for an amplifier is to use a transformer, which can be used to achieve impedance transformations over a broad range of frequencies [*Bloom*, 2012c]. In many applications the impedance of the transistor used is much lower than the characteristic impedance of the system. An efficient broadband method of matching the characteristic impedance of the external system to a significantly lower impedance is to use a transformer, as was discussed in Section 6.1. Ferrite can be used as the core of the transformer to allow lower frequency operation than would be possible with air as the "core". Using a transformer on the input and output in the design of an amplifier is a well established technique to broaden the operating frequencies, or bandwidth, of an amplifier. The ICEBEAR amplifiers utilize transformers in multiple amplification stages to obtain broadband operation.

6.4.3 Amplifier Characteristics

Some important properties of amplifiers include the gain, the maximum power output, the harmonic distortion and the noise figure [*Silver et al.*, 2012; *Bloom*, 2012c]. The characteristics important in the operation of the amplifier depend on its use. Low noise amplifiers are typically used in the receiver front end of a radar system, while power amplifiers are used in the transmitter front end.

Low Noise Amplifiers

The amplifiers on the receiver side can be placed at the antenna, or as a front end to the radio receiver. An amplifier at the antenna helps to minimize the effects from transmission cable loss, and an amplifier on the radio receiver front end can be used to amplify the signal so it is within the radio receiver measurement range. A discussion of the receiver chain for ICEBEAR, including the low noise amplifiers, is provided in Section 8.5.1. A description of how a received signal is measured and the receiver dynamic range will be covered in Section 6.6

On the receiver side, a low noise figure and a high gain are desirable characteristics for an amplifier [*Hallas*, 2012]. A low noise level on the receiver electronics improves the signal to noise ratio (SNR) at the receiver, providing less ambiguities in the data and reducing the errors in communications. The maximum power output for a receiver amplifier is typically below 1 W, due to the incoming signal being weak and radio receivers commonly operating below this power. The low noise amplifiers used with ICEBEAR (ZFL-500LN+ from Mini-Circuits) have a gain of $\approx$ 28 dB and a noise figure of $\approx$ 3 dB.

Power Amplifiers

For transmission (power) amplifiers, a low noise figure is less important. The important factors are the gain, the output power and the harmonic suppression [*Bloom*, 2012c]. The gain is important so that less amplifier stages are required to achieve the wanted output power. The power output is important due to the fact the amplifier must be able to achieve the output power necessary for the system to operate. The harmonics of the amplified signal are important as they determine whether or not the amplifier requires filtering on the output to fall within the Radio License regulations. The ICEBEAR power amplifiers were designed by myself, with the amplifiers discussed in Section 8.4.1.

The gain, power output, and harmonics are all linked to varying degrees. As the signal output power approaches the peak operational output power limit of an amplifier, the gain decreases and the harmonics generated on the signal increase. One can refer back to Figure 6.7 and observe how there is only a limited amount of distance along the CBQA load line before the output current reaches the maximum/minimum points. At these maximum and minimum points, the peaks of the waveform become distorted, which results in nonlinearities being introduced into the signal.

On an amplifier data sheet, the peak output power is typically listed as P1dB and P3dB values. An example of the linear amplifier output versus the actual output is shown in Figure 6.12, where the P1dB point is labelled. The P1dB and P3dB values refer to the output power when the gain is decreased by 1 dB (P1dB) and the output power when the gain is decreased by 3 dB (P3dB). At output powers above these values, the signal becomes more and more distorted, resulting in increased unwanted harmonics.

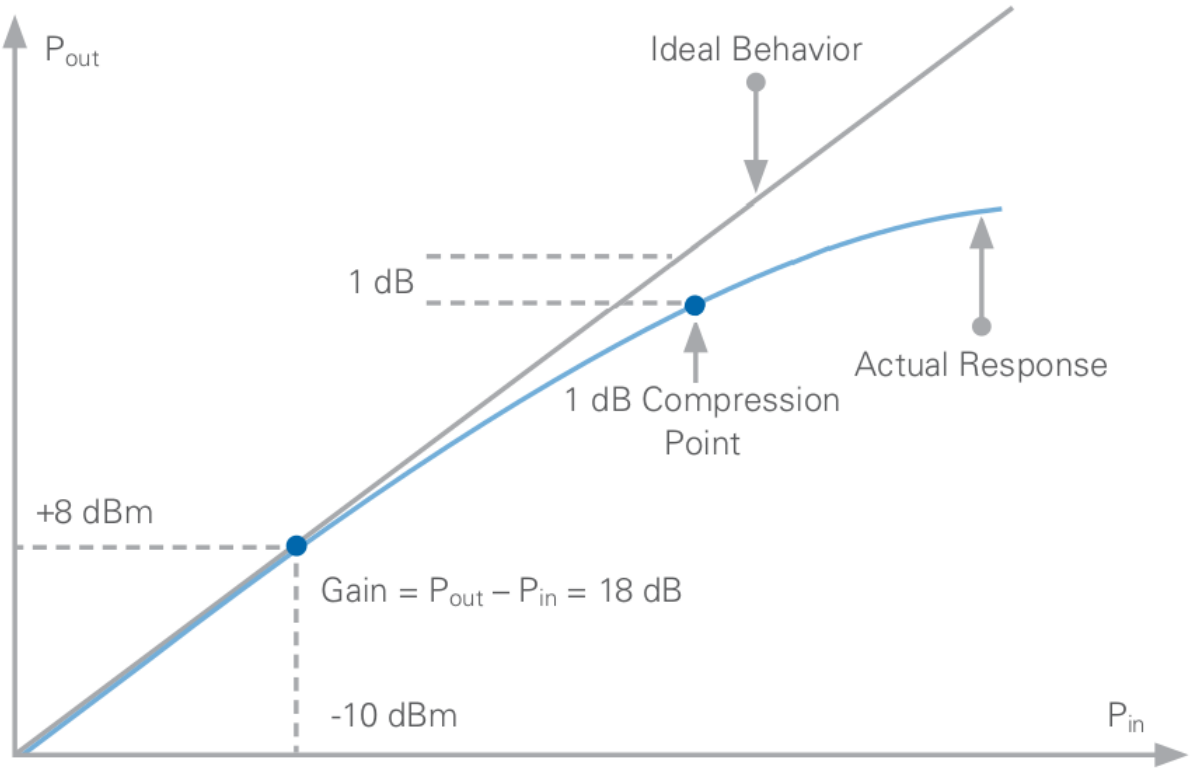

Figure 6.12: Plot of ideal amplifier gain vs actual gain, depicting the P1dB point. Adapted from *National Instruments* [2016].

6.4.4 Amplifier Cooling

Along with the gain, power output, harmonic suppression and the noise figure, there are other important amplifier parameters. One of these parameters is the transistor/amplifier efficiency. A less efficient amplifier will generate more heat, requiring a heat management system [*Bloom*, 2012c]. Data sheets include specifications for the thermal resistance of the transistor to the case (usually the same as the ground plate of the device) in units of °C/W. This refers to the temperature that the transistor will be compared to the transistor case for every watt of dissipated heat. For a typical high power amplifier, there will be multiple heat dissipation stages to keep the transistor as cool as possible. The transistors can be mounted to a heat spreader, typically made of copper, with heat spreader compound used in the interface between the two. The heat spreader compound decreases the thermal resistance between two surfaces. Attached to the heat spreader can be a large aluminum heat sink, that interfaces with the air to convect heat away from the device. The heat sink has fins or

other extrusions to accommodate increased heat convection. Forced air can also be used over the heat sink to increase the rate of cooling and decrease the temperature of the heat sink [*Bachman and Haiduk*, 2011].

There are also heat management methods using liquids to cool the heat spreader and these would take the place of the heat sink. Some issues with liquid cooling are that the cooling system is more complex, and expensive [*Mahajan et al.*, 2006]. As the ICEBEAR transmitter radar site is remote, any issues associated with liquid cooling would be difficult to diagnose and remedy. The ICEBEAR amplifiers therefore use forced air cooling in combination with a heat sink.

To calculate the temperature of the transistor, all heat sink factors must be included. This includes the thermal spreader paste used, where different thermal pastes have different thermal conductivities. An example equation for a thermal calculation is given as,

$$T_{transistor} = P_{diss}[\theta_{jc} + \theta_{tp1}] + P_{diss\_total}[\theta_{hsp} + \theta_{tp2} + (\theta_{hsi})(\eta_{fa})] + T_{air} \tag{6.4}$$

where P_{diss} is the power dissipated by each transistor, P_{diss_total} is the total power dissipated, θ_{jc} is the thermal resistance between the transistor junction and transistor case, θ_{tp1} is the thermal resistance of the thermal paste at the interface between the transistor and the heat spreader, θ_{tp2} is the thermal resistance of the thermal paste at the interface between the heat spreader and the heat sink, θ_{hsp} is the thermal resistance of the heat spreader, θ_{hsi} is the thermal resistance between the heat sink and air, η_{fa} is the increased cooling efficiency due to forced air cooling and T_{air} is the temperature of the air used to cool the heat sink. These are the same interfaces as used for the cooling system of the ICEBEAR amplifiers. The ICEBEAR system uses two transistors, with each transistor dissipating half the heat into the same heat spreader. For the final stage of the ICEBEAR amplifier, $\theta_{jc} = 0.13$ °C/W, $\theta_{tp1} \approx 0.021$ °C/W, $\theta_{hsp} = 0.0008$ °C/W, $\theta_{tp2} \approx 0.00065$ °C/W, and $\theta_{hsi} = 0.21$ °C/W.

A description of the efficiency factor for forced air cooling can be seen in Table 6.1. The air flow is listed in linear feet per minute (LFM), which is the cubic feet per minute (CFM) rated by the fan divided by the area of the fan. From the table, it should be noted that there are diminishing returns from increasing the airflow. The ICEBEAR amplifiers use fans with a LFM value of $\approx$ 800 ft/min, corresponding to a forced air cooling factor of 0.268 (η_{fa}).

Using this value with a total power dissipated of 800 W and an air temperature of 20 °C, the resulting temperature of the ICEBEAR amplifier heat spreader is ≈ 66 °C, with the transistors at ≈ 127 °C. This is well within the 200 °C temperature limit of the transistors.

LFM	Efficiency Factor
100	0.757
200	0.536
300	0.439
400	0.378
500	0.338
600	0.309
700	0.286
800	0.268
900	0.252
1000	0.239

Table 6.1: Table of forced air cooling efficiency factors [*Bachman and Haiduk*, 2011].

After the amplifiers, a radio signal is typically sent to an antenna to be transmitted. Antennas and antenna arrays are described in the next section.

6.5 Antennas

Antennas act as an impedance matching circuit between a voltage carrying conductor and the air (or vacuum). The varying voltage in a conductor corresponds to a varying electric field, where, when electrons are accelerated, they produce EM radiation (Appendix D). The antenna controls the EM radiation pattern produced by these accelerating electrons through the orientation and configuration of the antenna elements or components. In antenna design it is possible to use active and parasitic components, where the active components are driven by supplying a signal to them, and parasitic components re-radiate the EM radiation from active components to affect the radiation pattern [*Hutchinson et al.*, 2012].

On the reception side, the incoming EM wave produces an electric field in the antenna, which is experienced by the electrons [*Hutchinson et al.*, 2012]. This generates a wave at the same frequency as the incoming signal that propagates through the conductor and can be measured. The ICEBEAR system uses antennas at both the receiver and transmitter sites to transmit and receive the radio signal. A description of the ICEBEAR antennas is provided in Section 8.3.1. This section will investigate different antenna radiation patterns, and methods of using multiple antennas in an array to synthesize a larger antenna aperture, as is done with ICEBEAR.

6.5.1 The Dipole Antenna

A widely used antenna is the simple dipole [*Hutchinson et al.*, 2012]. For best results, this antenna is a conductor that has a length of an even integer fraction of the full wavelength of the wave to be transmitted, where the even integer fraction is chosen so that the standing wave generated on the antenna constructively interacts. Typically this is either $\lambda/2$ or $\lambda/4$. An example of a half-wavelength ($\lambda/2$) dipole antenna and the associated radiation pattern is shown in Figure 6.13. From the figure, it can be observed that the half-wavelength refers to the full antenna length, consisting of two quarter-wavelength ($\lambda/4$) conductor lengths. The radiation pattern from this antenna is donut shaped, with the nulls occurring parallel to the dipole.

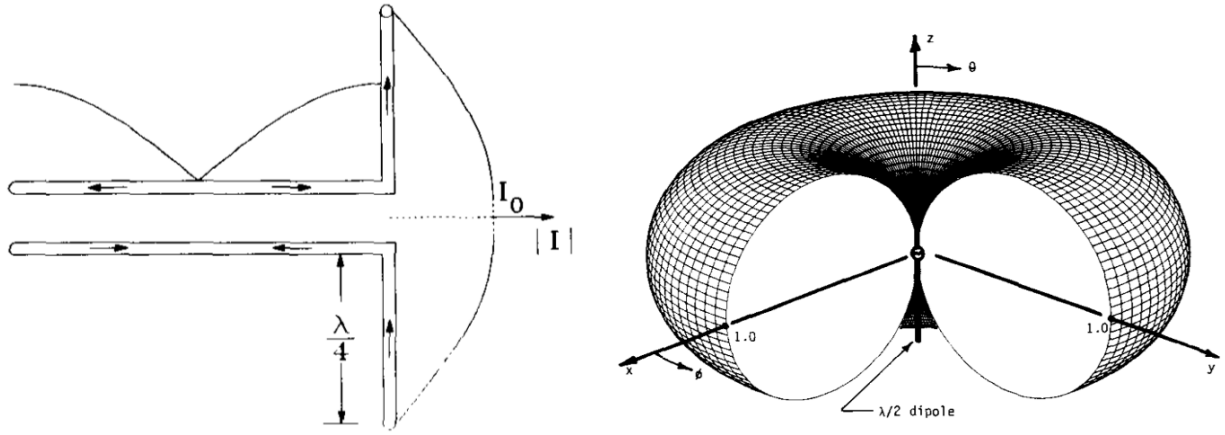

Figure 6.13: The current flow and radiation pattern of a half wavelength dipole antenna. Adapted from *Balanis* [1992].

The dipole antenna has a gain of 2.1 dBi, where dBi is the increase in power when compared to an isotropic radiator. This increase in power is due to concentration of the power in a certain direction. Many licensing and regulatory boards require the signal power expressed as the effective radiated power (ERP), which is the power emitted by the antenna multiplied by the gain achieved through antenna directivity. The gain and directivity of an antenna are determined by the shape, size, and configuration of the antenna.

6.5.2 The Yagi Antenna

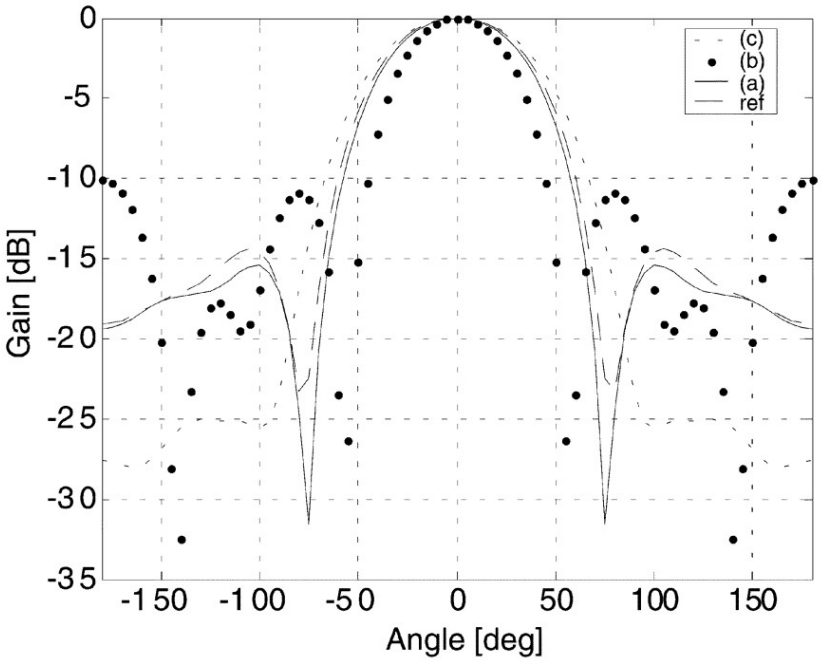

	Reference		(a)		(b)		(c)	
Element	Length	Space	Length	Space	Length	Space	Length	Space
1[λ]	0.490	---------	0.4850	---------	0.4804	---------	0.4930	---------
2[λ]	0.472	0.283	0.4742	0.2688	0.4522	0.2729	0.4756	0.2661
3[λ]	0.442	0.179	0.4474	0.1865	0.4412	0.2839	0.4444	0.1590
4[λ]	0.424	0.279	0.4286	0.262	0.4444	0.3004	0.3832	0.3443
Boom Length [λ]	0.741		0.7173		0.8572		0.7694	
Gain [dBi]	9.93		10.31		11.56		9.63	
VSWR	1.33		1.49		2.63		1.81	
Side lobe Level [dB]	-14.4		-15.43		-10.07		-25.04	

Figure 6.14: Radiation pattern for a 4-element Yagi antenna in azimuth. The different traces are for different spacing of the elements (shown in table). Adapted from *Kuwahara* [2005].

As indicated, it is possible to add passive components to the antenna to change the

radiation pattern. In the case of the dipole, "directors" and "reflectors" are able to be added to increase the directionality (and gain) of the forward radiation pattern. Directors are located parallel with the dipole in the direction of the forward radiation pattern. They are shorter than the dipole active antenna. Reflectors are located parallel with the dipole as well, but they are located in the opposite direction of the forward radiation pattern. These elements are longer than the dipole antenna. The combination of these passive directors and reflectors with an active dipole is called a Yagi-Uda antenna [*Uda and Mushiake*, 1954], where typical antenna gain values are dependent upon the number of reflectors and directors in the antenna design [*Kuwahara*, 2005]. The radiation pattern of a Yagi-Uda antenna is shown in Figure 6.14. The table included in the figure corresponds to the changes in the radiation pattern for different spacing between the antenna elements. Changing the spacing and length of the elements is shown to change the sidelobes of the radiation pattern significantly, though the main lobe remains relatively similar for all configurations shown here. The (b) configuration does increase the directionality of the radiation pattern, but the consequence is larger side lobes.

6.5.3 Antenna Ground Effects

Something to consider when modelling an antenna radiation pattern is the effect of a ground plane [*Straw et al.*, 2007]. The Earth acts as a non-ideal ground, where the composition of the soil and its water content can affect its conductivity. For most analysis done in this thesis, we consider the ground to be an ideal conductor, where signals are reflected from the ground to interfere constructively and destructively with the transmitted signal.

From the ground effects, the height at which an antenna is mounted with respect to the wavelength of the signal transmitted can affect the EM radiation pattern. An example of different antenna mounting heights and the resulting radiation pattern in the elevation domain for horizontally aligned antennas is shown in Figure 6.15. The ground reflects the radio signal and this results in constructive or destructive interference, corresponding to the elevation angle. Note that antennas closer to the ground produce fewer radiation pattern lobes and that the radiation pattern peaks at higher elevation angles. Due to the location of the ICEBEAR transmitter and receiver, for an altitude of 105 km at a distance of 700 km an

elevation angle of $\approx 5.5^\circ$ is required. From Figure 6.15, the ICEBEAR antennas are required to be at least 2-λ above the ground for this desired radiation pattern.

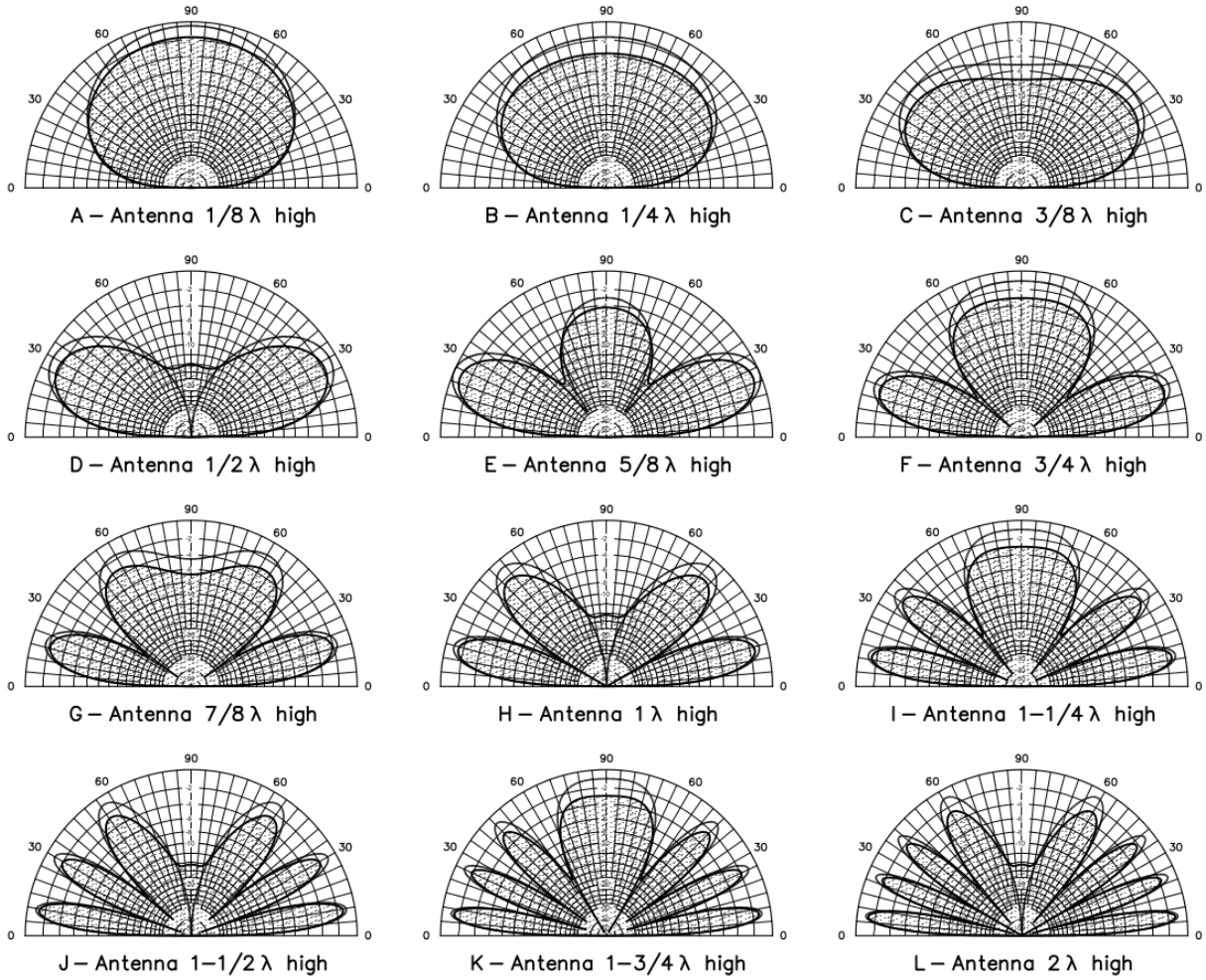

Figure 6.15: Radiation pattern in elevation for different horizontal dipole antenna heights. The shaded region refers to the radiation pattern with a typical, non-ideal, ground plane of the Earth. [*Straw et al.*, 2007]

6.5.4 Polarization Effects

The polarization of an EM wave is determined by the electric field associated with it [*Hutchinson et al.*, 2012]. Antennas are sensitive to this polarization, as the orientation of the antenna will determine how the EM wave interacts with the electrons in the conductor. For maximum coupling, the polarization of the EM wave should be oriented parallel to the antenna orientation. If the antenna and polarization are not parallel, there will be a reduction in the

power received.

A dipole antenna transmits linearized polarized radiation, though it is possible to transmit different polarizations with more advanced antenna designs. A cross dipole allows control of the electric field horizontally and vertically, providing the capability to transmit and receive different polarizations of an RF signal [*Hussey*, 1995]. ICEBEAR utilizes horizontally polarized antennas, and therefore only detects one dimension of the polarization of the incoming wave.

6.5.5 Antenna Feedlines

When receiving signals, often a pre-amplifier is placed directly at the antenna feed. This is to counteract transmission line losses from the antenna to the receiver due to the coaxial cable used. Higher frequency radio signals have larger losses, and therefore are more likely to require a pre-amplifier at the antenna [*Straw and Cutsogeorge*, 2012]. A table of different transmission cable types and their typical losses is shown in Figure 6.16. The ICEBEAR antenna feedlines are longer than 300 ft (91.44 m), with a frequency of $\approx$ 50 MHz. Since ICEBEAR operates in the VHF spectrum with a significant cable length, a coaxial cable similar to LMR-400 was chosen for the ICEBEAR antenna feedlines to minimize the attenuation of the radar signal (0.9 dB/100 ft, corresponding to 2.95 dB/100 m). A discussion on the feedline and system losses at the ICEBEAR receiver is provided in Section 8.5.1

Waveguides can also be used to carry the signal from the antenna to a receiver [*Straw and Cutsogeorge*, 2012; *Hysell*, 2018]. These are designed for certain frequencies and are typically hollow. The loss in signal level is significantly reduced with a properly designed waveguide, though they are much larger in size and more rigid than a coaxial cable. This can be an issue, depending on where an antenna is setup, and the length of the waveguide required. For ICEBEAR, the coaxial cable losses were sufficiently small to rule out using a waveguide for the transmission and reception of the ICEBEAR signal.

Coax Type		Outside Diameter	Dielectric Type	Velocity Factor	Loss - dB/100 feet						
					10MHz	30MHz	50MHz	150MHz	450MHz	900MHz	3000MHz
RG188		0.11	Teflon	0.695	3.8	6.58	7.9	13.7	23.7	31.8	58
LMR-100	*	0.110	Polyethylene	0.66	1.3	3.9	5.1	8.9	15.8	22.8	47.7
LMR/CNT-195	*	0.195	Poly Foam	0.75	1.37	2.38	3.1	5.3	9.2	13	24
RG58C/U	*	0.195	Polyethylene	0.659	1.4	2.4	4.1	7.1	11.8	20	37
RG58/U	*	0.195	Polyethylene	0.659	1.2	2.1	3.1	5.4	9.3	16	30
RG400		0.195	Teflon	0.695	1.2	2.1	2.7	4.7	10	14.2	26
RG8X (mini 8)	*	0.242	Poly Foam	0.78	1.12	1.94	2.5	4.3	7.5	12.8	23
LMR-240	*	0.24	Poly Foam	0.24	0.84	1.3	1.7	3.0	5.3	7.6	14.2
RG8/RG213	*	0.405	Polyethylene	0.659	0.66	1.14	1.5	2.6	4.5	10.4	19
Davis Bury-Flex	*	0.405	Poly Foam	0.82	0.52	0.9	1.1	1.9	3.3	4.9	8.9
WM106/CQ4XL	*	0.405	Poly Foam	0.82	0.5	0.85	1.1	1.9	3.3	4.7	8.6
Belden 9913F7	*	0.405	Poly Foam	0.85	0.6	0.9	1.1	1.9	3.3	4.7	9.8
9913		0.405	Poly/Air	0.89	0.4	0.86	0.9	1.56	2.7	4.2	7.7
LMR-400	*	0.405	Poly Foam	0.83	0.4	0.7	0.9	1.5	2.7	3.9	7.3
FSJ1-50A (¼")		0.3	Poly Foam	0.78	0.56	0.99	1.28	2.29	4.19	6.2	12.9
LMR-600		0.59	Poly Foam	0.87	0.3	0.4	0.8	0.99	1.72	2.4	4.5
LDF4-50A (½")		0.63	Poly Foam	0.88	0.21	0.37	0.78	0.85	1.51	2.3	4.38
LDF5-50 (7/8")		1.09	Poly Foam	0.89	0.11	0.20	0.26	0.46	0.83	1.23	2.53
LDF7-50 (1-5/8")		1.55	Poly Foam	0.89	0.08	0.15	0.19	0.34	0.62	0.91	1.86

Figure 6.16: Coaxial cable loss for different coaxial cable types and at different frequencies. [*Maple Leaf Communications*, 2018]

6.5.6 Interferometry and Beam Forming Using Antenna Arrays

Multiple coherent antennas can be used to generate a radiation pattern based on the phase and power of the signal sent to each antenna. The placement of the antennas in the arrangement, or array, is critical, as the placement can affect the radiation pattern resolution and occurrence of aliasing. The term coherent antenna means that each electrical path distance to each antenna is accounted for and/or equal. With advances in radio hardware and software, antenna arrays are becoming more and more common, allowing radiation beam patterns to be changed without mechanical moving parts [*Hysell*, 2018]. The ICEBEAR system utilizes a linear coherent antenna array at both the receiver and transmitter sites, which is described in Section 8.3.1.

An example of a radar array is the advanced modular incoherent scatter array (AMISR) [*Valentic et al.*, 2013]. The different beam look directions for the Poker Flat Incoherent Scatter Radar (PFISR) are shown in Figure 6.17. Each circle in the figure is a different beam direction that can be steered to electronically by phasing the large array of antennas. The overall beampattern for the ISR array is much more refined than the beam pattern for each individual element of the antenna array. Using electronic control allows for rapid changes to

the beam direction of the array, where the beams can be switched from one side of the FOV to the other side of the FOV quickly.

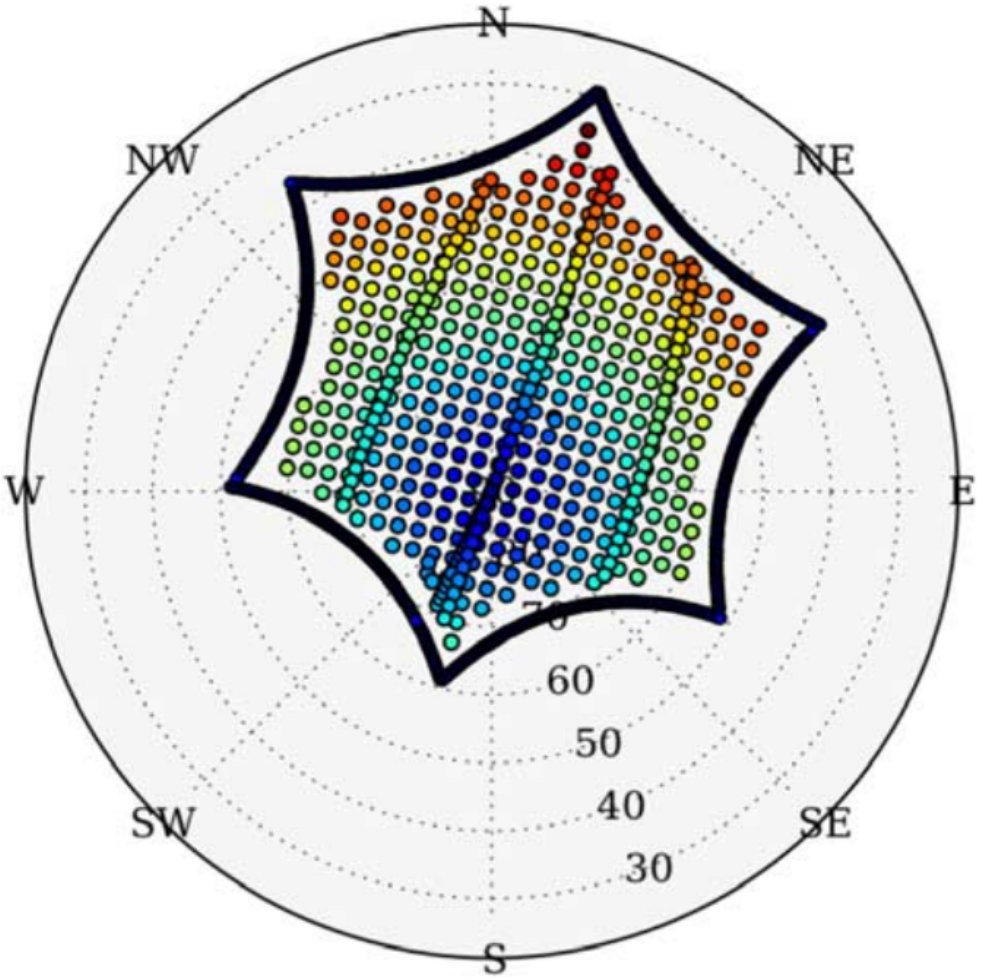

Figure 6.17: Different PFISR look directions that can be electronically steered to. [*Heinselman and Nicolls*, 2008]

To understand the basic theory of interferometry and beam forming, a linear array will first be considered. A plane EM wave approaching from a certain direction will have a phase difference at each antenna. An example is shown in Figure 6.18. If a phase gradient is applied across the antenna array, the array "look" direction can be shifted. When the antenna array is "pointed" in the same direction as the incoming EM wave, there will be a maximum in the power of the signal. A similar effect can be implemented when transmitting, where the phase of the signals across the array is a linear gradient, and the resulting radiation pattern will be directed due to this phase gradient. This is beamforming, and will be explored in

more detail shortly.

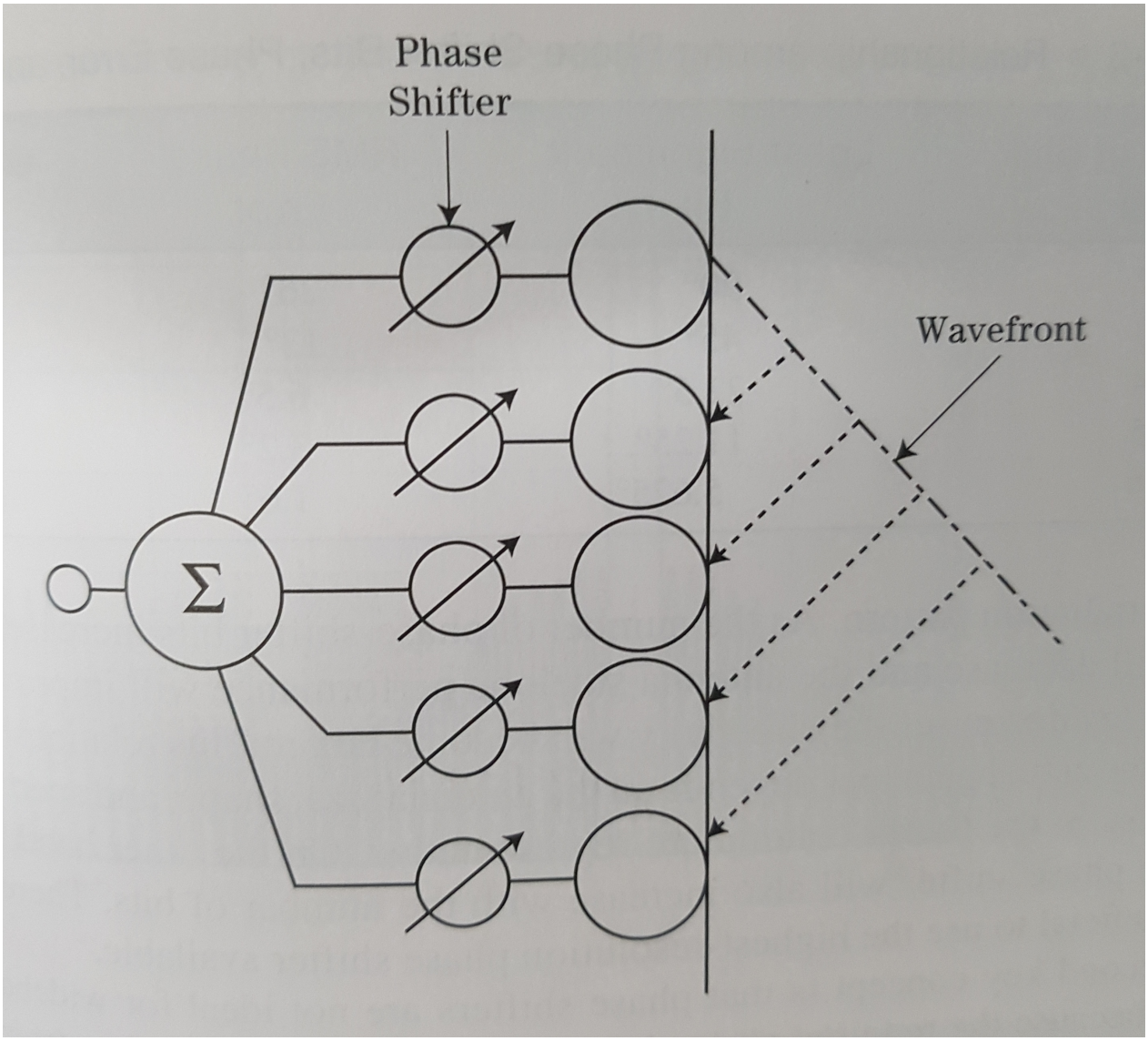

Figure 6.18: Example of plane wave on linear antenna array. [*Richards et al.*, 2010]

Interferometry

Another method to determine the origin of a signal is to use interferometry. Interferometry determines the phase difference of a signal at a given frequency between two or more antennas, and relates that phase difference to an angle of arrival. For interferometry, the antenna array is required to be coherent with individual receivers each measuring the complex voltage data arriving at each antenna. The equation relating the angle of arrival to the phase difference

is given by [*Richards et al.*, 2010],

$$\Delta\phi = \frac{2\pi d \sin\theta}{\lambda} \tag{6.5}$$

where $\Delta\phi$ is the phase difference between the antennas, d is the distance between the antennas, θ is the angle of arrival and λ is the wavelength of the incoming signal. The accuracy of these measurements will be dependent on the phase noise of the system. As d increases, the accuracy of the measurement also increases as the fluctuations in the phase generated by the system noise will result in a smaller fluctuation in the angle of arrival, but aliasing occurs at distances between antennas greater than half the wavelength of the signal. An example of aliasing can be observed in Figure 6.19. A signal coming from outside the expected FOV will alias into it, resulting in an incorrect angle of arrival measurement. Antenna radiation pattern sidelobes and possible strong signals from outside the FOV must be considered when determining the angle of arrival. It should be mentioned that it is possible to remove aliasing issues through the use of multiple antennas with unequal spacing, providing increased accuracy due to an increased inter-antenna distance without the drawback of aliasing [*Hysell*, 2018].

Beamforming

Another form of angle of arrival detection is using beam forming. Beam forming has the advantage of not assuming that the contents of each range-Doppler bin are from a single scattering volume. This allows the whole FOV to be mapped without potential multiple scattering volumes moving at the same velocity at the same range being combined into a single range-Doppler bin. Some forms of beam forming include incremental phase offsets of the antennas, the Capon method, and the Max entropy method, among many others. The equation for the weighting applied to each antenna in beamforming is given by [*Hysell*, 2018],

$$V(\theta, t) = w^{\dagger}(\theta, antenna)V(antenna, t) \tag{6.6}$$

where $w^{\dagger}(\theta, antenna)$ is the Hermitian matrix for the weighting applied to each antenna as a function of the angle of arrival and the antenna, and $V(antenna, t)$ is a matrix of the complex voltage samples as a function of the antenna and time. $V(\theta, t)$ is a matrix that contains the

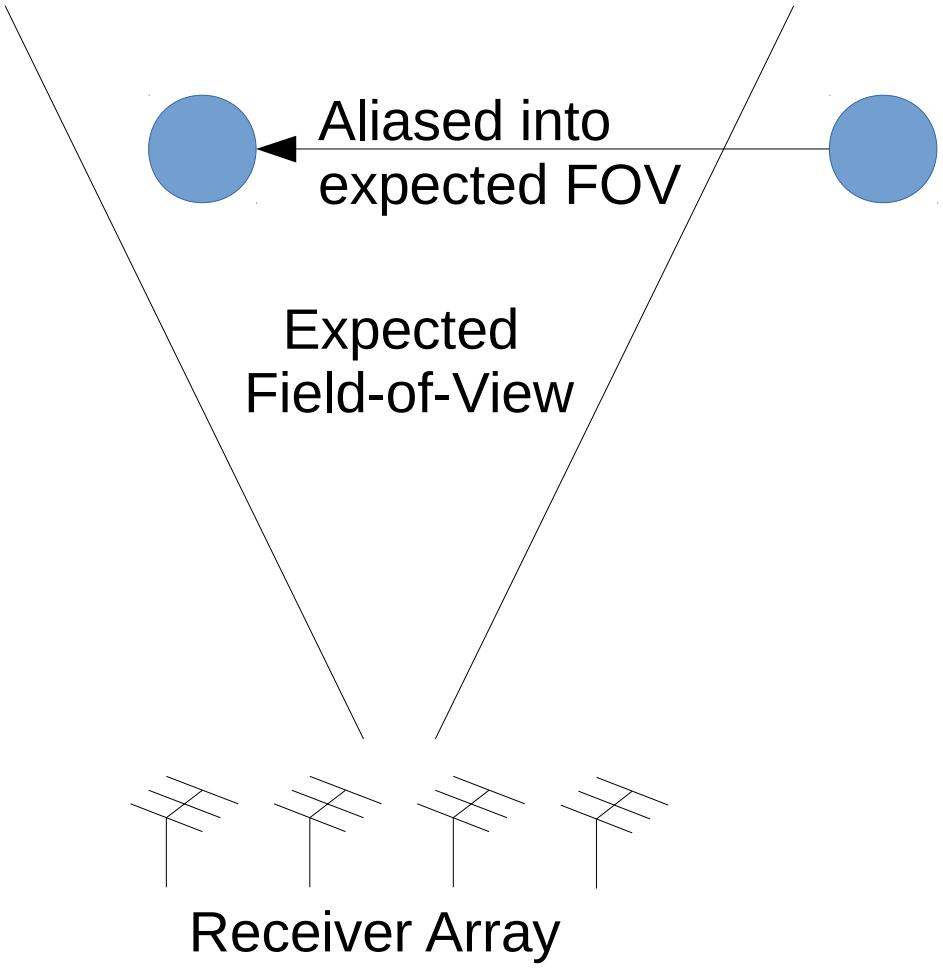

Figure 6.19: Example of radar object outside of FOV appearing inside FOV due to aliasing.

voltage samples as a function of look direction and time. The determination of $w^{\dagger}$ can be done many different ways, of which a couple are covered below.

The classical phase offset beam forming involves taking the voltage samples from each antenna and multiplying them by an associated phase offset [*Hysell*, 2018]. This effectively "steers" the beam in the direction specified. For a linear 1-D array, the equation for this process is given by,

$$V(\theta,t) = V(1,t)\exp\left(j\frac{2\pi d_1 \sin\theta}{\lambda}\right) + V(2,t)\exp\left(j\frac{2\pi d_2 \sin\theta}{\lambda}\right) + V(3,t)\exp\left(j\frac{2\pi d_3 \sin\theta}{\lambda}\right) + ... \tag{6.7}$$

where $V(1,t)$ are the voltage samples from antenna 1, $V(2,t)$ are the voltage samples from antenna 2, and so forth and the remaining terms have the same meanings as for Equation 6.5. This process can also be written as an antenna matrix, relating to Equation 6.6 as,

$$w^{\dagger}(antenna) = \left[1, \exp\left(j\frac{2\pi d_1 \sin\theta}{\lambda}\right), \exp\left(j\frac{2\pi d_2 \sin\theta}{\lambda}\right), ...\right] \tag{6.8}$$

By changing θ one can then steer the beam and create weightings for each beam direction. The different weighting matrices can be combined to generate a 2-D matrix in the form of $w^{\dagger}(\theta, antenna)$. When applied to the voltage samples of the antennas, this then provides a complex voltage array for each beam direction.

An alternative method of beamforming is the Capon method. This is described by the equation [*Stoica et al.*, 2003; *Hysell*, 2018],

$$w(antenna) = \frac{R^{-1}e}{e^{\dagger}R^{-1}e} \tag{6.9}$$

where R is the covariance matrix of the antenna data, and e is given by,

$$e^{\dagger}(antenna) = \left[1, \exp\left(j\frac{2\pi d_1 \sin\theta}{\lambda}\right), \exp\left(j\frac{2\pi d_2 \sin\theta}{\lambda}\right), ...\right] \tag{6.10}$$

The Capon method of beamforming requires the signal to be measured before the data is beamformed. This is due to the need to determine the covariance matrix of the data in the analysis. The computational requirements are larger than that of the classical beamformer, and some benefits include higher angular resolution and better interference rejection [*Stoica et al.*, 2003].

There are also more complex methods of beamforming, such as the max entropy and CLEAN methods, but the reader is referred to *Hysell* [2018] for more details.

The angle of arrival determination methods of interferometry and classical beamforming discussed here will be further investigated with regards to the ICEBEAR system in Chapter 9, where the initial results from the radar will be presented. Before any beamforming and/or interferometry analysis can be performed, the incoming signal must first be measured. The next section investigates how the voltage of the incoming wave is measured.

6.6 Signal Recording

There is often a front-end analog portion of a receiver system before the signal is digitized [*Hallas*, 2012]. This can consist of pre-amplifiers (Section 6.4), filters (Section 6.2.1), and RF mixers (Section 6.3.1). The different front end devices are used to filter out unwanted signals, amplify the incoming signal to be within the receiver voltage measurement range, and to convert the frequency to be within the receiver frequency measurement range. Once the analog front end has filtered the incoming signal, an analog to digital converter (ADC) measures the analog signal voltage and converts it to a digital value. The ICEBEAR system uses a receiver front end along with an ADC and digital filtering techniques to record the scattered radar signal. The different types of ADCs will not be discussed, as only the resulting characteristics of the ADC are important for ICEBEAR. An overview of the different transceivers considered for ICEBEAR is provided in Section 8.3.2.

Three of the primary characteristics of an ADC are the bit-resolution, the spurious free dynamic range (SFDR), and the sampling rate [*Bloom*, 2012a]. Typically high sampling rate ADCs have a low bit resolution, and vice versa. This is due to the design decisions that must be made to obtain the resulting output, grounded in the type of ADC used. With recent advances, ADCs have been able to have simultaneous high sampling rates and high bit-resolutions, though these are generally expensive. As well, with higher bit-resolution and sampling speeds, the data storage, data handling, and data throughput requirements increase. The data transfer rate is,

$$bps = B_r \times SPS \tag{6.11}$$

where bps is the transfer rate in bits per second, B_r is the bit-resolution and SPS is the samples per second. For ease of data handling, many times the data type is increased to the next 8-bit value (8-bit,16-bit,24-bit, etc.), resulting in a higher data transfer rate required. The benefit of having higher sampling rates was discussed in Section 6.3.2, where a large sampling rate provides a large range of frequencies to be digitized without the use of analog radio mixing front end electronics, and allows large bandwidth signals to be digitized.

Another important characteristic of an ADC is the spurious free dynamic range [*Bloom*,

2012a]. This refers to the difference between a signal at the full scale of the ADC and the highest spurious signal. Spurious signal refers to a signal that is the largest noise or harmonic distortion component.

The bit-resolution determines the dynamic range of the signals that can be recorded [*Bloom*, 2012a]. For example, consider an ADC that has 14-bit resolution with a maximum voltage of ± 1 V on the input. The maximum SNR for this ADC can be calculated from the equation [*Bloom*, 2012a],

$$\text{SNR} = (1.76 + 6.02B_r)\ \text{dB} \tag{6.12}$$

For a 14-bit ADC, the result is a SNR of ≈ 86 dB. This is the idealized maximum dynamic range of the ADC. In practice, this value will be lower. The 14-bit resolution with a ± 1 V measurement range corresponds to a voltage resolution of 0.122 mV. Other characteristics of ADCs include the noise level, harmonic and intermodulation distortion, full power bandwidth, and aperture delay jitter [*Bloom*, 2012a].

Measuring the voltage using a single ADC produces the real part of the voltage (Section 5.4). This only provides the positive frequency spectrum. If one wants to measure both the positive and negative frequencies surrounding a mixed to center frequency, the real and imaginary components of the voltage samples must be measured. This can be accomplished by splitting the signal and mixing the forks with a sine and cosine wave [*Bloom*, 2012a]. A block diagram depicting this is shown in Figure 6.20. Another method of directly obtaining the IQ samples is by measuring voltage samples using two ADCs with a timing offset of 90° with respect to the sampling frequency between them. Regardless of the measurement method, once the complex voltage samples are measured it is possible for frequencies up to the sampling rate to be determined without Nyquist aliasing.

Once the voltage measurements are made, the center frequency is typically shifted to baseband. This is accomplished using a digital down converter (DDC), which is essentially a digital mixer. A block diagram of a DDC device is shown in Figure 6.21. The shifting to baseband reduces the data rates and data footprint required to transfer and store the data [*Hollis and Weir*, 2003]. The DDC digitally mixes the samples with the center frequency, and then low pass filters the data for the given data rate requested. The data is then decimated to decrease the sampling rate and only observe the radio bandwidth required.

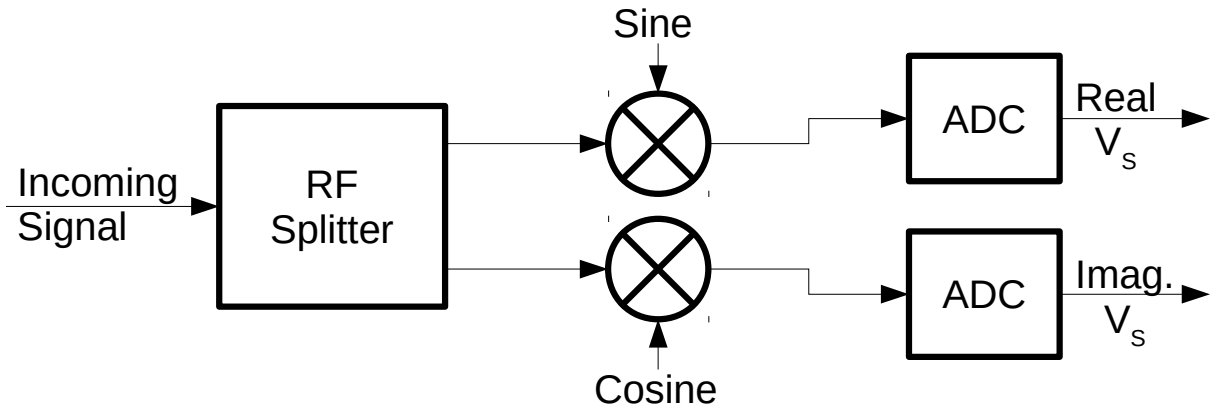

Figure 6.20: Method of obtaining the real and imaginary voltage samples from a signal.

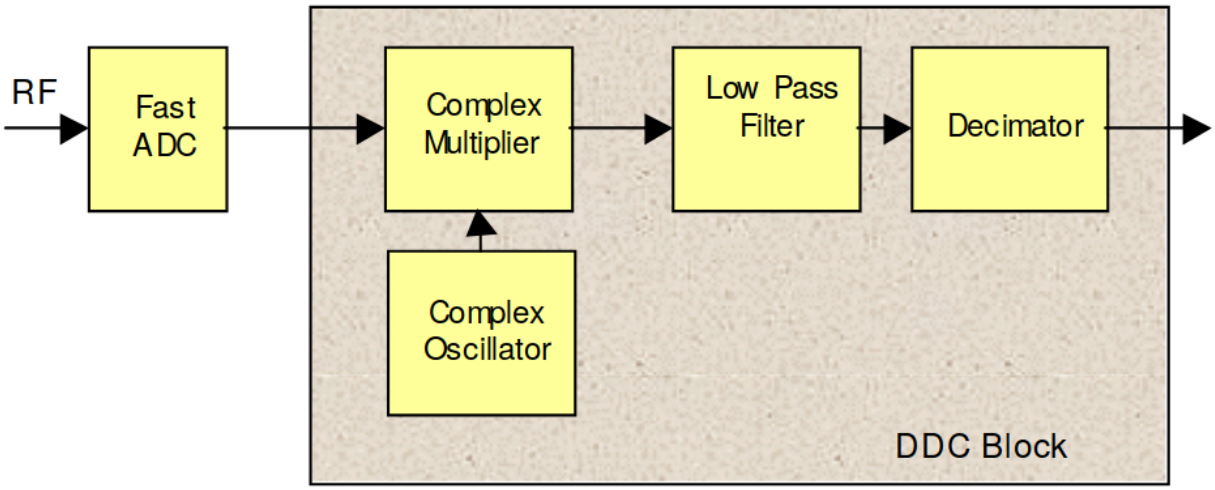

Figure 6.21: Block diagram of a digital down converter. [*Hollis and Weir*, 2003]

Decimation is the act of reducing the sampling rate of an already sampled signal [*Actel*, 2007]. This can be accomplished by different methods, such as by summing samples or removing samples. When samples are summed it effectively increases the bit-resolution of the ADC. Through this method of summing samples, high sampling rate ADCs with low bit-resolutions can increase their bit resolution at the expense of a lower effective sampling rate. Of course, there is a power of 2 diminishing return on this conversion, where for each extra bit of resolution the sampling rate is halved. The other method of decimation through removal of samples effectively destroys data, but is less computationally intensive and still lowers the sampling rate.

To perform the digital mixing and decimation operations, many electronics systems make use of field programmable gate arrays (FPGAs) [*Altera*, 2007; *Collins*, 2017]. These devices consist of a series of logic gates and computational blocks that can process data in close to real time. The conditioning of the data is performed in hardware, rather than software, allowing processes that would be computationally intensive in software to be performed at fast speeds in hardware. The FPGA also allows parallelization of processes, further increasing the speeds at which data can be processed. DDCs, decimators, and FFTs are some of the data processing tools that can be implemented on FPGAs.

Once the data is digitally mixed and down sampled, it is transferred to a storage device or a computer for processing. The data rate required for transfer can be significant, and a survey of the possible communication protocols is provided in Figure 6.22. From this figure it can be observed that there are multiple options for high data rate communications. Many of these are commonplace in computer communications. A more specialized protocol is Infiniband, which is a network protocol that can be further read about in *Mellanox Technologies* [2008].

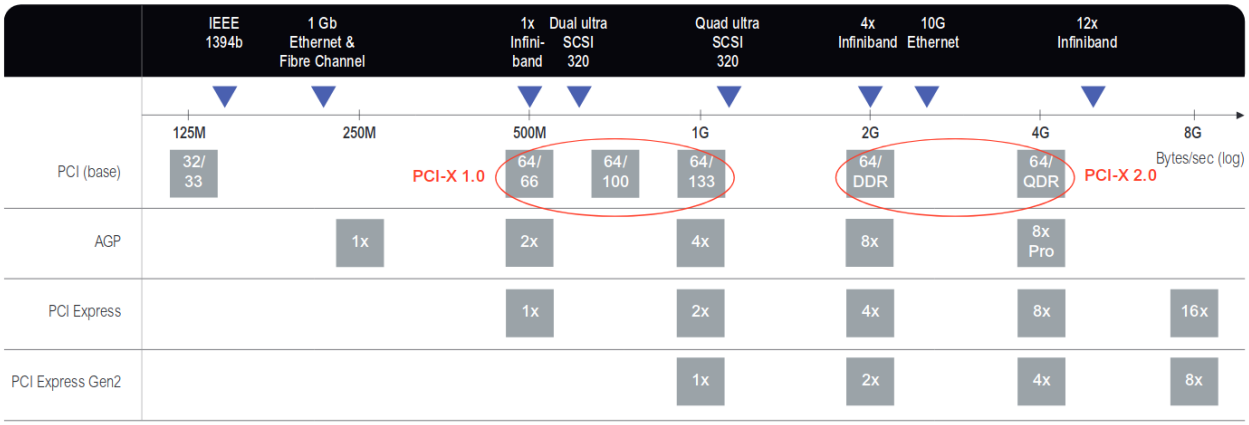

Figure 6.22: Diagram of different communication protocols and their associated speeds. Some of the acronyms in this figure include, accelerated graphics port (AGP), peripheral component interconnect (PCI), quad data rate (QDR), and small computer system interface (SCSI). [*Dobson*, 2008]

The different data transfer protocols were analyzed for use by the ICEBEAR transmitter and receiver systems. Ultimately, it was decided to use the 10 gigabit per second (Gbps) ethernet connection for ICEBEAR communications with the transceivers. This was due to the commonality of ethernet devices, the sufficient speed of the connection, and the ease of

connections to multiple transceiver units through a 10 Gbps ethernet switch. Another reason the 10 Gbps ethernet was chosen is that more advanced and/or niche systems typically have issues that are being resolved, which results in an extended development time and possible unforseeable issues. A description of the communications connections for the ICEBEAR system is provided in Sections 8.4.4 and 8.5.1.

Once the incoming signal is filtered, digitized, and stored, it can then be processed as required. An important component that is relevant to many of the electronic systems discussed is the clock. The next section will investigate the importance of maintaining coherence between devices and the sources of errors with using a distributed clock system.

6.7 Clocks, Oscillators and Measurement Coherence

Clocks are an essential part of a measurement system [*Keysight Technologies*, 2018]. The clock maintains synchronization between devices and provides a relative time. In the ICEBEAR system, clocks are used in many of the electronics. The ICEBEAR computers use a network time protocol (NTP) disciplined clock as the system clock, which determines when programs are run. A global positioning system (GPS) disciplined clock is used to synchronize the transceivers (Section 8.3.2) at the receiver and transmitter sites. Each of the amplifiers has a mini-computer with a clock that determines when amplifier monitoring diagnostics are recorded. The transceiver clock determines when voltage sample conversions occur, both analog to digital and digital to analog. A drifting clock will create offsets in measurements, and can introduce frequency and phase drifting in the voltage samples that is not due to the measurement medium of the radar system.

For bistatic systems, such as ICEBEAR, an accurate clock is essential. With multiple sites, a method must be used to synchronize both sites. Using NTP servers on the internet is accurate to tens of milliseconds [*Cisco Systems*, 2007], but for systems operating in the microsecond range, this is insufficient. GPS clocks can be used, which synchronize sites to within 50 ns, as long as there is a GPS lock [*Lewandowski et al.*, 1999]. ICEBEAR requires clock synchronization of at least ≈ 1 μs with the modulation implemented to obtain accurate range information, and therefore GPS synchronization is sufficient. If the GPS synchroniza-

tion lock is lost, the systems must rely on a stable clock for accurate results until the GPS signal is re-acquired. Depending on the clock drift, within minutes the synchronization between sites can be lost. This is why having proper timing and clocks in a radar system is essential. An overview of the clock synchronization system used by ICEBEAR is provided in Section 8.3.3.

There are a couple key characteristics that define a "good" clock. These include the amount of noise generated by the clock, and the drift of the clock synchronization over time. When referring to clock noise, it is considered clock "jitter" when the measurement is in the time domain, and phase noise when the measurement is in the frequency domain [*Integrated Device Technology*, 2008]. Small changes in the timing of a periodic waveform will serve to spread that waveform in frequency. An example of the phase noise is shown in Figure 6.23, where the power of the spectrum is spread from the desired clock frequency.

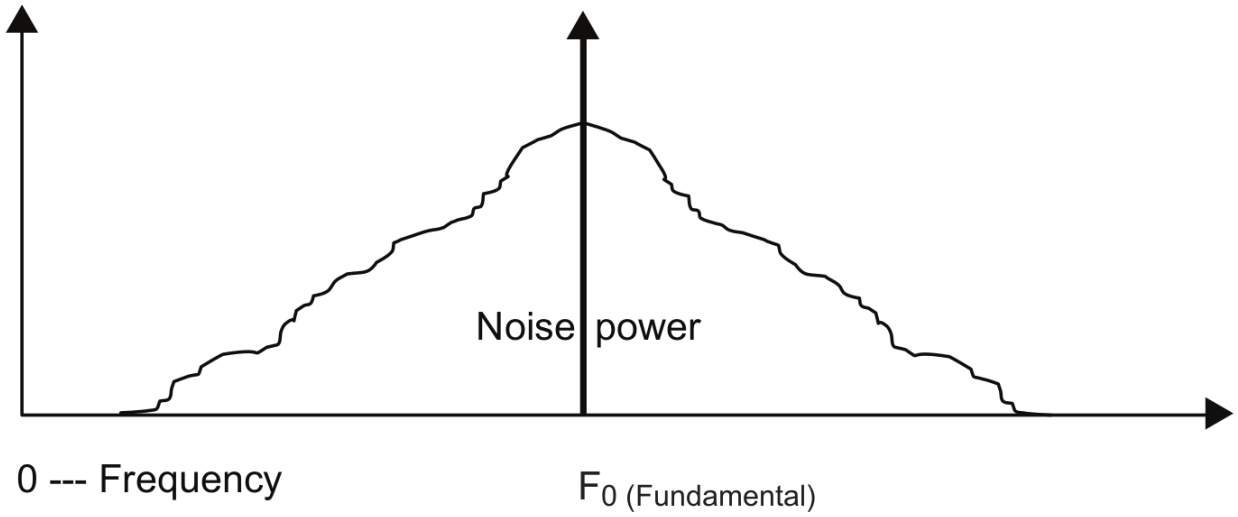

Figure 6.23: Example of clock noise in the frequency domain. [*Integrated Device Technology*, 2008]

The clock jitter can be related to the phase noise by the following equation [*Integrated Device Technology*, 2008],

$$j_{rms} = \sqrt{T_{area}} \tag{6.13}$$

where j_{rms} is the root mean squared (RMS) clock jitter and T_{area} is the area under the phase noise measurement on one side of the plot. The RMS jitter value refers to the change in the

RMS amplitude of the periodic waveform from cycle to cycle. The goal is to minimize this clock noise, and different types of clocks have been developed to do this.

There are many different types of clocks used for timing purposes in electronics. Depending on the purpose of the clock, cost is a significant driving factor when determining the clock accuracy required. Some clock types include the basic quartz crystal clock, the oven controlled oscillator, and the atomic clock. Figure 6.24 shows how some different types of clocks drift in frequency stability over time. From the figure it is evident that the hydrogen maser (HM) clock source is the most stable, followed by the cesium atomic clock, the rubidium atomic clock, and the quartz crystal clock.

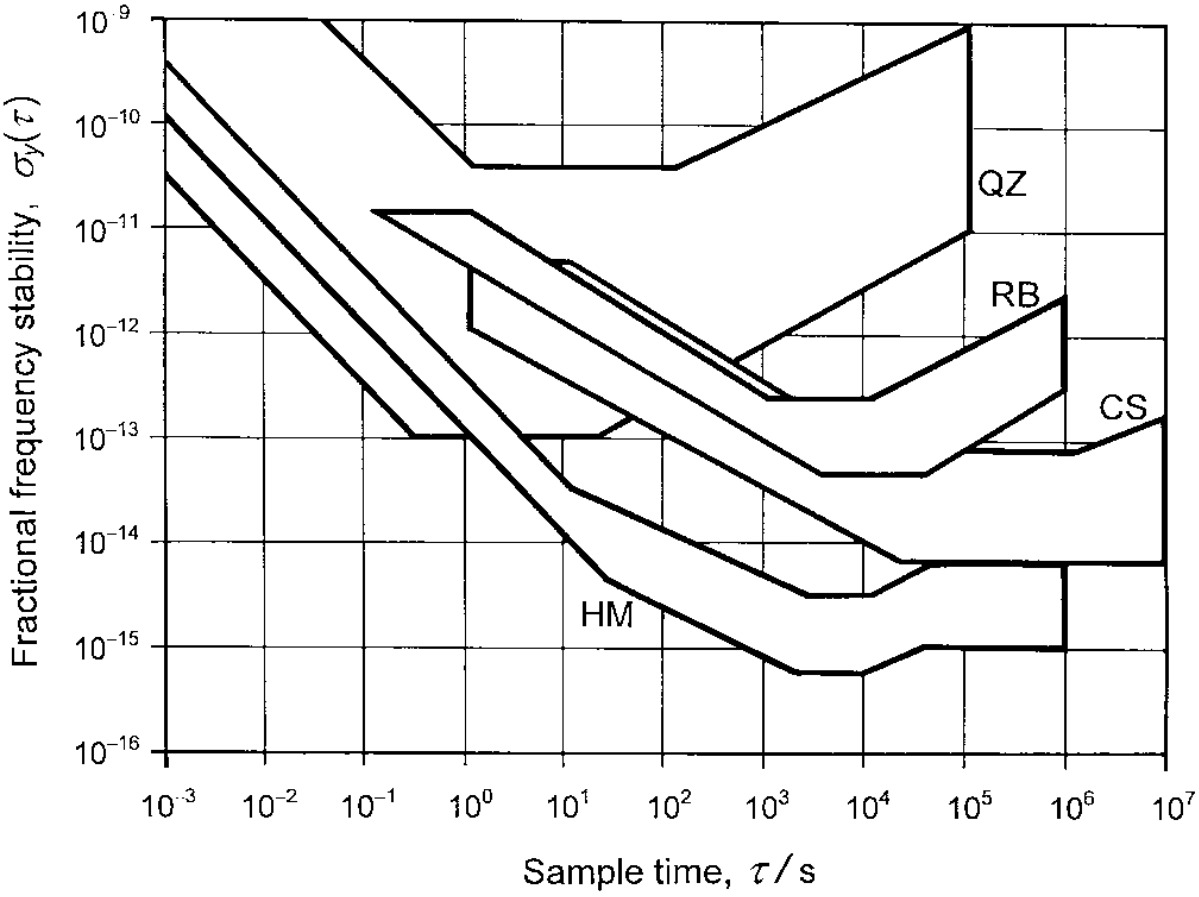

Figure 6.24: Different clock sources and how they differ in frequency stability. The different clock sources are quartz (QZ), rubidium (RB), cesium (CS), and hydrogen maser (HM). [*Lewandowski et al.*, 1999]

The frequency stability referenced on the y-axis of Figure 6.24 refers to the Allan variance of the clock source [*Allan*, 1987]. As a point of comparison, if a clock drifts 1 ns over 24 hours,

it corresponds to $1{\times}10^{-14}$ in frequency stability [*Lewandowski et al.*, 1999]. GPS conditioned clocks can be within an order of magnitude of this frequency stability with a GPS lock.

Once a clock source is selected and commissioned, it is required to be distributed to the different units that require accurate timing. This can be accomplished through a clock distribution unit and electrical length matched cables. The systems that are connected to this clock distribution unit are then synchronized.

The external clock source used for synchronization is commonly generated at a certain frequency, such as 10 MHz. The clock used by electronics systems is often larger than this value, so an increase to the clock rate is required. To do this a phase locked loop (PLL) can be used [*Stockton et al.*, 2012]. PLLs are used in the ICEBEAR transceiver to convert a 10 MHz incoming clock signal to a 200 MHz signal used by the device.

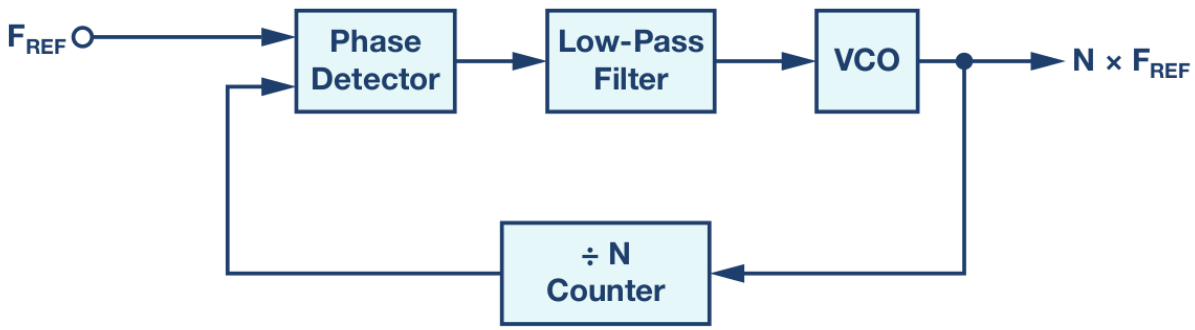

Figure 6.25: Block diagram of the components in a phase locked loop circuit. [*Collins*, 2018]

A block diagram of the operation of a PLL is shown in Figure 6.25. The phase detector outputs a voltage relative to the phase difference between the two input signals [*Stockton et al.*, 2012]. The low pass filter converts the signal input to it to a DC voltage. The DC voltage level controls the frequency of the signal generated by the voltage controlled oscillator (VCO). The output from the oscillator is used as a feedback through a frequency divider to the phase detector. If designed correctly, the output will incrementally approach the frequency desired at the output. The PLL is considered to be locked when the output from the frequency divider and the input signal match. As an example, to output a 40 MHz signal with a 10 MHZ input signal, the frequency divider would be set to $N = 4$.

6.8 Radar Hardware Overview

In this chapter the hardware of a digital radar system has been described, where a further in depth discussion on the ICEBEAR hardware is provided in Chapter 8. A discussion on the matching of different system impedances was included, followed by a brief overview of the design and implementation of signal filters. The generation of the radar signal, including an overview of mixing a baseband modulation with a carrier frequency, was reviewed, and a block diagram of a typical digital signal generation device was displayed. The signal generation and recording for ICEBEAR is performed by a radio transceiver, the selection of which is discussed in Section 8.3.2.

The amplification of a generated signal by power amplifiers was also discussed, where the ICEBEAR amplifiers are discussed later in Section 8.4.1. This was followed by an overview of antennas and feedlines. A description of the ICEBEAR antenna arrays is given in Section 8.3.1. The final two sections of Chapter 6 covered the recording of a radio signal, and the role of clocks in an RF measurement system. An overview of how the ICEBEAR system is synchronized is provided in Section 8.3.3. With a basic overview of these RF hardware topics covered, a review of previous E-region coherent scatter radars will now be presented.

Chapter 7

Previous Coherent Scatter Radars

Portions of this section, as well as Sections 7.6, 7.9, 7.10, and 7.11 were originally published in Huyghebaert, D., G. Hussey, J. Vierinen, K. McWilliams, and J.-P. St-Maurice (2019), ICEBEAR: An all-digital bistatic coded continuous-wave radar for studies of the E region of the ionosphere, *Radio Science*, *54*(4), 349–364, doi: 10.1029/2018RS006747.

The evolution in our understanding of the spectral types and what they imply for the E-region has advanced concurrently with the evolution and deployment of various coherent scatter radar techniques. For instance, CW observations performed by *Prikryl et al.* [1988, 1990] guided *St.-Maurice and Hamza* [2001] towards a description of the observed structures in terms of individual elongated structures that could be shown to slow down as they grew in amplitude. In general, CW measurements are rare for ionospheric radars but are extremely useful in that they can be used to continuously measure the evolution of ionospheric density structures, though this was typically at the expense of range resolution. To determine the range information of the radar scatter, traditionally pulsed radars were used.

The University of Saskatchewan has a long and extensive history using both CW and pulsed coherent scatter radars to research the ionosphere. Some of the radars operated by the researchers at the University of Saskatchewan include the Super Dual Auroral Radar Network (SuperDARN) [*Greenwald et al.*, 1995], the Saskatchewan Auroral Polarimetric Phased Ionospheric Radar Experiment (SAPPHIRE) [*Koehler et al.*, 1995], and a frequency modulated continuous-wave (FMCW) radar [*Cooper*, 2006]. This section provides a brief overview of many different coherent scatter radars that have been used in the past to probe the E-region

---

Portions of this section, as well as Sections 7.6, 7.9, 7.10, and 7.11 were originally published in *Huyghebaert et al.* [2019].

of the ionosphere, including those operated at the University of Saskatchewan. The different types of E-region scatter were previously discussed in Section 3.4.1. Here, the overview includes how ICEBEAR improves upon the techniques used in previous radars to make high spatiotemporal resolution measurements of E-region plasma density irregularities.

7.1 Cornell University Portable Radar Interferometer (CUPRI)

The Cornell University Portable Radar Interferometer (CUPRI) [*Riggin et al.*, 1986] radar operated at 50 MHz and was optimized to study ionospheric plasma density irregularities. It consisted of two 26-element colinear dipole array antennas, where one was used for transmitting and both were used for receiving. The peak transmitted power could reach 20 kW with a pulse duration of 50 μs. The radar was unique in that it was portable, and could be deployed out of a vehicle. The FOV was directed over the Arecibo Observatory allowing for multi-instrument studies (ISR and VHF coherent scatter) of the E-region during an experiment described in *Riggin et al.* [1986]. The study showed that, for midlatitudes, coherent spectra were measured when sporadic E-layers (confined altitude regions of enhanced plasma density) were present at altitudes around 105 km. The plasma density irregularities measured were aligned along the geomagnetic field ($< 0.5^\circ$ aspect angle). The ICEBEAR radar uses a phase modulated CW signal to obtain a range resolution comparable to a 10 μs pulse duration, which is a 5 times improvement upon the range resolution obtained with CUPRI. The ICEBEAR system has a similar average power to the CUPRI system, with a much larger FOV in the auroral zone of the Earth, as well unaliased measurements in range and Doppler.

7.2 Sporadic E Scatter Experiment (SESCAT)

The Sporadic E Scatter Experiment (SESCAT) [*Haldoupis and Schlegel*, 1993] was installed at midlatitudes to study ionospheric E-region irregularities. The radar used a frequency of 50.52 MHz, and scattered from irregularities of $\approx$ 3 m. The system was configured as a bistatic CW radar system, which resulted in high temporal resolution, but effectively no

range information, and a limited FOV characteristic of unmodulated CW waveform schemes. Four antennas transmitted the radio signal, each with a peak power of 250 W. The received signal was mixed down to 1 kHz through analog mixing and recorded on an analog tape deck. The radio signal was then digitized and saved on a computer. Some interesting midlatitude E-region measurements were made using this system, including the classical Type II E-region echoes, and high temporal resolution meteor echo measurements. ICEBEAR improves upon the SESCAT radar design through using a modulated CW signal to obtain range resolution, and a digitally phased array to obtain angle of arrival information over a large FOV. With advances in computing and digital storage, ICEBEAR is also able to record the entire signal much more easily than was done with SESCAT.

7.3 Super Dual Auroral Radar Network (SuperDARN)

The Super Dual Auroral Radar Network (SuperDARN) [*Greenwald et al.*, 1995] is a group of institutions and their corresponding radars. Each radar follows guidelines as to the measurements it takes and the setup of the system, resulting in continuity in measurement characteristics between the different institutions. These radars operate at frequencies between 8 and 20 MHz and the antenna array consists of 16 log-periodic Yagi antennas. Each transmitter is capable of supplying 500–800 W of peak power to each antenna, with a duty cycle of 6%. With this duty cycle the radar is limited to pulsed-mode operation. The transmitter and receiver are located at the same site (monostatic) and use the same antennas. There is therefore a transmit/receive switch in the system to prevent the transmitter signal being fed directly into the receiver, which would result in the destruction of the receiver. For a full scan of the FOV it takes 1–2 minutes, depending on the radar mode. The SuperDARN radars do make measurements of E-region plasma density irregularities, but their main research focus is the F-region ionosphere which can be well probed using the HF frequency band and its associated radio wave propagation characteristics in the F-region. Through the advanced radio techniques used by the ICEBEAR system, ICEBEAR will have an order of magnitude improved temporal and spatial resolution compared to the SuperDARN radars, however with more of a focus on the E-region ionosphere. Due to a significant FOV over-

lap between the Saskatoon SuperDARN radar and ICEBEAR, there is a great potential for collaborative multi-frequency coherent scatter studies using both systems.

7.4 Saskatchewan Auroral Polarimetric Phased Ionospheric Radar Experiment (SAPPHIRE)

The Saskatchewan Auroral Polarimetric Phased Ionospheric Radar Experiment (SAPPHIRE) [*Koehler et al.*, 1995] radar system operated at 50 MHz as a bistatic CW radar, and used digital phasing techniques to obtain spatial resolution. The purpose of this radar was to measure E-region plasma irregularities with high time resolution and rough "range" resolution information over a moderate FOV. Two transmitter sites were used, with a single receiver commissioned to record the ionospheric scatter. Each site utilized a 12 antenna array of 6-element Yagi antennas. Each radar beam consisted of a different frequency, and the "range" information was available from the overlap of the transmitter (TX) and receiver (RX) antenna beam patterns, as shown in Figure 7.1.

A direct digital synthesis (DDS) system was implemented to set the frequency and phase on each of the antennas, allowing multiple frequencies and phases to be transmitted on each antenna. The radar used this system to generate four separate beam directions, each with its own frequency, allowing for 32 different measurement locations for each SAPPHIRE site (two receivers and two transmitters). Each beam had 300 W of power, equalling 25 W per antenna per frequency (12 antennas, 4 frequencies/beams), before effective radiated power (ERP) was considered.

This radar was built in the 1990s before large amounts of data could be stored relatively easily. This constraint caused the system to be designed only to record data for large SNRs. Analysis was performed in real time as measurements were received, resulting in only pre-specified events to be recorded. The new 50 MHz ICEBEAR radar will have higher spatial resolution than SAPPHIRE, resulting in a much larger digital data footprint, as all the raw data received is recorded. This is possible due to advances in digital storage media resulting in lower costs and higher storage capabilities. The ICEBEAR system uses the same receiver antenna array used for the SAPPHIRE system, but with a newly commissioned transmitter

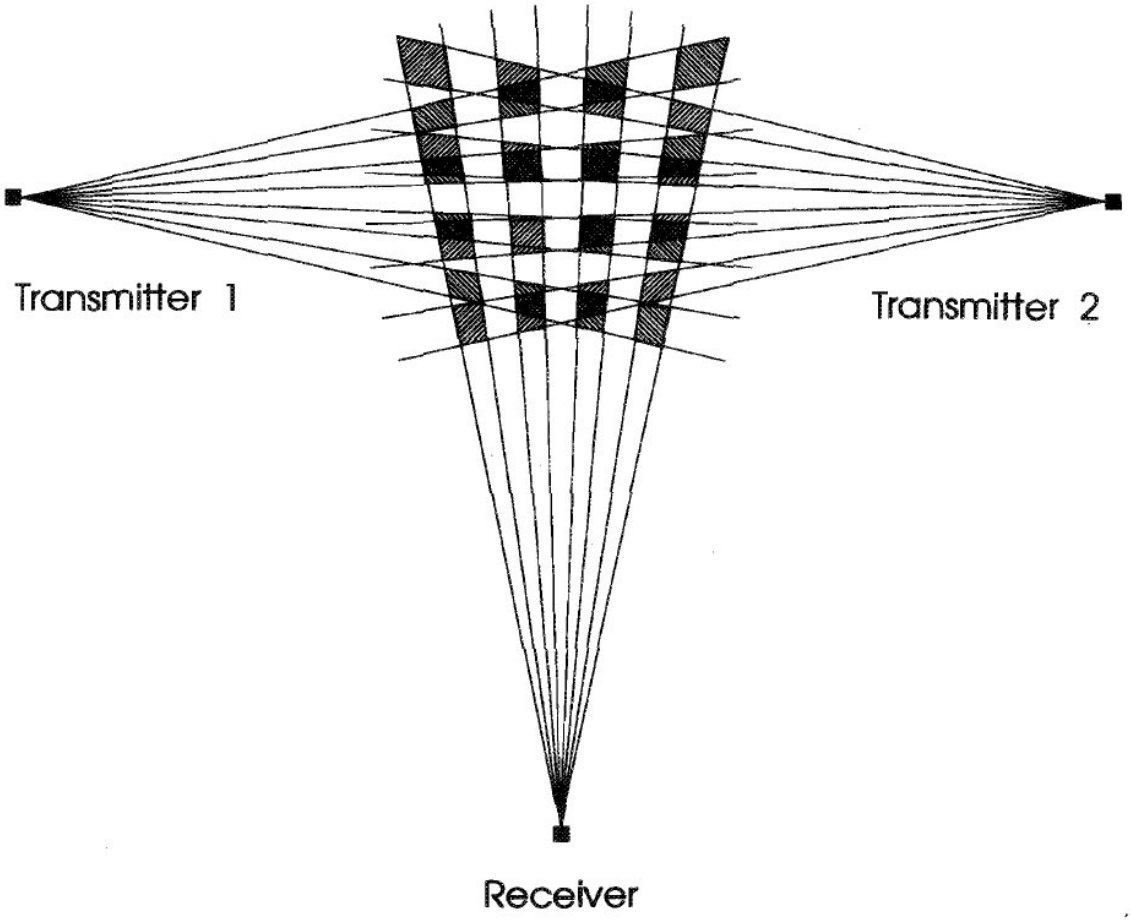

Figure 7.1: The intersecting RX and TX antenna beam patterns produced by the SAPPHIRE radar system to provide spatial, or "range", information. [From *Koehler et al.*, 1995]

site location.

7.5 São Luís 30 MHz Coherent Scatter Radar

The São Luís 30 MHz coherent scatter radar [*de Paula and Hysell*, 2004] had 2 arrays consisting of 16 5-element Yagi antennas that were directed vertically to measure equatorial ionospheric irregularities. These antennas were used for both transmission and reception, and were able to transmit a total peak power of 8 kW. Interferometry was implemented using the antenna arrays to determine location and characteristics of the ionospheric scatter. The radar operated with a duty cycle under 5%, resulting in only pulsed coded sequences being transmitted, though modulation was implemented within the pulses to improve the

range resolution. This radar was able to measure both ionospheric irregularities at E-region altitudes associated with the equatorial electrojet and at F-region altitudes due to the unique geometry at the magnetic equator. ICEBEAR also uses interferometry with an array of Yagi antennas, with a similar average power to the São Luís radar. The primary differences between the radars are: 1) ICEBEAR uses a CW phase modulated signal, improving the Doppler and range resolution of the spectra measured, 2) ICEBEAR uses a frequency of 50 MHz, reducing the effects of refraction due to the ionosphere, and 3) ICEBEAR measures the E-region in the auroral zone of the Earth, where interesting E-region coherent scatter spectra are still under investigation (Section 3.4.1).

7.6 Passive Radars

It has been shown that a passive CW technique can be applied to ionospheric measurements using FM radio stations as the transmitter sources [*Sahr and Lind*, 1997; *Lind et al.*, 1999, 2013]. Using an external radio signal source as the transmitter is known as "passive radar", and has the benefit of only requiring a receiver to make ionospheric measurements. Depending on the radio signal source, it is possible for this technique to have high spatial and temporal resolutions. Passive radars are typically bistatic as they operate using an external, uncontrolled transmission source. The spatial resolution of passive radars is dependent on the bandwidth (BW) used by the external radio source and is therefore not controllable by the radar user. This may result in differing spatial resolutions over time, thus making consistent measurements difficult. Another issue with passive radar for ionospheric studies is that there are very few sources of external RF signal with sufficient power for ionospheric scattering at frequencies of $\approx$ 50 MHz. This frequency is ideal as the signal undergoes minimal refraction from the ionosphere, but the wavelength is still sufficiently large to observe unique plasma phenomena. With a user controlled radio transmission source (no longer a passive radar), it is possible to make consistent measurements and control the frequency of the transmitted signal. This is the approach that was used for ICEBEAR to obtain consistent, high spatiotemporal resolution images of E-region plasma density irregularities.

7.7 Millstone Hill UHF Radar

There have also been E-region coherent scatter experiments performed at ultra high frequency (UHF) using the sidelobes of an incoherent scatter radar system operating at 440 MHz located at Millstone Hill, MA, USA [*Foster and Erickson*, 2000]. This experiment was able to map the electric field of the F-region of the ionosphere, measured using incoherent scatter techniques, along the magnetic field lines to a magnetically connected region in the E-region of the ionosphere where coherent scatter measurements were obtained from a radiation pattern side lobe of the radar at the same time. From the experiment it was shown that there is a linear relationship between the electric field and the power and the phase velocity of the coherent backscatter. This radar operated at a much higher frequency than the ICEBEAR system, so the plasma density irregularity dynamics may be different at these wavelengths. As well, this radar is located at midlatitudes, where charged particle precipitation and active ionospheric conditions are much less frequent. ICEBEAR is able to continuously measure a much larger field of view in the auroral zone of the Earth, and is able to frequently observe these active ionospheric conditions.

7.8 University of Saskatchewan FMCW radar

At the University of Saskatchewan a frequency modulated continuous-wave (FMCW) radar was developed by *Cooper* [2006] to measure E-region plasma density irregularities. This radar used parts of the SAPPHIRE system, including portions of the SAPPHIRE receiving antenna array as the transmitter and receiver antennas. To obtain range resolution of the CW signal, a frequency modulation scheme was used involving a triangular frequency modulation, where the frequency of the radar signal was increased and then decreased over time, also known as a frequency upsweep and downsweep. The shape of a frequency versus time plot then appears as a repeating triangle. By using this method, the range and Doppler of the analyzed received signal are coupled, similar to the concept of linear frequency modulation discussed in Section 5.5.3.

The FMCW radar was able to measure all four types of E-region coherent scatter, as well

as meteor echoes. The ICEBEAR radar builds upon the concept of modulated CW signals used in the FMCW radar; however, ICEBEAR uses a phase modulated signal rather than a frequency modulated signal. By using a phase modulated signal, the Doppler and range resolution become de-coupled, providing less ambiguity in the analysis of the received signal. The ICEBEAR radar does have the capability to generate similar waveforms to those used by the FMCW radar due to the advanced transceiver hardware utilized in the system, but this was not explored for this dissertation.

7.9 Homer Alaska 30 MHz Radar

An experimental setup by *Hysell et al.* [2012] used a coherent E-region imaging radar array to probe the auroral ionosphere. It was proposed that a combination of the spectral width and the radar line of sight Doppler information in Type I and Type II waves could be used to produce a map of the electric field responsible for the growth of the unstable structures. This may be a future avenue for ICEBEAR to explore. The coherent scatter measurements were supplemented with incoherent scatter and auroral imager measurements, providing simultaneous multi-instrument readings of the E-region ionosphere. The pulsed, coherent scatter radar system operated at 30 MHz, obtained a range resolution of 2.25 km and a temporal resolution of 5 s, and the Doppler aliased at $\pm$ 625 m/s. The ICEBEAR system removes the potential Doppler aliasing of the measured signal through the use of a coded, phase modulated, CW modulation scheme, and operates at 50 MHz, reducing the effects of ionospheric refraction on the radar signal.

7.10 Kühlungsborn Meteor Radar

A coherent scatter radar in Kühlungsborn, Germany, measured ionospheric E-region echoes during the St-Patrick storm of 17 March, 2015, from an experiment initially designed for meteor echoes [*Chau and St.-Maurice*, 2016]. This multi-link pulsed radar system obtained measurements at 36.2 and 32.55 MHz, with a temporal resolution of 10 s and a range resolution of 1.5 km. The angle of arrival in elevation and azimuth was able to be deduced through

the use of a 2-D interferometer, where the range aliased every 240 km due to the inter-pulse period used. It was from this set-up that the notion that Type III and Type IV echoes came from the lowest and highest altitudes of the unstable layer was developed, as was discussed in Section 3.4. Due to the location of the Kühlungsborn Meteor Radar, it is only very rarely, under extremely active ionospheric conditions, that E-region coherent scatter echoes are observed. With the optimized location of ICEBEAR for observing E-region echoes in the auroral zone, further investigation into the results obtained from this experiment are planned. As well, ICEBEAR removes the range aliasing that was experienced by this meteor radar system by using a coded CW phase modulated signal. The removal of aliasing will accurately reveal the spatial extent of E-region coherent scatter echoes in the auroral zone.

7.11 CW Phase Modulated Experiments

Vierinen et al. [2016] have shown that it is possible to obtain high resolution measurements of ionized meteor trails using a coded CW phase modulated radio signal with a 30 W transmitter. The phase modulation consisted of transmitting a binary phase code with a set baud (symbol) length. The radar obtained a range resolution of 1.5 km and operated at a frequency of 32.55 MHz. This low-powered, phase modulated CW radar was shown to provide similar results to pulsed meteor radars operating at much higher peak powers.

There have also been low latitude experiments using low power ($\approx$ 0.5 W), HF, phase modulated, CW radars to measure the F-region of the ionosphere that have shown promising results while using this modulation technique [*Hysell et al.*, 2016]. These HF radar systems operated at frequencies of 2.72 and 3.64 MHz, so that the bottom side of the ionosphere could be measured and characterized based on the range of the reflections. The HF radars were located near the Jicamarca ISR, in Peru, providing the opportunity for multi-instrument studies using this experimental setup.

The meteor and HF radars discussed here rely on strong signal reflections from large gradients in the plasma density of the ionosphere, and show the viability of using a phase modulated CW signal. The phase modulated CW signal technique used with these radars is similar to the modulation scheme used with ICEBEAR, with the important difference

being ICEBEAR transmits at much larger powers (> 10 times), allowing for scatter from ionospheric plasma density irregularities to be measured.

7.12 Previous Radars Overview

The radars discussed in this chapter use unique modulation schemes and radar hardware techniques to measure the ionosphere of the Earth. The ICEBEAR system utilizes a combination of these different techniques to produce unaliased, high spatiotemporal resolution ionospheric coherent scatter measurements. Some key characteristics of the ICEBEAR system include: 1) the coded CW phase modulated signal to obtain unaliased range and Doppler information, 2) a receiver antenna array to obtain azimuthal angle of arrival measurements, 3) an auroral zone FOV to measure effects of particle precipitation on E-region instability generation, and 4) a bistatic setup allowing for CW operation without saturating the receiver system. Using these characteristics, the ICEBEAR system is able to improve upon the measurements of previous systems, providing improved high spatiotemporal coherent scatter measurements of the E-region. The next chapter describes in detail the design, setup, and operation of the hardware and signal processing used in the ICEBEAR system.

Chapter 8

The ICEBEAR Radar

Portions of this section and Sections 8.1, 8.2, 8.3, 8.3.1, 8.3.2, 8.3.3, 8.3.4, 8.4, 8.4.1, 8.4.3, 8.4.4, 8.5, 8.5.1, and 8.5.3, as well as Figures 8.2, 8.12, 8.13, 8.17, 8.26, 8.28, and Table 8.2 were originally published in Huyghebaert, D., G. Hussey, J. Vierinen, K. McWilliams, and J.-P. St-Maurice (2019), ICEBEAR: An all-digital bistatic coded continuous-wave radar for studies of the E region of the ionosphere, *Radio Science*, *54*(4), 349–364, doi: 10.1029/2018RS006747.

Utilizing a combination of the modern radar techniques discussed in the previous chapters, a new E-region coherent scatter radar system was designed to provide enhanced resolution measurements to further the understanding of auroral E-region dynamics. This new radar is known as the Ionospheric Continuous-wave E-region bistatic Experimental Auroral Radar (ICEBEAR). ICEBEAR is located in Saskatchewan (SK), Canada, and observes the ionospheric E-region in the auroral zone of the Earth perpendicular, or near perpendicular, to the geomagnetic field direction. ICEBEAR operates at VHF frequencies (49.5 MHz) and utilizes the coded CW phase modulated signal technique (Section 5.5.4). A CW signal requires isolation between the transmitting and receiving antennas, or the transmitter signal will saturate the receiver. Due to this requirement the ICEBEAR transmitter and receiver sites are located approximately 240 km apart, which gives ICEBEAR its bistatic designation. The location of the ICEBEAR receiver was due to a previous experiment, while the location of the transmitter was selected due to a combination of optimized aspect angle geometry,

---

Portions of this section and Sections 8.1, 8.2, 8.3, 8.3.1, 8.3.2, 8.3.3, 8.3.4, 8.4, 8.4.1, 8.4.3, 8.4.4, 8.5, 8.5.1, and 8.5.3, as well as Figures 8.2, 8.12, 8.13, 8.17, 8.26, 8.28, and Table 8.2 were originally published in *Huyghebaert et al.* [2019].

being sufficiently far from the receiver site, and for the ease of site construction.

The Radio License obtained from Innovation, Science and Economic Development Canada allows the use of a 160 kHz radio bandwidth with a ERP of 23.613 kW and a center frequency of 49.5 MHz (Appendix H). Different modulations are able and allowed to be transmitted on this radio band, so long as they adhere to the Radio License regulations. As will be seen, the Radio License does limit the allowed power output of the ICEBEAR system.

This chapter describes the design, construction, and electronics hardware used in the ICEBEAR system. Section 8.1 covers the selection process for the ICEBEAR transmitter location, with the setup of the transmitter site covered in Section 8.2. This is followed by a description of the radio hardware common to both receiver and transmitter sites in Section 8.3. The hardware specific to the transmitter site is then described in Section 8.4, with the hardware specific to the receiver site discussed in Section 8.5. The processing of the received radar signal is also described in Section 8.5.

8.1 Selection of Transmitter Location for ICEBEAR

Multiple sites were examined to find a suitable transmitter location. The receiver location was fixed at the Bakker farm site $\approx$ 20 km north east of the University of Saskatchewan due to much of the radar infrastructure already existing there. To examine the viability of each site for the transmitter, aspect angle maps were created. An example of one of these aspect angle maps is shown in Figure 8.1. The maps did not consider any refraction of the radar signal due to the ionosphere. These maps therefore showed the amount of refraction required by the radar signal to become perpendicular to the magnetic field lines of the Earth for a given altitude, a key condition for coherent scattering from ionospheric irregularities. One thing to note is that the maps were created using magnetic field models from the year 2010, and since then the magnetic pole has been moving northward over the polar cap. The aspect angles were therefore off by as much as half a degree. More recent values for the magnetic field are now available, and are used in the analysis of ICEBEAR results. All the aspect angles generated used an altitude of 100 km for the hypothetical scatter altitude.

An abandoned farm site near Leader, Saskatchewan, was a potential location for the

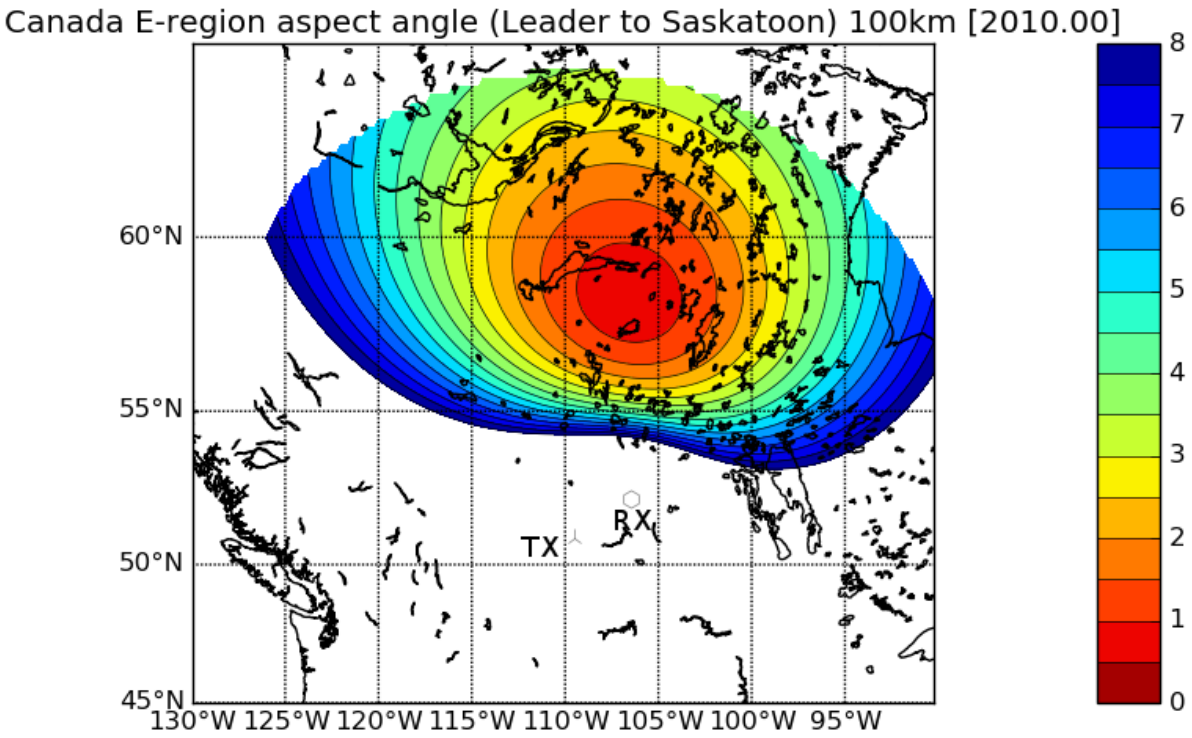

Figure 8.1: Aspect angle map for a transmitter located in Leader, SK (three lines) and the receiver located north east of Saskatoon, SK (hexagon). The color scale is in degrees off perpendicular to the geomagnetic field for the radar signal.

ICEBEAR transmitter. The aspect angle map for this site is displayed in the example map plot (Figure 8.1). The best aspect conditions for this transmitter site occur over northern Saskatchewan, where the signal would be very close to perpendicular with the magnetic field of the Earth ($< 1°$) without considering any refraction. Another benefit of this site was an existing electrical power service existed. The site is actually closer to Prelate, SK, which is a very small village with little to no amenities, not even a hotel.

Another potential site was located near Kerrobert, SK, which is in the westward region of the province of Saskatchewan. With a transmitter at this site, the signal would need to refract by 1.5° to become perpendicular to the magnetic field of the Earth at the lowest aspect angle. The 1.5° necessary for perpendicularity is possible [*Watermann*, 1990], but it

was preferred to have better aspect geometry for the radar.

Another potential location for the ICEBEAR transmitter array was Athabasca University in Alberta. Some benefits of this location were the ease of access, and having personnel available for routine maintenance of the site. Using this site for the transmitter would require the 49.5 MHz radar signal to refract at least 3° to become perpendicular to the magnetic field lines. With this setup less frequent scatter would be observed because of the amount of refraction required for the radar signal to be perpendicular with the magnetic field. Due to this, Athabasca University was determined to not be an ideal site for the ICEBEAR transmitter.

A site to the east of the ICEBEAR receiver was also examined as a potential transmitter location. This potential transmitter site was located in Dauphin, MB. With a transmitter in Dauphin, the signal would be at least 2° off aspect. Due to the lack of potential contacts in the area, and the non-ideal aspect conditions, this site was not chosen for the transmitter.

Other sites were also surveyed as potential locations for the ICEBEAR transmitter, but ultimately the site near Leader, SK, was chosen. The near perpendicular aspect conditions, existing electrical service, and knowing the owners of the land were deciding factors in the decision. Other factors that went into the transmitter location decision included a good overlap of the FOVs from the ICEBEAR transmitter and receiving antenna arrays, and a significant overlap with the Saskatoon Super Dual Auroral Radar Network (SuperDARN) [*Greenwald et al.*, 1995] radar FOV for future collaborative studies.

It should be noted that with only one transmitter-receiver link, plasma flows can only be measured in 1-D. To obtain a full 2-D velocity vector of the plasma, two independent measurements are required. This can be achieved by commissioning a second transmitter in the future. With this dual transmitter setup, obtaining 2-D velocities of the plasma will be possible, since the signals are scattering from different directions. This results in more accurate measurements of the plasma flows, at the expense of requiring more data to be stored and analyzed, and two transmitter sites being maintained. An interesting consequence of using the current ICEBEAR signal modulation scheme is that multiple transmitters can use the same frequency band through utilization of different pseudo-random phase codes, which can be independently extracted from the received signal at a common receiver site.

8.2 Setup of the ICEBEAR Transmitter Site

The ICEBEAR transmitter is located in the south west portion of the province of Saskatchewan, near Prelate, SK, Canada ($50.893°, -109.403°$), and the receiver is located north east of Saskatoon, SK, Canada ($52.243°, -106.450°$), close to the University of Saskatchewan. Both sites can be remotely controlled and operated via the internet. A map of the site locations is presented in Figure 8.2. The map is centered over north-west North America, with provincial and state boundaries realized using thick black lines. The green lines represent the approximate FOVs of the receiver and transmitter antennas. The magnetic inclination in degrees is represented by the black contour lines, which correspond to the expected ionospheric plasma flow direction (Section 3.2). The magenta contours represent an approximate calculation of the range of the potential ionospheric scatter in km. The majority of the FOV overlap occurs over northern Saskatchewan, with coordinates of $\approx$ 55-60°N, 100-112°W. A note of significance regarding the FOVs shown in Figure 8.2 is that they are larger than expected from the antenna parameters (3 dB beamwidth) given in the corresponding antenna specifications due to the large dynamic range in SNR associated with E-region coherent backscatter. This was verified through ionospheric scatter measurements at the edge of the shown FOVs, the location of which were determined through interferometry.

The ICEBEAR transmitter site is situated on an abandoned farm yard, which had a pre-existing electrical service. The pre-existing connection reduced the costs and time associated with commissioning this new radar site. The transmitter site radar shed is a retrofitted shipping (sea) container, with heaters and an air exchange system to control the temperature. A metal 20 ft sea container (shipping container) was chosen to be used as the transmitter site radar shed so that it could be easily shipped, and the majority of radar shed construction could be completed near the University of Saskatchewan before transport to the site. A local construction company was hired as the contractor to install a door, vents, a coaxial cable connector bulkhead, and insulation.

Coaxial feedline cables from the antennas connect to the bulkhead located on the transmitter shed, providing a method for implementing lightning protection. On the inside of the radar shed, this bulkhead has separate coaxial connections to each of the ICEBEAR power

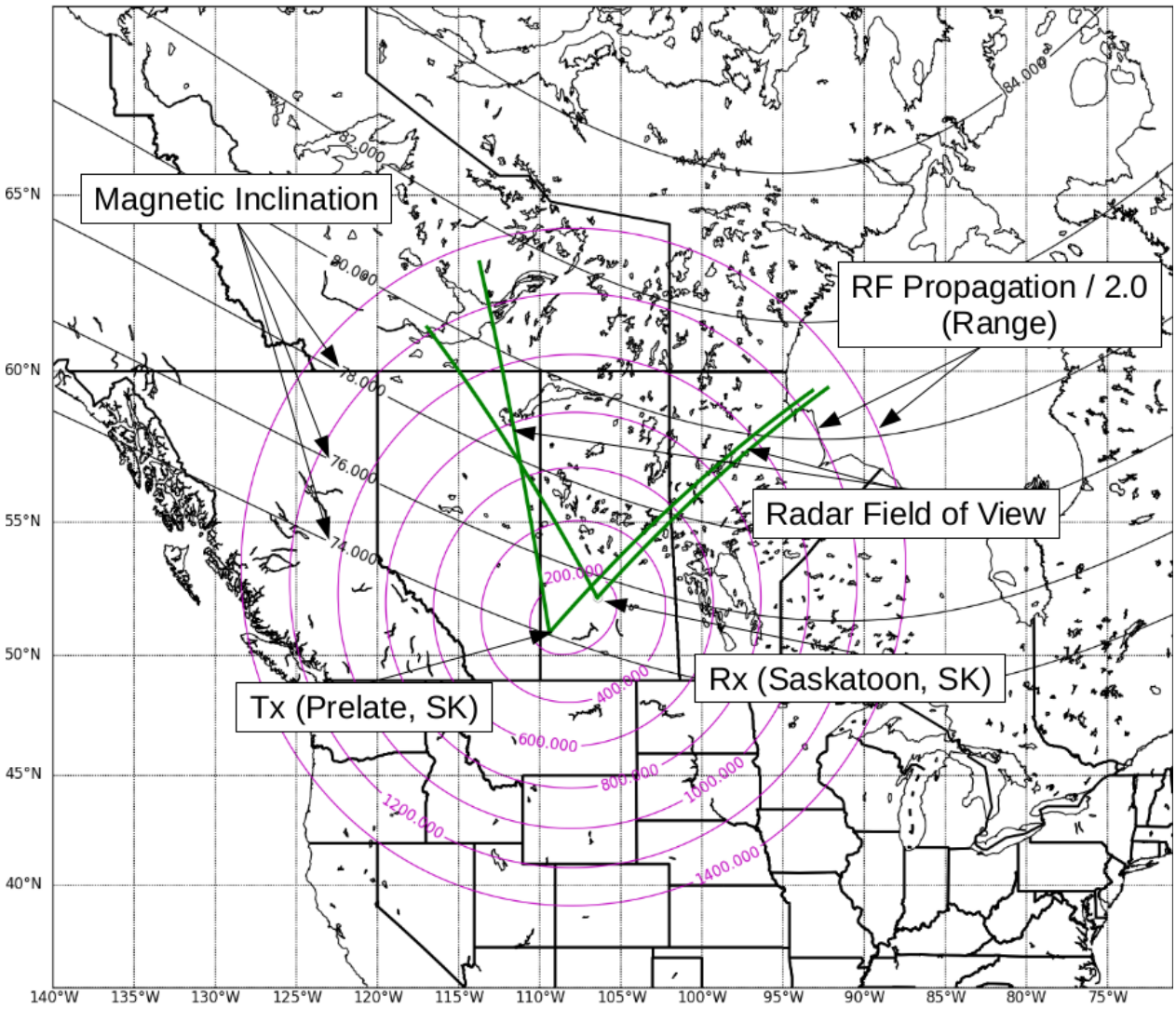

Figure 8.2: The locations and FOVs of the transmitter and receiver sites for the ICEBEAR radar, with a description of the different lines provided in the text. A zoomed in version of this figure, with ionospheric scatter and the aspect angle at an altitude of 100 km, is shown later in Figure 9.4.

Figure 8.3: Image of the exhaust fan in the ICEBEAR transmitter radar shed.

amplifiers. The site can be remotely controlled through a satellite internet connection, where the satellite dish is situated on the sea container roof.

The inside of the radar shed is separated into two separate rooms, one to house the computers and most of the RF electronics, and the other to house the amplifiers. The amplifiers are in a separate room to help with the thermal management of the shed. A temperature controlled ventilation system was installed, where a variable speed fan is used to exhaust air if the amplifier room becomes too hot. The fan is displayed in Figure 8.3. The air intake into the radar shed uses a furnace filter to remove unwanted particulate from entering the building. With this system, the temperature is approximately the same as the outdoor temperature. On hot summer days the radar can be operated at lower powers if there are concerns about overheating.

Once the transmitter shed was designed and built, and a site was selected, the shed was shipped to the site and construction began on the transmitter array. The antenna locations were surveyed in from a grid road to the south of the array. A Google Maps picture of the site is shown in Figure 8.4, with a representative antenna array overlaid on the image. The pointing direction of the array is 16° East of North, which provides good overlap with the receiver FOV. A rental truck was used to transport the antenna hardware, including the towers, guy rope, coaxial cable, and the antennas themselves to the TX site.

Figure 8.4: The Prelate, SK, ICEBEAR site on Google Maps with a representative overlay of the TX antenna array orientation.

Six people travelled to Leader, Saskatchewan, to set up the ICEBEAR transmitter site, including the antenna array. An initial 30 ft (10 m) tower was setup to be used as a pulley tower for the first 50 ft (16 m) antenna tower to be erected. The 30 ft tower was used as a cable tray once all antennas were erected. When attaching an antenna to an assembled 50 ft tower, scaffolding was used to rest the tower on so that the antenna would not be touching the ground and/or be damaged during hoisting. This setup is shown in Figure 8.5. During assembly, the antennas were tuned to 49.5 MHz. A description of the antennas and the antenna arrays are provided in Section 8.3.1.

Figure 8.6 shows the first tower erected, with the 30 ft (10 m) pulley tower also included in the image. Rebar was pounded into the ground using a sledge hammer, and was used to secure the guy ropes to the ground. In the image it can be observed that the pulley on the 30 ft tower is still attached to the 50 ft (15 m) tower. One useful tip to erecting a tower using this method was to attach the pulley rope near the top of the larger antenna tower to be hoisted. This provides more leverage on the tower while hoisting it, preventing the base from lifting from the ground. Once the first 50 ft tower was erected, it was used as the new pulley tower for the next antenna in the array, providing better leverage than the shorter

Figure 8.5: An example of the antenna setup.

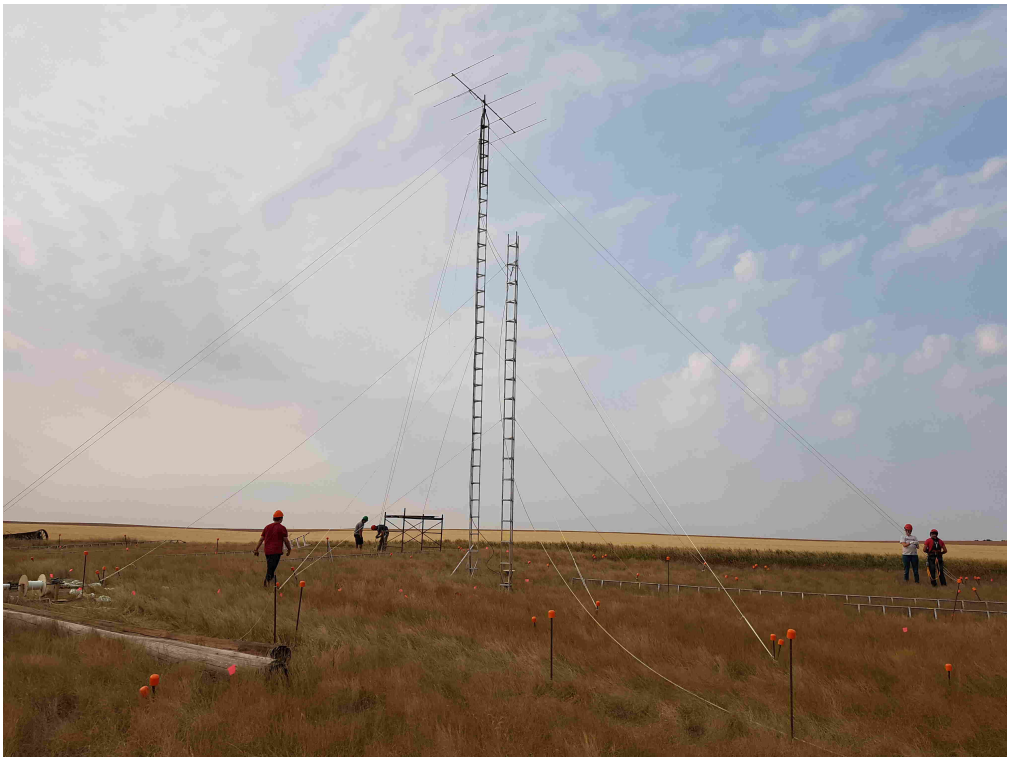

Figure 8.6: The first ICEBEAR TX antenna.

tower.

An image of the full TX antenna array is shown in Figure 8.7. With 6 people, it took approximately 4 days to assemble the antennas, situate the rebar, and erect the towers. The group that helped setup the array are shown in Figure 8.8, and their efforts are graciously acknowledged.

Shortly after the transmitter antenna array was installed, the electronics for inside the ICEBEAR transmitter shed were transported to the site and setup for system operations. Images of the ICEBEAR TX system inside the shed are shown in Figures 8.9, 8.10, and 8.11.

Figure 8.9 shows the rack mounted amplifiers. The input to each of these amplifiers is connected to a transceiver in the neighboring room, with the output connected to the bulkhead shown in Figure 8.10. An ethernet port on each of the amplifiers is connected to a network switch which is connected to the 1 Gbps local area network at the site. Each of the amplifiers has a 240 VAC power connection to the wall, with a 120 VAC control connection to a network controlled power distribution unit (PDU). More information on the amplifiers are provided in Section 8.4.1.

Figure 8.7: The ICEBEAR TX antenna array setup.

Figure 8.8: The people who helped setup the ICEBEAR transmitter array. From left to right there is Kevin Krieger, Marci Detwiller, Devin Huyghebaert, Keith Kotyk, Fraser Hird, and David Fairbairn.

Figure 8.9: The amplifiers and associated connections inside the back room of the transmitter shed.

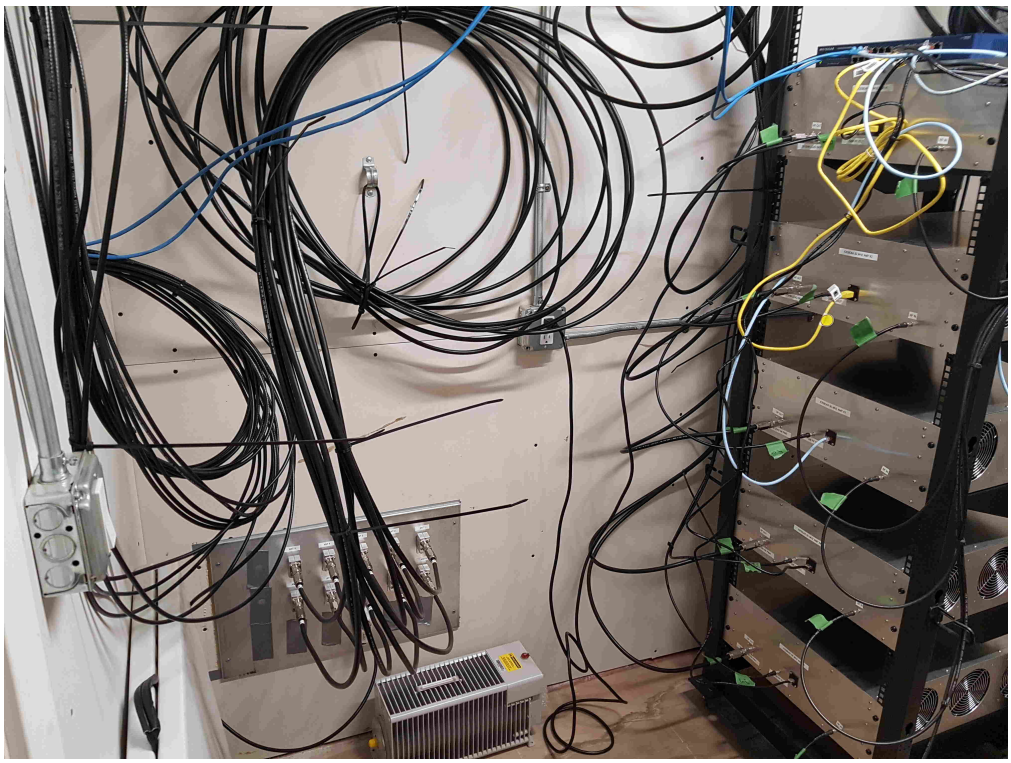

Figure 8.10: The RF bulkhead inside the ICEBEAR TX shed.

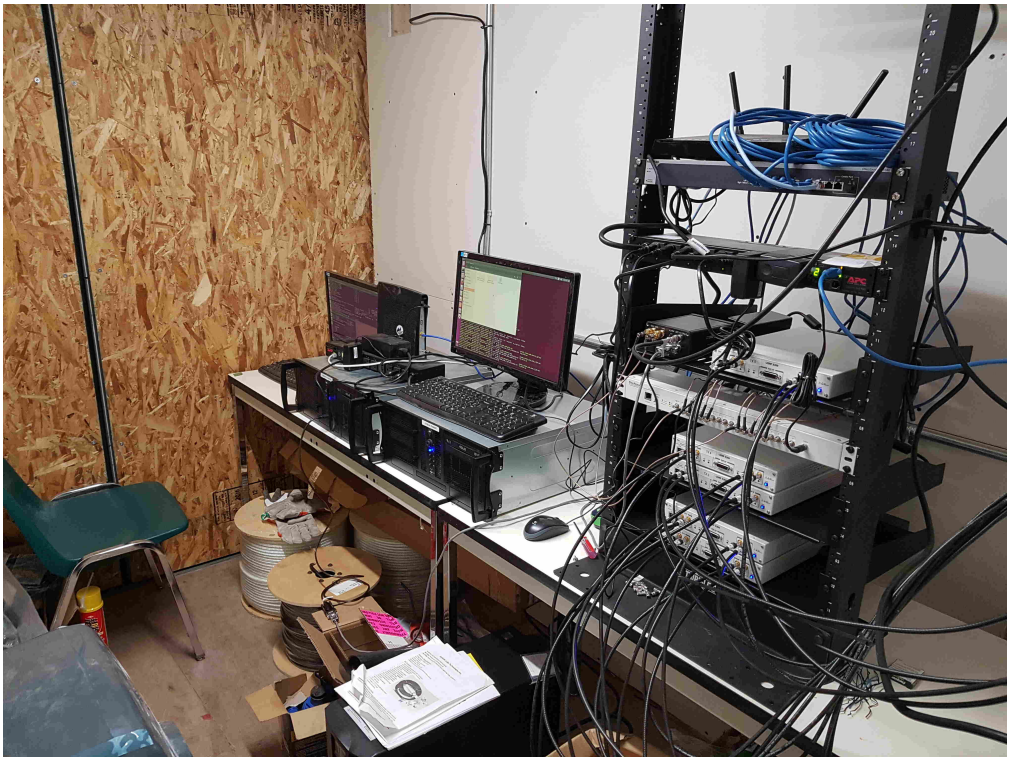

Figure 8.11: The electronics inside the ICEBEAR TX shed.

Figure 8.11 shows the electronics setup at the transmitter site. Included on the electronics rack are a 10 Gbps network switch, 5 transceivers, a clock distribution unit, a GPS disciplined clock, a network router, and a network controlled PDU. Next to the rack are two computers for control and monitoring of the site, and a network modem that is connected to satellite internet. A block diagram of the transmitter system is provided later, in Figure 8.12, with information on the communications connections provided in Section 8.4.4.

In summary, the ICEBEAR transmitter site consists of an antenna array with a transmitter radar shed and associated radio electronics. This transmitter site is located near Prelate, SK, the location of which is indicated in Figure 8.2. The radar shed contains the power amplifiers, radio transceivers, and other associated electronics used for the control and generation of the ICEBEAR radar transmission signals, which are described in detail in this chapter.

8.3 The ICEBEAR Radio Hardware

The ICEBEAR transmitter hardware and receiver hardware share many similarities. The ICEBEAR transmitter array consists of 10 antennas, and each antenna signal chain is controlled independently. The transmitter antenna signal chains are time synchronized and phase matched, allowing the array to operate as a digitally controlled phased array. In each transmitter chain there is a signal generator, power amplification, matched cables and an antenna. Similarly, the ICEBEAR receiver array consists of 10 antennas and each receiver antenna signal chain is sampled (and controlled) independently. As with the transmitter array, each receiver antenna signal chain is time-synchronized and phase matched, providing a digitally steerable phased array. Each receiver signal chain consists of an antenna, cables, pre-amps, filters, and a direct digitization sampler.

A block diagram of the transmitter system with the associated communications connections is shown in Figure 8.12. The TX site can be controlled remotely using a satellite internet connection, which is controlled by an internet modem and router. This router connects to a 1 Gbps local area network, that is connected to each of the amplifier control systems, the power distribution units, and the two computers located at the site. One of the computers is also connected to a 10 Gbps network, which is used to communicate with the transceivers, the Ettus Research X300. The selection process and a description of the transceiver is provided in Section 8.3.2. The radar signal is generated by the transceiver, and is amplified by University of Saskatchewan designed RF amplifiers, designed and constructed by the dissertation author, which are described in Section 8.4.1. The waveform generated by the transceiver is discussed in Section 8.3.4. To synchronize the transmitter and receiver sites a GPS disciplined clock is used, with a clock distribution device. The GPS clock is connected through a serial connection (shown in Figure 8.12), with a description of the synchronization system provided in Section 8.3.3. Once the signal is amplified, it is sent through lightning protection to the antennas, for which the antenna and array characteristics are described in Section 8.3.1.

The receiver system is shown in Figure 8.13 and, as mentioned, has many similarities to the transmitter setup. The receiver site network is connected to the University of Saskatchewan

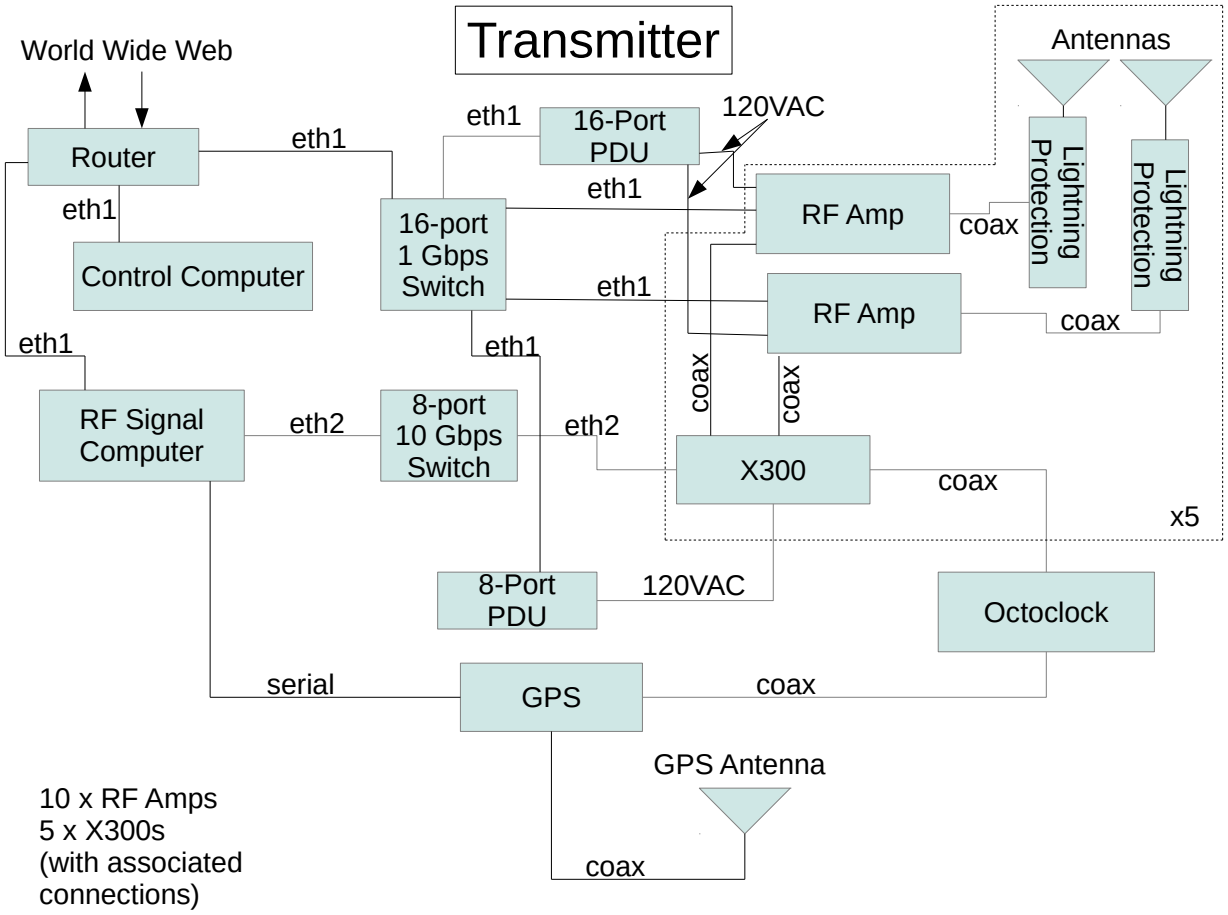

Figure 8.12: Block diagram of the transmitter hardware and the associated communication connections for the ICEBEAR radar.

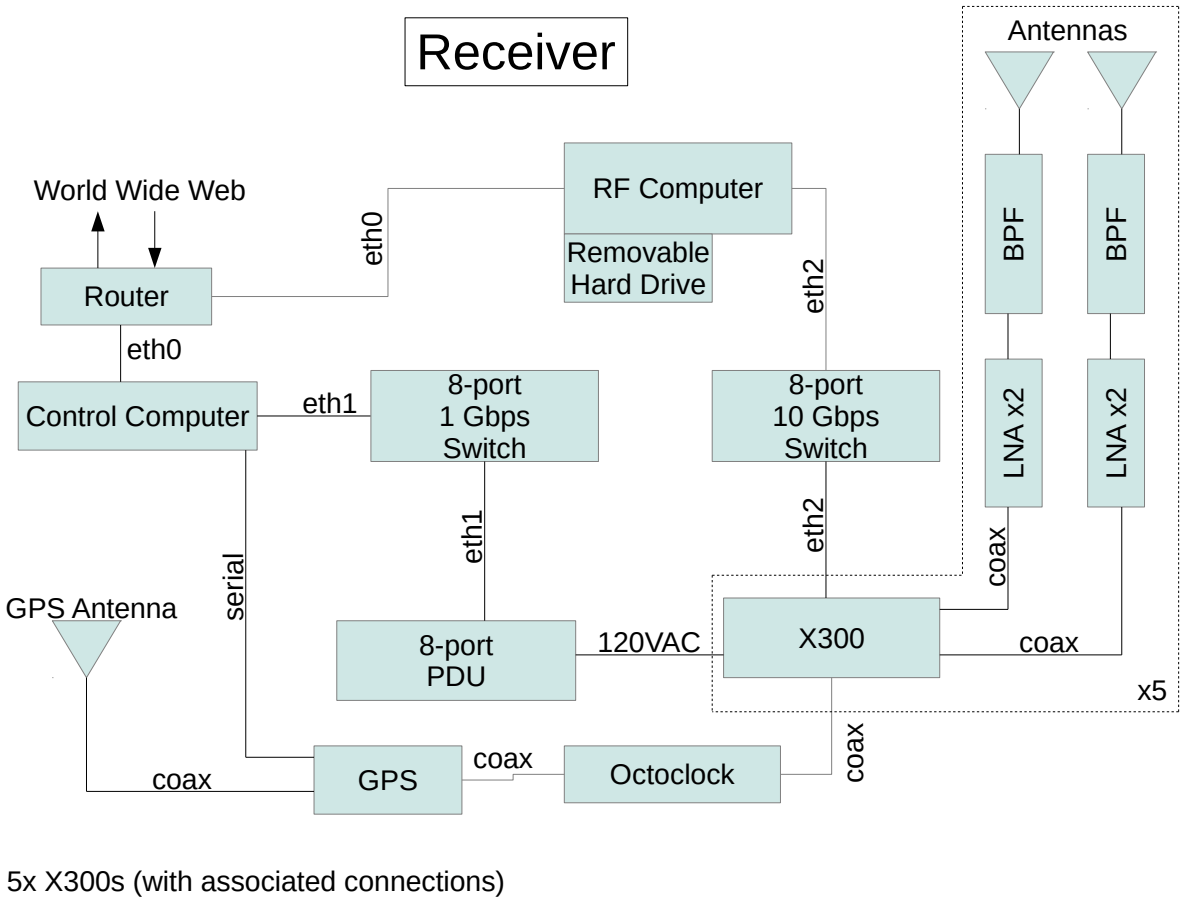

Figure 8.13: Block diagram of the receiver hardware and the associated communication connections for the ICEBEAR radar.

campus network, with a 1 Gbps local area network at the receiver site. The two computers located at the receiver site are connected to the network, as well as network controlled PDUs. One of the computers connects to a 10 Gbps network, which also has 5 Ettus Research X300s connected to it. The X300 is the same transceiver unit used at the ICEBEAR TX site. The antennas receive the scattered TX signal, where the TX and RX antenna arrays are similar, with the differences described in Section 8.3.1. From the antennas, the received signals each pass through a band pass filter and low noise amplifiers (Sections 8.5.1 and 8.5.3), and are finally measured by the X300 transceivers. The measured signals are then recorded on a HDD located in the RF computer (Section 8.5.1), and are transferred to an external hard drive to be transported to campus. On campus, the signal is processed to obtain useful measurements (Section 8.5.3).

The remainder of this Section 8.3 describes the hardware and concepts common to both sites, with a description of the site specific characteristics following.

8.3.1 The ICEBEAR Antenna Arrays

ICEBEAR uses CW phase modulation and interferometry techniques paired with modern radio hardware to obtain simultaneously high temporal and spatial resolution images of the E-region over a large FOV, while continuously sampling the ionospheric medium. These techniques remove aliasing in the frequency and range domains, although aliasing in the azimuthal and elevation domains must still be considered due to antenna spacing. A description of different antenna architectures, as well as antenna interferometry and beamforming techniques were provided in Section 6.5.

Currently, both the TX and RX sites of ICEBEAR are set up with 10 antenna linear arrays with an equal antenna spacing of 6 m. There are plans to re-configure the layout in the future to minimize or eliminate aliasing due to antenna spacing and also obtain elevation, along with unaliased azimuthal, angle of arrival information. ICEBEAR operates with a center frequency of 49.5 MHz, providing a ≈ 1 wavelength ($\lambda = 6.06$ m) spacing between the antennas in the arrays. The 6 m spacing of the receiver array is due to a previous experiment setup and the 6 m spacing of the transmitter array was chosen to match the receiver array. The receiver array is pointed 7° east of north and the transmitter array is pointed 16° east of north.

The 10-antenna linear array with 1-λ spacing provides a beamwidth of $\approx$ 3°. Grating lobes become significant when the beam is digitally steered $\pm \approx$ 30° off boresight. While this should not be a significant issue with the ICEBEAR radar, as the antennas chosen for the receiver and transmitter have beamwidths $\lesssim$ 52°, it must be considered as results obtained through interferometry do appear in these regions at the edge of the FOV.

ICEBEAR Transmitter Array

The antennas used in the ICEBEAR transmitter array are Cushcraft 50-5 antennas [*Cushcraft*, 2018], which are five-element antennas designed for use in the 50 MHz amateur radio band. These antennas are different than those at the previously established receiver site. This was

decided upon due to the Cushcraft 50-5 antennas being easier to assemble, having a broader beamwidth, and being easier to hoist when situated on the radar towers. Having a broader beamwidth can be beneficial for uniformly illuminating the FOV and for beamforming and/or interferometry. The transmitter antennas were tuned to 49.5 MHz – the center frequency used with the ICEBEAR system – and provide a signal gain of 10.5 dBi with a maximum power capability of 1000 W. Each antenna is mounted 15 m ($\approx$ 2.5 λ) above the ground on a tower and is located approximately 50 m from the radar shed. The antenna feedline consisted of 350 ft (110 m) of DRF-400 coaxial cable which has an attenuation factor of 0.9 dB/100 ft (2.95 dB/100 m) at 50 MHz. The mounting height of the antennas produces a multi-lobe radiation pattern in elevation, with a peak at $\approx 4^\circ$ elevation and a vertical beamwidth of $\approx 3^\circ$. This was determined through modelling and assuming an ideal ground plane and is presented in Figure 8.14. The top left panel in the figure shows the azimuthal beampattern for 10 antennas with 1-λ spacing, neglecting ground effects, but including the antenna radiation pattern. The bottom left panel shows the radiation pattern in the elevation plane considering the antenna radiation pattern for only a single antenna, along the boresight of the array. The right panels show the full radiation pattern in the area around the array, with the left panels displaying the radiation pattern at the edge of the grid.

The phase delay along each transmitter signal chain was measured, where a description of the measurement method is provided in Section 8.4.2. The phase measurements allow for digital phase corrections to the transmitted waveforms to be made, providing a fully coherent, and controllable, transmitter antenna array.

ICEBEAR Receiver Array

The ICEBEAR receiver antennas are the Cushcraft 617–6B 6m–wavelength Superboomer antennas with a forward gain of 16.15 dBi. These antennas are located $\approx$ 90 m north of the receiver radar shed, are mounted 15 m above the ground, and are arranged as a linear array (for approximately east to west azimuthal interferometry). The receiver antenna array characteristics are similar to those of the transmitter array, and have similar array characteristics as those shown in Figure 8.14. A picture of the receiver array is displayed in Figure 8.15, where an individual is replacing the guy ropes on the antenna tower. In the

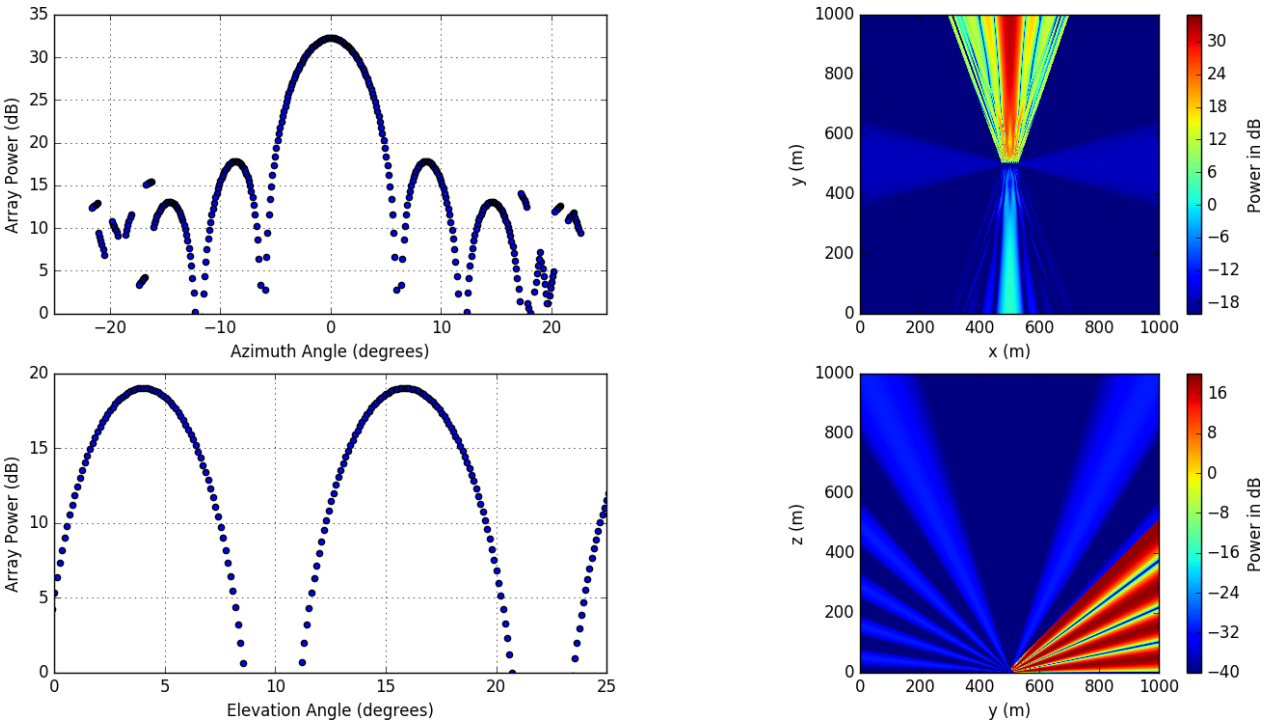

Figure 8.14: Modelled antenna array beampattern for a 10 antenna array with constrained individual antenna pattern due to antenna characteristics.

figure there are 12 antennas, but only 10 are used for the ICEBEAR array. The phase delays along each of the receiver paths were measured and corrected for in hardware and software (Section 8.5.2). The phase delays of the receiver and transmitter were determined starting at the input/output of the transceiver, the selection of which is described in the next section.

8.3.2 The ICEBEAR Transceiver

One of the primary things that must be selected for a radar system is the radio transceiver. Multiple different transmitter and receiver options were investigated to determine which product would satisfactorily meet the requirements for ICEBEAR. A discussion on the selection of the transceiver is provided below.

The first thing that was considered for ICEBEAR was the radio receiver. There were many different options for digital receivers. Most included an ADC and FPGA with DDC capability – an overview of digital receivers was provided in Section 6.6. Table 8.1 provides a list of the options considered for a digital receiver to measure signals around the 50 MHz radio band. The details of the different systems were collected in 2015. The receivers listed

Figure 8.15: The ICEBEAR receiver array, which existed from previous 50 MHz ionospheric experiments.

allowed either direct digital measurement of the signal or an aliased digital measurement of the signal.

Supplier	Digital Receiver	Number of Receiver Channels	ADC Sample Rate	ADC Resolution	Wideband SFDR	DDC?
Ettus Research	USRP1	4	64 MSPS	12-bit	85 dBc	Yes
Ettus Research	N200	2	100 MSPS	14-bit	88 dBc	Yes
Ettus Research	X300	2	200 MSPS	14-bit	88 dBc	Yes
Innovative Integration	X6-250M	8	250 MSPS	14-bit	77 dBc	Yes
Echotek	ECDR-GC214-PCI/TS	2	65 MSPS	14-bit	90 dBc	Yes
Pentek	Model 78661	4	200 MSPS	16-bit	90 dBc	Yes

Table 8.1: List of Digital Receiver Options.

There were some key characteristics of the receiver that were searched for. The ability to measure a signal around 50 MHz was essential, with a preference for direct digital measurement without the use of analog mixing. Each of the receiver channels were required to be synchronizable using an external clock so that the transmitter and receiver sites could be synchronized, as well as each antenna in each of the arrays. The bandwidth of the signal was required to be digitized, requiring a sampling rate of, at the very least, 160 kHz as this was

the Radio License obtained. Expandability of the system for future experiments was another key consideration. The ease of which the receiver could be implemented was also a factor, especially the compatibility with a corresponding transmitter. A DDC was also important to reduce the communication bandwidth required with the receiver devices, as 14-bit samples at a 100 megasamples per second (MSPS) sampling rate would require a 1.4 Gbps connection per receiver channel, which is excessive. As with most systems, the cost per receiver channel was also a consideration. With these key considerations in mind, the different receiver options in Table 8.1 are explored below.

USRP1

The USRP1 was a digital receiver with 4 ADCs, each having a 64 MSPS sampling rate and 12-bit resolution. This was a convenient option due to the price, but there were a couple problems for the radar design being considered. The 12-bit resolution was quite low compared to other options, resulting in a lower dynamic range, and there was no easy way to synchronize these units. The later models from Ettus Research (N200 and X300) had inputs for a 10 MHz clock and a pulse per second (PPS) signal, allowing multiple units from multiple sites to be synchronized. A 50 MHz signal would fall within the first Nyquist band (32-64 MHz) with sufficient bandwidth for a band pass filter to be used without worry of noise aliasing in. Due to the low bit resolution, and complexity to implement synchronization using these units, they were deemed insufficient for the ICEBEAR system.

N200

The N200 was another unit from Ettus Research. It had a 100 MSPS sampling rate ADC with 14-bit resolution. The cost was $\approx$ \$1,000 per receiver channel. These units had a 10 MHz external clock and a PPS input, which was a requirement for using a bistatic system, as both transmitter and receiver systems had to be synchronized. These units were able to be used at 50 MHz, though some sort of reconfiguration was required due to the noise aliasing into the measurement frequency band. With a signal around 50 MHz, the options were to either change the device clock, and thereby change the sample rate, use complex analog filtering, or use a crystal filter. Most band pass filters would not be applicable here, as the Q value would

have to be extremely high. If the bandwidth of a signal crossed over the 50 MHz threshold, a band pass filter would not be an option, and the device clock would have to be changed, or the incoming signal would have to be mixed using analog circuity to a different frequency. One problem with changing the device clock in the unit was that the phase locked loops (PLLs) in the FPGA are initialized in firmware. This means that to change the device clock a rebuild of the FPGA firmware was required, which would have required the appropriate development software and significant development time. If analog circuitry was used to mix the signal to avoid the 50 MHz sampling issues, it would have to be done for each receiver chain, resulting in multiple RF mixers and possible phase matching concerns. Due to the aliasing problems around 50 MHz, the N200 was an inadequate option for ICEBEAR.

X300

The X300 [*Ettus and Braun*, 2015] was a new unit released by Ettus Research at the time of the ICEBEAR transceiver selection. It had 4 ADCs in the system, but only 2 DDCs were available on the FPGA with the released firmware. This resulted in only two receiver chains being available on the unit unless FPGA development was performed. Each ADC on the unit sampled at 200 MSPS with a 14-bit resolution. With only two receiver chains available on purchase, each channel was $\approx$ \$2,750. This device was able to measure at 50 MHz, but being a new unit there was the possibility of problems. Some users of the device raised the issue of phase drift of signals over time, which is a large problem when systems need to be synchronized. This phase drift was measured in the GHz frequency range and was said to be more of an issue at those higher frequencies than in the much lower VHF range. A benefit of the X300 was that with time put into development of the FPGA firmware, there was the option of doubling the receiver chains provided to 4. An interesting option on the device was the capability to change the system master clock in software. This reduced the chance of aliasing issues being a detriment to the system. Another benefit to the system was that the Ettus Research options could be used as a transmitter and as a receiver, which reduced the development time of a corresponding transmitter solution. A discussion on the generation of a transmitter signal was provided in Section 6.3, with many of those concepts being implemented on the X300 device.

X6-250M

The X6-250M was a digital receiver released by Innovative Integration. This unit had 8 ADCs, with a significant amount of FPGA capability. Each ADC had a 250 MSPS sampling rate with 14-bit resolution. The FPGA was configurable to have either a large amount of DDCs with each having a small bandwidth, or to have 8 DDCs with large bandwidths. The cost resulted in $\approx$ \$1,800 per receiver chain. This was cheaper than the X300 option, but two of these units were required to be purchased to obtain at least 10 digital receiver channels (a minimum requirement for the ICEBEAR radar). The software for implementing the X300 had already been tested and used, while the software and interface of the X6-250M was an unknown. The development of software and interfacing was possibly a large time commitment when designing the system, so working with a known system was considered to be greatly beneficial. With this option another device would have been needed for transmitting the ICEBEAR signal.

ECDR-GC214-PCI/TS and Model 78661

Other options included the Pentek and Echotek receivers. The Echotek receiver was outdated and there were reported problems with the digitization bandwidth available. The X300 was similar in cost, but with greater capability than the Echotek. The Pentek receiver was overpriced for the capability available. Each of the X6-250M and X300 had more or similar capability, for at least half the price per receiver chain.

X300 Selected

From the options listed, the X300 was chosen as the transceiver of choice for the ICEBEAR system due to the ease of use and the cost. The same system could be used to transmit and receive the ICEBEAR signal, reducing the chance of timing offsets. Using the same system for both transmit and receive also reduced development time. The X300 also had the potential to be expanded to 4 receive channels per unit with FPGA development, which would provide double the number of receiver channels. This could result in new and innovative experiments.

To further expand upon the X300, it is an advanced radio transceiver that provides the

ability to digitally mix radio signals, when either transmitting or receiving, through the use of a field programmable gate array (FPGA), while simultaneously allowing time synchronization between multiple transceiver units. The radio front end of the system is adaptable through the use of daughtercards, which provide analog filtering, mixing (if needed), and amplification of the radio signal. ICEBEAR uses the BasicRX and BasicTX daughtercards, which allow signals in the range of 0–250 MHz to be transmitted (Tx) and received (Rx) using no analog mixing. As each X300 transceiver has two transmitter and two receiver channels available, two BasicTX daughtercards were required for the front end of the X300s on the ICEBEAR transmitter.

To generate a radio signal using an X300 a center frequency is selected, and complex voltage samples are generated and streamed by the device. The hardware in the X300s has a maximum complex voltage sampling generation rate of 200 MHz on the RX and TX channels, with digital radio frequency up converters and down converters implemented on a FPGA for frequencies within this range. Higher sampling rates provide more control over the radar waveform characteristics, such as the radio BW, and allow for the implementation of digital signal filtering. The FPGA on an X300 digitally mixes the stream of complex voltage samples to the defined center frequency before transmitting the signal in the case of a transmitting configuration.

X300 Transceiver Issues

One issue that has been witnessed with the ICEBEAR system is that the X300 will assumingly transmit the previous contents of the transmit buffer in the X300 before transmitting the waveform streamed to the device. This can create issues with sensitive RF equipment, as the initial transmission is unknown, especially after a power cycle or extended downtime. A solution to this is to transmit on the X300s for ≈ 30 s before turning on the amplifiers. This then prevents unwanted frequencies being transmitted by the amplifiers, which could have consequences pertaining to the radio licensing.

Something that must be noted with the X300 transceivers is that the time stamping for the received and transmitted samples has an offset. This offset exists even when the devices share the same clock. This is likely due to the FPGA signal processing not being

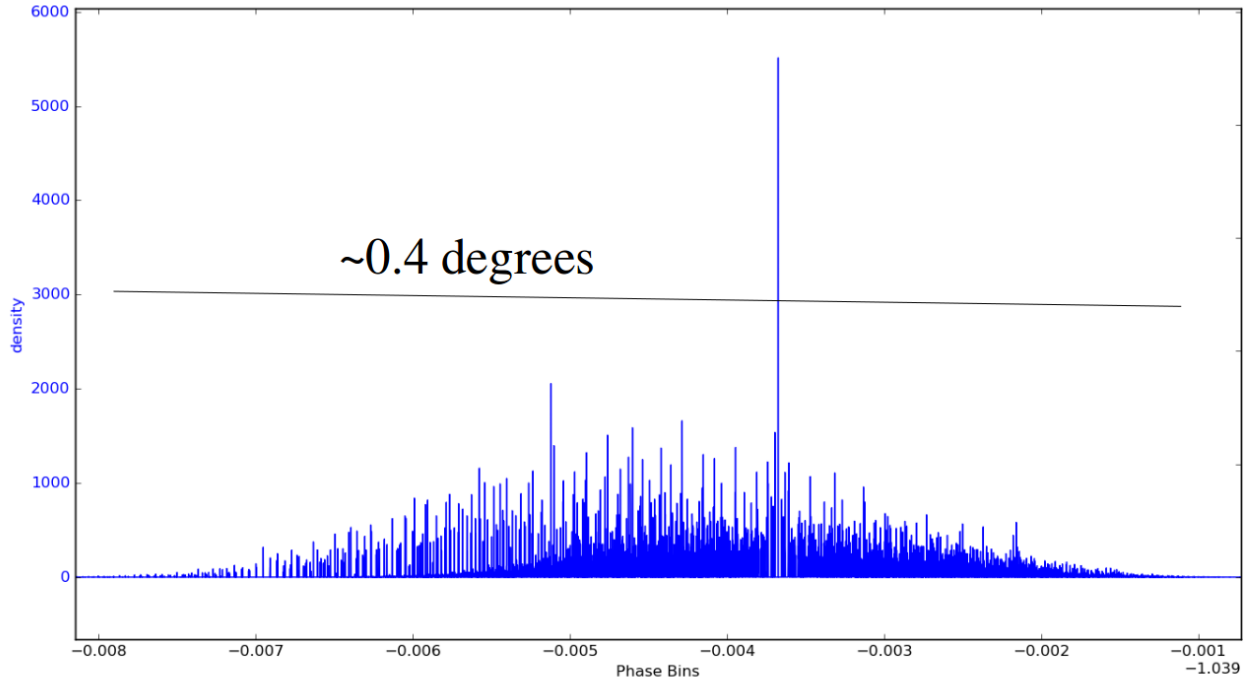

Figure 8.16: Phase Noise measurement of a X300 TX to RX with an external clock.

accounted for in the time stamping, as the offset between the transmitter and receiver time stamps varies, dependent on the center frequency and the sampling rate of the systems. For a 800 kHz transmitter sampling rate and a 200 kHz receiver sampling rate the timing offset is 130 μs, which corresponds to 39 km. The offset does not change as long as the center frequency and sampling rate are constant, so it can be corrected for during analysis.

X300 Phase Noise

To determine the expected level of phase errors in the system the X300 transceivers were tested in the lab , using the device as a transmitter and receiver. A plot of the phase spread of signals using an external clock with an X300 transmitter channel to an X300 receiver channel is shown in Figure 8.16. The measurements show that the phase errors due to the system should be on the order of 0.5° at 49.5 MHz. This test was performed using the 800 kHz transmitter waveform that ICEBEAR transmits with a 200 kHz sampling rate on the receiver. A 0.5° phase error on each receive channel corresponds to an error in the angle of arrival of $\approx 0.16°$ for a one wavelength spacing of the antennas.

As mentioned, one of the benefits of the X300 is the ease at which each transceiver can be synchronized to provide a coherent radar antenna array, and the ability to synchronize multiple geographically separate sites. The next section describes the clock and the clock distribution system that was decided upon to synchronize ICEBEAR.

8.3.3 ICEBEAR Site and System Synchronization

The X300 hardware can be synchronized between multiple geographically separate radar sites using an external clock. An overview of different clocks and clock characteristics were provided in Section 6.7. For ICEBEAR, synchronization is achieved between the receiver and transmitter sites by distributing a 10 MHz and PPS GPS disciplined signal to the X300s using phase delay matched coaxial cables and a clock distribution unit [*Lewandowski et al.*, 1999]. The common clock shared between transceivers makes each signal chain phase coherent. Combined with the fact that each transmitter signal chain is controlled independently, where each signal chain has its own amplifier and antenna, this allows for digital beam-steering and/or different transmissions on each antenna, providing the potential for unique experiments.

Multiple different GPS clock systems were investigated for use with ICEBEAR, including a system that is sold by Ettus Research. Ultimately the Fury GPSDO GPS-disciplined clock [*Jackson Labs*, 2018] suited the needs of ICEBEAR the best, with high accuracy and low clock drift during holdover situations (loss of GPS lock). The Fury GPSDO is designed and built by the same company that supplies Ettus Research with their GPS clock units, so compatibility with the X300s was not an issue. The device drifts less than 7 μs/24 hours with no GPS lock, and the PPS signal is within 20 ns with a GPS lock. The device can be polled using a serial connection to determine if and when the GPS lock is lost, providing details on when the ICEBEAR measurements may be shifted in time, and therefore in range. With that being said, loss of GPS lock is not expected for periods of time greater than an hour, and each range gate for ICEBEAR is 10 μs long. To put this in perspective, for a 7 μs clock drift in a 24 hour period, the error in the range of the measurements would be less than 1.5 km (the length of each ICEBEAR range gate) in this worst case scenario. With this in mind, minimal errors are expected for the ICEBEAR range measurements, even with a

bistatic setup.

For the clock distribution unit the Ettus Research Octoclock [*Ettus Research*, 2018] was chosen. This device allows up to 8 Ettus research transceivers to be synchronized, with a 10 MHz and PPS external signal input. By using the Octoclock and the Fury GPSDO, it was possible to create a fully coherent bistatic radar system. With this fully coherent radar system, a coded signal could be transmitted and received, with the timing of the code used for range determination of the scatter. This coded waveform is described in the next section.

8.3.4 ICEBEAR Signal Modulation

The modulation of the radar signal for nominal ICEBEAR operations is discussed in this section. The ambiguity functions for different radar waveforms were shown in Section 5.5, where the pseudo random coded CW phase modulated waveform is used with the ICEBEAR system. The different modulations are further described in Section 6.3.2. The CW phase modulated radar signal waveform is for normal operations of ICEBEAR, though the radar is able to transmit many different waveforms. The symbol, or baud, length of the code is 10 μs, which corresponds to a BW of 100 kHz. This provides a total path length resolution of 3 km, as calculated from Equation 5.8. Total path length is the complete radio path length to and from the scattering region, and is used instead of range due to the bistatic nature of the ICEBEAR system.

The pseudo-random noise (PRN) code generated for the transmission signal is 10,000 symbols long, resulting in a code length of 100 ms. Using coded sequences in radars is known as pulse-compression, and serves to increase the range resolution, and thereby bandwidth, of the radar signal. The increase in the bandwidth due to this pulse compression is why radars utilizing a coded signal are known as "spread-spectrum" radars [*Kelley and Weber*, 1985]. One benefit of using this "spread-spectrum" technique is that the PRN phase code provides a point-like radar ambiguity function, i.e., a point-like resolution in Doppler frequency and range space (e.g., Figure 5.8, and *Sulzer* [1989]; *Richards et al.* [2010]). The range resolution is dependent upon the symbol length, and the Doppler resolution is dependent upon the sampling period. With a 100 ms code length used with ICEBEAR, the Doppler resolution is 10 Hz, which is determined from Equation 5.10.

The PRN phase code is resistant to noise and interference, as well as appearing as noise to other radio systems. Using a PRN code makes it possible to obtain measurements even in a noisy environment. Due to this characteristic, the PRN code allows multiple radar transmitters to make use of the same band, providing the capability for multi-direction simultaneous measurements of a common volume at the same frequency. For the initial ICEBEAR operations, an optimal PRN code was not rigorously searched for, though most 10,000 length pseudo-random binary codes have very similar characteristics with regards to their peak-to-sidelobe ratio (all being $\approx$ 28 dB).

The 100 ms code length value used is the typical temporal resolution of each ICEBEAR measurement before averaging to improve the SNR. The measurements do not alias in the frequency domain until $\pm$ 50 kHz, which corresponds to $\approx \pm$ 150 km/s, and do not alias in the spatial domain until a radio path length of $\approx$ 30,000 km. Signals scattered from ionospheric irregularities are expected within 2,000 km of the radar, and within a Doppler shift range of $\pm$ 500 Hz, which means that aliasing is not expected in the frequency and range domains for the ICEBEAR radar system. At ranges greater than 2,000 km no scatter is expected due to the geomagnetic field perpendicularity condition of the plasma density irregularities, and no scatter is expected outside of these Doppler frequency shifts due to previous ionospheric radar measurements (Chapter 7).

With the aspects of the ICEBEAR system common to both transmitter and receiver covered, the next section discusses the characteristics of the system specific to the transmitter. This includes the RF power amplifiers which the author designed and built (Section 8.4.1), the phase measurements of the transmitter system (Section 8.4.2), the transmission waveform which is modified from what was discussed here (Section 8.4.3), and information on the transmitter site communications (Section 8.4.4).

8.4 The ICEBEAR Transmitter

The selection of the transmitter site, as well as the setup of the transmitter site, was previously discussed in Sections 8.1 and 8.2. This section describes the RF hardware and techniques that are unique to the transmitter portion of ICEBEAR. A block diagram of the communication

connections of the transmitter was shown in Figure 8.12, where a further description of these connections is given in Section 8.4.4. The next section describes the RF power amplifier that is used to amplify the ICEBEAR transmitted signal described later in Section 8.4.3.

8.4.1 The ICEBEAR Power Amplifiers

Part of the development of ICEBEAR included designing and building solid-state linear CW power amplifiers, and a description of different RF amplifiers was provided in Section 6.4. The ICEBEAR amplifiers were designed with remote monitoring and control capabilities. A partnership with a local technology company, Scientific Instrumentation Ltd. (SIL), was formed to design and build these amplifiers. SIL has expertise in electronics assembly and the design of electronics hardware enclosures, as well as construction of some scientific radars, such as the power amplifiers for the HF network of SuperDARN radars [*Greenwald et al.*, 1995] and CADI ionosondes [*MacDougall et al.*, 1995]. The design goal for the amplifier output power was 1 kW, with minimal harmonics and signal distortion. On the monitoring side, there were requirements to be able to remotely monitor the temperature, fan speed and output standing wave ratio (SWR) of the amplifier. The final specifications versus the goals are presented in Table 8.2. The specifications were all met, except for a slightly lower power output and gain of the power amplifier. An amplifier gain of 57 dB was achieved, with a CW power output of 59 dBm. When operated at 50 MHz, the third harmonic on the output was measured to be at least 26 dB below the peak signal power of 58 dBm, while the second harmonic was below the measurement range. The amplifier has operational frequencies in the range of 20–50 MHz, though this frequency band can be lowered with minor modifications to the amplifier. The amplifier monitoring systems were all successfully implemented within the amplifier enclosure, and the enclosure is rack mountable.

Figure 8.17 shows a block diagram of the ICEBEAR power amplifier. The amplifier was designed by myself, including the integration of different electronics, and the design of the amplifier enclosure. The amplifier consists of 3 stages, and the output from the final stage is passed through a directional coupler, which allows for the forward and reverse signal to be measured using a logarithmic power measurement circuit. Multiple designs were tested for the output directional coupler, and the design described in *Wade* [2010] was selected. This

Characteristic	Goal	Result
Amplifier Gain	60 dB	57 dB
Power Output	60 dBm	59 dBm
Temp. Monitoring	yes	yes
Fan Monitoring	yes	yes
Output Monitoring	yes	yes
Remote Control	yes	yes
Rack Mountable	yes	yes
Harmonics @ 50 MHz	best possible	26 dB down
Frequency Span	2-50 MHz	20-50 MHz
Duty Cycle	100% (CW)	100% (CW)

Table 8.2: ICEBEAR Amplifier Specifications

selection was due to accurate representation of the throughput signal at VHF frequencies, with sufficient isolation between the throughput signal and the sampled signal.

A picture of the amplifier can be seen in Figure 8.18. This picture is of the prototype amplifier under construction, with the cover of the enclosure removed. The different components are labelled, and are connected as shown in Figure 8.17. The front of the amplifier is on the right side of the image, while the back of the amplifier is on the left. For sufficient airflow when rack mounted, an open sided rack is required due to the vents being on the sides of the amplifier enclosure.

First Stage

The first stage amplifier was designed by myself. An evaluation board was initially expected to be used, but for cost savings a new design was created and implemented. The first stage amplifier has a gain of approximately 18 dB and operates at frequencies of 20–50 MHz. To amplify lower frequency signals this amplifier would need to be replaced with a different design. The P1dB point is $\approx$ 19 dBm. The first stage and the Raspberry Pi monitoring computer share a 5 V power supply.

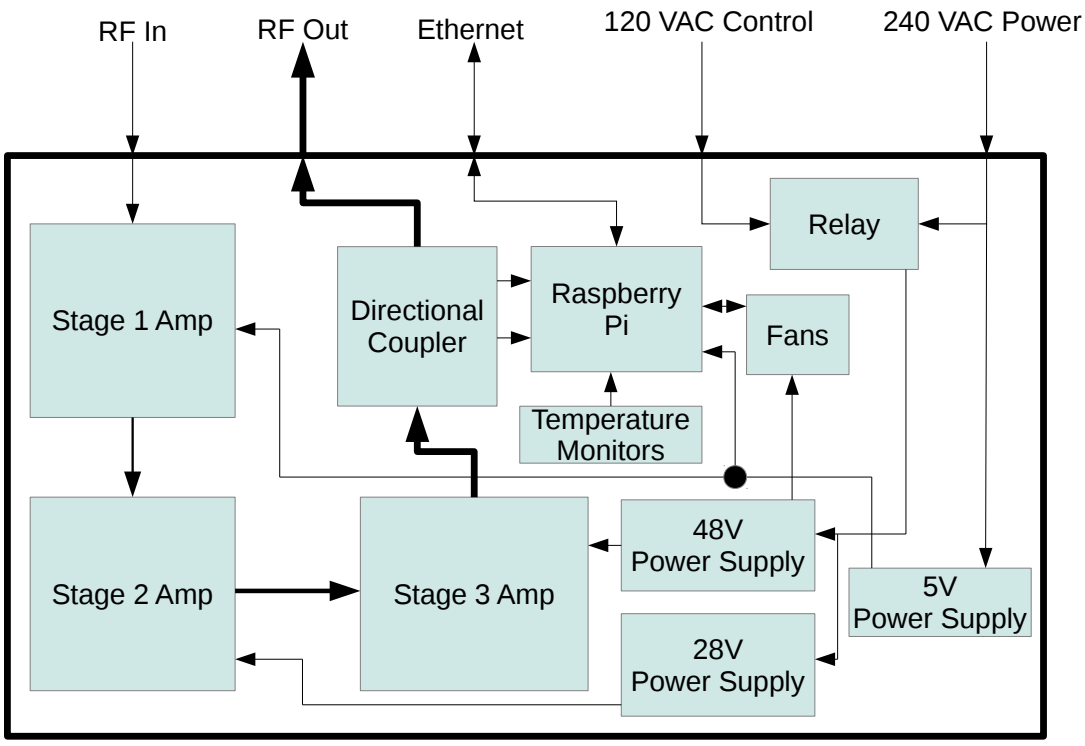

Figure 8.17: Block diagram of the power amplifier enclosure designed and built for the ICEBEAR transmitter system.

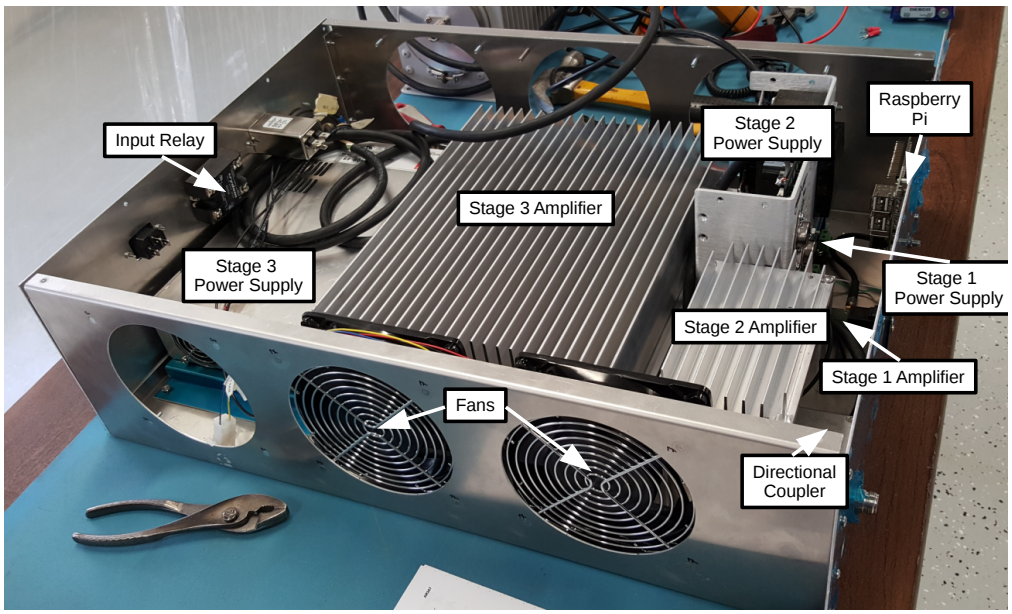

Figure 8.18: Prototype RF power amplifier internal setup.

Second Stage

The second stage amplifier is a SuperDARN driver amplifier [*Scientific Instrumentation Ltd.*, 1993] that was re-designed by myself. Some key changes include increasing the frequencies of operation from 5–30 MHz to 5–50 MHz, and changing the duty cycle from 6% to 100%. With the re-design, at the lower end of the frequency band harmonics are evident in the output signal and require filtering for operation at these frequencies. In hindsight, it would have been more practical to design a completely new amplifier. As it is, the second stage is one of the limiting factors in the amplifier operation at higher power levels. It has a gain that begins to decrease at an output power of approximately 38 dBm (6.3 W). An aluminum heat sink was attached to the heat spreader base plate to compensate for the increased heating caused by increasing the duty cycle.

Third Stage

The third stage amplifier is the AR347 from Communication Concepts Inc., which is based on the design by *Granberg* [1990]. This amplifier can operate from 2 to 50 MHz, though the lower frequencies require a high power filter on the output to reduce harmonics. The power output can reach 1200 W, but this requires significant heat sinking. The current heat sink allows operation of the amplifier with power outputs as high as 800 W. Something of note is that during testing the amplifier output into a 1 kW RF dummy load, erratic values were being measured through the directional coupler. These values would fluctuate over time which was concerning. It was determined the problem was related to the RF dummy load overheating due to lack of air convection over the load. Once a fan was setup to cool the RF load the amplifier measurements stabilized.

For operations around 50 MHz, the amplifier suppresses harmonics by > 26 dB, which is required for the Radio License. This allows operation without the use of any filtering on the output. The antenna also acts as a band pass filter for the outgoing signal, helping to further suppress harmonics.

Monitoring Circuit

The output of the amplifier is passed through a directional coupler that is connected to an amplifier monitoring circuit. The amplifier monitoring circuit takes the RF signal and converts it to a DC voltage proportional to its logarithmic power. The monitoring circuit board has three functions: 1) it uses an ADC to convert the logarithmic amplifier DC voltage values to a digital signal, 2) it includes the electronic components required for temperature monitoring and, 3) it provides the circuitry to control and monitor the amplifier enclosure fans.

To communicate with the monitoring circuit, the general purpose input-output (GPIO) pins of a Raspberry Pi [*Halfacree and Upton*, 2012] were used. Temperature sensors measure the temperature of the heat sinks on the second and third stage amplifiers, as well as the air temperature at the intake of the amplifier enclosure. The second and third stage power supplies are located inside the amplifier enclosure and are controlled by the Raspberry Pi and an external network controlled power distribution unit (PDU). The PDU supplies a 120 VAC (volts alternating current) control source to a relay inside the enclosure and, when a 120 VAC is applied, the relay engages the 240 VAC connection to the second and third stage amplifier power supplies. The first amplifier stage and the Raspberry Pi are always powered when connected to a 240 VAC power source. The design was implemented in this manor so the amplifier could be monitored and controlled remotely at all times. There is also an SMA coaxial connector output (not shown in Figure 8.17) on the front of the amplifier enclosure which provides an output signal, at an attenuated level of approximately -70 dB, for sampling and testing. The ICEBEAR transmitter radar signal is supplied to each power amplifier through a coaxial cable connected to a signal generator and this amplified signal is then sent via coaxial cables to RF connectors on an aluminum bulkhead. This bulkhead is well grounded with lightning protection incorporated.

Amplifier Results

Results from the prototype amplifier testing are shown in Figures 8.19, 8.20, 8.21, and 8.22. Further testing was performed on each of the production amplifiers, the results of which are

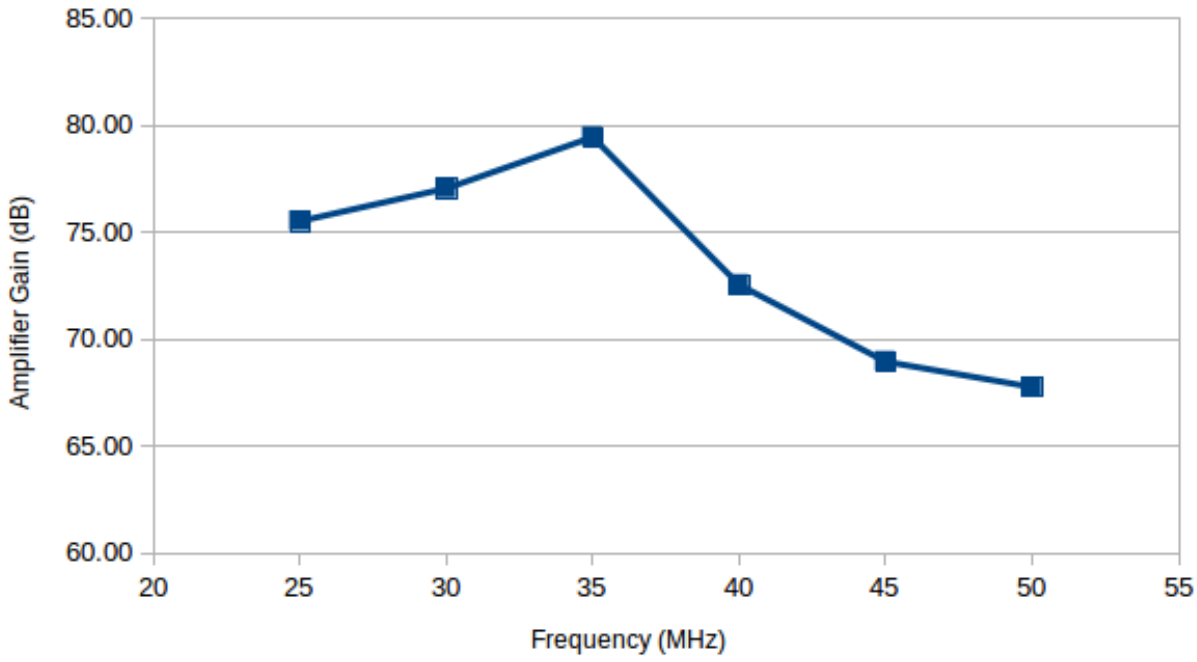

Figure 8.19: Low power (≈ –25 dBm input) gain measurements for the ICEBEAR amplifier plotted against the frequency of the amplified signal.

not shown here. The figures provide an overview of the characteristics of the amplifier system designed and built for ICEBEAR.

Figure 8.19 shows how the gain of the amplifier varies with frequency. A peak gain is reached at ≈ 35 MHz, with decreasing gains away from this point. As the ICEBEAR system was focused on 50 MHz operation, only low power input signals (≈ –25 dBm) were used to determine the gain at the various frequencies. This provides a basis for future development if lower frequency operation is desired for these amplifiers. For operation below 20 MHz, minor adjustments can be made to the amplifier to reduce harmonics and provide a more uniform gain over the frequency band.

Figure 8.20 provides the isolation between the throughput and sampled forward power signal for the directional coupler in the ICEBEAR amplifier. The figure shows a decrease in the isolation with an increase in the frequency. While not shown here, this directional coupler design was chosen due to a accurate representation of the throughput signal on the sampled output. The isolation relationship between the frequency and sampled signal is important when using the directional coupler to determine the output power of the amplifier at a given

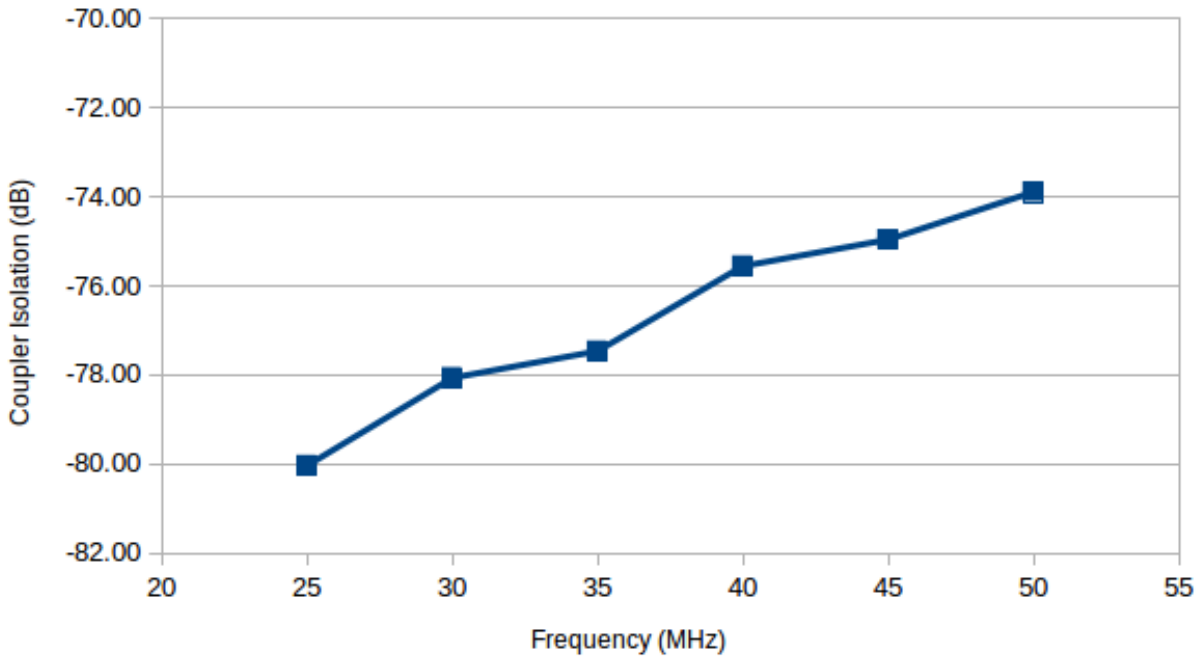

Figure 8.20: The isolation provided by the directional coupler between the forward/reverse power and the throughput signal for various frequencies.

frequency.

Figure 8.21 shows the temperature of the third stage heat sink for various output powers of the amplifier. At 650 W CW output the heat sink reached a temperature of 57 °C. This is with the forced air cooling system of the amplifier implemented. Without the forced air cooling the amplifier is not able to operate at these CW power levels. The monitoring system of the amplifier shuts down the amplifier if a fan fails to protect the transistors from overheating.

Figure 8.22 shows how the output power varies with the input power of the ICEBEAR amplifier. While it is preferred to have a 1:1 relationship between the input and output powers, that is not seen here. This is due to gain compression on the second stage of the amplifier. Even with this gain compression of the system, the harmonics are suppressed on the output due to the third amplifier stage filtering the signal. Future improvements to the amplifier could include an improvement to the second stage of the amplifier, providing an 1:1 relationship between the input and output powers. With a 0 dBm (1 mW) input signal to the amplifier, the gain of the system is just over 58 dB. The amplifiers were tested to a

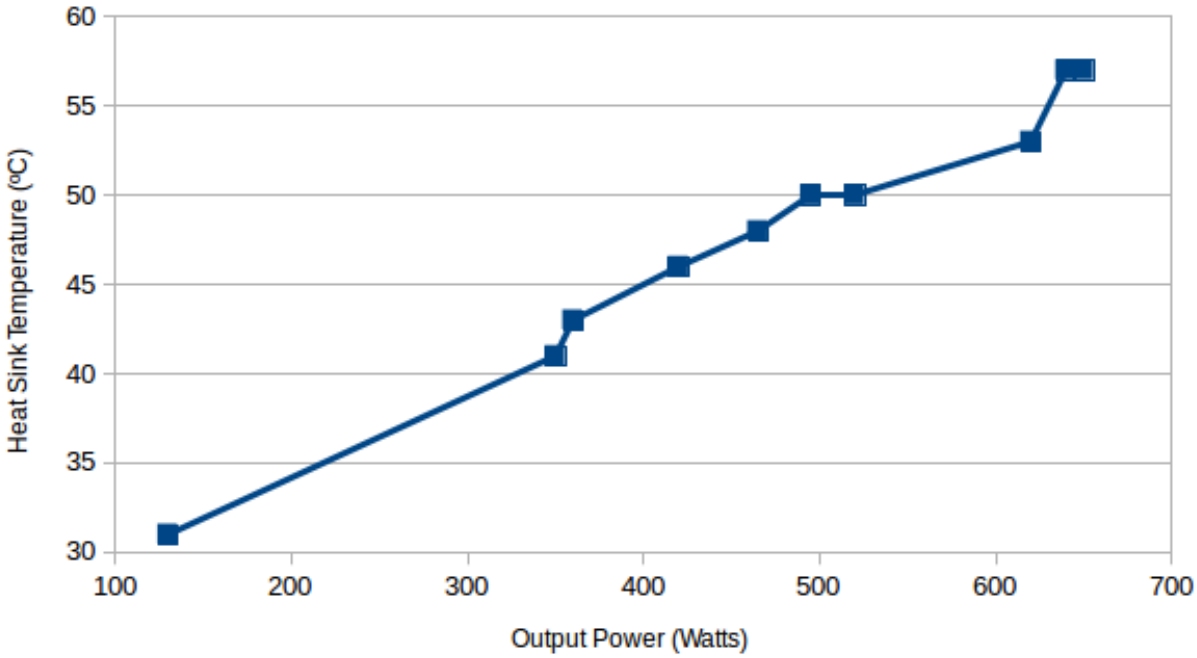

Figure 8.21: The temperature of the final stage heat sink of the ICEBEAR amplifier plotted against the output power.

59 dBm output, but are not expected to be operated at these power levels in the field due to the Radio License acquired for ICEBEAR operations.

More detailed documentation of the construction and testing of the amplifiers has been provided to both SIL and my Ph.D. supervisor. This includes part lists, step-by-step construction instructions, testing diagrams, and printed circuit board schematics. This documentation has not been included in the thesis due to the commercial nature of the amplifier system, as this was a joint effort with a commercial company with product and marketing interests.

8.4.2 TX Phase Measurements

The phase difference of each transmitter antenna path was measured for calibration. A diagram of the phase measurement setup is shown in Figure 8.23. A network analyzer was used to make the phase measurements of the signal path. Two measurements were made, a two port measurement from the X300 up to the bulkhead (M_1), and a single port measurement from the bulkhead to the radar antenna (M_2). The M_2 phase measurement

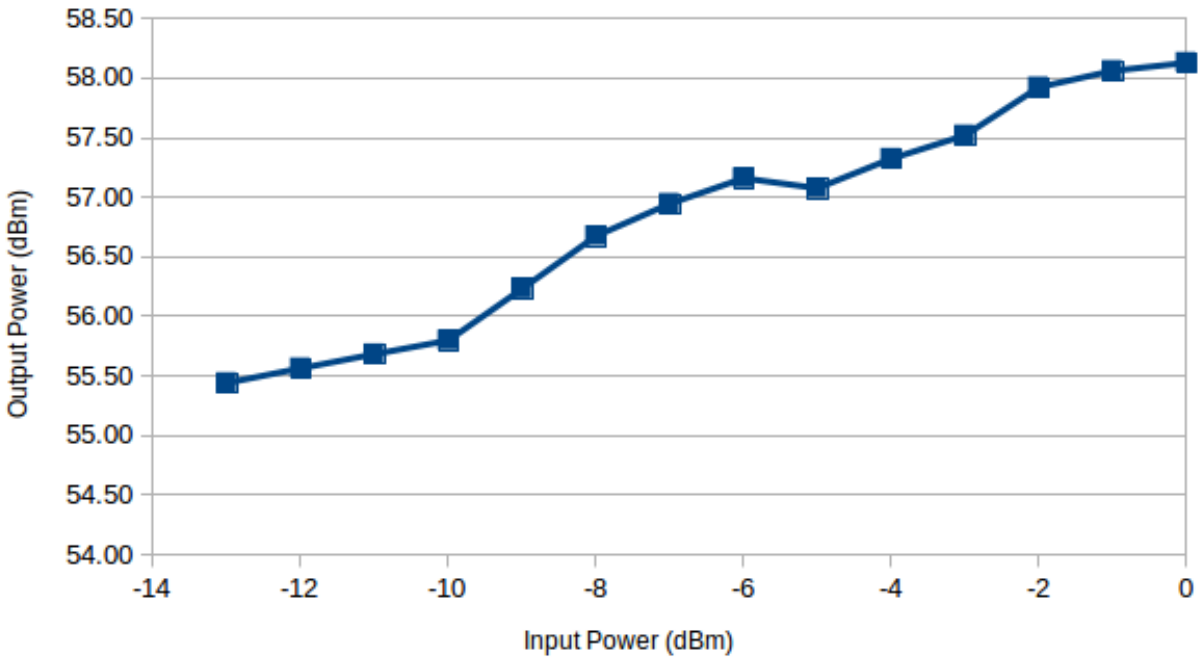

Figure 8.22: The input power plotted against the output power for the ICEBEAR amplifiers.

is approximately double what the actual phase delay is, due to the signal travelling to the antenna and back, and must be considered when determining the total phase offset. The M_1 phase measurement could also be taken from the sampling port at the front of the amplifier, though there could be phase mismatches due to the coaxial cables within the amplifier and the splitter used for the sampling port. As the amplifier has a gain on the order of 60 dB, and can output powers up to 59 dBm, an RF sampler with an attenuated signal should be used when making the M_1 measurement. If there is a spare directional coupler, it can be used for the phase measurement, as long as the same coupler is used for each measurement. From the phase measurements, the phase differences between the different transmitter paths can be determined and phase calibrations for ICEBEAR were made.

8.4.3 The ICEBEAR Transmitted Signal

The accurate timing, provided by the GPS clock, of each RF complex voltage sample transmitted within the modulation scheme makes it possible to accurately determine the range of targets from which the radar signal scatters. In the case of the ICEBEAR system, the radar

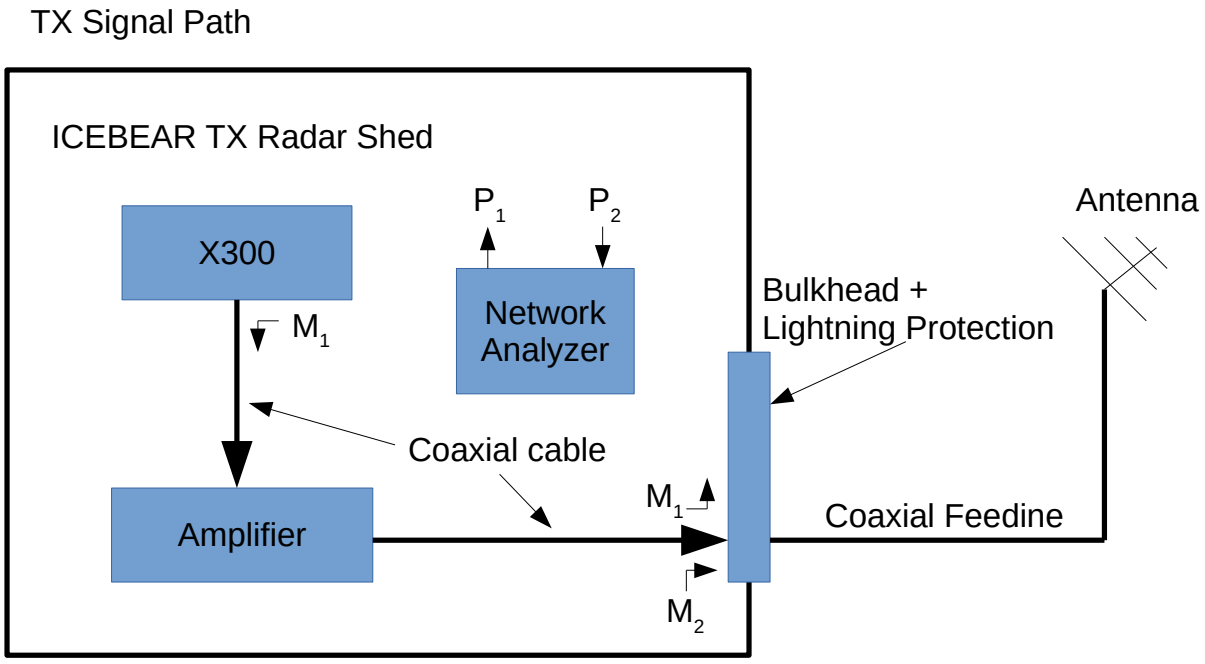

Figure 8.23: Transmitter path phase measurement setup.

transmits a phase modulated CW signal (Section 8.3.4). By modulating the CW signal it is possible to obtain high temporal and high spatial resolution simultaneously, while avoiding aliasing.

The current implementation of ICEBEAR uses an 800 kHz sampled complex voltage signal for transmission. This meets the necessary phase modulation rate of 100 kHz for a path length resolution of 3 km, and also includes filtering of the signal to reduce side bands through the use of amplitude modulation to meet radio frequency licensing requirements. A sampling rate of 800 kHz was chosen as a compromise between excessive streaming bandwidth over ethernet to the X300s, and the need to accurately filter the signal. The filter used consisted of a running average of the TX signal to be transmitted, which is effectively a low pass filter. The complex voltage sampling rate can be converted to a communication throughput data rate by recognizing that each complex voltage sample is a 32-bit complex number. For the 800 kHz sampling rate used by each ICEBEAR transmitter signal chain, there is a 25.6 Mbps communication data rate per signal chain. This is the minimum data rate required between the transmitter host computer and an X300 for one transmission channel for the ICEBEAR

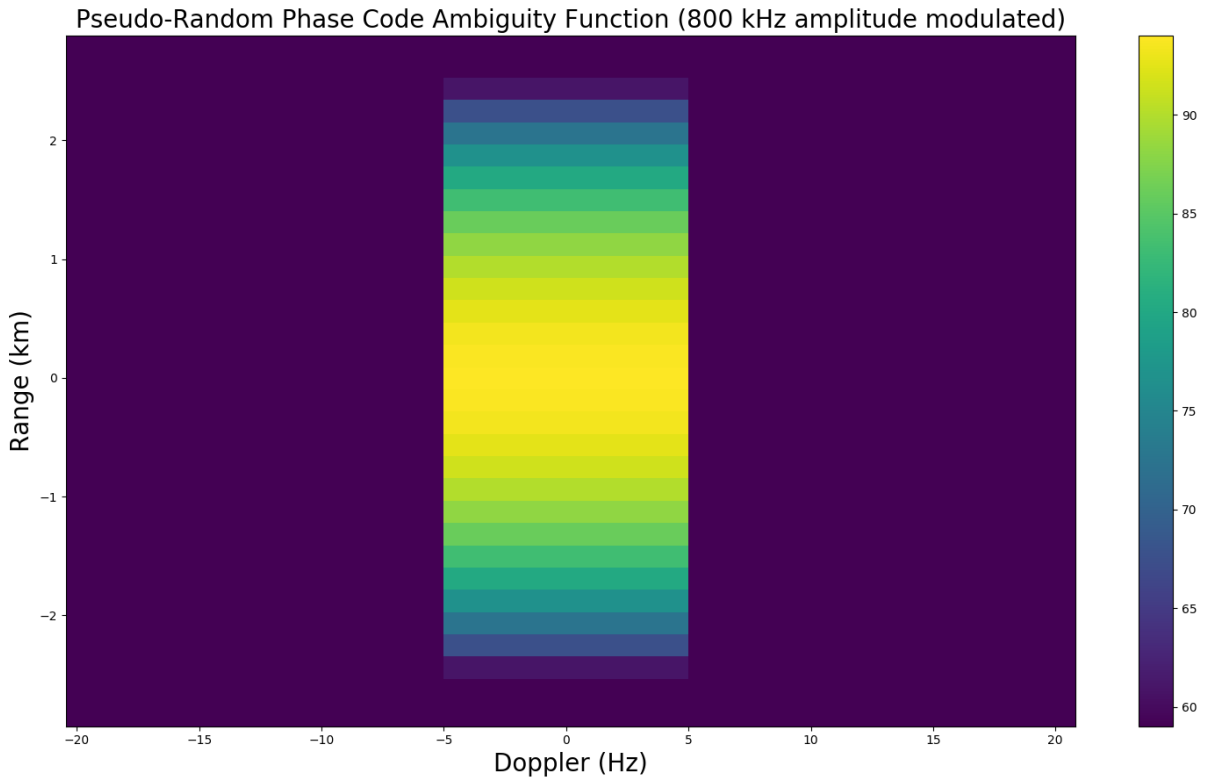

Figure 8.24: Ambiguity function of the 800 kHz sampled ICEBEAR transmitted signal.

configuration.

From the 800 kHz amplitude and phase modulated signal, the theoretical ICEBEAR ambiguity function is provided in Figure 8.24. In the figure it can be observed that the Doppler resolution is unaffected by the amplitude modulation, though the range resolution of the ambiguity function is spread. At the first range gate (1.5 km in Figure 8.24), the ambiguity function power is ≈10 dB down from the peak, and by 3 km, the power is comparable to the signal clutter floor. This resolution is acceptable for the ICEBEAR system, and allows fulfillment of the Radio License requirements.

8.4.4 ICEBEAR Transmitter Communications

An overview of the complete ICEBEAR transmitter system was presented as a block diagram in Figure 8.12. One computer is needed for the overall control and generation of the transmitted waveform for the ICEBEAR transmitter (RF Signal Computer), while the other

computer is used to monitor the transmitter amplifiers, the GPS clock synchronization and to perform diagnostics on the overall radar site health (Control Computer). The computers operate using Ubuntu Linux [*Thomas*, 2006]. On the RF Signal Computer, the GNURadio [*Blossom*, 2004] software suite and the USRP Hardware Driver (UHD) [*Ettus and Braun*, 2015] are used to interface with the X300s. The code used to operate the X300s at the transmitter site is provided in Appendix F. A 10 Gbps ethernet connection between the RF Signal Computer and a 10 Gbps switch is used to communicate with the 5 X300 transceivers (2 channels per transceiver) on the same network. The 10 Gbps connection provides a large communication BW connection to the X300s providing the capability to transmit high sampling rate generated radio signals.

The ICEBEAR transmitter site can be accessed remotely using a satellite internet connection. Each of the amplifiers and X300s can be individually operated. The temperature of the transmitter site is monitored, along with the GPS lock and amplifier statistics, such as output SWR and fan speed. With the remote monitoring and control system in place, the ICEBEAR radar can be started/stopped and monitored with simple commands using an internet connection.

The next section discusses the RF hardware and techniques that are unique to the receiver side of the ICEBEAR system. This includes a discussion of the hardware and the communications connections for the ICEBEAR receiver site (Section 8.5.1), the signal path phase measurements taken at the receiver site (Section 8.5.2), and the processing of the received ICEBEAR signal (Section 8.5.3).

8.5 The ICEBEAR Receiver

A great deal of the ICEBEAR transmitter system is mirrored by the ICEBEAR receiver system, but there are some differences. As with the ICEBEAR transmitter system, the ICEBEAR receiver system consists of a linear array of 10 antennas with 6 m spacing. The receiver site is located $\approx$ 240 km NE of the transmitter site, and $\approx$ 20 km NE of the University of Saskatchewan in Saskatoon, SK, Canada. The receiver radar shed and antenna array existed from previous ionospheric radar experiments, and were re-purposed and modified for

Figure 8.25: The ICEBEAR receiver shed located on Bakker farm 20 km NE of Saskatoon, SK.

use by the ICEBEAR radar. New ICEBEAR radar electronics were installed in the radar shed, and both the radar shed and antenna array were renovated, with new cables and a new cable tray leading to the array constructed. Figure 8.25 displays the ICEBEAR receiver radar shed, and the ICEBEAR receiver antenna array was previously shown in Figure 8.15.

The new ICEBEAR electronics installed at the receiver site were necessary to achieve the high spatiotemporal observations and extract new and detailed information about the ionospheric plasma contained within the scattered radar signal. A further description of these electronics is provided in this section.

8.5.1 ICEBEAR Receiver Hardware and Communications

A block diagram of the ICEBEAR receiver system was presented in Figure 8.13, with a photograph of the actual ICEBEAR receiver system hardware shown in Figure 8.26. The hardware is located in the receiver shed, shown in Figure 8.25. A description of the connections between the different devices in Figure 8.26 follows.

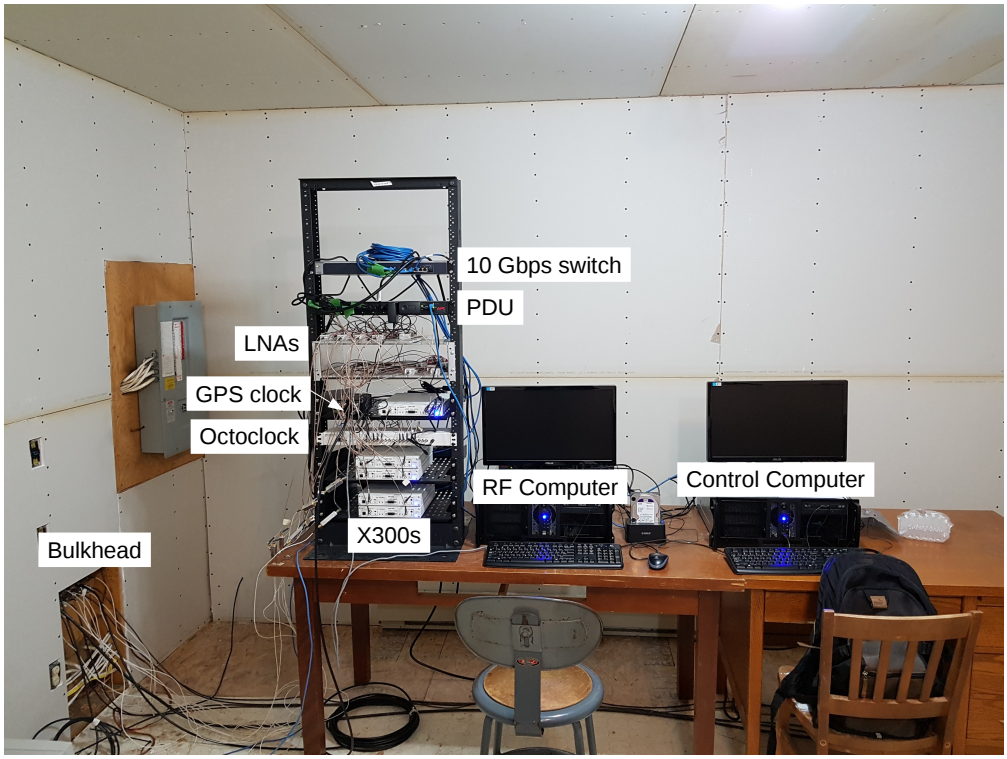

Figure 8.26: The ICEBEAR receiver electronics. On the electronics rack (on left) are the pre-amps, the X300s, the GPS clock, the Octoclock distribution unit and the PDU. Directly to the right of the rack is the RF computer that controls the X300s and next to it is the monitoring control computer. There is an external HDD docking device next to the RF computer for transfer of data from the RF computer for later analysis.

From each receiver antenna ≈ 600 ft (200 m) of DRF-400 coaxial cable was used to connect to a bulkhead on the receiver radar shed. From the bulkhead each receiver antenna signal chain connects to a band pass filter (3333-SMA from KR Electronics [*KR Electronics*, 2017]) and two low noise amplifiers (LNAs) with 28 dB gain each (ZFL-500LN+ from Mini-Circuits [*Mini-Circuits*, 2018]). The band pass filter is required to attenuate nearby radio and TV signals and has a typical insertion loss of 6.1 dB. Signals from the antenna are therefore attenuated ≈ 12 dB before they are amplified at the LNAs (≈ 6 dB loss from feedline). This results in the system noise being slightly higher than the sky noise due to the LNA noise additions (≈ 2.9 dB per LNA), where the sky noise is typically 15 dB above that of the thermal noise generated by the antennas at 49.5 MHz [*ITU-R*, 2016]. The LNAs are required to amplify the signal to be detectable by the receiver. Signals from the LNAs are transferred to the Ettus Research X300 transceivers, where the received radar signal is directly digitized using the BasicRX daughtercards as the front end on the transceiver. The phase delay along each receiver signal chain has been characterized and is corrected for in software, beyond the careful cable phase matching already performed. The phase delay measurements are discussed in Section 8.5.2.

The X300s communicate with the RF computer through a 10 Gbps switch, where the directly digitized radio signals are written to a hard disk drive (HDD). The ICEBEAR RX computers operate using Ubuntu Linux. The Control Computer monitors the site and GPS lock, while the RF Computer receives a stream of radio samples from the X300s and records the data on a HDD. The RF Computer uses the GNURadio software suite and the UHD driver to interface with the X300s. To record the data, the open source MIT Haystack Observatory DigitalRF software suite is used [*Rideout et al.*, 2018]. The DigitalRF software indexes the complex voltage data samples streamed from the X300s and saves the samples in files using the HDF5 format [*The HDF Group*, 1997-2018]. The HDF5 format is a platform independent method of storing and accessing data efficiently and effectively. DigitalRF corrects for dropped data samples and also records metadata for any given experiment. The code used to interface with the X300 transceivers at the receiver site is provided in Appendix G.

The X300 transceivers have a minimum sampling rate of 200 kHz in receiving mode, and this exceeds the current BW requirement of 100 kHz for a 3 km path length resolution. Each

of the 10 receiver signal chains have the raw complex voltage data individually recorded and saved on a HDD. The data rate resulting from this 10 receiver signal chain setup is 8 MBps, or $\approx$ 700 GB per day if run continuously. Although keeping the raw complex voltage samples has large data storage requirements, it allows for variable time scale integrations and different beamforming/interferometry techniques to be implemented on the data. The data storage requirements of 700 GB per day are somewhat excessive at the moment, but with the cost of data storage decreasing and the amount of data that can be stored on a single device increasing, it should be manageable to run ICEBEAR continuously in the future.

The current setup of the X300 receiver results in dropped samples at variable intervals when streaming to a computer. The duration of the dropped samples are typically seconds in length, and the times between dropped samples are on the order of hours. This issue has been determined to be likely due to CPU interrupts on the computer processor. A possible solution is to designate certain processors to only run the GNURadio interface with the X300s, thereby reducing the risk of the streaming received samples being interrupted. With the current implementation, when there are dropped samples, DigitalRF pads the end of that measurement with zeros (0s) to keep the samples aligned. The proposed solution to reduce, or potentially eliminate these dropped samples will be implemented in the future.

The receiver site can be accessed remotely through a connection to the University of Saskatchewan network. Once a connection is made the receiver can be started, and data will be stored on the HDD of the computer. An external HDD port is available to connect a HDD for transfer of the data to the University of Saskatchewan. As there is a large amount of data being stored, the current setup involves picking up the HDD from the receiver site and post-processing the data off site. This procedure may be modified in the future, where processing will be performed on site and only data with an SNR above a threshold value are recorded.

8.5.2 RX Phase Measurements

To determine the phase differences between each receiver signal path a network analyzer was used. The locations of where the phase was measured are shown in Figure 8.27. The M_1 measurement was a two port measurement on the network analyzer, and the M_2 measurement

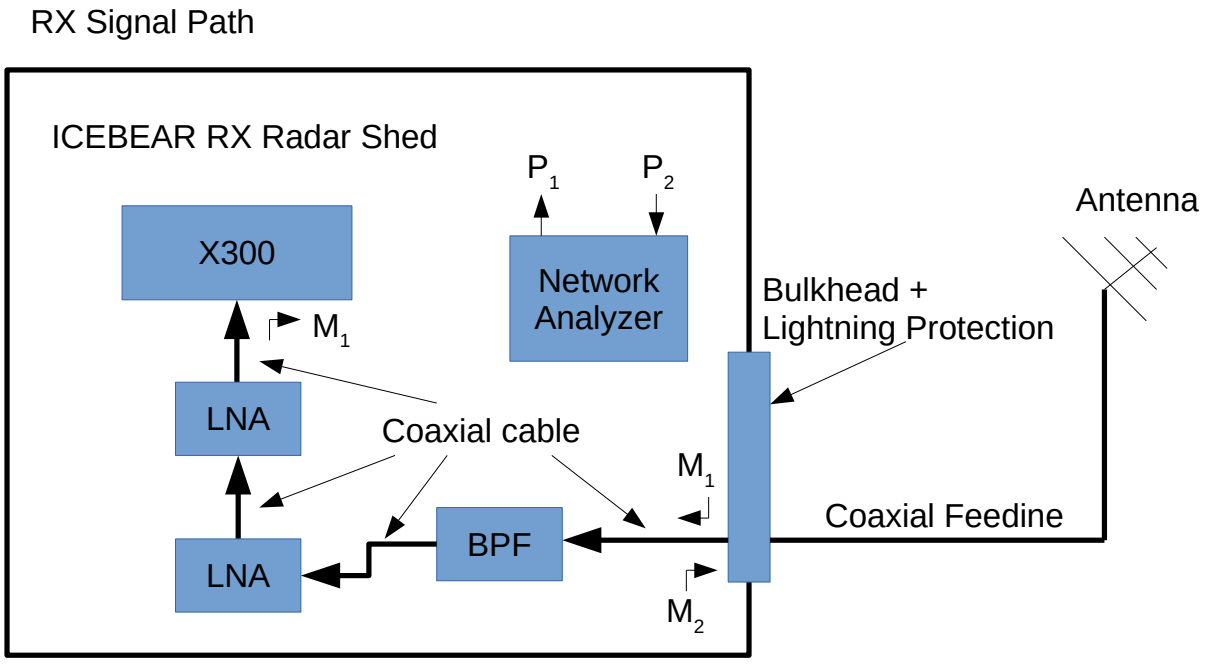

Figure 8.27: Receiver path phase measurement setup.

was a one port measurement. The M_2 measurement measures from the bulkhead to the antenna, and back to the bulkhead. The resulting M_2 phase difference between different receiver paths must be divided by two, as the measurement doubles the phase difference due to the feedline length. The M_1 measurement is used to determine the phase difference due to the cables, band pass filters, and LNAs inside the receiver shed. With the two LNAs in the receiver path providing 56 dB of gain, care must be taken when using the network analyzer to take the phase measurement. The generated signal from an analyzer must be attenuated so that the signal does not saturate the LNAs. Attempts were made to match the receiver paths in hardware using these phase measurements, with any post-hardware correction phase mismatches corrected for in software.

With the hardware and the corrections to the phase of each receiver path described, the processing of the RF signal can be discussed. This is done in the next section, where the hardware and software processing performed on the modulated received signal is described.

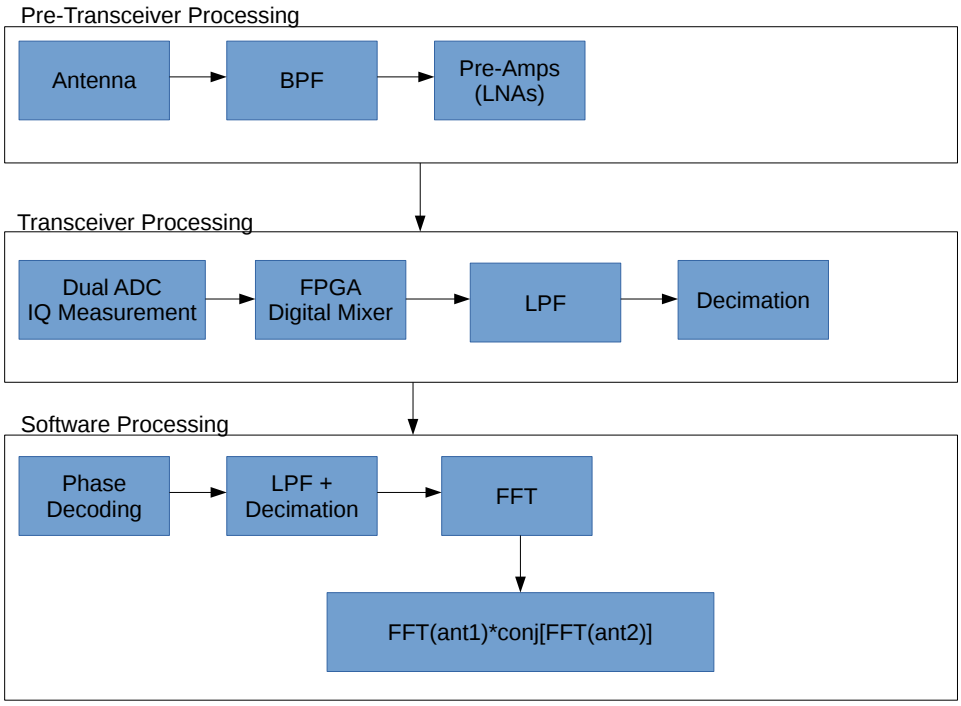

Figure 8.28: Block diagram of the processing of the radar signal, described in the text.

8.5.3 ICEBEAR Signal Processing

With the PRN coded CW phase modulation described in Section 8.3.4, the processing of the signal can now be discussed. A large amount of signal processing is required on the ICEBEAR raw complex voltage data to obtain scattered signal parameters, such as the power, spectral width and Doppler velocity. With optimized analysis code in C it was possible to achieve a processing time slightly faster than real time for two receiver signal chains (antennas) on a single Intel i7-7700K CPU core. Processing the full array in real time can be accomplished using multiple cores, and/or a graphics processing unit (GPU).

A block diagram of the hardware and software analysis processes are presented in Figure 8.28. The processing required to obtain the radar measurement spectral width, Doppler shift, and power may be divided into three steps: pre-transceiver processing, transceiver processing, and software processing.

Pre-Transceiver Processing

For pre-transceiver processing, the antenna acts as a band pass filter centered around 50 MHz, suppressing, but not eliminating, signals outside of the band. Once received at the antenna, the signal travels along 200 m of coaxial cable and is then filtered at the radar shed by a band pass filter (BPF), followed by two LNAs. Some general characteristics of antennas, amplifiers, and filters were discussed previously in Chapter 6. After the BPF and LNAs, the signal is digitized by an X300 transceiver.

Transceiver Processing

For transceiver processing, each X300 transceiver is able to measure the RF signal from two signal chains at an ADC sampling rate of 200 MHz per chain. A description of a generalized digital receiver was provided in Section 6.6. Each channel has a dual-ADC setup that provides the in-phase and quadrature (IQ) voltage samples of the respective RF signal chain at 200 MHz. The digitized signal is digitally mixed using the onboard FPGA in the X300 to baseband from the center frequency selected, which is 49.5 MHz for ICEBEAR. A digital low pass filter and decimation stage is also implemented in the FPGA, reducing the data rates required to stream and record the signal. In the case of ICEBEAR the data is decimated from a data rate of 200 MHz to a data rate of 200 kHz.

Software Processing

The software processing stage extracts the physical quantities from the complex voltage sample data, which have been mixed, filtered, decimated, and stored from the previous transceiver processing stage. This is accomplished by decoding the phase of the received samples by multiplying them with the complex conjugate of the transmitted PRN coded CW phase modulated waveform (which is repeated every 10,000 samples), decimating the decoded signal, then finally converting to the frequency domain by performing a fast-fourier transform (FFT) on the resulting samples, as described below. This is similar to the processing used for the ambiguity function generation (Section 5.5), but now the data set the code is multiplied with is actual data.

For $N + r$ raw complex voltage samples given by an array,

$$V[t] = [V[0], V[1], ..., V[r \ + \ N - 1]], \tag{8.1}$$

and the N sample complex code transmitted given by an array,

$$C[t] = [C[0], C[1], ..., C[N - 1]], \tag{8.2}$$

one can then express the decoded voltage as a function of effective range and time as,

$$V_f[r, t] = \begin{bmatrix} V[0]C^*[0] & V[1]C^*[1] & \dots & V[N-1]C^*[N-1] \\ V[1]C^*[0] & V[2]C^*[1] & \dots & V[N]C^*[N-1] \\ \vdots & \vdots & \vdots & \vdots \\ V[r]C^*[0] & V[r+1]C^*[1] & \dots & V[r+N-1]C^*[N-1] \end{bmatrix}, \tag{8.3}$$

where t is the samples in time, r is the largest range and V_f is the decoded voltage as a function of range and sample (time) number. ICEBEAR operates with a PRN code of length $N = 10000$.

Once the phase is decoded, each range has a voltage time series that is unique to that range. For ICEBEAR, after filtering, the samples are decimated from 200 kHz to 1 kHz, as this typically covers the range of Doppler frequencies expected and significantly reduces the FFT computation time. This provides a $\pm$ 500 Hz Doppler range, corresponding to an $\approx \pm$ 1.5 km/s velocity range for the E-region ionospheric scatter. An FFT is calculated at each range, which produces a range-Doppler-intensity (RDI) spectrum for a given time for one antenna. The FFT also contains the phase information of each range-Doppler bin. The phase data are used for interferometry with 2 or more antenna signal chains. For a 100 ms scan, the Doppler resolution is 10 Hz, while the processed RF propagation distance (total path length) resolution is determined by the receiver sampling rate, given by the equation:

$$\Delta r = \frac{c}{f_s}, \tag{8.4}$$

where Δr is the RF propagation distance resolution, c is the speed of light, and f_s is the sampling rate (200 kHz). This provides a $\Delta r = 1.5$ km. Note that the path length resolution of the radar is based on the baud length of the waveform transmitted, not the receiver

sampling rate. If a radar signal is oversampled, it will appear to have a higher range resolution than is possible from the transmitted waveform.

A cross-correlation is performed between the range-Doppler bins of one antenna and the corresponding complex conjugate of the range-Doppler bins from another antenna. For 2 antenna signal chains, 1 and 2, this is given as,

$$S_{1-2}[r, f] = S_{ant1}[r, f] * S^*_{ant2}[r, f], \tag{8.5}$$

where S_{1-2} is the cross-spectrum between antenna 1 and 2, $S_{ant1}(r, f)$ is the range-Doppler spectrum of antenna 1, and $S^*_{ant2}(r, f)$ is the complex conjugate range-Doppler spectrum of antenna 2. From the cross-spectrum it is possible to determine the phase difference of a signal between two antennas at a given frequency.

Consecutive cross-spectra were incoherently averaged over time to suppress the variance of the noise in the measurements. Incoherent averaging was described in Section 5.5. At this time the analysis involves 50 ICEBEAR scans of 100 ms each that are averaged to provide a time resolution of 5 s. The data can be re-processed using fewer (or more) cross-spectra in the averaging to study the evolution and decay of plasma irregularities in higher (lower) temporal resolution, but this is for future analysis. The analysis presented here provides a total path length resolution of 1.5 km, with the signal being sampled at 200 kHz, though the effective path length resolution is 3 km due to the transmitter waveform used. It should also be highlighted that meteor trails have been detected regularly with no averaging in a single 100 ms observation, showing that usable measurements are possible with $\ll$ 5 s temporal resolution.

Along with the range and temporal information provided by ICEBEAR, it is also possible to obtain azimuthal interferometry information through the use of the multiple antennas in the receiving array (Section 6.5.6). This is accomplished by using the phase difference between the antennas of the received signal to obtain an angle of arrival, which was expressed in Equation 6.5. Calculating the angle of arrival using this method assumes that the received signal was a plane wave. The antennas are spaced at 1-λ intervals, so phase "wrapping" must be considered when determining the angle of arrival. This phase wrapping occurs at angles of arrival outside of $\pm$ 30 degrees from the boresight of the array. Such situations will

result in measurements appearing in the FOV, though originating from outside of it. For the geometry in this experiment, the location of scatter would have to be at large aspect angles for this to be a significant issue. Scatter at these large aspect angles are not expected due to the previous ionospheric scatter work referenced in Section 3.4 and Chapter 7. The determination of the azimuthal angle of arrival, along with the range, of the scatter for each Doppler bin makes it possible to map the scatter source locations, providing details of the ionospheric plasma dynamics over a large FOV. An example of one of these maps can be found in Chapter 9, where the derivation for the determination of the latitude and longitude of the scatter can be found in Appendix E.

8.6 ICEBEAR Hardware Summary

In summary, the ICEBEAR radar uses modern radar hardware and signal processing techniques to obtain unaliased high spatiotemporal resolution (3 km, < 5 s) measurements of the E-region of the ionosphere in the northern auroral zone of the Earth. This chapter described the selection and setup of the ICEBEAR transmitter site, the different hardware components of the system, and an overview of the signal processing required to obtain useful measurements. As discussed, the receiver and transmitter sites have similar setups, including 10 antenna linear arrays, the same transceivers (Ettus Research X300s), the array and site synchronization methods (Fury GPSDO and Octoclock), and the overall architecture of the network setup (separate 10 Gbps and 1 Gbps local networks). Some differences between the sites include the types of amplifiers used, the types of antennas used, and the transmitting and receiving sampling rates. The amplifiers designed for the transmitter portion of ICEBEAR were a large portion of the design, which was spearheaded by myself. Much of the documentation of the amplifier design was not provided here due to industry interests, though it consists of ≈ 100 pages of construction and testing documentation, as well as PCB and mechanical schematics and parts lists. The results obtained from the code processing described in Section 8.5.3 are provided in Chapter 9.

Chapter 9

ICEBEAR Results

Portions of Sections 9.1, and 9.2, as well as Figures 9.1, 9.2, and 9.4, and Table 9.1 were originally published in Huyghebaert, D., G. Hussey, J. Vierinen, K. McWilliams, and J.-P. St-Maurice (2019), ICEBEAR: An all-digital bistatic coded continuous-wave radar for studies of the E region of the ionosphere, *Radio Science*, *54*(4), 349–364, doi: 10.1029/2018RS006747.

The ICEBEAR system has provided high spatiotemporal resolution measurements of the E-region for multiple days of high ionospheric activity. These measurements provide glimpses into the creation and propagation of different ionospheric E-region plasma density instabilities and irregularities. The previous chapters have provided an overview of the knowledge pertaining to the ionosphere, E-region plasma density instabilities, radio wave propagation in a plasma medium, radar physics, the basics of radar electronics engineering, and the design and construction of the ICEBEAR radar. This chapter is the culmination of these efforts, with some initial preliminary ICEBEAR observations presented.

9.1 The ICEBEAR Experiment

The ICEBEAR radar first started operating in December, 2017, and has been operating on a campaign basis as its capabilities and initial observations are interpreted. The experiment details of these first operations are provided in Table 9.1. ICEBEAR has typically been operated when the Kp-index is predicted to exceed 4, an indicator of likely magnetospheric activity [*Thomsen*, 2004]. As data management and data analysis are more fully developed,

---

Portions of Sections 9.1, and 9.2, as well as Figures 9.1, 9.2, and 9.4, and Table 9.1 were originally published in *Huyghebaert et al.* [2019].

Table 9.1: Specifications for initial ICEBEAR operations

Specification @ 49.5 MHz	**Value**
RX Location	$52.24319°, -106.450191°$
RX Pointing dir	7° East of North
TX Location	$50.893467°, -109.403151°$
TX Pointing dir	16° East of North
Transmitter Peak Power	300 W
Antenna Spacing	$\approx$ 1 λ (6 m)
Modulation type	Binary PSK
TX Symbol Length	10 μs
TX Path Length Resolution	3.0 km
RX Sampling Rate	200 kHz
CW Modulation Code Length	10,000 samples
Range Aliasing	30,000 km
Frequency Aliasing	$\pm$ 100 kHz
Sample Size	32-bit IQ
Data Rate (10 RX)	8 MBps

ICEBEAR will be operated more often, with the goal of continuous operation for collaborative research.

The first operations of the ICEBEAR system used 4 transmitters operating at 300 W at a center frequency of 49.5 MHz. Each of the transmitters transmitted the same pseudo-random code, with no phase shift applied to the array. This resulted in 150 W, after attenuation from the coaxial cable, radiated from each of the 4 antennas. As each transmitter antenna has a gain of $\approx$ 10 dB, this provides a 1.5 kW effective radiated signal power (ERP) at each antenna. For the full ten antenna array, the radiation pattern is shown in Section 8.3.1. Using only 4 antennas broadens the beamwidth of the radiation pattern compared to the 10 antenna array, shown previously in Figure 8.14. The value of 1.5 kW ERP per antenna assumes the antennas are 100% efficient and a SWR of 1.0, which is rarely the case. The actual measured SWR is $\approx$ 1.25 for each antenna at 49.5 MHz. The antenna array gain

factor has also not been included in this ERP calculation, but would increase the ERP of the transmission and narrow the beam. At this output power there have been no issues obtaining ICEBEAR observations of E-region plasma irregularities.

As mentioned in Section 8.3.4, a PRN binary phase code was transmitted using phase modulation, also known as phase shift keying (PSK) in communications theory, with a symbol duration (length) of 10 μs and a code length of 10,000 symbols. This resulted in a time of 100 ms for the complete code length, corresponding to the 100 ms temporal resolution for each processed scan. The 10 μs symbols were sub-sampled at 1.25 μs on the transmitter signal to allow for amplitude modulation of the signal to reduce sidebands (Section 8.4.3). This was required to keep the signal within the 160 kHz BW allowed by the Radio License.

The bistatic nature of the ICEBEAR configuration makes operations and analysis more complicated than a monostatic system in some regards. The range is not simply proportional to the time delay divided by 2, but is instead dependent on where the scatter occurs within the FOV, with two propagation paths of typically unequal length from the transmitter to the scattering location and from the scattering location to the receiver. Also, depending on where the scatter occurs within the FOV, the wavelength of the plasma density irregularities from which the radar signal scatters from will vary slightly. This effect was described for the SAPPHIRE radar [*Koehler et al.*, 1995] and the SESCAT radar [*Haldoupis and Schlegel*, 1993], including references therein. The wavelength of the plasma density irregularities that the radio signal scatters from was given in Section 4.3, where the effect is given by,

$$k_{ir} = 2k_r \cos(\theta/2), \tag{9.1}$$

where $k_{ir} = 2\pi/\lambda_{ir}$ is the wave vector of the irregularities, $k_r = 2\pi/\lambda_r$ is the wave vector of the radar signal, and θ is the angle between the rays from the transmitter to the scattering volume and the scattering volume to the receiver.

For the ICEBEAR configuration, the bisector between the propagation paths from the transmitter to the scattering location and from the receiver to the scattering location varies, with the bisector angle near 0° on the eastward side of the FOV and $\approx$ 15° on the westward side of the FOV. This corresponds to ionospheric irregularity wavelengths between 3.03 m and 3.14 m for the 49.5 MHz signal. The direction of the Doppler velocity will also slightly

vary with different scattering locations, with the velocity vector pointing toward the bisector of the receiver and transmitter sites. At present, these wavelength and bisector variances are not taken into account, as they are small.

With the experiment setup described, the results from the ICEBEAR system will be presented in the next section.

9.2 ICEBEAR Measurements

From the cross-spectra determined through the signal processing described in Chapter 7, the Doppler frequency, power, spectral width, range, and angle of arrival (interferometry) of ionospheric radar scatter are available. During the day very little ionospheric scatter was detected, as is expected, other than meteor echoes. Ionospheric scatter is typically detected between local dusk and dawn, peaking around local magnetic midnight. March 10, 2018, was one date in particular that provided ionospheric scatter for over 9 hours, with all 4 types of E-region radar echoes observed.

An example from this active day of a range-Doppler-intensity (RDI) plot is shown in Figure 9.1. Figure 9.2 shows the corresponding phase difference determined through interferometry (Sections 6.5.6 and 8.5.3). Data from all 10 receiver antennas was processed to generate the figures mentioned in this section. Only data with a SNR greater than 1.0 (0.0 dB) were plotted, where the noise value was taken as the median value of the RDI spectrum, and each plot was a 50-scan average (5 s). All four types of E-region radar echoes were observed simultaneously in Figure 9.1, but there is clearly more structure beyond the 4 types. The different types of E-region radar echoes were discussed in Section 3.4.1.

From the interferometry data presented in Figure 9.2, the Type II echo (wide spectral width centered at $\approx$ 20 Hz (60 m/s)) appears to be from the middle of the FOV and the Type I-like echo (strong echo at $\approx$ 150 Hz (450 ms)) is more to the East. Echoes from closer ranges have a Doppler shift closer to 0 Hz, while further range echoes tend to be moving towards the radar at greater velocities. A short-lived Type IV echo can be observed at a Doppler shift of $\approx$ 350 Hz, corresponding to a velocity of $\approx$ 1050 m/s. There is also a Type III echo located at one of the further scatter ranges with a Doppler shift of $\approx$ 90 Hz (270 m/s).

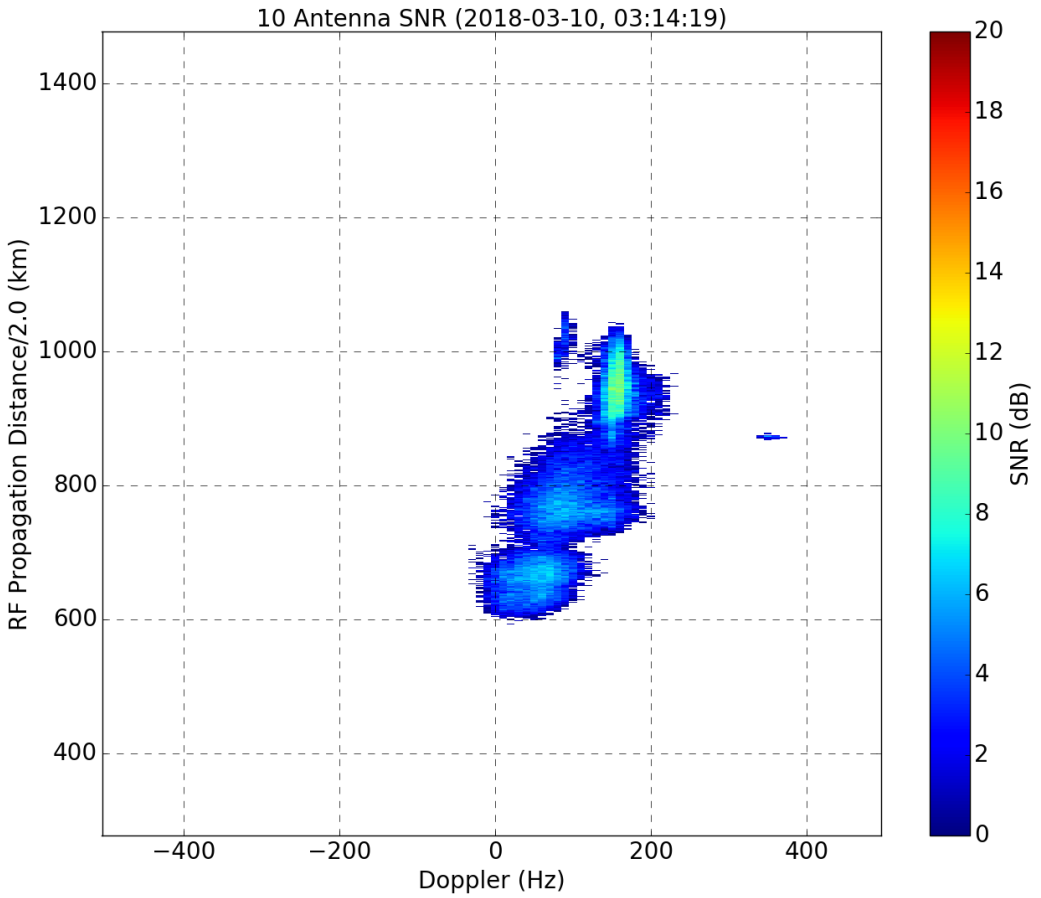

Figure 9.1: This plot shows all 4 types of echoes in the same 5 s measurement. The SNR is in dB, with the bottom axis being the Doppler shift in frequency and the left axis the RF propagation distance divided by two. The measurement was taken on 10 March, 2018, from 3:14:15 UTC – 3:14:20 UTC. This corresponds to a local time of 9:14pm.

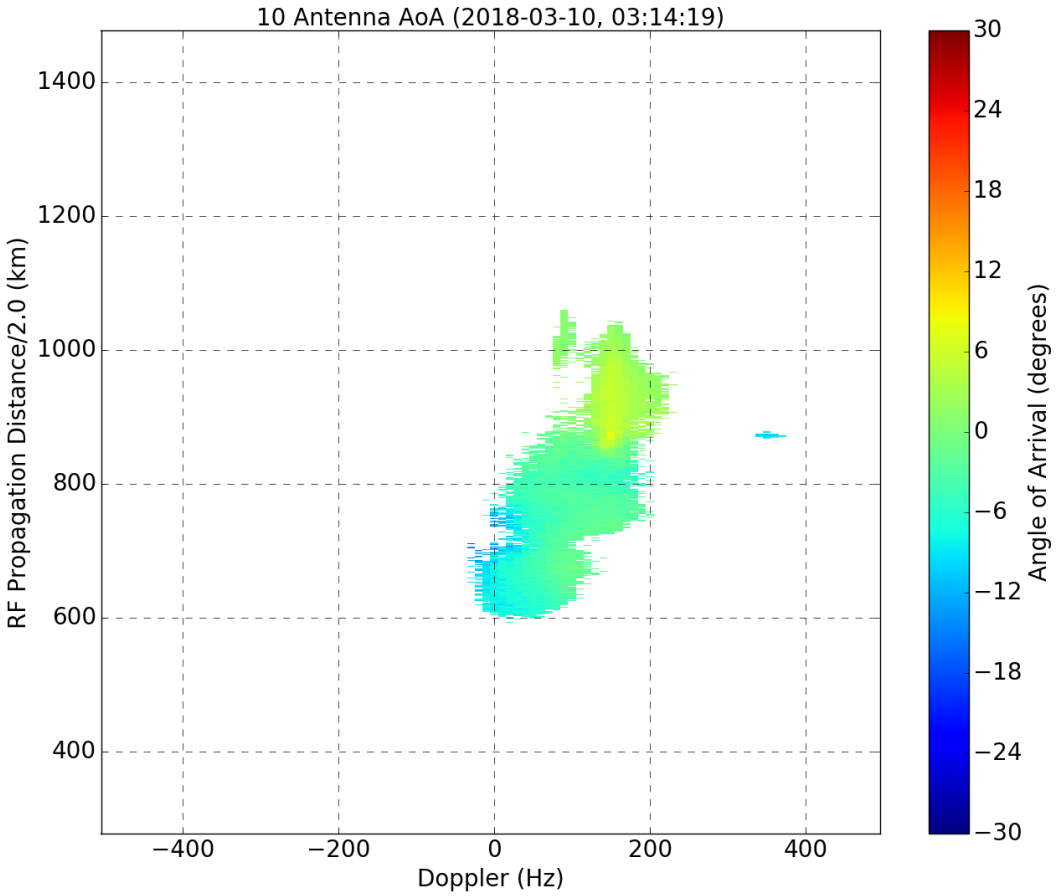

Figure 9.2: This plot shows the angle of arrival off boresight calculated using 10 antennas corresponding to data in Figure 9.1. The axes are the same as the SNR plot. Negative angle of arrival values are for scatter coming from the West, while positive ones are for scatter from the East.

By observing multiple 5 s averaged measurements in a sequence, one can examine the evolution of these ionospheric plasma density irregularities. A panel of six 5 s averaged plots are shown in Figure 9.3, where the 30 s time spans from 03:14:00–03:14:30 UTC, which corresponds to 21:14:00–21:14:30 local time (LT). A structure with a SNR of $\approx$ 12 dB, located at $\approx$ 750 km, and moving with a Doppler shift of $\approx$ 150 Hz (450 m/s), is observed to "disappear" in the 30 s sequence. The Type IV echo in the figure exists for $\approx$ 1 minute, but does vary in Doppler and range during this time. It is evident from these plots that the ionospheric plasma is very dynamic, even on the short time scales that ICEBEAR is able to measure.

Presenting the interferometry and Doppler velocity data together on a geographic map of the ICEBEAR FOV allows for the format presented in Figure 9.4. In this image the horizontal and vertical axes represent the longitude and latitude, respectively, the greyscale contour map represents the aspect angle at 100 km altitude (refraction was not considered), the magenta contour lines represent the total RF propagation distance divided by two (RF Propagation/2.0), and the black contour lines represent the magnetic inclination. The green lines indicate the edges of the transmitter and receiver FOVs, and the color scale to the right represents the Doppler velocity of the scatter. The size of the velocity points are not scaled properly to azimuth, although they are scaled approximately correctly in range. The ionospheric scatter is very structured, with the Doppler properties of the scatter varying in both range and azimuth. Most of the scatter presents as a continuous distribution, except for the Type IV ionospheric scatter region which is clearly separated from the rest of the scatter. The Type IV echoes are located to the West of the main ionospheric scatter, at $\approx$ $59°N$, $107°W$, separated by a region of no scatter.

Similar to what was done in Figure 9.3, the map plots can be plotted sequentially. An example of this is shown in Figure 9.5, where the maps correspond to the same times as those shown in Figure 9.3. With the current ICEBEAR system implementation it is therefore possible to observe how the plasma density irregularities evolve in 2-D space and time. Wave-like signatures have been observed in the coherent scatter data when plotted sequentially. Movies have also been created (not included here), displaying the evolution of these auroral structures over hours of time.

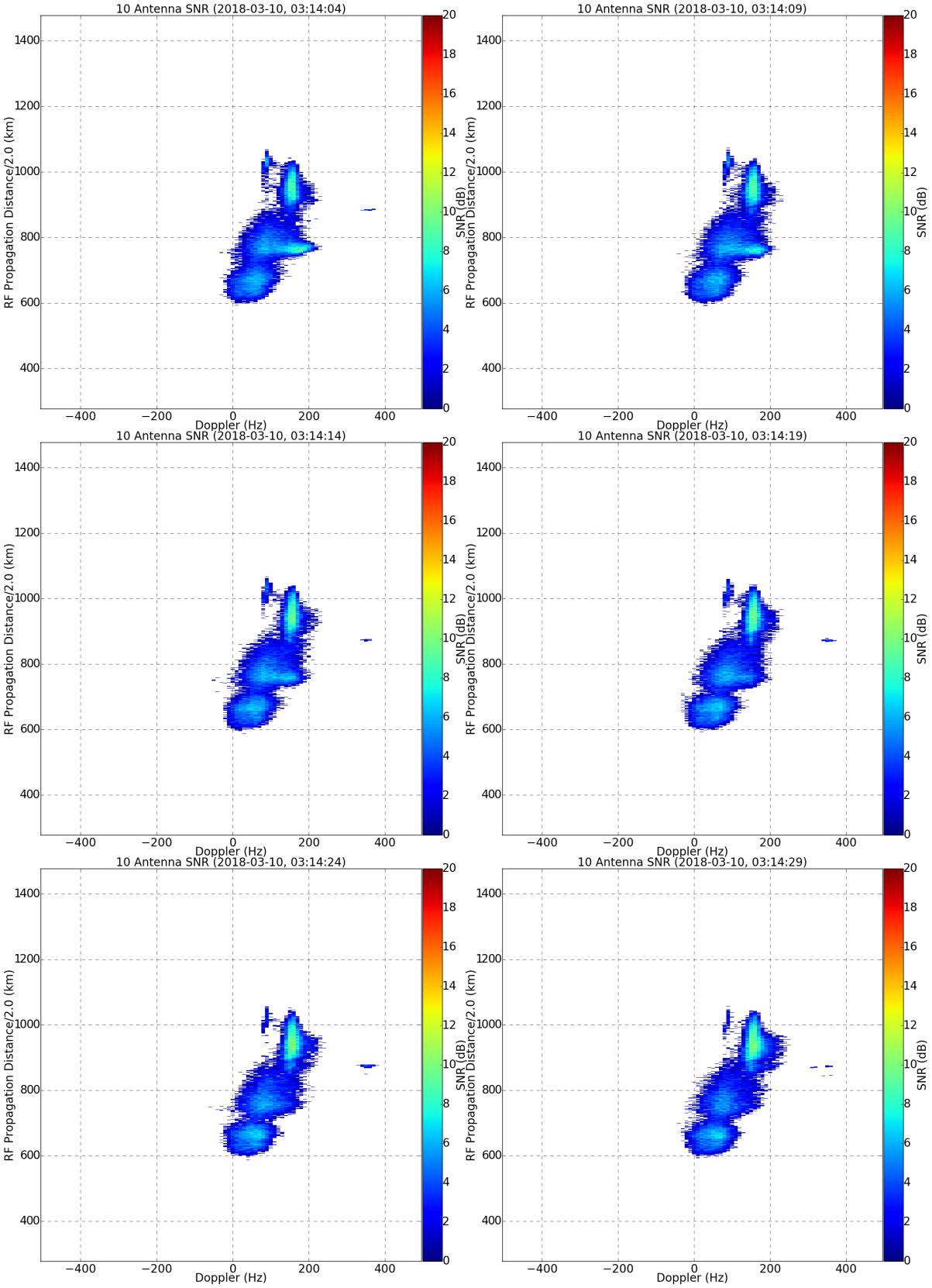

Figure 9.3: Sequential ICEBEAR SNR plots with 5 s averaging.

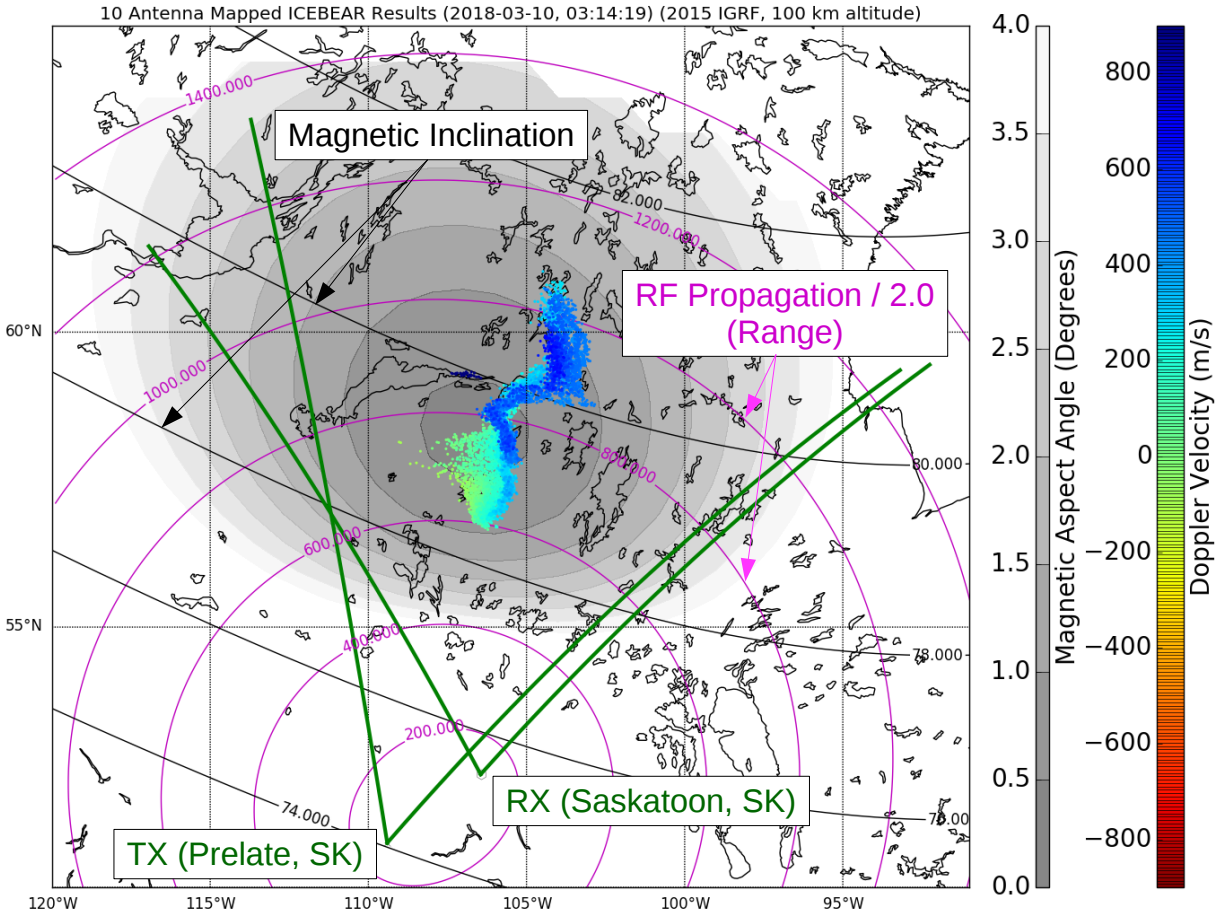

Figure 9.4: Plot of the ionospheric scatter mapped to geographic coordinates, which is described in the text. This plot corresponds to the same time as Figures 9.1 and 9.2. The Type IV echo is located at $\approx$ $59°N$, $107°W$, immediately to the east of Lake Athabasca.

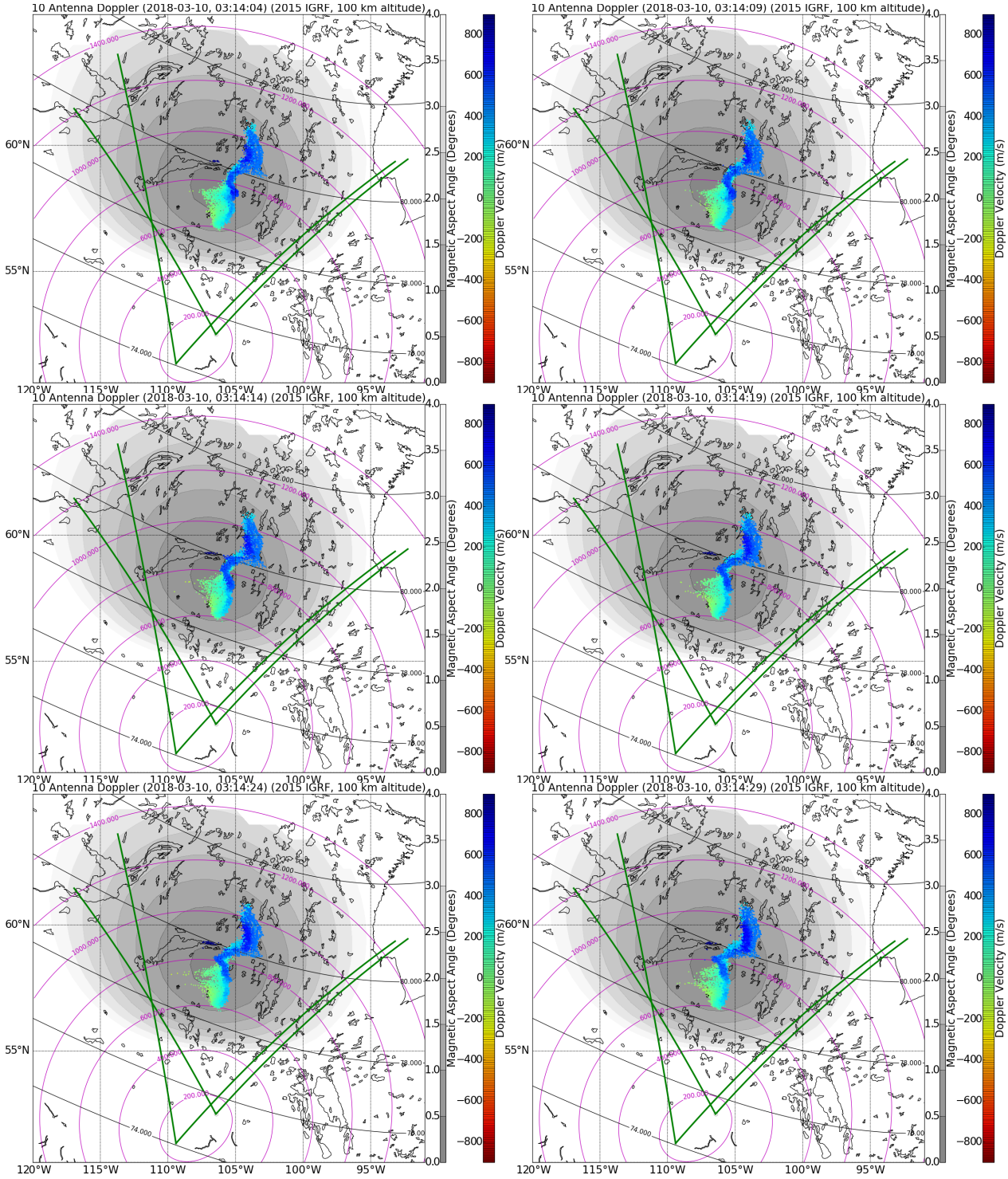

Figure 9.5: Sequential ICEBEAR maps with 5 s averaging.

This same data can be plotted through beamforming, as mentioned in Section 6.5.6. Data from measurements taken at 2:30:00-2:30:05 UTC (20:30:00-20:30:05 LT) have been beamformed using beamforming techniques (multiplying each antenna by a incremental/decremental phase), as opposed to the interferometry techniques, and plotted. One of the benefits of storing the raw voltage samples from each ICEBEAR receiver antenna is that the ICEBEAR measurements can be re-processed using different angle of arrival determination techniques. The calculated spectra for each beam are shown as multiple panels in Figures 9.6, 9.7, and 9.8. Beam 1 corresponds to the westward side of the FOV (17° West of North), and there is a 3° separation between each beam. Beam 9 is the boresight of the array, which is 7° East of North. From the plots in each of the panels, it can be observed that there are differences in the spectra from different angles of arrival. The coherent scatter in beams 3–14 is moving towards the radar while the coherent scatter in the most westward beams (beams 1 and 2) is moving at slow speeds away from the radar. Beamforming can be useful if multiple objects are moving at the same speed at the same range in the FOV. Using interferometry, the analysis of the scattered signal is combined into a single range-Doppler bin, resulting in a potential loss of information with the benefit of finer azimuthal angle of arrival resolution. For more information on these angle of arrival determination methods, refer back to Section 6.5.6.

The beamformed data plotted to a map is shown in the top panel of Figure 9.9, where the Doppler speed for the peak SNR of each range was plotted. The coherent scatter is spread over the FOV, but it must be remembered that using classic beamforming only provides an isolation between beams of $\approx$ 15 dB (Figure 8.14). Neighboring beams have an isolation less than this value, which must be considered when interpreting the results. The same data has been plotted on a map using interferometry techniques, shown in the bottom panel of Figure 9.9. Comparing the maps, the coherent scatter using the interferometry technique appears to be much more localized than the coherent scatter plotted using the classical beamforming technique.

With interferometry, the strongest scatter for a given range and Doppler shift will bias the angle of arrival measurements to that location. This is great for isolated scatter, such as what has been observed for Type IV and meteor radar echoes.

A meteor detection is plotted in Figure 9.10. The localized measurement occurred over

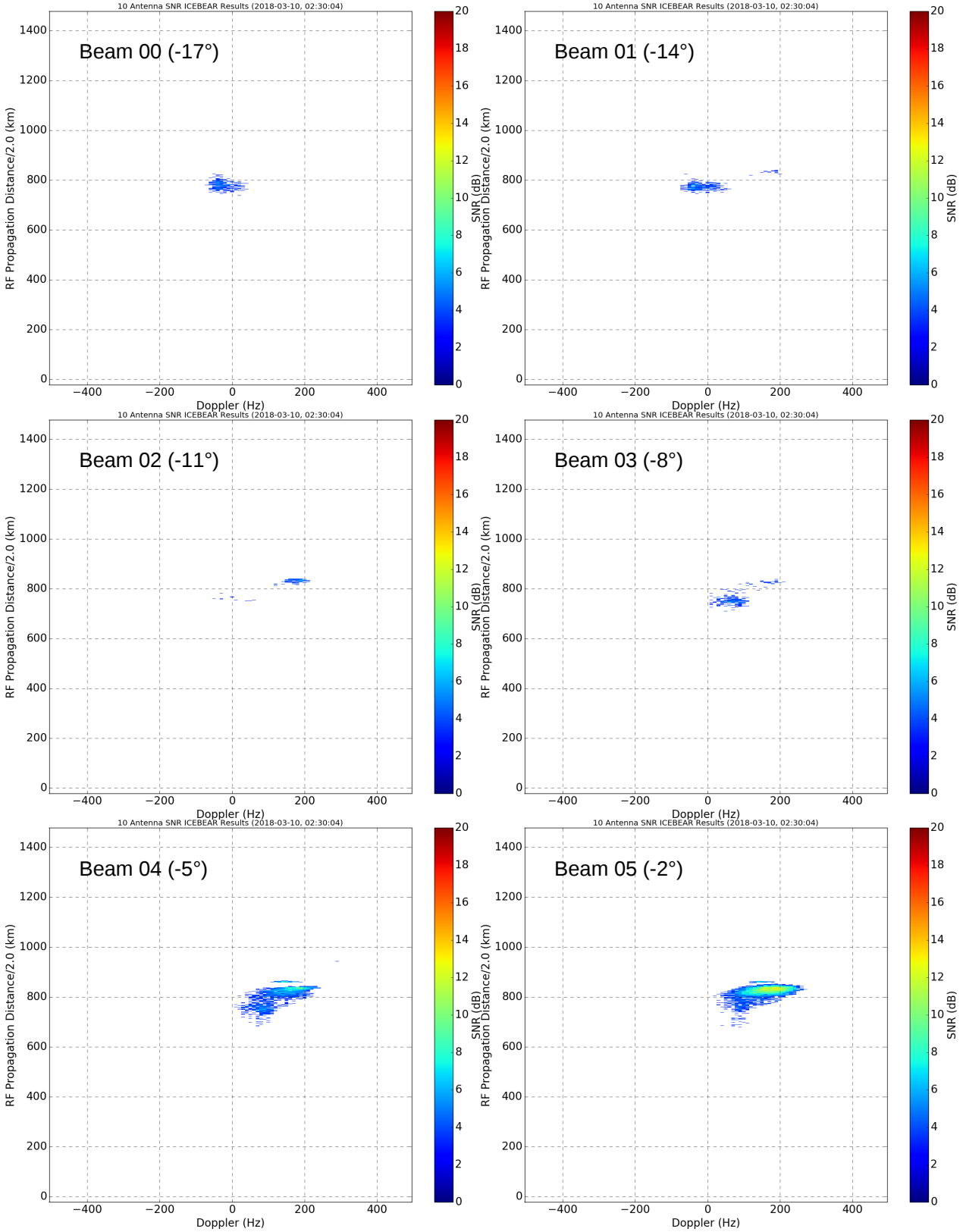

Figure 9.6: The different spectra for each ICEBEAR beam determined using classical beamforming techniques, with the heading displayed being degrees East of North.

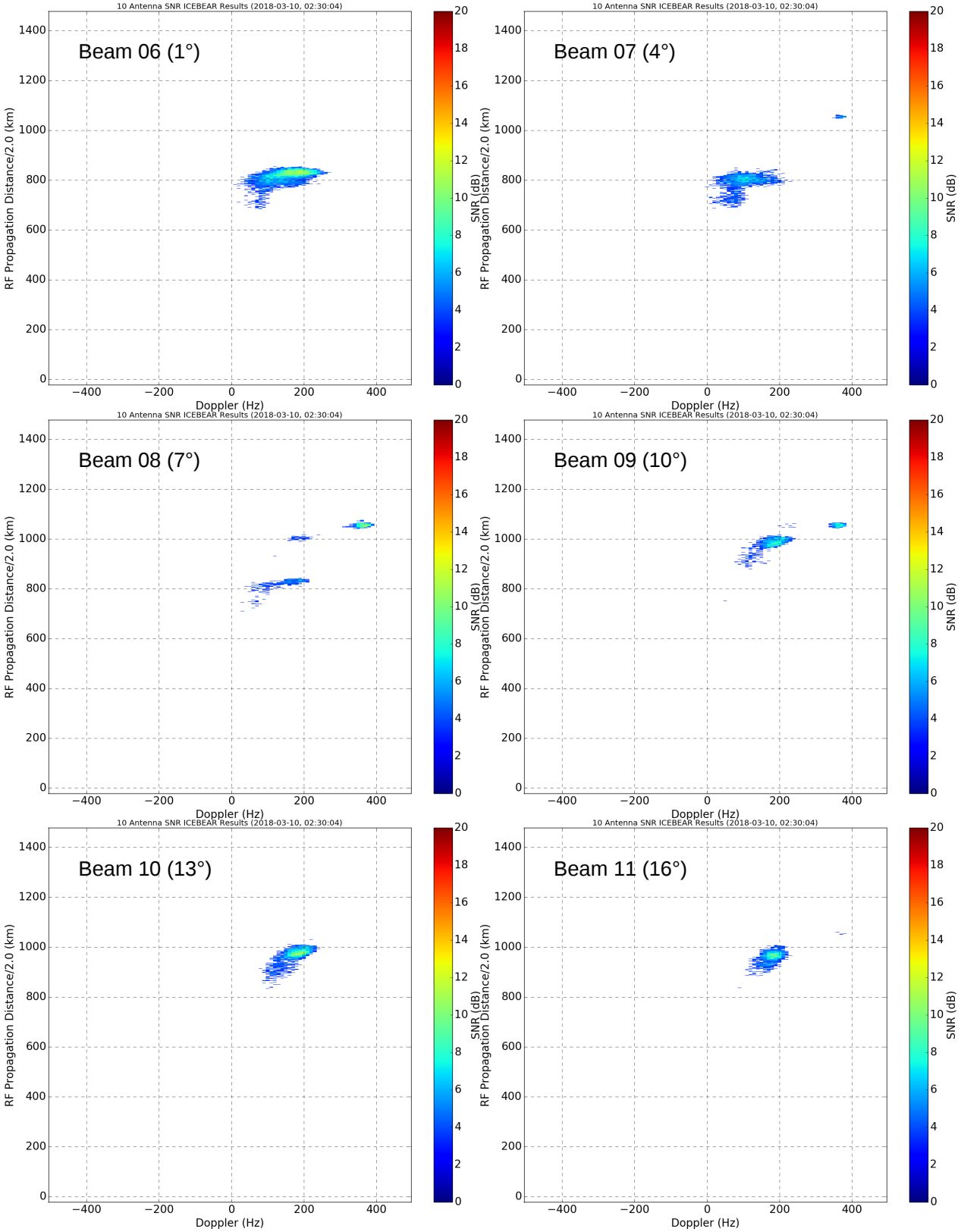

Figure 9.7: The different spectra for each ICEBEAR beam determined using classical beamforming techniques, with the heading displayed being degrees East of North.

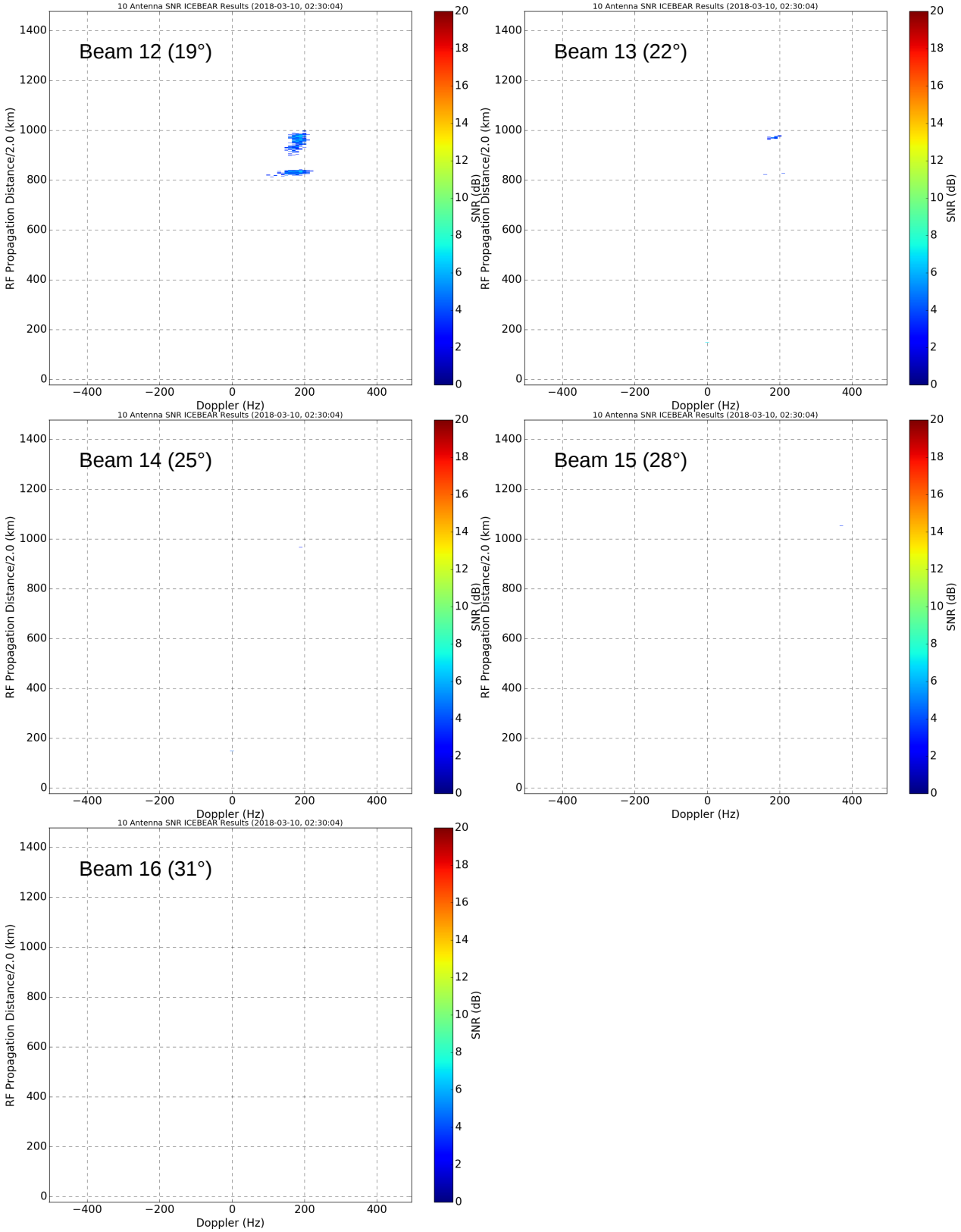

Figure 9.8: The different spectra for each ICEBEAR beam determined using classical beamforming techniques, with the heading displayed being degrees East of North.

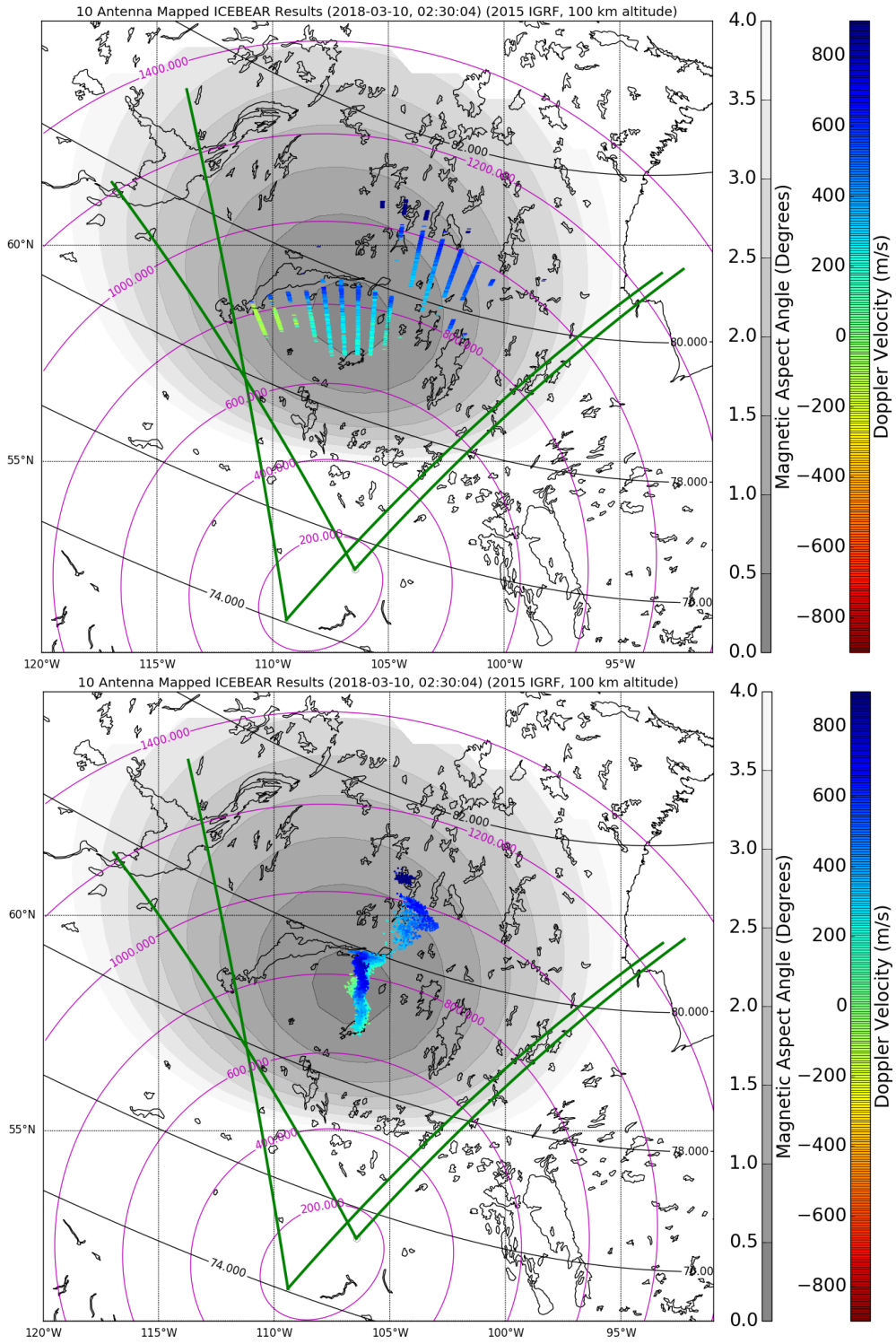

Figure 9.9: The classical beamformed ICEBEAR data plotted on a map in the top panel, similar to that shown in Figure 9.4. The bottom panel is the same data, with interferometry analysis performed to determine the angle of arrival of the coherent scatter.

a few range gates around 600 km, and over Doppler bins of -10 Hz and -20 Hz. This measurement was for a 100 ms scan. Meteor detections are common with ICEBEAR, but are typically averaged out when analyzing the data for ionospheric scatter. Meteor analysis software will be developed in the future to further analyze the meteor detections measured by ICEBEAR.

Referring back to Figure 9.9, using interferometry it is possible to determine the location of the Type IV echoes in greater detail when comparing the two techniques. With that said, the interferometry technique does miss much of the "spread" of the coherent scatter echoes over the FOV seen using the classical beamforming technique. There are more advanced beamforming techniques that have been developed to increase the isolation between each of the radar beams, further refining the azimuthal resolution using beamforming. These advanced techniques will be explored in the future to investigate their use with ICEBEAR, where the ability to use different spatial determination methods on the same data set is an important capability of the ICEBEAR system.

With the high spatiotemporal resolution of ICEBEAR it is also possible to detect wavelike structures in the ionospheric coherent scatter. An example of one of these structures is shown in Figure 9.11. The coherent scatter is observed to have a structure with a spatial periodicity on the order of 10s of km, which is detectable with the resolution of ICEBEAR being 3 km or better. It is not shown here, but the evolution of this structure can be examined through the high temporal resolution of ICEBEAR, where the structure propagates from further ranges until it reaches the point shown in the figure. This shows that waves are evident in the ICEBEAR data, and that analysis of these fluctuating plasma density structures is possible using the radar.

A gaussian fit to the ICEBEAR spectra determined through interferometry was performed, which provided the spectral width and the Doppler shift for a given range. From these parameters, 2-D histograms were created, showing the occurrence of different spectra in the ICEBEAR coherent scatter data. One hour of data from March 10, 2018 from 2:30–3:30 UTC is provided in Figure 9.12. The previously defined Type IV spectra can be observed to have a separate distribution from the majority of the scatter at a velocity of $\approx$ 1000 m/s. The main distribution in the figure contains the Type I, Type II, and Type III spectra with

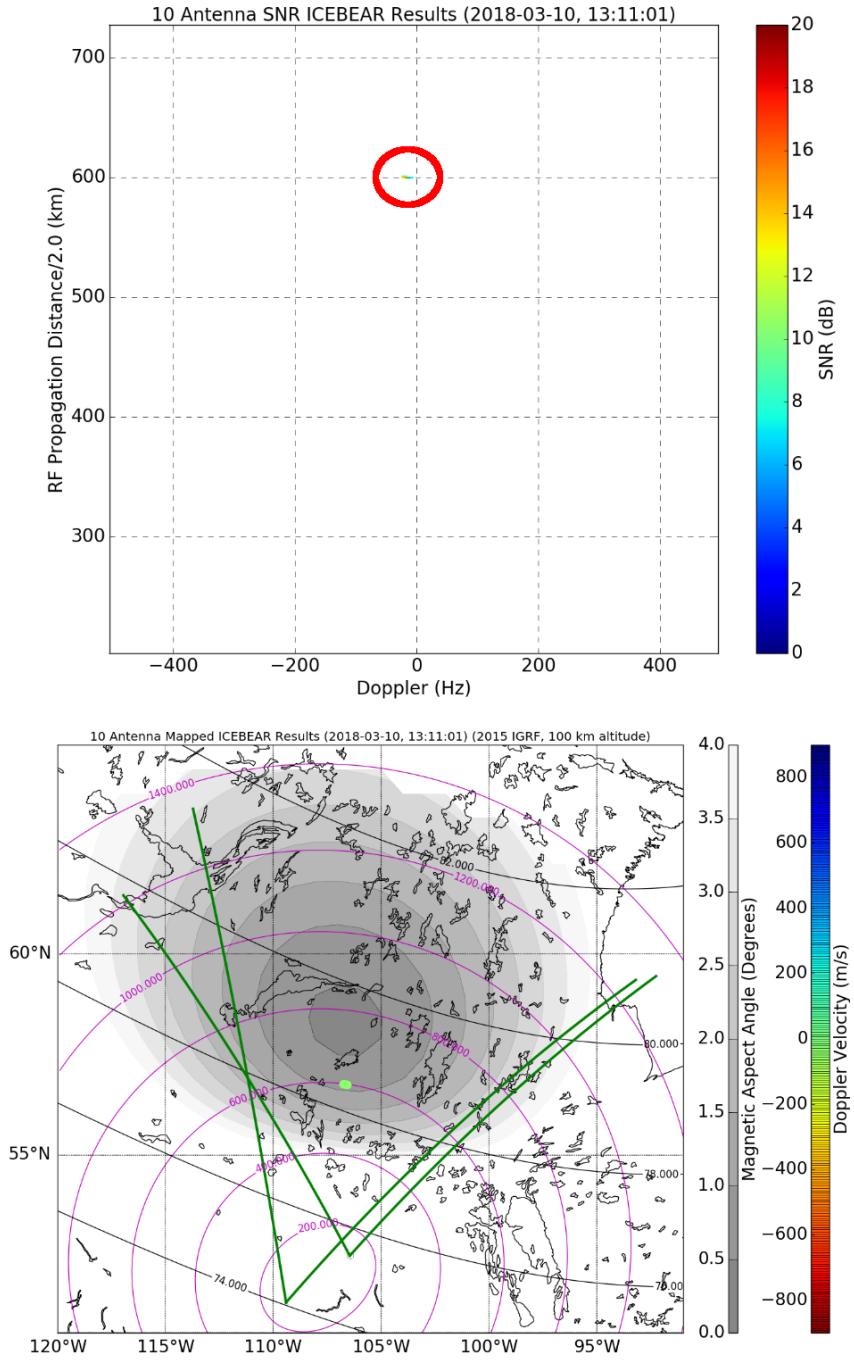

Figure 9.10: This is an example of meteor scatter measured by ICEBEAR. The top panel is the SNR for a 100 ms scan from ten antennas, where only scatter above 6 dB SNR were plotted. The red ellipse displays where the meteor echo is located in the SNR plot. The bottom panel is a plot of this meteor scatter on a map. The meteor detection occurred over two range gates, with the size of the points on the map expanded to be noticeable.

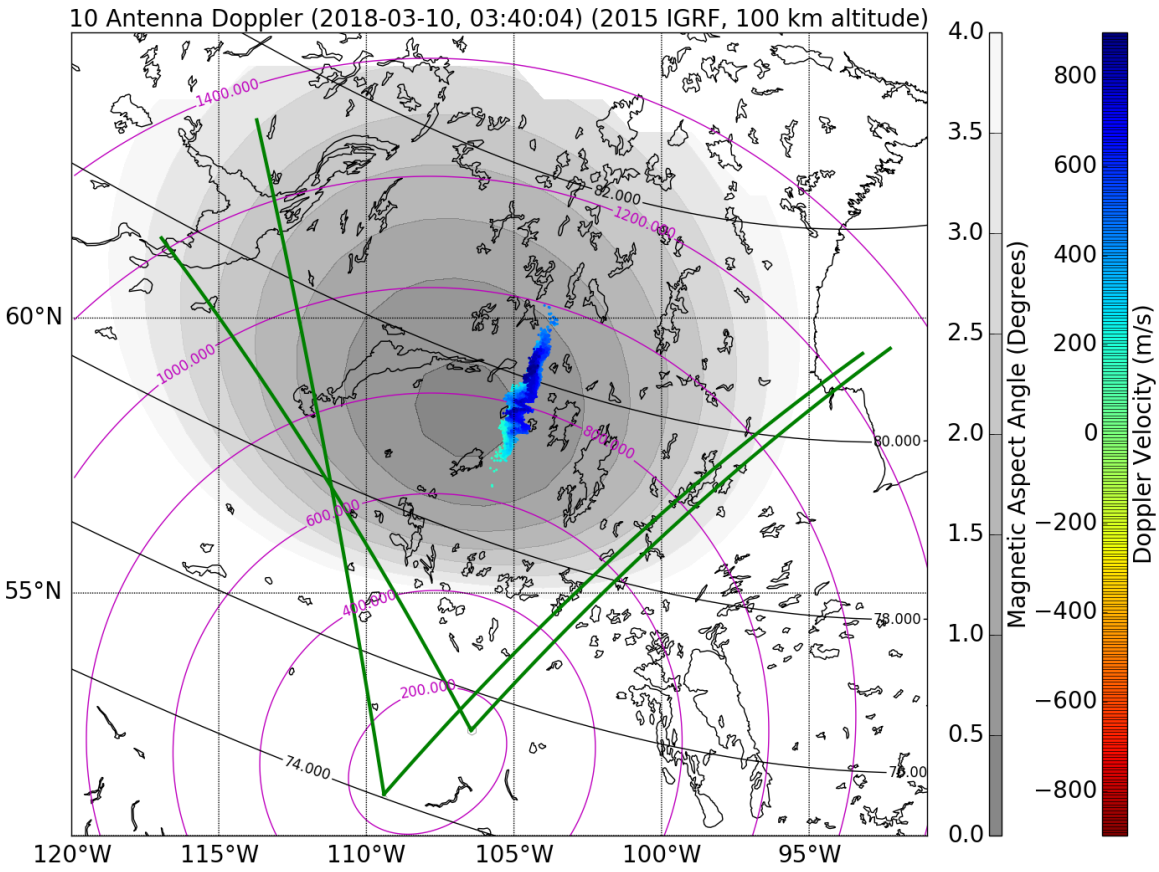

Figure 9.11: Example of a wavelike structure in the ICEBEAR coherent scatter measurements. More analysis is required to further investigate these structures, but it is evident that ICEBEAR can detect them on km scales.

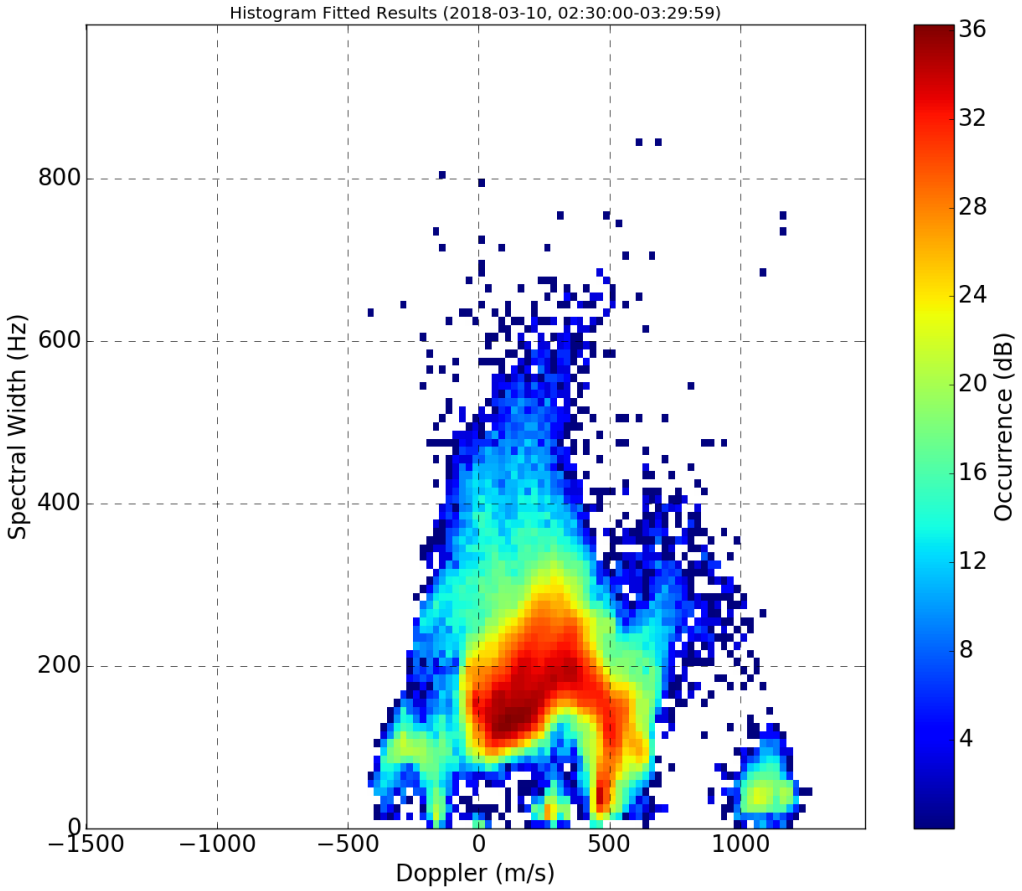

Figure 9.12: Histogram of the different spectra measured using the ICEBEAR system on March 10, 2018, from 02:30–03:30 UTC.

much more complexity in the distributions than previously described. This is an example of the future statistics that can be performed using the ICEBEAR system. Interpretation of this data is left to the reader and for future research.

9.3 Multi-Instrument Measurements

One of the reasons for the ICEBEAR radar being situated where it is, is the potential for multi-instrument studies. Some preliminary examples of multi-instrument studies are provided here. These multi-instrument studies include a brief discussion of ICEBEAR measurements with the SuperDARN Saskatoon radar [*Greenwald et al.*, 1995], and the e-POP

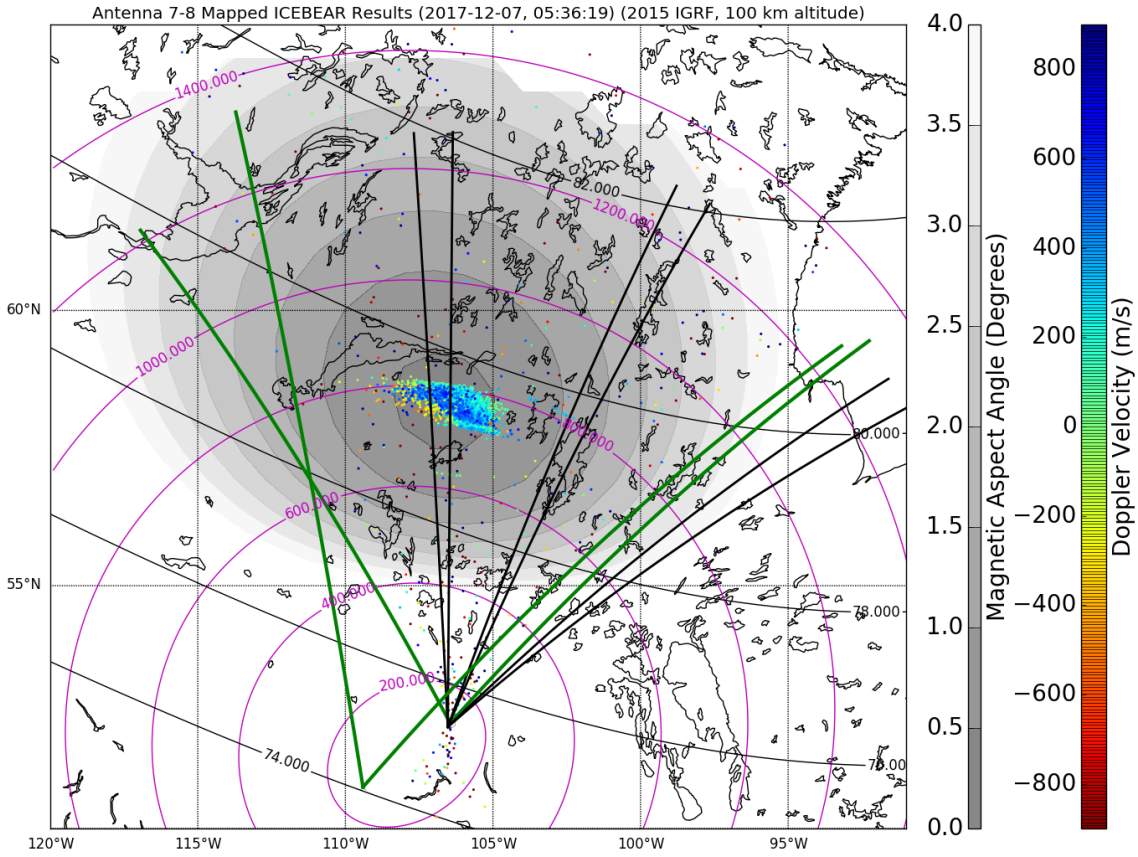

Figure 9.13: The ICEBEAR and SuperDARN FOVs are plotted. Beams 1, 8, and 16 are plotted in black for the SuperDARN array.

satellite [*Yau et al.*, 2006].

9.3.1 SuperDARN

Figure 9.13 shows a 2 antenna interferometer measurement of ICEBEAR with the Saskatoon SuperDARN radar beams 1, 8, and 16 displayed in the Figure as black lines originating from Saskatoon, SK. This measurement was one of the first ICEBEAR coherent scatter recordings, taken on December 7, 2017 at 5:36:19 UTC (23:36:19 LT). The ICEBEAR coherent scatter measurement is partially within the SuperDARN FOV, so SuperDARN measurements were investigated to determine if the same ionospheric structure was evident in both data sets.

The Saskatoon SuperDARN FOV measurement for a similar time as that in Figure 9.13

is shown in Figure 9.14. During this time a special SuperDARN mode was operating, which increased the temporal resolution of the measurements but reduced the number of beams recorded. Due to the special operating mode, the times generated for the plots from the the Virginia Tech SuperDARN website (http://vt.superdarn.org) were not necessarily correct, as the timing resolution was better than 1 minute/scan. The SuperDARN temporal and spatial resolution ($<$ 1 minute, 45 km) from this operating mode is still more coarse than that of ICEBEAR, but the plot shows that both radars measured scatter in a similar location. The SuperDARN measurement was taken with a radar frequency of 10.6 MHz, resulting in the signal being significantly refracted by the ionospheric plasma medium. This refraction provides a much larger potential scattering area than ICEBEAR, due to a large area over which the signal can become perpendicular to the geomagnetic field at E-region altitudes. Conversely, it can be more difficult to determine precisely where the coherent scatter measurements are originating from due to this refraction.

The SNR, Doppler velocity and spectral width measurements from beam 5 of the Saskatoon SuperDARN radar around the time of Figures 9.13, and 9.14, are plotted in Figure 9.15. Starting at around 5:34 UTC, there appears to be an increase in ionospheric activity at $\approx$ 800 km range, where there is strong coherent scatter with Doppler velocities of $>$ 450 m/s. This range matches well with where the ICEBEAR coherent scatter is originating from. Once again, SuperDARN and ICEBEAR conjunction measurements are something for future research, but these preliminary results show promise for the potential of multi-frequency studies of the plasma density irregularities in the E-region ionosphere.

9.3.2 e-POP Auroral Imager

Another instrument that has been used to further analyze the ionosphere in conjunction with ICEBEAR is the auroral imager onboard the e-POP satellite [*Yau et al.*, 2006]. An example of an ICEBEAR measurement with a simultaneous e-POP auroral imager observation overlaid is shown in Figure 9.16. The time of the measurement is 5:22:34 UTC on March 10, 2018. The ICEBEAR data was plotted using interferometry from 2 antennas, and the e-POP satellite imager was pointed towards the center of the FOV of ICEBEAR as it passed overhead. The images are only roughly aligned, as the map projections are different. Even with this

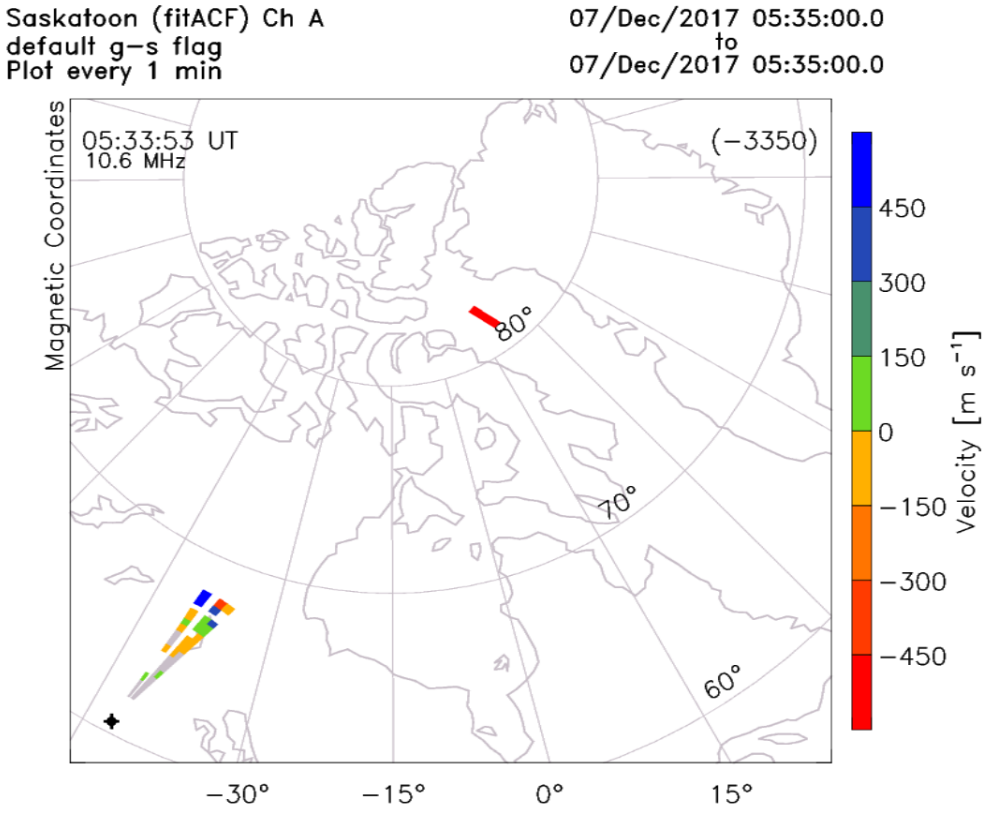

Figure 9.14: A SuperDARN FOV plot for a similar time to that of Figure 9.13, generated from the Virginia Tech SuperDARN website (http://vt.superdarn.org). As mentioned in the text, only several beams were being operated during this time.

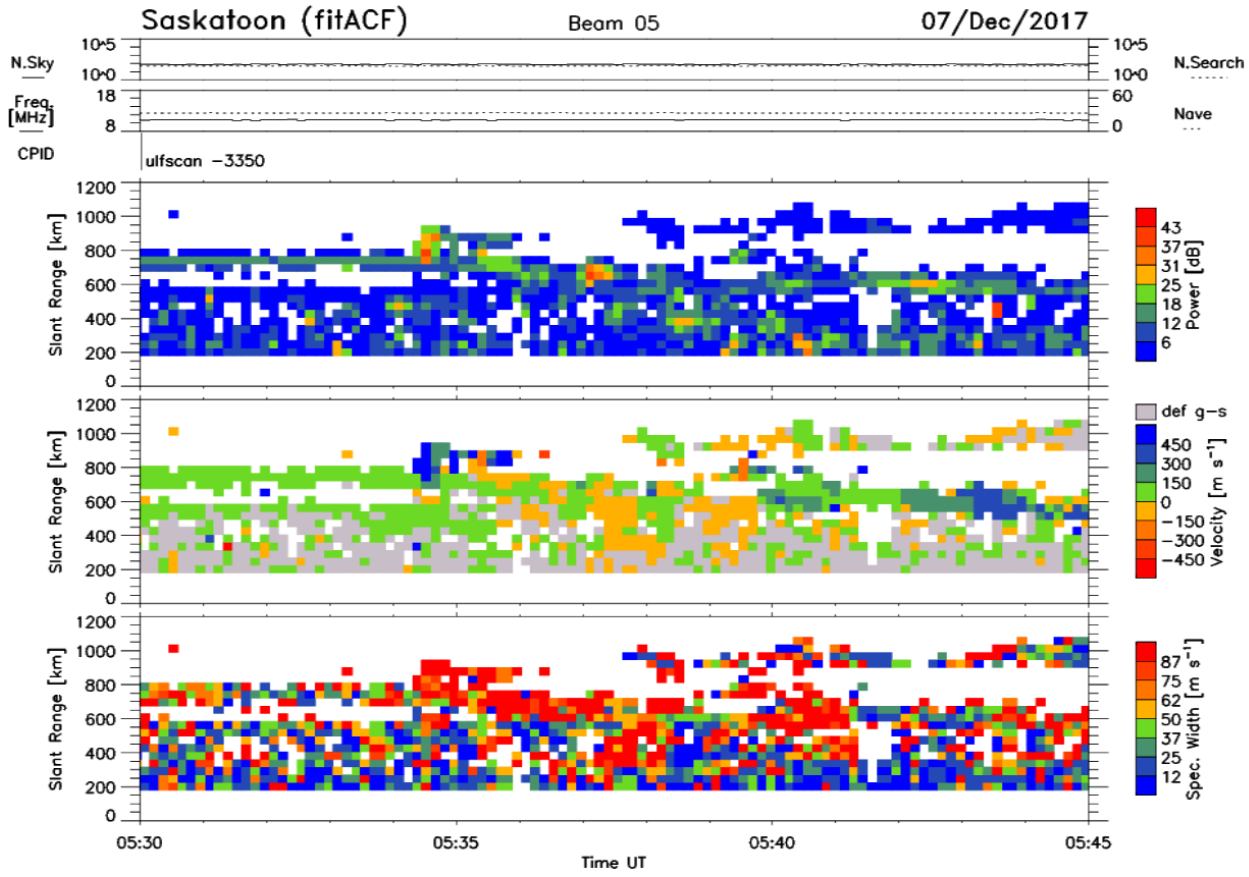

Figure 9.15: SuperDARN time series for beam 5, generated from the Virginia Tech SuperDARN website (http://vt.superdarn.org).

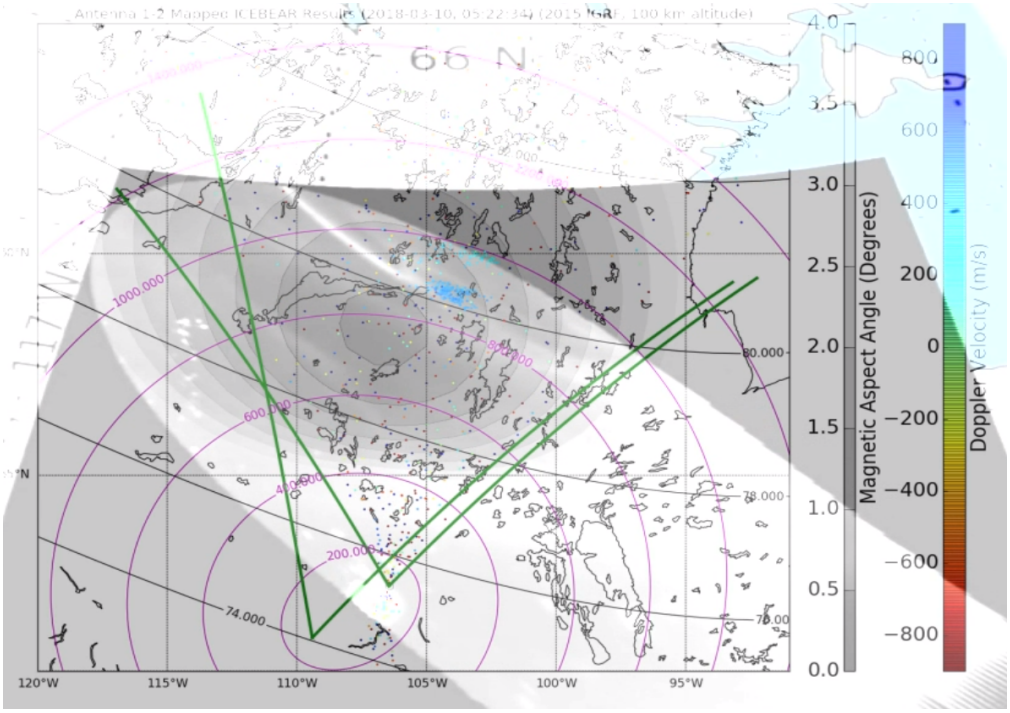

Figure 9.16: Example of an all sky imager on the e-POP satellite in conjunction with ICEBEAR. The imager and ICEBEAR data were roughly aligned, though the projections of each data set are different.

crude attempt at analysis, the scatter appears to be originating from the edge of the auroral emissions. The timing of the satellite pass was unfortunate, as during this short 10 minute time interval the auroral ionosphere was relatively inactive, when compared to the rest of the very active evening as observed by ICEBEAR. Extremely active periods with coherent scatter filling the ICEBEAR FOV occurred prior to and after the satellite pass. More imager studies and e-POP joint experiments are planned to further investigate how the auroral emissions correspond to ICEBEAR coherent scatter measurements.

9.4 ICEBEAR Results Overview

From the results shown in this chapter, it is evident that the ICEBEAR radar has measured all 4 previously defined types of E-region coherent scatter echoes. With the high spatiotemporal resolution of the measurements it is now possible to observe how these ionospheric plasma density structures evolve over time and space. By recording the raw voltage samples from each coherent receiver antenna it is possible to utilize multiple different beamforming techniques on

the same data set, providing a better understanding of the physics of the ionospheric scatter. It is also possible to change the temporal resolution of the results by increasing or decreasing the number of spectra averaged. Some preliminary multi-instrument examples were presented to display the potential for future collaborative studies utilizing the ICEBEAR system. The next chapter provides a discussion on the topics covered in this Ph.D. dissertation, as well as possible future studies that can be accomplished using this novel coherent scatter radar.

Chapter 10

Conclusions

Portions of Sections 10.1 and 10.2 were originally published in Huyghebaert, D., G. Hussey, J. Vierinen, K. McWilliams, and J.-P. St-Maurice (2019), ICEBEAR: An all-digital bistatic coded continuous-wave radar for studies of the E region of the ionosphere, *Radio Science*, *54*(4), 349–364, doi: 10.1029/2018RS006747.

As discussed in Chapter 2, the Sun is the dominant driver of many of the processes that occur in the ionosphere of the Earth. This is due to the EM flux emitted from the Sun, the solar magnetic field, and the charged particles expelled from the Sun interacting with the magnetic field and atmosphere of the Earth [*Kelley*, 2009]. By predicting when active periods occur on the Sun, it is possible to predict ionospheric conditions, which is when ICEBEAR is more likely to see ionospheric coherent scatter in the auroral region of the Earth. Magnetic reconnection and magnetospheric Alfvén waves are two mechanisms by which the magnetic fields of the Earth and Sun interact and influence the ionosphere of the Earth.

Chapter 3 investigated the formation and dynamics of the ionosphere. The plasma in the ionosphere is formed through photoionization of the neutral atmosphere and energetic charged particle precipitation. The absorption of light by different species of atmospheric particles creates different layers in the ionosphere, each layer with different properties and characteristics. The layer that ICEBEAR measures is the E-region, located at altitudes of 90–150 km. An important characteristic of this region is that the electrons follow the $\mathbf{E} \times \mathbf{B}$ drift while the ions follow the electric field and neutral atmospheric particles due to the associated collisional cross sections of the charged particles. The ionosphere is perturbed by interactions between the solar magnetic field and the geomagnetic field, and through charged

---

Portions of Sections 10.1 and 10.2 were originally published in *Huyghebaert et al.* [2019].

particle precipitation, which can create gradients in the ionospheric plasma density.

The plasma density gradients, in association with the geomagnetic field, can cause instabilities in the ionospheric plasma density to form. MHD equations and Fourier analysis were used to describe plasma instability growth conditions. These instabilities are aligned along the magnetic field lines due to the diffusion rate perpendicular to the magnetic field being smaller than the diffusion rate parallel with the magnetic field. The Farley-Buneman and gradient drift instabilities are the likely candidates for generating the majority of large scale plasma density perturbations (on the order of meters) in the E-region ionosphere. The ICEBEAR radar signal scatters from the plasma density irregularities with ≈ 3 m wavelengths.

Chapter 4 described the interaction between radio waves and plasmas with a background magnetic field. Plasma in the presence of a background magnetic field results in complex interactions with EM waves. This is described through the Appleton-Hartree equation. When a charged particle experiences an EM wave, it is predominantly accelerated due to the electric field of the wave. In the ionosphere, EM waves cause electrons to accelerate, where this acceleration then causes the electron to emit EM radiation at the same frequency. This is known as Thomson scatter for radio wavelengths that are greater than the Compton wavelength of the charged particle. Thomson scatter is the physical process by which coherent scatter radars measure plasma density structures in the ionosphere. From the geometry of the scattering process, only plasma density structures with a Fourier component that is half the radar wavelength (for a monostatic system) produce EM radiation that interferes constructively in the direction of the incoming radar signal.

Chapter 5 covered the basics of radar signals and waveforms. Radars operate by measuring a signal that has reflected or scattered off a remote object. By determining the Doppler shift and the time delay between the transmission and reception of the measured signal, it is possible to determine the range and velocity of the object [*Richards et al.*, 2010]. To improve the Doppler and range resolution of the measurements, different radar waveforms can be used. The range and Doppler resolution for a given waveform is modelled by creating an ambiguity function of that waveform. Different waveform ambiguity functions were plotted when determining the optimal radar waveform for ICEBEAR. The waveform that was chosen to be used with ICEBEAR was the PRN coded CW phase modulated waveform. This

waveform produces a thumbtack-like response in the Doppler and range domains, with an approximately uniform self-clutter floor. To produce the radar waveform, various electronics devices and RF hardware are required.

To conclude the background information, the basics of a digital radar were provided in Chapter 6. A digital radar consists of many different devices, working in concert to transmit and receive a radio signal. On the transmitter side, a modulated signal is generated, shifted to the carrier frequency, amplified, then transmitted using an antenna. The radar signal scatters off a remote object, and the scattered signal is captured by a receiving antenna. The signal is then passed through a receiver front end, consisting of amplifiers and filters, and recorded by a receiver using an analog to digital converter. The antenna can consist of a simple dipole, a complex antenna design, or multiple antennas working in conjunction as an array. An accurate reference clock is used to synchronize the multiple devices used in the radar, where different types of clocks have different clock drift rates. After the background material was discussed, an overview of previous E-region coherent scatter radars was provided.

Chapter 7 briefly described some of the previous E-region coherent scatter radar systems. This included radars that were operated by the University of Saskatchewan, as well as other E-region radars around the world. ICEBEAR improves upon the measurements made by these previous systems, which were discussed in the chapter. After an overview of previous radars was provided, the ICEBEAR radar could be described.

10.1 ICEBEAR Summary

In Chapter 8, the design, construction, and operation of the ICEBEAR system was described. The ICEBEAR radar has been operational since December, 2017. It is operating on a campaign basis during periods of high Kp. It uses a PRN coded CW phase modulated signal to obtain high temporal and spatial resolution images of the E-region, with a FOV over northern Saskatchewan in Canada. The use of a CW signal requires isolation between the receiver and transmitter antennas, resulting in the ICEBEAR transmitter and receiver sites being separated by $\approx$ 240 km. The phase modulation scheme used by ICEBEAR and the separation of the sites is only possible due to the implementation of modern radio hardware

and techniques. Through the use of GPS synchronized clocks and clock distribution units it is possible to operate multiple geographically separated radar sites and properly synchronize the radio samples. The Ettus Research X300 transceiver [*Ettus and Braun*, 2015] and Octoclock [*Ettus Research*, 2018] allow this synchronization to be implemented with relative ease. The X300 transceiver also allows the direct digitization of radio samples in the VHF range with no front end analog filtering and mixing required. This, along with the advances in digital storage and computer processoring capability, provides a means by which the raw voltage data can be stored and analyzed in real time.

For the initial ICEBEAR operations, the effective spatial resolution was 3 km, and the temporal resolution was 5 s, though, as shown, meteors can be detected with a temporal resolution of 100 ms. Both spatial and temporal resolutions will be improved as the radar abilities are further explored, but the spatial resolution is constrained by Radio License BW limits, and the temporal resolution is constrained by requiring a sufficient SNR for detectable ionospheric scatter. Signal processing has currently been implemented for real time processing of two antennas, but is being expanded upon to make use of graphics processing units (GPUs). By using a GPU it will be possible to process the 10 antennas of the receiving array faster than real time.

In Chapter 9 the initial measurements of ICEBEAR were presented. The ICEBEAR radar has observed all four previously classified and measured E-region radar echo types, as well as meteor echoes. Currently the receiver and transmitter antennas are arranged as linear arrays providing angle of arrival in the azimuthal (East-West) direction through interferometry, though future research plans include incorporating a 2-D array of antennas to obtain both azimuthal and elevation angle of arrival measurements, as will be discussed in Section 10.2.

It is possible to sequentially view the ICEBEAR measurements to observe how plasma density irregularities evolve in space and time over a large FOV. Some preliminary results of multi-instrument studies involving the Saskatoon SuperDARN radar [*Greenwald et al.*, 1995] and the e-POP satellite [*Yau et al.*, 2006] auroral imager separately, and at different times, with the ICEBEAR radar were presented. Other complementary space physics instruments are planned to be collaborated with in the future.

Some of the defining and novel characteristics of the ICEBEAR ionospheric coherent

scatter radar are as follows:

1) The ICEBEAR system is the first continuous-wave spread spectrum coherent scatter radar to make measurements of auroral E-region plasma density irregularities.

2) With the signal modulation scheme implemented by ICEBEAR, Doppler and range aliasing is effectively removed (± 100 kHz, 30,000 km before aliasing occurs). Aliasing was a drawback to many previous E-region coherent scatter systems.

3) By using different beamforming and interferometry techniques through re-processing of the same data set, it is possible to isolate different ionospheric plasma density irregularities based upon their measured spectra. Some examples are the Type IV coherent scatter measurements shown in Chapter 9. Both Type IV events revealed isolated fast moving coherent scatter structures separate from the majority of the coherent scatter measured. This is not necessarily always the case, which is an interesting result in and of itself.

4) By recording the raw complex voltage data from each antenna, the ICEBEAR system design allows relatively easy reconfiguration of the receiver antenna array. Through re-arranging the receiver array it is possible to remove azimuthal aliasing and provide elevation angle of arrival information of the coherent scatter. This is discussed in Section 10.2.

5) The transmitter and receiver sites are remotely controlled via the internet, allowing the system to be operated on short notice. The only constraint preventing the system from operating continuously over long periods of time is hard drive storage and the current implementation of post-recording analysis. With advances in electronic data storage, and faster than real time processing of the ICEBEAR data, continuous operation should be attainable in the near future.

ICEBEAR makes it possible to study many of the mysteries still surrounding E-region plasma dynamics. The measurements from ICEBEAR examine exciting auroral events that will be studied for years to come. The next section provides some future studies that are made possible through this novel coherent scatter radar system.

10.2 Future Studies

With a new measurement system, there are an abundance of new studies that can be performed. Listed here are just a few of the future projects and future studies that are made possible through the ICEBEAR system being commissioned and now operational:

1) An important project is the implementation of real time analysis of incoming ICEBEAR data. This will allow for continuous operation of the system, where only data with set parameters would be recorded.

2) The X300 transceivers can be expanded to have 4 DDCs on the FPGA, making it possible to simultaneously receive 4 signals on each transceiver unit. This would double the number of receiver channels that are available, reducing the cost of doubling the number of receiver antenna chains in the receiving array.

3) An exciting future direction with ICEBEAR is to implement a 2-D receiver array, providing beamformed data with both azimuthal and elevation angle of arrival information. This would allow the spectra for a given 3-D location to be isolated and fit to theoretical spectra, providing derived parameters relating to the ionospheric plasma. *Hysell et al.* [2012] have performed something similar by using empirical formulas to derive the electric fields from the coherent scatter spectra.

4) The phase modulated signal utilized by ICEBEAR allows multiple transmitting signals on the same frequency band. This is due to the PRN phase code appearing as noise when processed using a different code. With different codes transmitted at different locations by different transmitters, multiple measurements of the same ionospheric plasma volume at the same frequency may be obtained. These measurements could be used to produce 2-D or 3-D vectors of the plasma velocity to provide further insights into E-region plasma dynamics and scattering physics.

5) The transmitter site is capable of transmitting at separate frequencies located around 50 MHz, Radio License permitting. Transmitting at two separate frequencies at the

same time could be used to determine how the ionospheric plasma affects the propagation of the radio signals at different frequencies. This could be used to measure the electron density, as shown by *Gillies et al.* [2009] with SuperDARN.

6) Utilizing the high spatiotemporal resolution of the ICEBEAR system, it is possible to search for Alfvénic wave signatures in the coherent scatter measured. These Alfvén wave studies are planned for the future.

7) There are many meteor detections evident in the ICEBEAR data using time scales of 100 ms. These meteor detections can be further analyzed to determine the neutral wind velocity at that location. This could then be further improved upon once a 2-D receiver array is implemented, providing neutral wind velocities for multiple altitudes.

8) An instrument suite that will provide ample opportunity for collaboration with ICEBEAR is the Transition Region Explorer (TREx) installation, which is planned to have optical auroral imagery and total electron content (TEC) data over a significant portion of the ICEBEAR FOV (https://www.ucalgary.ca/aurora/projects/trex). Once this project is commissioned, conjunction events can be analyzed using multiple measurement techniques providing enhanced insights into the ionospheric plasma processes during energetic charged particle precipitation.

9) There are opportunities to collaborate with a multitude of other ionospheric measurement instruments. As shown in Section 9.3, there have already been preliminary attempts to compare and analyze measurements made from the Saskatoon SuperDARN radar and the e-POP satellite. Other data sets that have yet to be explored with ICEBEAR include the magnetometer networks that span across Canada, and other satellite measurements of the ionosphere.

To summarize, the ICEBEAR system makes high spatiotemporal resolution images of E-region coherent scatter over a large field of view. Many of the future studies discussed here are in the planning stages, or underway, and will produce scientifically significant results in the near future. There are likely studies that are unconceived that will be performed in the future, and, due to the recording of the raw voltage data from each antenna, can be

made possible. Re-analysis of ICEBEAR data as new and unique beamforming techniques are implemented and developed will be exciting from an ionospheric radar technique perspective, let alone advancing E-region plasma physics science.

The ICEBEAR system is now operational, and providing novel measurements of ionospheric plasma density irregularities that will be of use in ionospheric studies for years to come.

References

Actel (2007), Improving ADC results through oversampling and post-processing of data, *Tech. rep.*, Actel.

Akasofu, S. I. (1981), Energy coupling between the solar wind and the magnetosphere, *Space Science Reviews*, *28*(2), 121–190, doi: 10.1007/BF00218810.

Alfvén, H. (1942), Existence of electromagnetic-hydrodynamic waves, *Nature*, *150*(3805), 405.

Allan, D. (1987), Time and frequency (time-domain) characterization, estimation, and prediction of precision clocks and oscillators, *IEEE transactions on ultrasonics, ferroelectrics, and frequency control*, *34*(6), 647–654.

Altera (2007), Using Cyclone III FPGAs for emerging wireless applications, *Tech. rep.*, Altera, rev 1.0.

Appleton, E., and M. Barnett (1925), Local reflection of wireless waves from the upper atmosphere, *Nature*, *115*, 333–334, doi: http://dx.doi.org/10.1038/115333a0.

Appleton, E., and W. Beynon (1940), The application of ionospheric data to radio-communication problems: part I, *Proceedings of the Physical Society*, *52*(4), 518–533, doi: 10.1088/0959-5309/52/4/311.

Bachman, P., and R. Haiduk (2011), The effect of forced air cooling on heat sink thermal ratings, *Tech. rep.*, Crydom Inc.

Balanis, C. (1992), Antenna theory: A review, *Proceedings of the IEEE*, *80*(1), 7–23.

Bame, S. J., B. E. Goldstein, J. T. Gosling, J. W. Harvey, D. J. McComas, M. Neugebauer, and J. L. Phillips (1993), Ulysses observations of a recurrent high speed solar wind stream and the heliomagnetic streamer belt, *Geophysical Research Letters*, *20*(21), 2323–2326, doi: 10.1029/93GL02630.

Banks, P. M., C. R. Chappell, and A. F. Nagy (1974), A new model for the interaction of auroral electrons with the atmosphere: Spectral degradation, backscatter, optical emission, and ionization, *Journal of Geophysical Research*, *79*(10), 1459–1470, doi: 10.1029/JA079i010p01459.

Belrose, J. S., and M. J. Burke (1964), Study of the lower ionosphere using partial reflection: 1. experimental technique and method of analysis, *Journal of Geophysical Research*, *69*(13), 2799–2818, doi: 10.1029/JZ069i013p02799.

Berkner, L. V. (1937), The electrical state of the Earth's outer atmosphere, *The Scientific Monthly*, *45*(2), 126–141.

Bloom, A. (2012a), DSP and software radio design, in *The ARRL Handbook for Radio Communications 2013*, edited by H. Silver, S. Ford, and M. Wilson, chap. 15, pp. 15.1–15.34, The American Radio Relay League, Inc.

Bloom, A. (2012b), Modulation, in *The ARRL Handbook for Radio Communications 2013*, edited by H. Silver, S. Ford, and M. Wilson, chap. 8, pp. 8.1–8.24, The American Radio Relay League, Inc.

Bloom, A. (2012c), RF power amplifiers, in *The ARRL Handbook for Radio Communications 2013*, edited by H. Silver, S. Ford, and M. Wilson, chap. 17, pp. 17.1–17.58, The American Radio Relay League, Inc.

Blossom, E. (2004), GNU radio: tools for exploring the radio frequency spectrum, *Linux journal*, *2004*(122), 4.

Born, M. (1926), Quantenmechanik der stoßvorgänge, *Zeitschrift für Physik*, *38*(11), 803–827, doi: 10.1007/BF01397184.

Boyle, C. B., P. H. Reiff, and M. R. Hairston (1997), Empirical polar cap potentials, *Journal of Geophysical Research: Space Physics*, *102*(A1), 111–125, doi: 10.1029/96JA01742.

Bradbury, N. E. (1938), Ionization, negative-ion formation, and recombination in the ionosphere, *Terrestrial Magnetism and Atmospheric Electricity*, *43*(1), 55–66, doi: 10.1029/TE043i001p00055.

Brigham, E. O. (1988), *The fast Fourier transform and its Applications*, Prentice Hall.

Brown, L. (1999), *A Radar History of World War II*, Institute of Physics Publishing.

Browning, P. K. (1991), Mechanisms of solar coronal heating, *Plasma Physics and Controlled Fusion*, *33*(6), 539.

Budden, K. (1961), *Radio Waves in the Ionosphere*, Cambridge University Press.

Buneman, O. (1963), Excitation of field aligned sound waves by electron streams, *Phys. Rev. Lett.*, *10*, 285–287, doi: 10.1103/PhysRevLett.10.285.

Carrington, R. C. (1863), *Observations of the Spots on the Sun: from November 9, 1853, to March 24, 1861, made at Redhill*, Williams and Norgate.

Chapman, S. (1931a), The absorption and dissociative or ionizing effect of monochromatic radiation in an atmosphere on a rotating Earth, *Proceedings of the Physical Society*, *43*(1), 26.

Chapman, S. (1931b), The absorption and dissociative or ionizing effect of monochromatic radiation in an atmosphere on a rotating Earth part II. grazing incidence, *Proceedings of the Physical Society*, *43*(5), 483.

Chaston, C., J. Bonnell, C. Carlson, M. Berthomier, L. Peticolas, I. Roth, J. McFadden, R. Ergun, and R. Strangeway (2002), Electron acceleration in the ionospheric Alfvén resonator, *Journal of Geophysical Research: Space Physics (1978–2012)*, *107*(A11), SMP–41.

Chaston, C., C. Carlson, J. McFadden, R. Ergun, and R. Strangeway (2007), How important are dispersive Alfvén waves for auroral particle acceleration?, *Geophysical Research Letters*, *34*(7), doi: 10.1029/2006GL029144.

Chau, J., and J.-P. St.-Maurice (2016), Unusual 5 m E region field-aligned irregularities observed from northern Germany during the magnetic storm of 17 March 2015, *Journal of Geophysical Research: Space Physics*, *121*(10), 10,316–10,340, doi: 10.1002/2016JA023104.

Chen, F. (2006), *Introduction to Plasma Physics and Controlled Fusion Volume 1: Plasma Physics*, Springer.

Cisco Systems (2007), What time is it?, *Tech. rep.*, Cisco Systems, Inc.

Close, S., M. Oppenheim, S. Hunt, and A. Coster (2004), A technique for calculating meteor plasma density and meteoroid mass from radar head echo scattering, *Icarus*, *168*(1), 43 – 52, doi: https://doi.org/10.1016/j.icarus.2003.11.018.

Collins, A. (2017), All programmable RF-Sampling solutions, *Tech. rep.*, Xilinx, rev 1.0.1.

Collins, I. (2018), Phase-locked loop (PLL) fundamentals, *Analog Dialogue*, *52*.

Compton, A. H. (1923), A quantum theory of the scattering of x-rays by light elements, *Phys. Rev.*, *21*, 483–502, doi: 10.1103/PhysRev.21.483.

Cooper, J. (2006), A 50 MHz FMCW radar for the study of E-region coherent backscatter, Master's thesis, University of Saskatchewan.

Cowling, T. G. (1933), The magnetic field of sunspots, *Monthly Notices of the Royal Astronomical Society*, *94*, 39–48.

Cravens, T. E. (1997), *Physics of Solar System Plasmas*, Cambridge University Press.

Cushcraft (2018), A50-5S, *www.cushcraftamateur.com*.

Das, J. (2004), Passive filters-potentialities and limitations, *IEEE transactions on industry applications*, *40*(1), 232–241.

de Paula, E. R., and D. L. Hysell (2004), The São Luís 30 MHz coherent scatter ionospheric radar: system description and initial results, *Radio Science*, *39*(1).

de Toma, G. (2011), Evolution of coronal holes and implications forhigh-speed solar wind during the minimum between cycles 23 and 24, *Solar Physics*, *274*(1), 195–217, doi: 10.1007/s11207-010-9677-2.

DeRosa, M., A. Brun, and J. Hoeksema (2012), SOLAR MAGNETIC FIELD REVERSALS AND THE ROLE OF DYNAMO FAMILIES, *The Astrophysical Journal*, *757*(1), 96, doi: 10.1088/0004-637x/757/1/96.

Dimant, Y., and R. Sudan (1997), Physical nature of a new cross-field current-driven instability in the lower ionosphere, *Journal of Geophysical Research: Space Physics*, *102*(A2), 2551–2563, doi: 10.1029/96JA03274.

Dobson, I. (2008), The role of PCI express in wired communications systems, *Tech. rep.*, Integrated Device Technology, Inc.

Durney, B. R., D. S. De Young, and I. W. Roxburgh (1993), On the generation of the large-scale and turbulent magnetic fields in solar-type stars, *Solar Physics*, *145*(2), 207–225, doi: 10.1007/BF00690652.

Dyrud, L. P., M. M. Oppenheim, and A. F. vom Endt (2001), The anomalous diffusion of meteor trails, *Geophysical Research Letters*, *28*(14), 2775–2778, doi: 10.1029/2000GL012749.

Dyson, P., and J. Bennett (1979), General formulae for absorption of radio waves in the ionosphere, *Journal of Atmospheric and Terrestrial Physics*, *41*(4), 367 – 377, doi: https://doi.org/10.1016/0021-9169(79)90033-3.

Ettus, M., and M. Braun (2015), The universal software radio peripheral (USRP) family of low-cost SDRD, *Opportunistic Spectrum Sharing and White Space Access: The Practical Reality*, pp. 3–23.

Ettus Research (2018), Octoclock, *www.ettus.com*.

Farley, D. (1963a), A plasma instability resulting in field-aligned irregularities in the ionosphere, *Journal of Geophysical Research*, *68*(22), 6083–6097.

Farley, D. T. (1963b), Two-stream plasma instability as a source of irregularities in the ionosphere, *Phys. Rev. Lett.*, *10*, 279–282, doi: 10.1103/PhysRevLett.10.279.

Fejer, B., and M. Kelley (1980), Ionospheric irregularities, *Reviews of Geophysics*, *18*(2), 401–454, doi: 10.1029/RG018i002p00401.

Fejer, B., J. Providakes, D. Farley, and W. Swartz (1986), Auroral E region plasma waves and elevated electron temperatures, *Journal of Geophysical Research: Space Physics*, *91*(A12), 13,583–13,592, doi: 10.1029/JA091iA12p13583.

Ferguson, E. E. (1967), Ionospheric ion-molecule reaction rates, *Reviews of Geophysics*, *5*(3), 305–327, doi: 10.1029/RG005i003p00305.

Fioletov, V. E. (2009), Estimating the 27-day and 11-year solar cycle variations in tropical upper stratospheric ozone, *Journal of Geophysical Research: Atmospheres*, *114*(D2), doi: 10.1029/2008JD010499.

Forbes, T. G. (2000), A review on the genesis of coronal mass ejections, *Journal of Geophysical Research: Space Physics*, *105*(A10), 23,153–23,165, doi: 10.1029/2000JA000005.

Foster, J. C., and P. J. Erickson (2000), Simultaneous observations of E-region coherent backscatter and electric field amplitude at F-region heights with the Millstone Hill UHF Radar, *Geophysical Research Letters*, *27*(19), 3177–3180, doi: 10.1029/2000GL000042.

Fox, K. (2014), Journey of light, `https://nasaviz.gsfc.nasa.gov/11537`, accessed: 2018-06-15.

Gellert, W., M. Hellwich, H. Kästner, and H. Küstner (2012), *The VNR concise encyclopedia of mathematics*, Springer Science & Business Media.

Gillies, R. G., G. C. Hussey, G. J. Sofko, K. A. McWilliams, R. A. D. Fiori, P. Ponomarenko, and J.-P. St.-Maurice (2009), Improvement of SuperDARN velocity measurements by estimating the index of refraction in the scattering region using interferometry, *Journal of Geophysical Research: Space Physics*, *114*(A7), doi: 10.1029/2008JA013967.

Gillies, R. G., G. C. Hussey, G. J. Sofko, and H. G. James (2010), Relative O- and X-mode transmitted power from SuperDARN as it relates to the RRI instrument on ePOP, *Annales Geophysicae*, *28*(3), 861–871, doi: 10.5194/angeo-28-861-2010.

Gondarenko, N. A., and P. N. Guzdar (2004), Plasma patch structuring by the nonlinear evolution of the gradient drift instability in the high-latitude ionosphere, *Journal of Geophysical Research: Space Physics*, *109*(A9), doi: 10.1029/2004JA010504.

Granberg, H. (1990), A Compact 1-kW 2-50 MHz Solid-State Linear Amplifier, *Tech. rep.*, Motorola Inc.

Greenhow, J., and E. Neufeld (1955), The diffusion of ionized meteor trails in the upper atmosphere, *Journal of Atmospheric and Terrestrial Physics*, *6*(1), 133 – 140, doi: https://doi.org/10.1016/0021-9169(55)90020-9.

Greenwald, R. A., et al. (1995), DARN/SuperDARN, *Space Science Reviews*, *71*(1), 761–796, doi: 10.1007/BF00751350.

Griffiths, D. J. (1999), *Introduction to Electrodynamics*, Prentice Hall.

Grydeland, T., F. D. Lind, P. J. Erickson, and J. M. Holt (2005), Software Radar signal processing, *Annales Geophysicae*, *23*(1), 109–121.

Gurnett, D. A., W. S. Kurth, L. F. Burlaga, and N. F. Ness (2013), In situ observations of interstellar plasma with Voyager 1, *Science*, *341*(6153), 1489–1492, doi: 10.1126/science.1241681.

Hahn, M., and D. W. Savin (2014), Evidence for wave heating of the quiet-Sun corona, *The Astrophysical Journal*, *795*(2), 111.

Haldoupis, C. (1989), A review on radio studies of auroral E-region ionospheric irregularities, *Annales Geophysicae*, *7*, 239–258.

Haldoupis, C., and K. Schlegel (1993), A 50MHz radio Doppler experiment for midlatitude E region coherent backscatter studies: System description and first results, *Radio Science*, *28*(6), 959–978, doi: 10.1029/93RS01373.

Halfacree, G., and E. Upton (2012), *Raspberry Pi user guide*, John Wiley & Sons.

Hallas, J. (2012), Receivers, in *The ARRL Handbook for Radio Communications 2013*, edited by H. Silver, S. Ford, and M. Wilson, chap. 12, pp. 12.1–12.41, The American Radio Relay League, Inc.

Hamza, A., and J.-P. St.-Maurice (1993), A turbulent theoretical framework for the study of current-driven E region irregularities at high latitudes: Basic derivation and application to gradient-free situations, *Journal of Geophysical Research: Space Physics*, *98*(A7), 11,587–11,599, doi: 10.1029/92JA02836.

Hanzo, L., S. Ng, W. Webb, and T. Keller (2004), *Quadrature Amplitude Modulation: From basics to adaptive trellis-coded, turbo-equalised and space-time coded OFDM, CDMA and MC-CDMA systems*, IEEE Press-John Wiley.

Hartree, D. R. (1931), The propagation of electromagnetic waves in a refracting medium in a magnetic field, *Mathematical Proceedings of the Cambridge Philosophical Society*, *27*(1), 143162, doi: 10.1017/S0305004100009440.

Hathaway, D. H. (2010), The solar cycle, *Living Reviews in Solar Physics*, *7*(1), 1, doi: 10.12942/lrsp-2010-1.

Heinselman, C., and M. Nicolls (2008), A bayesian approach to electric field and E-region neutral wind estimation with the Poker Flat advanced modular incoherent scatter radar, *Radio Science*, *43*(5).

Hernández-Pajares, M., J. M. Juan, J. Sanz, À. Aragón-Àngel, A. García-Rigo, D. Salazar, and M. Escudero (2011), The ionosphere: effects, GPS modeling and the benefits for space geodetic techniques, *Journal of Geodesy*, *85*(12), 887–907, doi: 10.1007/s00190-011-0508-5.

Hollis, T., and R. Weir (2003), The theory of digital down conversion, *Tech. rep.*, Hunt Engineering.

Hunsucker, R. D., and J. K. Hargreaves (2007), *The high-latitude ionosphere and its effects on radio propagation*, Cambridge University Press.

Hussey, G. (1995), The polarisation of 50 MHz auroral backscatter, Ph.D. thesis, University of Saskatchewan.

Hutchinson, C., H. Silver, A. Applegate, and J. Moell (2012), Antennas, in *The ARRL Handbook for Radio Communications 2013*, edited by H. Silver, S. Ford, and M. Wilson, chap. 21, pp. 21.1–21.88, The American Radio Relay League, Inc.

Huyghebaert, D., G. Hussey, J. Vierinen, K. McWilliams, and J.-P. St-Maurice (2019), ICE-BEAR: An all-digital bistatic coded continuous-wave radar for studies of the E region of the ionosphere, *Radio Science*, *54*(4), 349–364, doi: 10.1029/2018RS006747.

Hysell, D. (2016), The radar aurora, *Auroral Dynamics and Space Weather, Geophysical Monograph*, *215*, 193–209.

Hysell, D. (2018), *Antennas and Radar for Environmental Scientists and Engineers*, Cambridge University Press.

Hysell, D., R. Miceli, J. Munk, D. Hampton, C. Heinselman, M. Nicolls, S. Powell, K. Lynch, and M. Lessard (2012), Comparing VHF coherent scatter from the radar aurora with incoherent scatter and allsky auroral imagery, *Journal of Geophysical Research: Space Physics*, *117*(A10), doi: 10.1029/2012JA018010.

Hysell, D., M. Milla, and J. Vierinen (2016), A multistatic HF beacon network for ionospheric specification in the Peruvian sector, *Radio Science*, *51*(5), 392–401, doi: 10.1002/2016RS005951.

Hysell, D. L., H. C. Aveiro, and J. L. Chau (2014), *Ionospheric Irregularities*, chap. 18, pp. 217–240, American Geophysical Union (AGU), doi: 10.1002/9781118704417.ch18.

Integrated Device Technology (2008), The role of jitter in timing signals, *Tech. rep.*, Integrated Device Technology, Inc.

ITU-R (2016), Recommendation ITU-R P.372-13 - radio noise, *Tech. rep.*, International Telecommunications Union.

Jackson Labs (2018), Fury GPS disciplined oscillator, *www.jackson-labs.com*.

Johnson, C. (1969), Ion and neutral composition of the ionosphere., *Annals of the IQSY*, *5*, 197–213.

Kapinchev, K., A. Bradu, F. Barnes, and A. Podoleanu (2015), GPU implementation of cross-correlation for image generation in real time, in *2015 9th International Conference on Signal Processing and Communication Systems (ICSPCS)*, pp. 1–6.

Kelley, K., and C. Weber (1985), Principles of spread spectrum radar, in *MILCOM 1985 - IEEE Military Communications Conference*, vol. 3, pp. 586–590, doi: 10.1109/MILCOM.1985.4795104.

Kelley, M. C. (2009), *The Earth's Ionosphere*, Academic Press.

Kester, W. (2009), What the Nyquist criterion means to your sampled data system design, *Analog Devices*, pp. 1–12.

Keysight Technologies (2018), Understanding and testing multi-channel RF systems with signal generators, *Tech. rep.*, Keysight Technologies.

Kivelson, M., and C. Russell (1995), *Introduction to Space Physics*, Cambridge University Press.

Klimchuk, J. A. (2006), On solving the coronal heating problem, *Solar Physics*, *234*(1), 41–77, doi: 10.1007/s11207-006-0055-z.

Knox, F. (1964), A contribution to the theory of the production of field-aligned ionisation irregularities in the equatorial electrojet, *Journal of Atmospheric and Terrestrial Physics*, *26*(2), 239 – 249, doi: https://doi.org/10.1016/0021-9169(64)90150-3.

Koehler, J., G. Sofko, D. Andr, M. Maguire, R. Osterried, M. McKibben, J. Mu, D. Danskin, and A. Ortlepp (1995), The SAPPHIRE auroral radar system, *Canadian Journal of Physics*, *73*(3-4), 211–226, doi: 10.1139/p95-029.

KR Electronics (2017), *3333-SMA*, KR Electronics.

Kulsrud, R. M. (2001), Magnetic reconnection: Sweet-Parker versus Petschek, *Earth, Planets and Space*, *53*(6), 417–422, doi: 10.1186/BF03353251.

Kuwahara, Y. (2005), Multiobjective optimization design of Yagi-Uda antenna, *IEEE Transactions on Antennas and Propagation*, *53*(6), 1984–1992, doi: 10.1109/TAP.2005.848501.

Le, G., J. A. Slavin, and R. J. Strangeway (2010), Space technology 5 observations of the imbalance of regions 1 and 2 field-aligned currents and its implication to the cross-polar cap Pedersen currents, *Journal of Geophysical Research: Space Physics*, *115*(A7), doi: 10.1029/2009JA014979.

Lei, J., J. P. Thayer, J. M. Forbes, E. K. Sutton, and R. S. Nerem (2008), Rotating solar coronal holes and periodic modulation of the upper atmosphere, *Geophysical Research Letters*, *35*(10), doi: 10.1029/2008GL033875.

Lewandowski, W., J. Azoubib, and W. Klepczynski (1999), GPS: primary tool for time transfer, *Proceedings of the IEEE*, *87*(1), 163–172, doi: 10.1109/5.736348.

Lewis, J. (2012), *Physics and Chemistry of the Solar System*, Academic Press.

Li, S., and H. Li (2006), Parallel AMR code for compressible MHD or HD equations, *Los Alamos National Laboratory*.

Lind, F., J. Sahr, and D. Gidner (1999), First passive radar observations of auroral E-region irregularities, *Geophysical Research Letters*, *26*(14), 2155–2158, doi: 10.1029/1999GL900457.

Lind, F., P. Erickson, A. Coster, J. Foster, J. Marchese, Z. Berkowitz, and J. Sahr (2013), Intercepted signals for ionospheric science, *Radio Science*, *48*(3), 248–264, doi: 10.1002/rds.20034.

Linson, L. M., and J. B. Workman (1970), Formation of striations in ionospheric plasma clouds, *Journal of Geophysical Research*, *75*(16), 3211–3219, doi: 10.1029/JA075i016p03211.

Lockwood, M., S. Cowley, and M. Freeman (1990), The excitation of plasma convection in the high-latitude ionosphere, *Journal of Geophysical Research: Space Physics*, *95*(A6), 7961–7972, doi: 10.1029/JA095iA06p07961.

Losada, R. (2004), Practical FIR filter design in MATLAB, *Tech. rep.*, The Math Works, Inc.

Loureiro, N. F., and D. A. Uzdensky (2016), Magnetic reconnection: from the Sweet-Parker model to stochastic plasmoid chains, *Plasma Physics and Controlled Fusion*, *58*(1), 014,021.

Lysak, R. L. (1991), Feedback instability of the ionospheric resonant cavity, *Journal of Geophysical Research: Space Physics (1978–2012)*, *96*(A2), 1553–1568.

MacDougall, J., I. Grant, and X. Shen (1995), The Canadian advanced digital ionosonde: design and results, *URSI INAG Ionospheric Station Inf. Bulletin, UAG-104*.

Mahafza, B. R. (2002), *Radar systems analysis and design using MATLAB*, CRC press.

Mahajan, R., C.-p. Chiu, and G. Chrysler (2006), Cooling a microprocessor chip, *Proceedings of the IEEE*, *94*(8), 1476–1486.

Makarevich, R. (2009), Coherent radar measurements of the doppler velocity in the auroral E region, *URSI Radio Science Bulletin*, *2009*(328), 33–46, doi: 10.23919/URSIRSB.2009.7909539.

Maple Leaf Communications (2018), Typical losses in 50 ohm coaxial cables, `http://www.mapleleafcom.com/PDFs_Downloads/CoaxLossChart.pdf`, accessed: 2019-02-04.

Marsch, E. (2006), Kinetic physics of the solar corona and solar wind, *Living Reviews in Solar Physics*, *3*(1), 1, doi: 10.12942/lrsp-2006-1.

Marshall, R. A., and J. Bortnik (2018), Pitch angle dependence of energetic electron precipitation: Energy deposition, backscatter, and the bounce loss cone, *Journal of Geophysical Research: Space Physics*, *123*(3), 2412–2423, doi: 10.1002/2017JA024873.

Masuda, S., T. Kosugi, H. Hara, S. Tsuneta, and Y. Ogawara (1994), A loop-top hard X-ray source in a compact solar flare as evidence for magnetic reconnection, *Nature*, *371*(6497), 495.

McComas, D. J., H. A. Elliott, N. A. Schwadron, J. T. Gosling, R. M. Skoug, and B. E. Goldstein (2003), The three-dimensional solar wind around solar maximum, *Geophysical Research Letters*, *30*(10), doi: 10.1029/2003GL017136.

Mellanox Technologies (2008), Introduction to InfiniBand, *Tech. rep.*, Mellanox Technologies, Inc., rev 1.90.

Meyer, F., and J. Nicoll (2008), Mapping ionospheric TEC using faraday rotation in full-polarimetric L-Band SAR data, in *7th European Conference on Synthetic Aperture Radar*, pp. 1–4.

Mini-Circuits (2018), *Coaxial Low Noise Amplifier ZFL-500LN+*, Mini-Circuits, rev. F.

Mitola, J. (1995), The software radio architecture, *IEEE Communications Magazine*, *33*(5), 26–38, doi: 10.1109/35.393001.

Modzelewska, R., and M. V. Alania (2013), The 27-day cosmic ray intensity variations during solar minimum 23/24, *Solar Physics*, *286*(2), 593–607, doi: 10.1007/s11207-013-0261-4.

Moorcroft, D. (2002), Outstanding issues in the theory of radar aurora: Evidence from the frequency dependence of spectral characteristics, *Journal of Geophysical Research: Space Physics*, *107*(A10), SIA 13–1–SIA 13–9, doi: 10.1029/2001JA009218.

NASA (2012), Milky Way and our location, `https://www.nasa.gov/mission_pages/sunearth/news/gallery/galaxy-location.html`, accessed: 2018-06-13.

National Instruments (2016), Basics of power amplifier and front end module measurements, *Tech. rep.*, National Instruments.

Newkirk, D., and R. Karlquist (2012), Mixers, modulators and demodulators, in *The ARRL Handbook for Radio Communications 2013*, edited by H. Silver, S. Ford, and M. Wilson, chap. 10, pp. 10.1–10.36, The American Radio Relay League, Inc.

Nicolet, M., and A. C. Aikin (1960), The formation of the D region of the ionosphere, *Journal of Geophysical Research*, *65*(5), 1469–1483, doi: 10.1029/JZ065i005p01469.

NXP Semiconductors (2018), *MRFX1K80H RF Power LDMOS Transistor: High Ruggedness N–Channel Enhancement–Mode Lateral MOSFET*, NXP Semiconductors, rev. 1.

Oppenheim, M., N. Otani, and C. Ronchi (1996), Saturation of the Farley-Buneman instability via nonlinear electron ExB drifts, *Journal of Geophysical Research: Space Physics*, *101*(A8), 17,273–17,286, doi: 10.1029/96JA01403.

Oppenheim, M. M., and Y. S. Dimant (2013), Kinetic simulations of 3-D Farley-Buneman turbulence and anomalous electron heating, *Journal of Geophysical Research: Space Physics*, *118*(3), 1306–1318, doi: 10.1002/jgra.50196.

Oppenheim, M. M., A. F. vom Endt, and L. P. Dyrud (2000), Electrodynamics of meteor trail evolution in the equatorial E-region ionosphere, *Geophysical Research Letters*, *27*(19), 3173–3176, doi: 10.1029/1999GL000013.

Otani, N. F., and M. Oppenheim (1998), A saturation mechanism for the Farley-Buneman instability, *Geophysical Research Letters*, *25*(11), 1833–1836, doi: 10.1029/98GL50868.

Otani, N. F., and M. Oppenheim (2006), Saturation of the Farley-Buneman instability via three-mode coupling, *Journal of Geophysical Research: Space Physics*, *111*(A3), doi: 10.1029/2005JA011215.

Otto, A. (2005), The magnetosphere, in *Space Weather: The Physics Behind a Slogan*, edited by K. Scherer, H. Fichtner, B. Heber, and U. Mall, pp. 133–192, Springer Berlin Heidelberg, Berlin, Heidelberg, doi: 10.1007/978-3-540-31534-6_5.

Papadopoulos, K. (1977), A review of anomalous resistivity for the ionosphere, *Reviews of Geophysics*, *15*(1), 113–127, doi: 10.1029/RG015i001p00113.

Parker, E. N. (1957), Sweet's mechanism for merging magnetic fields in conducting fluids, *Journal of Geophysical Research*, *62*(4), 509–520, doi: 10.1029/JZ062i004p00509.

Parsons, A., et al. (2008), A scalable correlator architecture based on modular FPGA hardware, reuseable gateware, and data packetization, *Publications of the Astronomical Society of the Pacific*, *120*(873), 1207–1221.

Paschmann, G., et al. (1979), Plasma acceleration at the Earth's magnetopause: Evidence for reconnection, *Nature*, *282*(5736), 243.

Perry, G. W. (2015), Large scale plasma density perturbations in the polar F-region ionosphere, Ph.D. thesis, University of Saskatchewan.

Petrinec, S. M., and C. T. Russell (1996), Near-earth magnetotail shape and size as determined from the magnetopause flaring angle, *Journal of Geophysical Research: Space Physics*, *101*(A1), 137–152, doi: 10.1029/95JA02834.

Petschek, H. E. (1964), Magnetic field annihilation, *NASA Special Publication*, *50*, 425.

Pfaff, R. F. (2012), The near-Earth plasma environment, *Space Science Reviews*, *168*(1), 23–112, doi: 10.1007/s11214-012-9872-6.

Planck, M. (2013), *The Theory of Heat Radiation*, Courier Corporation.

Pocock, E., and C. Luetzelschwab (2012), Propagation of radio signals, in *The ARRL Handbook for Radio Communications 2013*, edited by H. Silver, S. Ford, and M. Wilson, chap. 19, pp. 19.1–19.34, The American Radio Relay League, Inc.

Prikryl, P., D. André, G. Sofko, and J. Koehler (1988), Doppler radar observations of harmonics of electrostatic ion cyclotron waves in the auroral ionosphere, *Journal of Geophysical Research: Space Physics*, *93*(A7), 7409–7424, doi: 10.1029/JA093iA07p07409.

Prikryl, P., D. André, J. Koehler, G. Sofko, and M. McKibben (1990), Evidence of highly localized auroral scatterers from 50-MHz CW radar interferometry, *Planetary and Space Science*, *38*(7), 933 – 944, doi: https://doi.org/10.1016/0032-0633(90)90060-4.

Prölss, G. (2012), *Physics of the Earth's Space Environment: an Introduction*, Springer Science & Business Media.

Qian, L., and S. Solomon (2012), Thermospheric density: An overview of temporal and spatial variations, *Space Science Reviews*, *168*(1), 147–173, doi: 10.1007/s11214-011-9810-z.

Rees, M., and R. Jones (1973), Time dependent studies of the aurora–II. spectroscopic morphology, *Planetary and Space Science*, *21*(7), 1213 – 1235, doi: https://doi.org/10.1016/0032-0633(73)90207-9.

Reid, G. (1968), The formation of smallscale irregularities in the ionosphere, *Journal of Geophysical Research*, *73*(5), 1627–1640, doi: 10.1029/JA073i005p01627.

Reiff, P. (1982), Sunward convection in both polar caps, *Journal of Geophysical Research: Space Physics*, *87*(A8), 5976–5980, doi: 10.1029/JA087iA08p05976.

Reiff, P. H., R. W. Spiro, and T. W. Hill (1981), Dependence of polar cap potential drop on interplanetary parameters, *Journal of Geophysical Research: Space Physics*, *86*(A9), 7639–7648, doi: 10.1029/JA086iA09p07639.

Reimer, A. S. (2018), Improved SuperDARN radar signal processing: A first principles statistical approach for reliable measurement uncertainties and enhanced data products, Ph.D. thesis, University of Saskatchewan.

Richards, M., J. Scheer, and W. Holm (2010), *Principles of Modern Radar: Basic Principles*, Scitech Publishing.

Rideout, B., J. Vierinen, F. Lind, R. Volz, and J. Swoboda (2018), Digital RF, *https://github.com/MITHaystack/digital_rf*.

Ridley, A. J., and E. A. Kihn (2004), Polar cap index comparisons with AMIE cross polar cap potential, electric field, and polar cap area, *Geophysical Research Letters*, *31*(7), doi: 10.1029/2003GL019113.

Riggin, D., W. Swartz, J. Providakes, and D. Farley (1986), Radar studies of longwavelength waves associated with midlatitude sporadic E layers, *Journal of Geophysical Research: Space Physics*, *91*(A7), 8011–8024, doi: 10.1029/JA091iA07p08011.

Rorabaugh, C. (1997), *Digital Filter Designer's Handbook: with C++ Algorithms*, McGraw-Hill.

Russell, C. T. (2004), Outer planet magnetospheres: a tutorial, *Advances in Space Research*, *33*(11), 2004 – 2020, doi: https://doi.org/10.1016/j.asr.2003.04.049, comparative Magnetospheres.

Russell, C. T., and R. C. Elphic (1978), Initial ISEE magnetometer results: magnetopause observations, *Space Science Reviews*, *22*(6), 681–715, doi: 10.1007/BF00212619.

Sahr, J., and B. Fejer (1996), Auroral electrojet plasma irregularity theory and experiment: A critical review of present understanding and future directions, *Journal of Geophysical Research: Space Physics*, *101*(A12), 26,893–26,909, doi: 10.1029/96JA02404.

Sahr, J., and F. Lind (1997), The Manastash Ridge radar: A passive bistatic radar for upper atmospheric radio science, *Radio Science*, *32*(6), 2345–2358, doi: 10.1029/97RS02454.

Schlegel, K. (1996), Coherent backscatter from ionospheric E-region plasma irregularities, *Journal of Atmospheric and Terrestrial Physics*, *58*(8), 933 – 941, doi: https://doi.org/10.1016/0021-9169(95)00124-7.

Schunk, R., and A. Nagy (2009), *Ionospheres: Physics, Plasma Physics, and Chemistry*, Cambridge University Press.

Scientific Instrumentation Ltd. (1993), SuperDARN Driver Amplifier Circuit Schematic, *Tech. rep.*, Scientific Instrumentation Ltd.

Sedra, A., and K. Smith (2004), *Microelectronic Circuits*, 5th ed., Oxford University Press.

Sedra, A., and K. Smith (2010), *Microelectronic Circuits*, 6th ed., Oxford University Press.

Sergeev, V. A., V. Angelopoulos, D. G. Mitchell, and C. T. Russell (1995), In situ observations of magnetotail reconnection prior to the onset of a small substorm, *Journal of Geophysical Research: Space Physics*, *100*(A10), 19,121–19,133, doi: 10.1029/95JA01471.

Shepherd, S. G., R. A. Greenwald, and J. M. Ruohoniemi (2002), Cross polar cap potentials measured with super dual auroral radar network during quasisteady solar wind and interplanetary magnetic field conditions, *Journal of Geophysical Research: Space Physics*, *107*(A7), SMP 5–1–SMP 5–11, doi: 10.1029/2001JA000152.

Sibeck, D. G., R. E. Lopez, and E. C. Roelof (1991), Solar wind control of the magnetopause shape, location, and motion, *Journal of Geophysical Research: Space Physics*, *96*(A4), 5489–5495, doi: 10.1029/90JA02464.

Silver, H. (2012), Electrical fundamentals, in *The ARRL Handbook for Radio Communications 2013*, edited by H. Silver, S. Ford, and M. Wilson, chap. 2, pp. 2.1–2.75, The American Radio Relay League, Inc.

Silver, H., L. Kay, W. Hayward, B. Larkin, J. Brown, P. Wade, and J. Taylor (2012), RF techniques, in *The ARRL Handbook for Radio Communications 2013*, edited by H. Silver, S. Ford, and M. Wilson, chap. 5, pp. 5.1–5.37, The American Radio Relay League, Inc.

Skellett, A. M. (1935), The ionizing effects of meteors, *Proceedings of the Institute of Radio Engineers*, *23*(2), 132–149, doi: 10.1109/IRE.1935.6449184.

Sonnerup, B. U., G. Paschmann, I. Papamastorakis, N. Sckopke, G. Haerendel, S. J. Bame, J. R. Asbridge, J. T. Gosling, and C. T. Russell (1981), Evidence for magnetic field reconnection at the earth's magnetopause, *Journal of Geophysical Research: Space Physics*, *86*(A12), 10,049–10,067, doi: 10.1029/JA086iA12p10049.

Sparke, L. S., and J. S. Gallagher III (2007), *Galaxies in the universe: an introduction*, Cambridge University Press.

St.-Maurice, J.-P., and J. Chau (2016), A theoretical framework for the changing spectral properties of meter-scale Farley-Buneman waves between 90 and 125km altitudes, *Journal of Geophysical Research: Space Physics*, *121*(10), 10,341–10,366, doi: 10.1002/2016JA023105.

St.-Maurice, J.-P., and A. M. Hamza (2001), A new nonlinear approach to the theory of E region irregularities, *Journal of Geophysical Research: Space Physics*, *106*(A2), 1751–1759, doi: 10.1029/2000JA000246.

St.-Maurice, J.-P., P. Prikryl, D. Danskin, A. Hamza, G. Sofko, J. Koehler, A. Kustov, and J. Chen (1994), On the origin of narrow non-ion-acoustic coherent radar spectra in the high-latitude E region, *Journal of Geophysical Research: Space Physics*, *99*(A4), 6447–6474, doi: 10.1029/93JA02353.

Stasiewicz, K., et al. (2000), Small scale Alfvénic structure in the aurora, *Space Science Reviews*, *92*(3), 423–533, doi: 10.1023/A:1005207202143.

Stockton, D., F. Telewski, and J. DeHaven (2012), Oscillators and synthesizers, in *The ARRL Handbook for Radio Communications 2013*, edited by H. Silver, S. Ford, and M. Wilson, chap. 9, pp. 9.1–9.54, The American Radio Relay League, Inc.

Stoica, P., Z. Wang, and J. Li (2003), Robust Capon beamforming, *IEEE Signal Processing Letters*, *10*(6), 172–175.

Straw, D., and G. Cutsogeorge (2012), Transmission lines, in *The ARRL Handbook for Radio Communications 2013*, edited by H. Silver, S. Ford, and M. Wilson, chap. 20, pp. 20.1–20.31, The American Radio Relay League, Inc.

Straw, R., L. Cebik, D. Hallidy, D. Jansson, R. Lewallen, R. Severns, and F. Witt (Eds.) (2007), *The ARRL Antenna Book 21st Edition*, The American Radio Relay League, Inc.

Streltsov, A., T. Pedersen, E. Mishin, and A. Snyder (2010), Ionospheric feedback instability and substorm development, *Journal of Geophysical Research: Space Physics*, *115*(A7), doi: 10.1029/2009JA014961.

Sturrock, P. A. (1999), Chromospheric magnetic reconnection and its possible relationship to coronal heating, *The Astrophysical Journal*, *521*(1), 451.

Sudan, R. N., J. Akinrimisi, and D. T. Farley (1973), Generation of small-scale irregularities in the equatorial electrojet, *Journal of Geophysical Research*, *78*(1), 240–248, doi: 10.1029/JA078i001p00240.

Sugar, G. R. (1964), Radio propagation by reflection from meteor trails, *Proceedings of the IEEE*, *52*(2), 116–136, doi: 10.1109/PROC.1964.2801.

Sulzer, M. (1989), Recent incoherent scatter techniques, *Advances in Space Research*, *9*(5), 153 – 162, doi: https://doi.org/10.1016/0273-1177(89)90353-0.

Takahashi, Y., Y. Okazaki, M. Sato, H. Miyahara, K. Sakanoi, P. Hong, and N. Hoshino (2010), 27-day variation in cloud amount in the western Pacific warm pool region and relationship to the solar cycle, *Atmospheric Chemistry and Physics*, *10*(4), 1577–1584.

Texas Instruments (2017), *DAC38RF8x Dual-Channel, Differential-Output, 14-Bit, 9-GSPS, RF-Sampling DAC With JESD204B Interface, On-Chip PLL and Wide-Band Interpolation*, Texas Instruments, rev. B.

The HDF Group (1997-2018), Hierarchical data format, version 5, http://www.hdfgroup.org/HDF5/.

Thébault, E., et al. (2015), International geomagnetic reference field: the 12th generation, *Earth, Planets and Space*, *67*(1), 79, doi: 10.1186/s40623-015-0228-9.

Thomas, K. (2006), *Beginning Ubuntu Linux: From novice to professional*, Apress.

Thomsen, M. (2004), Why Kp is such a good measure of magnetospheric convection, *Space Weather*, *2*(11), doi: 10.1029/2004SW000089.

Thomson, J. (1906), *Conduction of Electricity Through Gases*, Cambridge University Press.

Titheridge, J. (1972), Determination of ionospheric electron content from the Faraday rotation of geostationary satellite signals, *Planetary and Space Science*, *20*(3), 353 – 369, doi: https://doi.org/10.1016/0032-0633(72)90034-7.

Tonne, J., H. Silver, D. Tayloe, and D. Gordon-Smith (2012), RF and AF filters, in *The ARRL Handbook for Radio Communications 2013*, edited by H. Silver, S. Ford, and M. Wilson, chap. 11, pp. 11.1–11.52, The American Radio Relay League, Inc.

Treumann, R. A. (2001), Origin of resistivity in reconnection, *Earth, planets and space*, *53*(6), 453–462.

Tsuda, T., T. Sato, and K. Maeda (1966), Formation of sporadic E layers at temperate latitudes due to vertical gradients of charge density, *Radio Science*, *1*(2), 212–225, doi: 10.1002/rds196612212.

Tsunoda, R. (1988), High-latitude F region irregularities: A review and synthesis, *Reviews of Geophysics*, *26*(4), 719–760.

Tu, C.-Y., and E. Marsch (1997), Two-fluid model for heating of the solar corona and acceleration of the solar wind by high-frequency Alfvén waves, *Solar Physics*, *171*(2), 363–391, doi: 10.1023/A:1004968327196.

Uda, S., and Y. Mushiake (1954), *Yagi-Uda Antenna*, Research Institute of Electrical Communication, Tohoku University.

Valentic, T., J. Buonocore, M. Cousins, C. Heinselman, J. Jorgensen, J. Kelly, M. Malone, M. Nicolls, and A. Van Eyken (2013), AMISR the advanced modular incoherent scatter radar, in *2013 IEEE International Symposium on Phased Array Systems & Technology,*, pp. 659–663, IEEE.

van Ballegooijen, A. A., M. Asgari-Targhi, S. R. Cranmer, and E. E. DeLuca (2011), Heating of the solar chromosphere and corona by Alfvén wave turbulence, *The Astrophysical Journal*, *736*(1), 3.

Vickrey, J. F., and M. C. Kelley (1982), The effects of a conducting E layer on classical F region cross-field plasma diffusion, *Journal of Geophysical Research: Space Physics*, *87*(A6), 4461–4468, doi: 10.1029/JA087iA06p04461.

Vierinen, J., J. Chau, N. Pfeffer, M. Clahsen, and G. Stober (2016), Coded continuous wave meteor radar, *Atmospheric Measurement Techniques*, *9*(2), 829–839, doi: 10.5194/amt-9-829-2016.

Vogler, L., and J. Hoffmeyer (1993), A model for wideband HF propagation channels, *Radio Science*, *28*(06), 1131–1142, doi: 10.1029/93RS01607.

Wade, P. (2010), High-power directional couplers with excellent performance, *Tech. rep.*, retrieved on March 4, 2019 from http://www.w1ghz.org/antbook/conf/High-Power_Directional_Couplers_with_Excellent_Performance.pdf.

Wang, J., Z. Guo, Y. Ge, A. Du, C. Huang, and P. Qin (2018), The responses of the Earth´s magnetopause and bow shock to the IMF Bz and the solar wind dynamic pressure: a parametric study using the AMR-CESE-MHD model, *J. Space Weather Space Clim.*, *8*, A41, doi: 10.1051/swsc/2018030.

Warren, H. P., and D. H. Brooks (2009), The temperature and density structure of the solar corona. I. observations of the quiet Sun with the EUV imaging spectrometer on Hinode, *The Astrophysical Journal*, *700*(1), 762.

Watermann, J. (1990), Refraction of 50-MHz radar waves in a realistic ionospheric model, *Radio Science*, *25*(5), 805–812, doi: 10.1029/RS025i005p00805.

Watt, R., A. Wilkins, and E. Bowen (1937), The return of radio waves from the middle atmosphere—I, *Proceedings of the Royal Society of London A: Mathematical, Physical and Engineering Sciences*, *161*(905), 181–196, doi: 10.1098/rspa.1937.0140.

Weiss, N. (2002), Dynamos in planets, stars and galaxies, *Astronomy & Geophysics*, *43*(3), 3.9–3.14, doi: 10.1046/j.1468-4004.2002.43309.x.

Willis, N. J. (2005), *Bistatic Radar*, vol. 2, SciTech Publishing.

Withbroe, G. L. (1988), The temperature structure, mass, and energy flow in the corona and inner solar wind, *The Astrophysical Journal*, *325*, 442–467.

Wong, G. S. K. (1986), Speed of sound in standard air, *The Journal of the Acoustical Society of America*, *79*(5), 1359–1366, doi: 10.1121/1.393664.

Wu, Y., and J. Li (1998), The design of digital radar receivers, *IEEE Aerospace and Electronic Systems Magazine*, *13*(1), 35–41.

Yang, C., M. Miller, T. Nguyen, and E. Blasch (2007), Comparative study of coherent, non-coherent, and semi-coherent integration schemes for GNSS receivers (preprint), *Tech. rep.*, Sigtem Technology, Inc.

Yau, A., G. James, and W. Liu (2006), The Canadian enhanced polar outflow probe (e-POP) mission in ILWS, *Advances in Space Research*, *38*(8), 1870 – 1877, doi: https://doi.org/10.1016/j.asr.2005.01.058, magnetospheric dynamics and the international living with a star program.

Appendix A

Electrodynamics

A general understanding of electrodynamics is the basis needed to achieve the research objectives of this dissertation. This includes understanding Maxwell's equations, the continuity equation and the equation of motion for charged particles.

A.1 Maxwell's Equations

Maxwell's equations provide a framework of the physics governing magnetic and electric fields [*Griffiths*, 1999; *Chen*, 2006]. This section describes the different equations.

The first Maxwell equation states that the divergence of an electric field is proportional to the charge density of an object. Larger charge densities produce stronger electric fields. The equation is given as,

$$\nabla \cdot \mathbf{E} = \frac{\rho}{\epsilon_0} \tag{A.1}$$

where $\mathbf{E}$ is the electric field vector, ρ is the charge density, and ϵ_0 is the permittivity of free space.

Magnetic fields do not diverge, as can be seen in equation A.2. This equation states that magnetic fields must create a loop,

$$\nabla \cdot \mathbf{B} = 0 \tag{A.2}$$

where $\mathbf{B}$ is the magnetic field vector.

Equation A.3 states that the "rotation" or curl of an electric field is proportional to the change in the magnetic field over time. The curl can also be thought of as the spatial rate of change in the perpendicular direction of the electric field.

$$\nabla \times \mathbf{E} = -\frac{\partial \mathbf{B}}{\partial t} \tag{A.3}$$

where t is the time.

The fourth Maxwell equation is given in equation A.4. This equation states that the curl of a magnetic field vector is related to the current density ($\mathbf{J}$) and the change in the electric field over time, with μ_0 being the permeability of free space. The equation states that there will be a magnetic field acting in a circular direction around a flow of current or a time varying electric field.

$$\nabla \times \mathbf{B} = \mu_0 \left(\mathbf{J} + \epsilon_0 \frac{\partial \mathbf{E}}{\partial t} \right) \tag{A.4}$$

The equations can also be written in integral form. Equation A.5 states that the electric field exiting a surface is proportional to the volume of charge within that surface.

$$\oiint_{S(V)} \mathbf{E} \cdot \mathrm{d}\mathbf{S} = \frac{1}{\epsilon_0} \iiint_{V} \rho \, \mathrm{d}\mathbf{V} \tag{A.5}$$

Equation A.6 states that the flux of the magnetic fields exiting and entering a closed surface must equal 0.

$$\oiint_{S(V)} \mathbf{B} \cdot \mathrm{d}\mathbf{S} = 0 \tag{A.6}$$

Equation A.7 states that the electric field on a line around an area is equal to the change in magnetic flux through that area, where magnetic flux is defined as the magnetic field multiplied by the area that magnetic field exists in,

$$\oint_{l(A)} \mathbf{E} \cdot \mathrm{d}\mathbf{l} = -\frac{\partial}{\partial t} \iint_{A} \mathbf{B} \cdot \mathrm{d}\mathbf{A} \tag{A.7}$$

Equation A.8 states that the magnetic field on a closed loop around an area is equal to the current through the area and the change in electric flux through the area,

$$\oint_{l(A)} \mathbf{B} \cdot \mathrm{d}\mathbf{l} = \mu_0 \iint_{A} \mathbf{J} \cdot \mathrm{d}\mathbf{A} + \mu_0 \epsilon_0 \frac{\partial}{\partial t} \iint_{A} \mathbf{E} \cdot \mathrm{d}\mathbf{A} \tag{A.8}$$

These equations provide a basis on how electric and magnetic fields are created and defined. They can be used to predict EM behaviour in given situations.

A.2 Magnetohydrodynamic Plasma Equations

Along with the EM fields, charged particles must be considered in a system. The first thing that can be considered is the density of the medium in a given region, not including the charged nature of the particles. To model the density of a medium, the continuity equation can be used. This is given by the equation [*Chen*, 2006],

$$\frac{\partial n}{\partial t} + \nabla \cdot (n\mathbf{v}) = q - l \tag{A.9}$$

where n is the density of the medium, $\mathbf{v}$ is the velocity of the medium, q is the production function and l is the loss function. The production and loss functions are used to model the creation and recombination of the plasma ions and electrons due to external and internal factors. The continuity equation shows how the density changes as a function of time.

Another important equation is the plasma equation of motion. This equation equates the change in momentum of a fluid over time with the sum of the forces acting on that fluid. The equation given below is the equation of motion for the ions in a plasma. Notice that there are EM force terms and a friction term for collisions with the neutral particles in the plasma [*Chen*, 2006]. The equation is,

$$nm(\frac{\partial}{\partial t} + \mathbf{v} \cdot \nabla)\mathbf{v} = nm\mathbf{g} + qn(\mathbf{E} + \mathbf{v} \times \mathbf{B}) - \nabla p - nm\nu(\mathbf{v} - \mathbf{u}) \tag{A.10}$$

where n is the density of the species, m is the mass of the species, $\mathbf{v}$ is the velocity of the species, $\mathbf{g}$ is gravity, q is the charge of the species, $\mathbf{E}$ is the electric field, $\mathbf{B}$ is the magnetic field, p is the pressure (Section A.3), ν is the collision rate with other species, and $\mathbf{u}$ is the velocity of the other species. $(\frac{\partial}{\partial t} + \mathbf{v} \cdot \nabla)$ is the convective derivative of a parameter, where it includes the rate of change due to a moving reference frame.

Using the Maxwell equations, the plasma equation of motion, and the continuity equation it is possible to model the behaviour of a plasma. One thing that can be derived is the oscillation frequency of a plasma. The oscillations in a plasma are considered to be small compared to the background electric fields and plasma density. This allows the equations to be linearized using Fourier theory, where $E = E_0 + E_1 \exp(j[\mathbf{k} \cdot \mathbf{r} - \omega t])$, $n_e = n_{0e} + n_{1e} \exp(j[\mathbf{k} \cdot \mathbf{r} - \omega t])$, and $v = v_0 + v_1 \exp(j[\mathbf{k} \cdot \mathbf{r} - \omega t])$. In these equations k is the wave vector

of the oscillation, and ω is the frequency of the oscillation, with the 1 subscript referring to the amplitude of the perturbation. The oscillation frequency of a plasma can be derived using equation A.1, the plasma equation of motion, and the continuity equation, following the derivation in *Chen* [2006].

The linearized divergence of the electric field is,

$$jkE_1 = -\frac{n_{1e}e}{\epsilon_0} \tag{A.11}$$

The plasma equation of motion for electrons can be linearized and reduced to,

$$m_e(-j\omega v_{1e} + jkv_{0e}v_{1e}) = -eE_1 \tag{A.12}$$

The linearized electron continuity equation, neglecting the production and loss terms, is,

$$-j\omega n_{1e} + jk(n_{0e}v_{1e} + n_{1e}v_{0e}) = 0 \tag{A.13}$$

Combining Equations A.11, A.12, and A.13 together one arrives at,

$$(m_e j\omega)\frac{j\omega - jkv_{0e}}{jkn_{0e}}n_{1e} - (m_e jkv_{0e})\frac{j\omega - jkv_{0e}}{jkn_{0e}}n_{1e} = -e\frac{n_{1e}e}{jk\epsilon_0} \tag{A.14}$$

Grouping terms and simplifying,

$$(\omega - kv_{0e})^2 = \frac{e^2 n_{0e}}{m_e\epsilon_0} \tag{A.15}$$

If the plasma is stationary ($v_{0e} = 0$),

$$\omega = \omega_{pe} = \sqrt{\frac{e^2 n_e}{m_e\epsilon_0}} \tag{A.16}$$

where ω_{pe} is defined as the plasma frequency and is the frequency that electrons in the plasma oscillate at. Radio frequencies below this are reflected by the plasma, while frequencies above this frequency can pass through. A discussion on radio wave propagation in the ionosphere is provided in Chapter 4.

A.3 Plasma Pressure

The pressure force is an important factor in fluid dynamics. For gases, the Ideal Gas Law is used to model the pressure of a system, and is given by *Chen* [2006],

$$p = nk_BT \tag{A.17}$$

where n is the number density of the gas, k_B is the boltzmann constant, and T is the temperature of the gas. If the gas experiences adiabatic compression rather than isothermal compression (temperature changes due to compression/expansion), the gradient of the pressure with respect to the gradient of the density is given by,

$$\nabla p = \gamma \frac{\nabla n}{n} p \tag{A.18}$$

The value for the adiabatic constant (γ) is based on the number of degrees of freedom of the molecules in the gas. The gradient of pressure term in equation A.10 is therefore,

$$\nabla p = \gamma k_B T \nabla n \tag{A.19}$$

A.4 Charged Particle Motion with a Magnetic Field

Charged particles travel easily along magnetic field lines but have difficulty travelling perpendicular to them. Any movement perpendicular to the magnetic field causes the charged particle to be deflected in a direction perpendicular to both its motion and the magnetic field. This arises from the fact that magnetic fields exert a force relative to the cross-product of $\mathbf{v}$ and $\mathbf{B}$, where $\mathbf{v}$ is the velocity of the charged particle and $\mathbf{B}$ is the magnetic field vector [*Chen*, 2006]. This is provided by the equation,

$$\mathbf{F}_{mag} = q(\mathbf{v} \times \mathbf{B}) \tag{A.20}$$

where q is the charge of the particle.

A charged particle with a background constant electric and magnetic field will experience a drift in the direction perpendicular to both the electric and magnetic fields. This can be shown using a force balance equation for EM forces acting on a charged particle,

$$m \frac{\partial \mathbf{v}}{\partial t} = q(\mathbf{E} + \mathbf{v} \times \mathbf{B}) \tag{A.21}$$

where m is the mass of the particle, q is the charge of the particle, and $\mathbf{E}$ is the electric field.

If we solve for the system at equilibrium, we can solve for the velocity of the charged particles. Setting ($\partial \mathbf{v}/\partial t = 0$), the plasma equation of motion becomes,

$$\mathbf{E} + \mathbf{v} \times \mathbf{B} = 0 \tag{A.22}$$

Multiplying the Equation A.22 by the cross-product of the magnetic field, one arrives at,

$$\mathbf{E} \times \mathbf{B} + (\mathbf{v} \times \mathbf{B}) \times \mathbf{B} = 0 \tag{A.23}$$

Use the vector triple product rule to obtain,

$$\mathbf{E} \times \mathbf{B} - \mathbf{v}(\mathbf{B} \cdot \mathbf{B}) + \mathbf{B}(\mathbf{v} \cdot \mathbf{B}) = 0 \tag{A.24}$$

By solving for the charged particle velocity, the equation becomes,

$$\mathbf{v}_D = \frac{\mathbf{E} \times \mathbf{B}}{B^2} + \frac{\mathbf{B}}{B^2}(\mathbf{v} \cdot \mathbf{B}) \tag{A.25}$$

If one separates the equation into perpendicular and parallel components with respect to the magnetic field, the velocity perpendicular to the magnetic field is,

$$\mathbf{v}_{D\perp} = \frac{\mathbf{E} \times \mathbf{B}}{B^2} \tag{A.26}$$

and the velocity parallel to the magnetic field is,

$$\mathbf{v}_{D\parallel} = \frac{\mathbf{B}}{B^2}(\mathbf{v} \cdot \mathbf{B}) \tag{A.27}$$

From this it is evident that the parallel velocity is constant. Note that this is derived considering a system at equilibrium, where an electric field parallel to the magnetic field would accelerate a charged particle in the direction of the magnetic field with no deflection of the trajectory.

Equation A.26 states that a charged particle in equilibrium with a constant background magnetic and electric field will travel with a velocity of $(\mathbf{E} \times \mathbf{B})/B^2$ that is perpendicular to both the electric and magnetic fields. This drift is charge neutral, meaning it affects ions and electrons the same way. The result is that both ions and electrons will experience the same drift velocity in the same direction. Parallel to the magnetic field the charged particle would experience a force just due to the electric field component parallel to the magnetic field.

The case above was for a straight line magnetic field. This is not physical as the divergence of a magnetic field is zero, meaning there is some curvature of a magnetic field. For the ionosphere, the charged particle motion due to the curvature of the background magnetic

field is considered small, and will not be considered to simplify the analysis. Therefore the charged particle motion is considered to be in the $\mathbf{E} \times \mathbf{B}$ direction, without including other effects such as collisions. The neglected effects have a significant effect in real world situations, and are covered in the derivation of the ionospheric convection and conductance provided in Appendix B.

A.5 Charged Particle Frozen-in Condition

When considering low collision rate plasmas, an interesting phenomenon happens, where the magnetic field and the plasma become bound together. This is due to the lack of collisions, which corresponds to an extremely large conductivity. One instance where this occurs is in the solar wind, and is known as the frozen-in condition. The derivation shown here follows that of *Kelley* [2009].

From Equation A.3, we know that,

$$\frac{\partial \mathbf{B}}{\partial t} = -\nabla \times \mathbf{E} \tag{A.28}$$

and the current density is given by,

$$\mathbf{J} = \sigma(\mathbf{E} + \mathbf{v} \times \mathbf{B}) \tag{A.29}$$

where σ is the conductivity of the plasma.

Substituting the electric field from equation A.29 into equation A.28,

$$\frac{\partial \mathbf{B}}{\partial t} = \nabla \times (\mathbf{v} \times \mathbf{B}) - \frac{1}{\sigma}(\nabla \times \mathbf{J}) \tag{A.30}$$

If $\sigma \to \infty$, the change in the magnetic field over time becomes,

$$\frac{\partial \mathbf{B}}{\partial t} = \nabla \times (\mathbf{v} \times \mathbf{B}) \tag{A.31}$$

As an aside, if one substitutes Equation A.31 into Equation A.28,

$$-\nabla \times \mathbf{E} = \nabla \times (\mathbf{v} \times \mathbf{B}) \tag{A.32}$$

From this, the electric field for an infinitely conducting plasma is given by,

$$\mathbf{E} = -\mathbf{v} \times \mathbf{B} \tag{A.33}$$

This has interesting consequences as it relates to the electric fields that occur in the ionosphere of the Earth, as discussed in Section 2.4.2.

If we now consider the magnetic flux through an area of plasma, we can write the change in flux over time as,

$$\frac{\partial \phi_B}{\partial t} = \oiint_A \frac{\partial \mathbf{B}}{\partial t} \cdot \mathrm{d}\mathbf{A} + \int_{l(A)} \mathbf{B} \cdot (\mathbf{v} \times \mathrm{d}\mathbf{l}) \tag{A.34}$$

where the left term is the change in flux due to time variation, and the right term is due to the motion of the surface.

The right term can be re-arranged to match the format of the left term,

$$\int_{l(A)} \mathbf{B} \cdot (\mathbf{v} \times \mathrm{d}\mathbf{l}) = -\int_{l(A)} (\mathbf{B} \times \mathbf{v}) \cdot \mathrm{d}\mathbf{l} = -\oiint_A \nabla \times (\mathbf{v} \times \mathbf{B}) \cdot \mathrm{d}\mathbf{A} \tag{A.35}$$

This results in the following equation,

$$\frac{\partial \phi}{\partial t} = \oiint_A \left[\frac{\partial \mathbf{B}}{\partial t} - \nabla \times (\mathbf{v} \times \mathbf{B}) \right] \cdot \mathrm{d}\mathbf{A} \tag{A.36}$$

From this result and equation A.31, as long as the conductivity of the plasma approaches infinity (very low collisions), the change in the magnetic flux over time will be 0. This is known as the "frozen-in" condition. The conductivity approaching infinity in the solar wind plasma is a valid approximation [*Kelley*, 2009], which is due to the low density of the plasma resulting in very few collisions between charged particles ($\omega_{ce}, \omega_{ci} \gg \nu_e, \nu_i$). ω_{ce} is the cyclotron frequency of the electrons, ω_{ci} is the cyclotron frequency of the ions, ν_e is the collision frequency of the electrons, and ν_i is the collision frequency of the ions.

Appendix B

Ionospheric Convection and Conductivity

A basic discussion of the steady state plasma dynamics with a background magnetic field was provided in Appendix A, where only the background electric and magnetic fields were considered in the analysis. For the derivation of the steady state motion of the plasma in the ionosphere, we will include the neutral particles. This derivation follows the derivation in *Kelley* [2009].

Starting with the ion equation of motion given by,

$$n_i m_i \left(\frac{\partial}{\partial t} + \mathbf{v}_i \cdot \nabla \right) \mathbf{v}_i = n_i m_i \mathbf{g} + q_i n_i (\mathbf{E} + \mathbf{v}_i \times \mathbf{B}) - \nabla p - n_i m_i \nu_{in} (\mathbf{v}_i - \mathbf{u}) \tag{B.1}$$

where n_i is the ion number density, m_i is the ion mass, $\mathbf{v}_i$ is the ion velocity, $\mathbf{g}$ is gravity, q_i is the charge of the ion, $\mathbf{E}$ is the background electric field, $\mathbf{B}$ is the magnetic field of the Earth, p is the pressure, ν_{in} is the collision frequency between the ions and neutrals and $\mathbf{u}$ is the neutral wind velocity.

Neglecting the pressure and gravity terms and considering the system at equilibrium (no acceleration), the equation becomes,

$$0 = q_i (\mathbf{E} + \mathbf{v}_i \times \mathbf{B}) - m_i \nu_{in} (\mathbf{v}_i - \mathbf{u}) \tag{B.2}$$

From this it is possible to determine the ion velocity. The electric field and the neutral wind can be combined into one force, given by,

$$\mathbf{F} = q_i \mathbf{E} + m_i \nu_{in} \mathbf{u} \tag{B.3}$$

This results in the equation,

$$\mathbf{v}_i = \frac{1}{m_i \nu_{in}} \left[q_i (\mathbf{v}_i \times \mathbf{B}) + \mathbf{F} \right] \tag{B.4}$$

Taking the cross-product of this with the magnetic field results in,

$$\mathbf{v}_i \times \mathbf{B} = \frac{1}{m_i \nu_{in}} \left[q_i \mathbf{B}(\mathbf{v}_i \cdot \mathbf{B}) - q_i B^2 \mathbf{v}_i + \mathbf{F} \times \mathbf{B} \right] \tag{B.5}$$

Taking the dot product of Equation B.4 with the magnetic field results in,

$$\mathbf{v}_i \cdot \mathbf{B} = \frac{\mathbf{F} \cdot \mathbf{B}}{m_i \nu_{in}} \tag{B.6}$$

Substituting the cross-product and dot product with the magnetic field into equation B.4, the result is,

$$\mathbf{v}_i = \frac{1}{m_i \nu_{in}} \left[\frac{q_i}{m_i \nu_{in}} \left[\frac{q_i}{m_i \nu_{in}} (\mathbf{F} \cdot \mathbf{B}) \mathbf{B} - q_i B^2 \mathbf{v}_i + \mathbf{F} \times \mathbf{B} \right] + \mathbf{F} \right] \tag{B.7}$$

The equation for the cyclotron frequency of a charged particle is given by [*Chen*, 2006],

$$\omega_{ci,ce} = \frac{q_{i,e} B}{m_{i,e}} \tag{B.8}$$

where $\omega_{ci,ce}$ is the ion or electron cyclotron frequency, $q_{i,e}$ is the charge of the ion or electron, B is the magnetic field and $m_{i,e}$ is the mass of the ion or electron. While electrons have the same mass, the ion mass will be dependent on the atom or molecule under consideration.

Equation B.7 can be solved for $\mathbf{v}_i$, resulting in the equation,

$$\mathbf{v}_i = \frac{1}{m_i \nu_{in}} \left[\frac{\omega_{ci}^2}{\nu_{in}^2 + \omega_{ci}^2} (\mathbf{F} \cdot \mathbf{b}) \mathbf{b} + \frac{\omega_{ci} \nu_{in}}{\nu_{in}^2 + \omega_{ci}^2} (\mathbf{F} \times \mathbf{b}) + \frac{\nu_{in}^2}{\nu_{in}^2 + \omega_{ci}^2} \mathbf{F} \right] \tag{B.9}$$

where $\mathbf{b} = \mathbf{B}/B$.

If the z-axis of the coordinate system is taken to be the direction of the magnetic field, the force vector can be separated into parallel and perpendicular components ($\mathbf{F}_\parallel \equiv \mathbf{F_z}$, $\mathbf{F}_\perp \equiv \mathbf{F_x} + \mathbf{F_y}$),

$$\mathbf{v}_i = \frac{1}{m_i \nu_{in}} \left[\frac{\omega_{ci}^2}{\nu_{in}^2 + \omega_{ci}^2} \mathbf{F}_\parallel + \frac{\omega_{ci} \nu_{in}}{\nu_{in}^2 + \omega_{ci}^2} (\mathbf{F}_\perp \times \mathbf{b}) + \frac{\nu_{in}^2}{\nu_{in}^2 + \omega_{ci}^2} \mathbf{F}_\perp + \frac{\nu_{in}^2}{\nu_{in}^2 + \omega_{ci}^2} \mathbf{F}_\parallel \right] \tag{B.10}$$

$$\mathbf{v}_i = \frac{1}{m_i \nu_{in}} \left[\mathbf{F}_\parallel + \frac{\omega_{ci} \nu_{in}}{\nu_{in}^2 + \omega_{ci}^2} (\mathbf{F}_\perp \times \mathbf{b}) + \frac{\nu_{in}^2}{\nu_{in}^2 + \omega_{ci}^2} \mathbf{F}_\perp \right] \tag{B.11}$$

This can be re-written as a tensor,

$$\mathbf{v}_i = \overset{\leftrightarrow}{\mathbf{k}}_i \mathbf{F} \tag{B.12}$$

$$\overleftrightarrow{\mathbf{k}}_i = \frac{1}{m_i \nu_{in}} \begin{pmatrix} \frac{\nu_{in}^2}{\nu_{in}^2+\omega_{ci}^2} & \frac{\omega_{ci}\nu_{in}}{\nu_{in}^2+\omega_{ci}^2} & 0 \\ -\frac{\omega_{ci}\nu_{in}}{\nu_{in}^2+\omega_{ci}^2} & \frac{\nu_{in}^2}{\nu_{in}^2+\omega_{ci}^2} & 0 \\ 0 & 0 & 1 \end{pmatrix} \tag{B.13}$$

Substituting the terms back in for $\mathbf{F}$, the velocity of the ions is,

$$\mathbf{v}_i = \overleftrightarrow{\mathbf{k}}_i(q_i\mathbf{E} + m_i\nu_{in}\mathbf{u}) \tag{B.14}$$

A similar analysis can be performed for the electrons to determine the electron velocity. The only difference in the analysis is the change of sign for the charge. The electron tensor is therefore,

$$\overleftrightarrow{\mathbf{k}}_e = \frac{1}{m_e \nu_{en}} \begin{pmatrix} \frac{\nu_{en}^2}{\nu_{en}^2+\omega_{ce}^2} & -\frac{|\omega_{ce}|\nu_{en}}{\nu_{en}^2+\omega_{ce}^2} & 0 \\ \frac{|\omega_{ce}|\nu_{en}}{\nu_{en}^2+\omega_{ce}^2} & \frac{\nu_{en}^2}{\nu_{en}^2+\omega_{ce}^2} & 0 \\ 0 & 0 & 1 \end{pmatrix} \tag{B.15}$$

and the equation for the electron velocity is then,

$$\mathbf{v}_e = -\overleftrightarrow{\mathbf{k}}_e(|q_e|\mathbf{E} - m_e\nu_{en}\mathbf{u}) \tag{B.16}$$

Current is defined as the movement of charge, where the particles that carry charge are ions or electrons. Current is therefore the movement of electrons and ions. From this we can define the current density in a plasma as the density of plasma (assuming quasi-neutrality) multiplied by the difference between the ion and electron velocities.

The current is then given by,

$$\mathbf{J} = n_e(q_i\mathbf{v_i} - |q_e|\mathbf{v_e}) \tag{B.17}$$

Substituting in Equations B.16 and B.14 (the magnitudes of q_i and q_e are considered to be equal and constant),

$$\mathbf{J} = n_e|q_e|(\overleftrightarrow{\mathbf{k}}_i(q_i\mathbf{E} + m_i\nu_{in}\mathbf{u}) - [-\overleftrightarrow{\mathbf{k}}_e(|q_e|\mathbf{E} - m_e\nu_{en}\mathbf{u})]) \tag{B.18}$$

$$\mathbf{J} = n_e|q_e|(q_i\overleftrightarrow{\mathbf{k}}_i\mathbf{E} + m_i\nu_{in}\overleftrightarrow{\mathbf{k}}_i\mathbf{u} + |q_e|\overleftrightarrow{\mathbf{k}}_e\mathbf{E} - m_e\nu_{en}\overleftrightarrow{\mathbf{k}}_e\mathbf{u}) \tag{B.19}$$

$$\mathbf{J} = n_e|q_e|^2(\overleftrightarrow{\mathbf{k}}_i + \overleftrightarrow{\mathbf{k}}_e)\mathbf{E} + n_e|q_e|(m_i\nu_{in}\overleftrightarrow{\mathbf{k}}_i - m_e\nu_{en}\overleftrightarrow{\mathbf{k}}_e)\mathbf{u} \tag{B.20}$$

Re-writing the right side of the equation in tensor format, the equation becomes,

$$\mathbf{J} = \overleftrightarrow{\sigma}_E \mathbf{E} + \overleftrightarrow{\sigma}_u \mathbf{u} \tag{B.21}$$

where,

$$\overleftrightarrow{\sigma}_E = n_e|q_e|^2 \begin{pmatrix} \frac{1}{m_i}\frac{\nu_{in}}{\nu_{in}^2+\omega_{ci}^2} + \frac{1}{m_e}\frac{\nu_{en}}{\nu_{en}^2+\omega_{ce}^2} & \frac{1}{m_i}\frac{\omega_{ci}}{\nu_{in}^2+\omega_{ci}^2} - \frac{1}{m_e}\frac{|\omega_{ce}|}{\nu_{en}^2+\omega_{ce}^2} & 0 \\ \frac{1}{m_e}\frac{|\omega_{ce}|}{\nu_{en}^2+\omega_{ce}^2} - \frac{1}{m_i}\frac{\omega_{ci}}{\nu_{in}^2+\omega_{ci}^2} & \frac{1}{m_i}\frac{\nu_{in}}{\nu_{in}^2+\omega_{ci}^2} + \frac{1}{m_e}\frac{\nu_{en}}{\nu_{en}^2+\omega_{ce}^2} & 0 \\ 0 & 0 & \frac{1}{m_i\nu_{in}} + \frac{1}{m_e\nu_{en}} \end{pmatrix} \tag{B.22}$$

and,

$$\overleftrightarrow{\sigma}_u = n_e|q_e| \begin{pmatrix} \frac{\nu_{in}^2}{\nu_{in}^2+\omega_{ci}^2} - \frac{\nu_{en}^2}{\nu_{en}^2+\omega_{ce}^2} & \frac{\nu_{in}\omega_{ci}}{\nu_{in}^2+\omega_{ci}^2} + \frac{\nu_{en}|\omega_{ce}|}{\nu_{en}^2+\omega_{ce}^2} & 0 \\ -\frac{\nu_{in}\omega_{ci}}{\nu_{in}^2+\omega_{ci}^2} - \frac{\nu_{en}|\omega_{ce}|}{\nu_{en}^2+\omega_{ce}^2} & \frac{\nu_{in}^2}{\nu_{in}^2+\omega_{ci}^2} - \frac{\nu_{en}^2}{\nu_{en}^2+\omega_{ce}^2} & 0 \\ 0 & 0 & 0 \end{pmatrix} \tag{B.23}$$

The different terms in the conductivity tensor ($\overleftrightarrow{\sigma}_E$) are labelled as the Pedersen, Hall and Parallel conductivities, as shown by,

$$\overleftrightarrow{\sigma}_E = \begin{pmatrix} \sigma_P & \sigma_H & 0 \\ -\sigma_H & \sigma_P & 0 \\ 0 & 0 & \sigma_\parallel \end{pmatrix} \tag{B.24}$$

where,

$$\sigma_P = n_e|q_e|^2 \left(\frac{1}{m_i}\frac{\nu_{in}}{\nu_{in}^2+\omega_{ci}^2} + \frac{1}{m_e}\frac{\nu_{en}}{\nu_{en}^2+\omega_{ce}^2} \right) \tag{B.25}$$

$$\sigma_H = n_e|q_e|^2 \left(\frac{1}{m_i}\frac{\omega_{ci}}{\nu_{in}^2+\omega_{ci}^2} - \frac{1}{m_e}\frac{|\omega_{ce}|}{\nu_{en}^2+\omega_{ce}^2} \right) \tag{B.26}$$

and,

$$\sigma_\parallel = n_e|q_e|^2 \left(\frac{1}{m_i\nu_{in}} + \frac{1}{m_e\nu_{en}} \right) \tag{B.27}$$

The Pedersen conductivity (σ_P) is perpendicular to the magnetic field and parallel with the electric field, the Hall conductivity (σ_H) is perpendicular to both the electric and magnetic fields and the parallel conductivity ($\sigma_\parallel$) is parallel with the magnetic field. These equations describe the steady state plasma convection that occurs in the ionosphere.

Appendix C

The Farley-Buneman Instability

The following derivation is based on MHD equations and fluid theory, with the aid of Fourier analysis to determine the perturbation characteristics. It roughly follows the derivation in *Kelley* [2009], but includes more terms. First, we consider the momentum equation for ions,

$$n_i m_i(\frac{\partial}{\partial t} + \mathbf{v_i} \cdot \nabla)\mathbf{v_i} = n_i m_i \mathbf{g} + e n_i(\mathbf{E} + \mathbf{v_i} \times \mathbf{B}) - \nabla p - n_i m_i \nu_{in}(\mathbf{v_i} - \mathbf{u}) \tag{C.1}$$

where the different terms were defined in Appendix B for Equation B.1.

If one neglects gravity, sets $\nabla\phi = \mathbf{E_1}$, where ϕ is the electric potential, and linearize using Fourier analysis,

$$\begin{aligned} -j\omega m_i \mathbf{v_{i1}} + j m_i \mathbf{v_{i1}}(\mathbf{k} \cdot \mathbf{v_{i0}}) = e\mathbf{E_0} + e(j\mathbf{k}\phi) + e([\mathbf{v_{i0}} + \mathbf{v_{i1}}] \times \mathbf{B}) - j\mathbf{k}\gamma_i k_B T_i \frac{n_{i1}}{n_{i0}} \\ -m_i \nu_{in}(\mathbf{v_{i0}} + \mathbf{v_{i1}}) + m_i \nu_{in}\mathbf{u} \end{aligned} \tag{C.2}$$

The same can be considered for electrons, except v_{0e} is not 0 due to the low collision rate of the electrons with the neutrals,

$$\begin{aligned} -j m_e \mathbf{v_{e1}}(\omega - \mathbf{k} \cdot \mathbf{v_{e0}}) = -e\mathbf{E_0} - e(j\mathbf{k}\phi) - e([\mathbf{v_{e0}} + \mathbf{v_{e1}}] \times \mathbf{B}) - j\mathbf{k}\gamma_e k_B T_e \frac{n_{e1}}{n_{e0}} \\ -m_e \nu_{en}(\mathbf{v_{e0}} + \mathbf{v_{e1}}) + m_e \nu_{en}\mathbf{u} \end{aligned} \tag{C.3}$$

Only the perturbation is considered, where the $\mathbf{v_{e0}}$ and $\mathbf{E_0}$ terms get cancelled out on the right side of the equation when $\mathbf{v_{e0}}$ is substituted in as the steady state background flow. The neutral wind, $\mathbf{u}$ is considered to be zero in this case to simplify the derivation. With these considerations, the electron equation of motion is,

$$-j m_e \mathbf{v_{e1}}(\omega - \mathbf{k} \cdot \mathbf{v_{e0}}) = -e(j\mathbf{k}\phi) - e(\mathbf{v_{e1}} \times \mathbf{B}) - j\mathbf{k}\gamma_e k_B T_e \frac{n_{e1}}{n_{e0}} - m_e \nu_{en}\mathbf{v_{e1}} \tag{C.4}$$

and the ion equation of motion from before (C.2) becomes,

$$-jm_i\mathbf{v_{i1}}(\omega - \mathbf{k}\cdot\mathbf{v_{i0}}) = e(j\mathbf{k}\phi) + e(\mathbf{v_{i1}}\times\mathbf{B}) - j\mathbf{k}\gamma_i k_B T_i\frac{n_{i1}}{n_{i0}} - m_i\nu_{in}\mathbf{v_{i1}} \tag{C.5}$$

The continuity equations also need to be considered. For electrons the continuity equation is,

$$\frac{\partial n_e}{\partial t} + \nabla\cdot(n_e\mathbf{v_e}) = 0 \tag{C.6}$$

which, when Fourier analyzed, becomes,

$$j\omega n_{e1} - jn_{e1}(\mathbf{k}\cdot\mathbf{v_{e0}}) - jkv_{e1y}n_{e0} = 0 \tag{C.7}$$

For ions, the Fourier analyzed continuity equation is,

$$j\omega n_{i1} - jn_{i1}(\mathbf{k}\cdot\mathbf{v_{i0}}) - jkv_{i1y}n_{i0} = 0 \tag{C.8}$$

$(\mathbf{k}\cdot\mathbf{v_{e0}})$ and $(\mathbf{k}\cdot\mathbf{v_{i0}})$ can be converted to $kv_{e0}\cos\theta_e$ and $kv_{i0}\cos\theta_i$ respectively, where the angle is measured between the direction of the wave vector and the associated steady state species convection.

Separating the equations of motion into the x- and y- components, considering $\mathbf{k}$ is in the y-direction and $\mathbf{B}$ is in the z-direction, the equations become,

$$e_x : -jm_e v_{e1x}(\omega - kv_{e0}\cos\theta_e) = -e(v_{e1y}B) - m_e\nu_{en}v_{e1x} \tag{C.9}$$

$$e_y : -jm_e v_{e1y}(\omega - kv_{e0}\cos\theta_e) = -e(jk\phi) + e(v_{e1x}B) - jk\gamma_e k_B T_e\frac{n_{e1}}{n_{e0}} - m_e\nu_{en}v_{e1y} \tag{C.10}$$

$$i_y : -jm_i v_{i1y}(\omega - kv_{i0}\cos\theta_i) = e(jk\phi) - e(v_{i1x}B) - jk\gamma_i k_B T_i\frac{n_{i1}}{n_{i0}} - m_i\nu_{in}v_{i1y} \tag{C.11}$$

If we consider $\omega_{ci} << \nu_{in}$,

$$i_y : -jm_i v_{i1y}(\omega - kv_{i0}\cos\theta_i) = e(jk\phi) - jk\gamma_i k_B T_i\frac{n_{i1}}{n_{i0}} - m_i\nu_{in}v_{i1y} \tag{C.12}$$

Solving for v_{e1x} from equation C.9,

$$e_x : v_{e1x} = -\frac{eBv_{e1y}}{m_e\nu_{en} - jm_e(\omega - kv_{e0}\cos\theta_e)} \tag{C.13}$$

Substitute v_{e1x} into equation C.10,

$$\begin{aligned} e_y : -jm_e v_{e1y}(\omega - kv_{e0}\cos\theta_e) = -e(jk\phi) - eB\Big(\frac{eBv_{e1y}}{m_e\nu_{en} - jm_e(\omega - kv_{e0}\cos\theta_e)}\Big) \\ -jk\gamma_e k_B T_e\frac{n_{e1}}{n_{e0}} - m_e\nu_{en}v_{e1y} \end{aligned} \tag{C.14}$$

From the ion continuity equations, the equations for the electron and ion velocities in the y-direction are,

$$v_{e1y} = \Big(\frac{\omega - kv_{e0}\cos\theta_e}{k}\Big)\frac{n_{e1}}{n_{e0}} \tag{C.15}$$

and

$$v_{i1y} = \Big(\frac{\omega - kv_{i0}\cos\theta_i}{k}\Big)\frac{n_{i1}}{n_{i0}} \tag{C.16}$$

Substitute v_{e1y} and v_{i1y} into Equations C.14 and C.12. This results in the equations,

$$\begin{aligned} e_y : -jm_e(\omega - kv_{e0}\cos\theta_e)\Big(\frac{\omega - kv_{e0}\cos\theta_e}{k}\Big)\frac{n_{e1}}{n_{e0}} = \\ -e(jk\phi) - eB\Big(\frac{eB}{m_e\nu_{en} - jm_e(\omega - kv_{e0}\cos\theta_e)}\Big)\Big(\frac{\omega - kv_{e0}\cos\theta_e}{k}\Big)\frac{n_{e1}}{n_{e0}} \\ -jk\gamma_e k_B T_e\frac{n_{e1}}{n_{e0}} - m_e\nu_{en}\Big(\frac{\omega - kv_{e0}\cos\theta_e}{k}\Big)\frac{n_{e1}}{n_{e0}} \end{aligned} \tag{C.17}$$

and

$$\begin{aligned} i_y : -jm_i(\omega - kv_{i0}\cos\theta_i)\Big(\frac{\omega - kv_{i0}\cos\theta_i}{k}\Big)\frac{n_{i1}}{n_{i0}} = e(jk\phi) - jk\gamma_i k_B T_i\frac{n_{i1}}{n_{i0}} \\ -m_i\nu_{in}\Big(\frac{\omega - kv_{i0}\cos\theta_i}{k}\Big)\frac{n_{i1}}{n_{i0}} \end{aligned} \tag{C.18}$$

Equation C.18 can be used to solve for ϕ, resulting in the equation,

$$\begin{aligned} \phi = \Big[-jm_i(\omega - kv_{i0}\cos\theta_i)\Big(\frac{\omega - kv_{i0}\cos\theta_i}{k}\Big)\frac{n_{i1}}{n_{i0}} + jk\gamma_i k_B T_i\frac{n_{i1}}{n_{i0}} \\ +m_i\nu_{in}\Big(\frac{\omega - kv_{i0}\cos\theta_i}{k}\Big)\frac{n_{i1}}{n_{i0}}\Big]\Big[\frac{1}{ejk}\Big] \end{aligned} \tag{C.19}$$

Substitute the value obtained for ϕ into Equation C.17 and set $\frac{n_{i1}}{n_{i0}} = \frac{n_{e1}}{n_{e0}}$ due to quasi-neutrality. This substitution results in the equation,

$$\begin{aligned} e_y : -jm_e(\omega - kv_{e0}\cos\theta_e)\Big(\frac{\omega - kv_{e0}\cos\theta_e}{k}\Big)\frac{n_{e1}}{n_{e0}} = \\ jm_i(\omega - kv_{i0}\cos\theta_i)\Big(\frac{\omega - kv_{i0}\cos\theta_i}{k}\Big)\frac{n_{i1}}{n_{i0}} \\ -jk\gamma_i k_B T_i\frac{n_{i1}}{n_{i0}} - m_i\nu_{in}\Big(\frac{\omega - kv_{i0}\cos\theta_i}{k}\Big)\frac{n_{i1}}{n_{i0}} \\ -\Big(\frac{e^2B^2}{m_e\nu_{en} - jm_e(\omega - kv_{e0}\cos\theta_e)}\Big)\Big(\frac{\omega - kv_{e0}\cos\theta_e}{k}\Big)\frac{n_{e1}}{n_{e0}} \\ -jk\gamma_e k_B T_e\frac{n_{e1}}{n_{e0}} - m_e\nu_{en}\Big(\frac{\omega - kv_{e0}\cos\theta_e}{k}\Big)\frac{n_{e1}}{n_{e0}} \end{aligned} \tag{C.20}$$

One way to simplify this is to claim the convective derivative of the electrons is very small due to m_e being small ($jm_e\mathbf{v_{e1}}(\omega - \mathbf{k}\cdot\mathbf{v_{e0}}) \approx 0$). All the $\frac{n_{i1}}{n_{i0}}$ and $\frac{n_{e1}}{n_{e0}}$ terms cancel, resulting in the equation,

$$\begin{aligned} e_y : 0 = {} & jm_i(\omega - kv_{i0}\cos\theta_i)\Big(\frac{\omega - kv_{i0}\cos\theta_i}{k}\Big) \\ & -jk\gamma_i k_B T_i - m_i\nu_{in}\Big(\frac{\omega - kv_{i0}\cos\theta_i}{k}\Big) \\ & -\Big(\frac{e^2B^2}{m_e\nu_{en}}\Big)\Big(\frac{\omega - kv_{e0}\cos\theta_e}{k}\Big) \\ & -jk\gamma_e k_B T_e - m_e\nu_{en}\Big(\frac{\omega - kv_{e0}\cos\theta_e}{k}\Big) \end{aligned} \tag{C.21}$$

Multiplying both sides by jk and simplifying, the equation becomes,

$$\begin{aligned} e_y : 0 = {} & -m_i(\omega - kv_{i0}\cos\theta_i)^2 + k^2\gamma_i k_B T_i - jm_i\nu_{in}(\omega - kv_{i0}\cos\theta_i) \\ & -j\frac{e^2B^2}{m_e\nu_{en}}(\omega - kv_{e0}\cos\theta_e) + k^2\gamma_e k_B T_e - jm_e\nu_{en}(\omega - kv_{e0}\cos\theta_e) \end{aligned} \tag{C.22}$$

Setting $\omega = \omega_R + j\gamma$, allows separation into imaginary and real components. The equation for the real component is,

$$\begin{aligned} real : 0 = {} & -m_i(\omega_R^2 - \gamma^2) + 2\omega_R m_i k v_{i0}\cos\theta_i - (kv_{i0}\cos\theta_i)^2 + k^2(\gamma_e k_B T_e + \gamma_i k_B T_i) \\ & +\gamma(m_i\nu_{in} + m_e\nu_{en}) + \gamma\frac{e^2B^2}{m_e\nu_{en}} \end{aligned} \tag{C.23}$$

and the equation for the imaginary component is,

$$\begin{aligned} imag : 0 = {} & -2m_i\omega_R\gamma + 2m_i k v_{i0}\cos\theta_i\gamma + m_i\nu_{in}kv_{i0}\cos\theta_i - m_i\nu_{in}\omega_R \\ & +\frac{e^2B^2}{m_e\nu_{en}}kv_{e0}\cos\theta_e - \frac{e^2B^2}{m_e\nu_{en}}\omega_R + m_e\nu_{en}kv_{e0}\cos\theta_e - m_e\nu_{en}\omega_R \end{aligned} \tag{C.24}$$

Simplifying the real component,

$$real : (\omega_R - kv_{i0}\cos\theta_i)^2 = k^2\frac{\gamma_e k_B T_e + \gamma_i k_B T_i}{m_i} + \gamma^2 + \gamma\frac{\omega_{ce}\omega_{ci}}{\nu_{en}} + \gamma\frac{m_i\nu_{in} + m_e\nu_{en}}{m_i} \tag{C.25}$$

Taking the square root of the right side and dividing by k gives,

$$\frac{\omega_R}{k} = v_{io}\cos\theta_i \pm \sqrt{\frac{\gamma_e k_B T_e + \gamma_i k_B T_i}{m_i} + \frac{\gamma^2}{k^2} + \frac{\gamma}{k^2}\frac{\omega_{ce}\omega_{ci}}{\nu_{en}} + \frac{\gamma}{k^2}\frac{m_i\nu_{in} + m_e\nu_{en}}{m_i}} \tag{C.26}$$

If we consider that $\frac{\gamma}{k}$ is small, and only the positive root is physical,

$$\frac{\omega_R}{k} = v_{io}\cos\theta_i + \sqrt{\frac{\gamma_e k_B T_e + \gamma_i k_B T_i}{m_i}} \tag{C.27}$$

This equation shows that the phase speed of these instabilities will always be greater than that of the background ion velocity in the direction of the wave vector.

We can now simplify the complex component. Solving for the growth rate of the instability,

$$\begin{aligned} imag: 2m_i\gamma(\omega_R - kv_{i0}\cos\theta_i) = m_i\nu_{in}kv_{i0}\cos\theta_i + m_e\nu_{en}kv_{e0}\cos\theta_e \\ -m_i\nu_{in}\omega_R - m_e\nu_{en}\omega_R - \frac{e^2B^2}{m_e\nu_{en}}\omega_R + \frac{e^2B^2}{m_e\nu_{en}}kv_{e0}\cos\theta_e \end{aligned} \tag{C.28}$$

Dividing by $2m_i(\omega_R - kv_{i0}\cos\theta_i)$,

$$\begin{aligned} imag: \gamma = -\frac{\omega_{ce}\omega_{ci}}{2\nu_{en}}\Big(\frac{\omega_R - kv_{e0}\cos\theta_e}{\omega_R - kv_{i0}\cos\theta_i}\Big) - \frac{\nu_{in}}{2}\Big(\frac{\omega_R - kv_{i0}\cos\theta_i}{\omega_R - kv_{i0}\cos\theta_i}\Big) \\ -\frac{m_e\nu_{en}}{2m_i}\Big(\frac{\omega_R - kv_{e0}\cos\theta_e}{\omega_R - kv_{i0}\cos\theta_i}\Big) \end{aligned} \tag{C.29}$$

$$imag: \gamma = \frac{1}{2}\Big(\frac{\omega_{ce}\omega_{ci}}{\nu_{en}} + \frac{m_e\nu_{en}}{m_i}\Big)\Big(\frac{kv_{e0}\cos\theta_e - \omega_R}{\omega_R - kv_{i0}\cos\theta_i}\Big) - \frac{\nu_{in}}{2} \tag{C.30}$$

One thing to note is that the instability will not grow if the ion velocity and electron velocity are equal. This is due to the fact that the phase speed of these instabilities ($\frac{\omega}{k}$), shown in Equation C.27, is greater than the velocity of the ions. Growth of the instability only occurs when γ is positive ($\omega = \omega_R + j\gamma$), which means that v_{eo} must be greater than $\frac{\omega_R}{k}$ for growth to occur.

If the background ion drift is considered to be stationary, the phase velocity and growth rate of the instability are given by,

$$real: \frac{\omega_R^2}{k^2} = \frac{\gamma_e k_B T_e + \gamma_i k_B T_i}{m_i} + \frac{\gamma^2}{k^2} + \frac{\gamma}{k^2}\frac{\omega_{ce}\omega_{ci}}{\nu_{en}} + \frac{\gamma}{k^2}\frac{m_i\nu_{in} + m_e\nu_{en}}{m_i} \tag{C.31}$$

and

$$imag: \gamma = \Big(\frac{\omega_{ce}\omega_{ci}}{2\nu_{en}} + \frac{m_e\nu_{en}}{2m_i}\Big)\Big(\frac{kv_{e0}\cos\theta_e}{\omega_R} - 1\Big) - \frac{\nu_{in}}{2} \tag{C.32}$$

For $\gamma << \omega_R$, the waves propagate at the ion-acoustic speed and grow when the background electron $\mathbf{E} \times \mathbf{B}$ drift is greater than the ion-acoustic speed. Recall $\omega = \omega_R + j\gamma$ and the waves are proportional to $\exp(j[\mathbf{k}\cdot\mathbf{r} - \omega t])$, resulting in the wave growing for positive values of γ.

These equations can be re-arranged and simplified to what is typically shown in the literature, such as *Kelley* [2009]. A simplification term is introduced, given the symbol ψ. This value of this term is shown by the equation,

$$\psi = \frac{\nu_{en}\nu_{in}}{\omega_{ce}\omega_{ci}} \tag{C.33}$$

The ion-acoustic speed was introduced in Section 3.4.2, which is,

$$C_s^2 = \frac{\gamma_e k_B T_e + \gamma_i k_B T_i}{m_i} \tag{C.34}$$

If one considers $\frac{m_e \nu_{en}}{2m_i}$ to be small due to the electron mass being much smaller than the ion mass, the growth rate becomes,

$$\gamma = \Big(\frac{\omega_{ce}\omega_{ci}}{2\nu_{en}}\Big)\Big(\frac{kv_{e0}\cos\theta_e}{\omega_R} - 1\Big) - \frac{\nu_{in}}{2} \tag{C.35}$$

Simplifying,

$$\gamma = \frac{\omega_{ce}\omega_{ci}}{2\nu_{en}}\Big(\frac{kv_{e0}\cos\theta_e}{\omega_R}\Big) - \frac{\nu_{in}\nu_{en} + \omega_{ce}\omega_{ci}}{2\nu_{en}} \tag{C.36}$$

$$\gamma\frac{2\nu_{en}}{\omega_{ce}\omega_{ci}} = \frac{kv_{e0}\cos\theta_e}{\omega_R} - \frac{\nu_{in}\nu_{en}}{\omega_{ce}\omega_{ci}} - 1 \tag{C.37}$$

Now, substituting in ψ, the equation becomes,

$$\omega_R\Big(1 + \psi + \gamma\frac{2\psi}{\nu_{in}}\Big) = kv_{e0}\cos\theta_e \tag{C.38}$$

If the growth rate is considered to be small ($\gamma << \nu_{in}$), the frequency of the perturbation is given as,

$$\omega_R = \frac{kv_{e0}\cos\theta_e}{1+\psi} \tag{C.39}$$

For the real portion of the equation, we consider $\omega_R >> \gamma$, and for $\frac{m_e\nu_{en}}{m_i}$ to be small. Simplifying Equation C.32,

$$\omega_R^2 - k^2C_s^2 = \gamma\frac{\omega_{ce}\omega_{ci}}{\nu_{en}} + \gamma\nu_{in} \tag{C.40}$$

Simplifying, one arrives at,

$$k^2C_s^2 - \omega_R^2 = -\gamma\frac{\omega_{ce}\omega_{ci} + \nu_{in}\nu_{en}}{\nu_{en}} \tag{C.41}$$

Substituting in ψ, the equation becomes,

$$\gamma = \frac{\psi}{\nu_{in}(1+\psi)}(\omega_R^2 - k^2 C_s^2) \tag{C.42}$$

This is similar to what is given in the literature for the Farley-Buneman instability growth rate.

The growth rate and phase velocity given by Equations C.31 and C.32 provide insight into the physical mechanisms by which this instability is formed, as the phase velocity is directly relatable to the ion-acoustic speed and there is positive growth when the electron drift is larger than the phase velocity, which is the ion-acoustic speed for stationary ions and a growth rate much smaller than the wave frequency. Equations C.31 and C.32 can be re-written with reference to ψ, where $\frac{m_e}{m_i}$ is considered negligible. The resulting equations are then,

$$\omega_R^2 = k^2 \frac{\gamma_e k_B T_e + \gamma_i k_B T_i}{m_i} + \gamma^2 + \gamma \nu_{in}\Big(\frac{1+\psi}{\psi}\Big) \tag{C.43}$$

and

$$\gamma = \frac{\nu_{in}}{2\psi}\Big(\frac{k v_{e0} \cos\theta_e}{\omega_R} - (1+\psi)\Big) \tag{C.44}$$

Referring back to Equations C.26 and C.30, it can be determined that the Farley-Buneman instability is not observed in the F-region of the ionosphere due to the electrons and ions both following the $\mathbf{E} \times \mathbf{B}$ drift. The phase velocity will be always greater than the ion drift velocity, where the instability requires an electron velocity greater than the phase velocity for positive growth. This results in a negative growth rate, or a damping, of the Farley-Buneman instability. In this analysis the wave propagated perpendicular to the background magnetic field. A 3-D growth rate and phase velocity are provided in Section 3.4.5.

Appendix D

Ionospheric Radio Scatter

With the Debye length and Compton wavelength considerations discussed in Chapter 4 kept in mind, we can derive the scattering RF spectrum from the ionospheric plasma. The following derivation references several sources (*Griffiths* [1999]; *Richards et al.* [2010]), but essentially follows the derivation from *Perry* [2015], and the references therein once the E-field is determined. If we consider the signal to be in the far field (decay at $1/r^2$), the intensity of the radio signal at a distance r_t is [*Richards et al.*, 2010],

$$Q_r = \frac{P_t}{4\pi r_t^2} \tag{D.1}$$

where Q_r is the power per unit area at a distance r_t, P_t is the transmitted power and r_t is the distance from the radar. For this analysis the gain of the antenna is considered part of P_t.

The intensity (power/area) of a EM wave due to the electric field in a vacuum is given by [*Griffiths*, 1999],

$$Q_r = \langle I \rangle = \frac{1}{2}\epsilon_0 c E^2 \tag{D.2}$$

where I is the intensity at a distance r and E is the electric field of the propagating wave.

This results in an electric field at the scattering location of,

$$E_0 = \sqrt{\frac{P_t}{2\pi\epsilon_0 c r_t^2}} \tag{D.3}$$

The equation for the change in the electric field over time and space for a EM wave is,

$$\mathbf{E}(\mathbf{r_t}, t) = E_0 \exp\left[j(\mathbf{k_t} \cdot \mathbf{r_t} - \omega_r t)\right]\hat{\mathbf{k}}_{t\perp} \tag{D.4}$$

where ω_r is the radio frequency and $\mathbf{k_t}$ is the radio wave vector. The $\mathbf{r}_t$ term is measured from the transmitter to the scattering location. We consider that $\mathbf{k}_t$ is in the direction of $\mathbf{E} \times \mathbf{B}$ for the EM wave, and the E-field and B-field are perpendicular to each other.

It is known that the electric field radiated from an accelerating charge is,

$$\mathbf{E}_{rad} = \frac{\mu_0 q}{4\pi r_s}[(\hat{\mathbf{r_s}} \cdot \mathbf{a})\hat{\mathbf{r_s}} - \mathbf{a}] \tag{D.5}$$

where μ_0 is the constant of permeability, q is the charge of the particle, $\mathbf{a}$ is the acceleration vector of the particle, and $\mathbf{r}_s$ is the range vector from the scatter location to the observer. The Poynting flux, or intensity, for this is then,

$$\langle \mathbf{S}_{rad} \rangle = \frac{1}{2}\epsilon_0 c E_{rad}^2 = \frac{\mu_0 q^2 a^2}{32\pi^2 c}\left(\frac{\sin^2\theta_a}{r_s^2}\right)\hat{\mathbf{r_s}} \tag{D.6}$$

where θ_a is the angle between the acceleration and the scatter direction ($\hat{\mathbf{r_s}}$) and c is the speed of light in free space.

The acceleration due to the incident EM wave is,

$$\mathbf{a} = -\frac{q\mathbf{E}}{m_e} \tag{D.7}$$

where m_e is the mass of an electron and the negative is due to considering electron motion.

Substituting in $\mathbf{E}_{rad}$ and $\mathbf{a}$ into Equation D.6,

$$\langle \mathbf{S}_{rad} \rangle = \frac{\mu_0 q^2}{32\pi^2 c}\left(\frac{q^2 P_t}{2\pi\epsilon_0 c m_e^2 r_t^2}\right)\left(\frac{\sin^2\theta_a}{r_s^2}\right)\hat{\mathbf{r}} \tag{D.8}$$

$$\langle \mathbf{S}_{rad} \rangle = P_t \frac{\mu_0 q^4}{64\pi^3\epsilon_0 c^2 m_e^2}\left(\frac{\sin^2\theta_a}{r_t^2 r_s^2}\right)\hat{\mathbf{r}} \tag{D.9}$$

This results in a radiation pattern of effectively the shape of a donut, where the maximum of the radiated power is perpendicular to the electron acceleration. The acceleration of the electron is perpendicular to the incident radio wave due to the EM field being perpendicular to the propagation path ($\mathbf{E} \times \mathbf{B}$).

This provides the scattered Poynting flux (intensity) of the EM wave for a single electron. Now we will investigate how the electric field is affected by scattering.

The radiation electric field is given by Equation D.5. We can substitute Equations D.7 and D.4 and solve for the re-radiated field,

$$\mathbf{E}_{rad}(\mathbf{r}, t) = \frac{\mu_0 q^2}{4\pi r_s m_e} E_{r0} \exp\left[j(\mathbf{k_t} \cdot \mathbf{r_t} - \omega_r t)\right] \exp\left[j(\mathbf{k_s} \cdot \mathbf{r_s})\right][(\hat{\mathbf{r_s}} \cdot \hat{\mathbf{k}}_{s\perp})\hat{\mathbf{r_s}} - \hat{\mathbf{k}}_{s\perp}] \tag{D.10}$$

If we substitute in Equation D.3,

$$\mathbf{E}_{rad}(\mathbf{r},t) = \frac{\mu_0 q^2}{4\pi m_e r_s r_t}\sqrt{\frac{P_t}{2\pi\epsilon_0 c}}\exp\left[j(\mathbf{k_t}\cdot\mathbf{r_t}-\omega_r t)\right]\exp\left[j(\mathbf{k_s}\cdot\mathbf{r_s})\right][(\hat{\mathbf{r}_s}\cdot\hat{\mathbf{k}}_{t\perp})\hat{\mathbf{r}_s}-\hat{\mathbf{k}}_{t\perp}] \quad \text{(D.11)}$$

$$\mathbf{E}_{rad}(\mathbf{r},t) = \frac{\mu_0 q^2}{4\pi m_e r_s r_t}\sqrt{\frac{P_t}{2\pi\epsilon_0 c}}\exp\left[j(\mathbf{k_t}\cdot\mathbf{r_t}-\omega_r t)\right]\exp\left[j(\mathbf{k_s}\cdot\mathbf{r_s})\right][\cos\theta_a\hat{\mathbf{r}_s}-\hat{\mathbf{k}}_{t\perp}] \quad \text{(D.12)}$$

Now consider the geometry of this system, including that the Poynting flux is given by Equation D.9, and the relation to the E-field is given by Equation D.6. With these equations in mind we can give an approximate value for E_{rad} as,

$$\mathbf{E}_{rad}(\mathbf{r},t) = \frac{\mu_0 q^2}{4\pi m_e r_s r_t}\sqrt{\frac{P_t}{2\pi\epsilon_0 c}}\exp\left[j(\mathbf{k_t}\cdot\mathbf{r_t}-\omega_r t)\right]\exp\left[j(\mathbf{k_s}\cdot\mathbf{r_s})\right]\sin\theta_a\hat{\mathbf{r}}_{s\perp} \quad \text{(D.13)}$$

where the EM wave is propagating perpendicular to the electric field.

There are some interesting points that come about from this scattering derivation. Without Faraday rotation, and if a linearly polarized wave is transmitted, there will be a null in the radiation pattern produced that is perpendicular to the incident radar wave. Higher frequency radio waves undergo less Faraday rotation, as described by Equation 4.15, and therefore the radiation pattern null could be significant at higher frequencies.

The equations above result in a changing scattered electric field that varies with position and is proportional to,

$$E_{rad} \propto \exp\left[j((\mathbf{k_t}\cdot\mathbf{r_t}+\mathbf{k_s}\cdot\mathbf{r_s})-\omega_r t)\right] \quad \text{(D.14)}$$

It must be remembered that these equations are valid for radio wavelengths much larger than the particle size. The electrons are the only species considered as they effectively shield the ions from the EM field. To directly probe the ions in the ionosphere it is required to transmit a radio signal with a wavelength less than the Debye length.

We now have the scattered E-field generated from a single electron, but we must consider the bulk plasma effects. In the case of the ionosphere we use the Born approximation [*Born*, 1926], which allows us to only consider the incident radio waves in the analysis, stating that the scattered waves are at much reduced powers and electric field strengths. Otherwise secondary wave scattering would be considered, making the analysis much more complicated.

$\mathbf{r}_s$ can be re-written as $\mathbf{r}_r - \mathbf{r}_t$ ($\mathbf{r}_s = \mathbf{r}_r - \mathbf{r}_t$), where the transmitter is considered to be the origin and $\mathbf{r}_r$ is the path from the transmitter to the receiver (Figure 4.3). To simplify the derivation, we will consider the scattered wave to be in the direction of the receiver, where small differences within the volume will be negligible in terms of θ_a. Again, we will not consider secondary scatter. The equation for a single electron is,

$$\mathbf{E}_{rad}(\mathbf{r},t) = \frac{\mu_0 q^2}{4\pi m_e r_s r_t}\sqrt{\frac{P_t}{2\pi\epsilon_0 c}}\exp\left[j(((\mathbf{k_t}\cdot\mathbf{r_t} - \mathbf{k_s}\cdot\mathbf{r_t}) + \mathbf{k_s}\cdot\mathbf{r_r}) - \omega_r t)\right]\sin\theta_a\hat{\mathbf{r}}_{s\perp} \quad \text{(D.15)}$$

We consider direct backscatter, so $\sin\theta_a = 1$, $\mathbf{k}_t = -\mathbf{k}_s$, $\mathbf{r}_r = 0$, and we will ignore the orientation of the E-field, only considering the phase. $\mathbf{r}_r$ is kept in the equation for consideration of a bistatic system. We also consider that the change in r_t is negligible with respect to the decay in the E-field strength, and therefore is not considered in the integration. $\mathbf{r}_r$ is a constant, and the direction of $\mathbf{k}_s$ does not significantly change over the region of interest. The contribution from multiple electron scatterers becomes,

$$E_{rad}(\mathbf{r},t) = \frac{\mu_0 q^2}{4\pi m_e r_s r_t}\sqrt{\frac{P_t}{2\pi\epsilon_0 c}}\exp\left[j(\mathbf{k_s}\cdot\mathbf{r_r} - \omega_r t)\right]\int V n(\mathbf{r}_t,t)\exp\left[j(2\mathbf{k_t}\cdot\mathbf{r_t})\right]\mathrm{d}\mathbf{r}_t \quad \text{(D.16)}$$

where V is the volume of the region, and $n(\mathbf{r}_t,t)$ is the plasma density of the region as a function of location and time.

The integral is a spatial Fourier transform. Consider $n(\mathbf{r}_t,t)$ to be $n(\mathbf{r}_t,t) = \bar{n} + \Delta n(\mathbf{r}_t,t)$. Solving for this integral results in,

$$E_{rad}(\mathbf{r},t) = \frac{\mu_0 q^2}{4\pi m_e r_s r_t}\sqrt{\frac{P_t}{2\pi\epsilon_0 c}}\exp\left[j(\mathbf{k_s}\cdot\mathbf{r_r} - \omega_r t)\right]V\Delta n(2\mathbf{k}_t,t) \quad \text{(D.17)}$$

We know that $k_t = 2\pi/\lambda_t$, where λ_t is the wavelength of the transmitted wave. This means that the scattered power is determined by the plasma density structures, or irregularities that are at half the wavelength of the transmitted radar wave for direct backscatter, $k_{irr} = 2k_t$, where k_{irr} is the wave vector of the irregularities. This is where the Bragg scattering condition for ionospheric plasma irregularity radar scatter originates from.

For direct backscatter we stated that $\mathbf{k}_s\cdot\mathbf{r}_t = -k_t r_t$, but this is not always the case. If it is not direct backscatter, we have $\mathbf{k_t}\cdot\mathbf{r_t} - \mathbf{k_s}\cdot\mathbf{r_t} = (1-\cos\theta)k_t r_t$, where θ is measured between the vectors $\mathbf{k}_s$ and $\mathbf{r}_t$. $|k_s| = |k_t|$ due to the scattered radiation being the same wavelength and frequency as the incoming radiation. Note that this θ is rotated 90 degrees

from the θ_a in Equation D.6 for the case of direct backscatter. If we take θ as $\theta - \pi$, to account for the backscattering of the signal, we obtain $(1 + \cos\theta)k_t r_t$. This can be re-written as $2\cos^2(\theta/2)k_t r_t$.

The literature shows that this value for a bistatic system should be $2\cos(\theta/2)$, but no error in the analysis has been found. In the body of this dissertation, the value used by the literature has been cited and used.

From this analysis, the irregularity wave vectors are $k_{irr} = 2\cos^2(\theta/2)k_r$. Without direct backscatter, the power of the scatter is also affected. This effect is based on the $\sin\theta_a$ term in Equation 4.18. For radio waves undergoing a large number of Faraday rotations while traversing through the ionosphere, this power correction term would be $\propto \sin^2\theta_a$ for the power.

We can see that the plasma density as a function of wave vector is embedded in Equation D.17. From this equation it is possible to determine the power expected for a given plasma density perturbation at a given wavelength.

If we convert Equation D.17 to an intensity, using Equation D.2,

$$\langle I(t)\rangle = \frac{\mu_0^2 q^4 P_t}{64\pi^3 m_e^2 r_s^2 {r_t}^2} V^2 [\Delta n(k_{irr}, t)]^2 \tag{D.18}$$

Now, if we take an FFT of both sides of the function,

$$\int \langle I(t)\rangle \, e^{(-j2\pi\omega t)} \, \mathrm{d}t = \int \frac{\mu_0^2 q^4 P_t}{64\pi^3 m_e^2 r_s^2 {r_t}^2} V^2 [\Delta n(k_{irr}, t)]^2 e^{(-j2\pi\omega t)} \, \mathrm{d}t \tag{D.19}$$

Taking the integral, one obtains,

$$\langle I(\omega)\rangle = \frac{\mu_0^2 q^4 P_t}{64\pi^3 m_e^2 r_s^2 {r_t}^2} V^2 [\Delta n(k_{irr}, \omega)]^2 \tag{D.20}$$

To convert this to a power we would have to consider the effective receiver aperture area. This can be given as A_e, resulting in the power spectrum as received at the receiver to be,

$$\langle P(\omega)\rangle = (P_t A_e)\left(\frac{\mu_0^2 q^4}{64\pi^3 m_e^2 r_s^2 {r_t}^2}\right) V^2 [\Delta n(k_{irr}, \omega)]^2 \tag{D.21}$$

The spectrum for a given wavelength is now encoded in the $\Delta n(k_{irr}, \omega)$ term, which can be used to model the expected frequency spectrum measured by a radar system for a given density distribution in the ionospheric plasma.

Appendix E

Spherical Coordinate Derivation

The total RF path length r_{pl}, the arc length between the receiver and transmitter d_{rt} and the angle of arrival at the receiver θ_s are known. The cosine rule for spherical trigonometry is [*Gellert et al.*, 2012],

$$\cos a = \cos b \cos c + \sin b \sin c \cos A \tag{E.1}$$

where a, b and c are the arc lengths in radians and A is the angle between the vectors from the receiver to the transmitter and the scattering volume to the transmitter ($A = \theta_{rt} + \theta_r + \theta_s$). θ_{rt} is the angle West of North from the receiver to the transmitter and θ_r is the bearing direction of the receiver array. The equation can be re-written as,

$$\cos(d_{ts}) = \cos(d_{rs})\cos(d_{rt}) + \sin(d_{rs})\sin(d_{rt})\cos(\theta_{rt} + \theta_r + \theta_s) \tag{E.2}$$

where d_{ts} is the arc length from the transmitter to the scattering volume and d_{rs} is the arc length from the receiver to the scattering volume. The total path length of the radio signal is equal to the path length from the transmitter to the scattering volume and the path length of the receiver to the scattering volume ($r_{pl} = d_{rs} + d_{ts}$). Substituting this in, the equation becomes,

$$\cos(r_{pl} - d_{rs}) = \cos(d_{rs})\cos(d_{rt}) + \sin(d_{rs})\sin(d_{rt})\cos(\theta_{rt} + \theta_r + \theta_s) \tag{E.3}$$

Expanding $\cos(r_{pl} - d_{rs})$ using a trigonometric identity ($\cos(A - B) = \cos A \cos B + \sin A \sin B$),

$$\cos(r_{pl})\cos(d_{rs}) + \sin(r_{pl})\sin(d_{rs}) = \cos(d_{rs})\cos(d_{rt}) + \sin(d_{rs})\sin(d_{rt})\cos(\theta_{rt} + \theta_r + \theta_s) \tag{E.4}$$

This can be simplified to,

$$\tan(d_{rs}) = \frac{\cos(d_{rt}) - \cos(r_{pl})}{\sin(r_{pl}) - \sin(d_{rt})\cos(\theta_{rt} + \theta_r + \theta_s)} \tag{E.5}$$

and solving for d_{rs} results in the equation,

$$d_{rs} = \tan^{-1}\left(\frac{\cos\left(d_{rt}\right) - \cos\left(r_{pl}\right)}{\sin\left(r_{pl}\right) - \sin\left(d_{rt}\right)\cos\left(\theta_{rt} + \theta_r + \theta_s\right)}\right) \tag{E.6}$$

Multiplying d_{rs} by the radius of the Earth provides the distance from the receiver to the scattering volume, assuming propagation along the spherical surface. With this information the ionospheric scatter can be plotted. While this analytical method does not produce the exact distance from the receiver to the scattering volume at an altitude of 100 km, it provides an approximate value that can be used as a first order estimate in numerical solutions, and allows the plotting of the data in a sufficiently accurate preliminary manner.

Appendix F

ICEBEAR X300 Transmitter Script

```
#!/usr/bin/env Python

from gnuradio import gr
from gnuradio import uhd
from gnuradio import blocks
from gnuradio import digital
import numpy as np

import sys, time, os, math, re, glob, numpy

r_tx = gr.enable_realtime_scheduling()

if r_tx == gr.RT_OK:
        print("Realtime scheduling enabled")
else:
        print "Note: failed to enable realtime scheduling"

sample_rate = 200000
sample_rate1 = 800000
center_freq = 49500000

#create a file source
file_tx_source_0 = blocks.file_source(gr.sizeof_gr_complex,
        "pseudo_random_code_8_lpf_attenuated.txt",
        True)
```

```
#throttle block with sample_rate0 as the code rate
throttle_0 = blocks.throttle(gr.sizeof_gr_complex, sample_rate1,True)

#create a uhd sink for the Tx
transmit_0 = uhd.usrp_sink(
        device_addr="addr0=192.168.10.2,addr1=192.168.10.3",
        stream_args=uhd.stream_args(
                cpu_format="fc32",
                otw_format="sc16",
                channels=range(4)))

#use the device clock (internal -> external for external clock source)
transmit_0.set_clock_source("external", uhd.ALL_MBOARDS)
transmit_0.set_time_source("external", uhd.ALL_MBOARDS)

#set the daughterboard, sampling rate and the carrier
#frequency for the transmitters
transmit_0.set_subdev_spec("A:AB B:AB",0)
transmit_0.set_subdev_spec("A:AB B:AB",1)
transmit_0.set_samp_rate(sample_rate1)
transmit_0.set_center_freq(center_freq,0)
transmit_0.set_center_freq(center_freq,1)
transmit_0.set_center_freq(center_freq,2)
transmit_0.set_center_freq(center_freq,3)

#find second to latch to
tt = time.time()
while tt-math.floor(tt) < 0.2 or tt-math.floor(tt) > 0.3:
        tt = time.time()
        time.sleep(0.01)
print("Latching at "+str(tt))

#next -> unknown for external PPS
#set the device time
transmit_0.set_time_unknown_pps(uhd.time_spec(math.ceil(tt)+1.0))
```

```
#set time for receiving and transmitting to start
transmit_0.set_start_time(uhd.time_spec(math.ceil(tt)+2.0))

fg = gr.top_block()

#TX Chain
fg.connect(file_tx_source_0,throttle_0)
fg.connect(throttle_0,(transmit_0,0))
fg.connect(throttle_0,(transmit_0,1))
fg.connect(throttle_0,(transmit_0,2))
fg.connect(throttle_0,(transmit_0,3))

fg.start()

while(True):
        try:
                time.sleep(1)
        except KeyboardInterrupt:
                fg.stop()
                print('done')
                sys.stdout.flush()
                sys.exit()
```

Appendix G

ICEBEAR X300 Receiver Script

```
#!/usr/bin/env Python

from gnuradio import gr
from gnuradio import uhd
from gnuradio import blocks
from gnuradio import digital
import numpy as np
import gr_drf

import sys, time, os, math, re, glob, numpy

r_tx = gr.enable_realtime_scheduling()

if r_tx == gr.RT_OK:
        print("Realtime scheduling enabled")
else:
        print "Note: failed to enable realtime scheduling"

sample_rate = 200000
center_freq = 49500000

#USRP Receiver
receive_0 = uhd.usrp_source(
        device_addr="addr0=192.168.10.2,addr1=192.168.10.3,\
                addr2=192.168.10.4,addr3=192.168.10.5,\
                addr4=192.168.10.6,recv_buff_size=1000000000",
```

```
        stream_args=uhd.stream_args(
                cpu_format="sc16",
                otw_format="sc16",
                channels=range(10)))

#internal -> external for external time/clock source
receive_0.set_clock_source("external", uhd.ALL_MBOARDS)
receive_0.set_time_source("external", uhd.ALL_MBOARDS)

#set the daughterboard, sampling rate and
#carrier frequency for receiver
receive_0.set_subdev_spec("A:AB B:AB",0)
receive_0.set_subdev_spec("A:AB B:AB",1)
receive_0.set_subdev_spec("A:AB B:AB",2)
receive_0.set_subdev_spec("A:AB B:AB",3)
receive_0.set_subdev_spec("A:AB B:AB",4)
receive_0.set_samp_rate(sample_rate)
receive_0.set_center_freq(center_freq,0)
receive_0.set_center_freq(center_freq,1)
receive_0.set_center_freq(center_freq,2)
receive_0.set_center_freq(center_freq,3)
receive_0.set_center_freq(center_freq,4)
receive_0.set_center_freq(center_freq,5)
receive_0.set_center_freq(center_freq,6)
receive_0.set_center_freq(center_freq,7)
receive_0.set_center_freq(center_freq,8)
receive_0.set_center_freq(center_freq,9)

                #find second to latch to
tt = time.time()
while tt-math.floor(tt) < 0.2 or tt-math.floor(tt) > 0.3:
        tt = time.time()
        time.sleep(0.01)
print("Latching at "+str(tt))

#next -> unknown for external PPS
```

```
#set the device time
receive_0.set_time_unknown_pps(uhd.time_spec(math.ceil(tt)+1.0))

#set time for receiving and transmitting to start
receive_0.set_start_time(uhd.time_spec(math.ceil(tt)+9.0))

sample_time = int(long(math.ceil(tt)+9.0)*sample_rate)

directory = '/data/icebear_test'

sample_dtype = np.dtype([('r', '<i2'), ('i', '<i2')])

#create HD5F file sinks for each stream (antenna)
# antenna 0
file_rx_sink_0 = gr_drf.digital_rf_sink(directory,
        #directory name (experiment name)
        "antenna0", #channel name
        sample_dtype, #size of each sample
        3600, #number of seconds per directory
        30000, #number of milliseconds per file
        sample_rate, #sample rate of data incoming
        1, #set to one unless lpf is used
        sample_time,
        #start sample index (seconds since epoch unix time * sample rate)
        False, #ignore tags
        True, #is complex?
        1, #number of subchannels
        None, #uuid
        center_freq, #center frequencies
        {}, #metadata
        True, #is continuous?
        0, #compression level
        False, #checksum
        True, #marching periods
        False, #stop on skipped?
        True) #debug
```

```
#antenna 1
file_rx_sink_1 = gr_drf.digital_rf_sink(directory,
        "antenna1",sample_dtype, 3600, 30000, sample_rate,
        1, sample_time, False, True, 1, None, center_freq,
        {},True,0,False,True,False,True)

#antenna 2
file_rx_sink_2 = gr_drf.digital_rf_sink(directory,
        "antenna2",sample_dtype, 3600, 30000, sample_rate,
        1, sample_time, False, True, 1, None, center_freq,
        {},True,0,False,True,False,True)

#antenna 3
file_rx_sink_3 = gr_drf.digital_rf_sink(directory,
        "antenna3",sample_dtype, 3600, 30000, sample_rate,
        1, sample_time, False, True, 1, None, center_freq,
        {},True,0,False,True,False,True)

#antenna 4
file_rx_sink_4 = gr_drf.digital_rf_sink(directory,
        "antenna4",sample_dtype, 3600, 30000, sample_rate,
        1, sample_time, False, True, 1, None, center_freq,
        {},True,0,False,True,False,True)

#antenna 5
file_rx_sink_5 = gr_drf.digital_rf_sink(directory,
        "antenna5",sample_dtype, 3600, 30000, sample_rate,
        1, sample_time, False, True, 1, None, center_freq,
        {},True,0,False,True,False,True)

#antenna 6
file_rx_sink_6 = gr_drf.digital_rf_sink(directory,
        "antenna6",sample_dtype, 3600, 30000, sample_rate,
        1, sample_time, False, True, 1, None, center_freq,
        {},True,0,False,True,False,True)
```

```
#antenna 7
file_rx_sink_7 = gr_drf.digital_rf_sink(directory,
        "antenna7",sample_dtype, 3600, 30000, sample_rate,
        1, sample_time, False, True, 1, None, center_freq,
        {},True,0,False,True,False,True)

#antenna 8
file_rx_sink_8 = gr_drf.digital_rf_sink(directory,
        "antenna8",sample_dtype, 3600, 30000, sample_rate,
        1, sample_time, False, True, 1, None, center_freq,
        {},True,0,False,True,False,True)

#antenna 9
file_rx_sink_9 = gr_drf.digital_rf_sink(directory,
        "antenna9",sample_dtype, 3600, 30000, sample_rate,
        1, sample_time, False, True, 1, None, center_freq,
        {},True,0,False,True,False,True)

fg = gr.top_block()

                #Rx Chain
fg.connect((receive_0,0),file_rx_sink_0)
fg.connect((receive_0,1),file_rx_sink_1)
fg.connect((receive_0,2),file_rx_sink_2)
fg.connect((receive_0,3),file_rx_sink_3)
fg.connect((receive_0,4),file_rx_sink_4)
fg.connect((receive_0,5),file_rx_sink_5)
fg.connect((receive_0,6),file_rx_sink_6)
fg.connect((receive_0,7),file_rx_sink_7)
fg.connect((receive_0,8),file_rx_sink_8)
fg.connect((receive_0,9),file_rx_sink_9)

fg.start()

while(True):
```

```
try:
        time.sleep(1)
except KeyboardInterrupt:
        fg.stop()
        print('done')
        sys.stdout.flush()
        sys.exit()
```

Appendix H
ICEBEAR Radio License

RADIO LICENCE

Issued under the authority of the Minister of Industry in accordance with the *Radiocommunication Act* and Regulations made thereunder.

This licence may be modified before the expiry date shown. For the latest legal version and status of this licence, please consult the Innovation, Science and Economic Development Canada web site at http://www.ic.gc.ca/spectrum

EFFECTIVE DATE	EXPIRY DATE	LICENCE NUMBER	ACCOUNT NUMBER
August 2, 2017	March 31, 2018	010734122-001	034100001425

LICENCE HOLDER TYPE
Radiocommunication user

Licence mailing address:

University of Saskatchewan Space & Atmospheric Studies
116 Science Place
Saskatoon SK
S7N 5E2

Authority to operate this (these) licenced station(s) is granted to:

University of Saskatchewan Space & Atmospheric Studies
116 Science Place
Saskatoon SK
S7N 5E2

THIS LICENCE AUTHORIZES THE OPERATION OF THE STATION(S) LISTED BELOW

LICENCE CONDITIONS / APPENDICES

SEE LICENCE ADDENDUM BELOW

STATION ID: 1 **CALL SIGN:** CFP524

STATION TYPE	LATITUDE (N)	LONGITUDE (W)	ZONE
Fixed radar station	50 53 36.000	109 24 10.000	Other area, Low congestion

STATION LOCATION
Leader, SK

LICENSEE REFERENCE
ICEBEAR Transmitter

STATION CONDITIONS / APPENDICES

Appendix R - Frequency Sharing Condition

This condition has been applied to your radio authorization since your assigned radio frequency(ies) is/are shared with other radio users. Please see the complete text of this appendix and take note of any restrictions or limitations imposed.

A copy of Appendix R can be viewed at: http:// www.ic.gc.ca/eic/site/smt-gst.nsf/eng/sf10811.html. You can also navigate to Appendix R on our website: www.ic.gc.ca/spectrum-conditions.

Appendix X - Non-Interference Condition (Action)

This condition has been applied to your radio authorization as your station has the potential to cause interference to other radio systems sharing the same assigned radio frequency. Please see the complete text of this appendix and take note of any restrictions or limitations imposed.

A copy of Appendix X can be viewed at http:// www.ic.gc.ca/eic/site/smt-gst.nsf/eng/sf10813.html. You can also navigate to Appendix X on our website: www.ic.gc.ca/spectrum-conditions.

Appendix Z - Non-Interference Condition (Monitoring)

This condition has been applied to your radio authorization as your station has the potential to cause interference to other radio systems sharing the same assigned radio frequency. Please see the complete text of this appendix and take note of any restrictions or limitations imposed.

A copy of Appendix Z can be viewed at: http:// www.ic.gc.ca/eic/site/smt-gst.nsf/eng/sf10814.html. You can also navigate to Appendix Z on our website: www.ic.gc.ca/spectrum-conditions.

RADIO LICENCE

Issued under the authority of the Minister of Industry in accordance with the *Radiocommunication Act* and Regulations made thereunder.

This licence may be modified before the expiry date shown. For the latest legal version and status of this licence, please consult the Innovation, Science and Economic Development Canada web site at http://www.ic.gc.ca/spectrum

EFFECTIVE DATE	EXPIRY DATE	LICENCE NUMBER	ACCOUNT NUMBER
August 2, 2017	March 31, 2018	010734122-001	034100001425

STATION ID: 1 **CALL SIGN:** CFP524

This Developmental licence is granted on a temporary basis only and does not confer upon the licensee any right of continued tenure for the radio spectrum assigned nor does it infer that an authorization will be granted upon subsequent application for the conversion of the authorization in the developmental service to another class of service. This authorization will terminate on March 31, 2021 and licence renewal is at the discretion of the Minister of Innovation, Science and Economic Development. The client must advise the department in writing prior to December 31, 2020 should there be a requirement for this authorization to continue beyond March 31, 2021. At the end of the authorization period, the licensee must provide a summary of the experimental activities performed by sharing with Innovation, Science and Economic Development Canada any relevant published articles or non-confidential reports, studies and/or presentations.

FREQUENCIES		REG. SERV.	EQUIVALENT VOICE CHANNEL		BANDWIDTH AND EMISSION	POWER AND TYPE	CONDITIONS
TX	RX		TX	RX			
49.50000 MHz		7	1		160K0F1D-N	23.613 kW ERP	

REGULATORY SERVICE(S)

7 - Developmental service

LICENCE ADDENDUM

This licence authorizes the licensee to establish and operate a radio station as described in the approved application, in accordance with specific items or conditions and applicable provisions of the *Radiocommunication Act* and its regulations. This authority should not be construed as approving the use of any antenna supporting structure which has not been approved by the Department of Transport from an aeronautical safety point of view. Except as provided in the regulations, no change in the apparatus or operations shall be made without the authority of the Minister, Innovation, Science and Economic Development Canada, and the licensee shall notify the Department in writing upon a change of address.

The Department may, at a future date, require the licensee to install filters, tone coding devices, reduce the effective radiated power and/or antenna height as appropriate.

Service indicates the category of service the station is authorized to perform.

For further information regarding your radio licence please contact your nearest Innovation, Science and Economic Development Canada District Office. The *Radiocommunication Act* and the Radiocommunication Regulations are available on Internet at:

http://www.ic.gc.ca/spectrum

Enquiries concerning this radio licence should be directed to your Innovation, Science and Economic Development Canada District Office.
You can consult our list of offices at :
http://www.ic.gc.ca/eic/site/smt-gst.nsf/eng/sf01742.html

Appendix I

Copyright Information

JOHN WILEY AND SONS LICENSE TERMS AND CONDITIONS

May 07, 2019

This Agreement between Mr. Devin Huyghebaert -- Devin Huyghebaert ("You") and John Wiley and Sons ("John Wiley and Sons") consists of your license details and the terms and conditions provided by John Wiley and Sons and Copyright Clearance Center.

License Number	4580270385304
License date	May 01, 2019
Licensed Content Publisher	John Wiley and Sons
Licensed Content Publication	Radio Science
Licensed Content Title	ICEBEAR: An All-Digital Bistatic Coded Continuous-Wave Radar for Studies of the E Region of the Ionosphere
Licensed Content Author	Devin Huyghebaert, Glenn Hussey, Juha Vierinen, et al
Licensed Content Date	Apr 30, 2019
Licensed Content Volume	0
Licensed Content Issue	0
Licensed Content Pages	16
Type of use	Dissertation/Thesis
Requestor type	Author of this Wiley article
Format	Electronic
Portion	Full article
Will you be translating?	No
Title of your thesis / dissertation	The Ionospheric Continuous-wave E-region Bistatic Experimental Auroral Radar (ICEBEAR)
Expected completion date	Oct 2019
Expected size (number of pages)	300
Requestor Location	Mr. Devin Huyghebaert Physics & Engineering Physics 116 Science Place Saskatoon, SK S7N5E2 Canada Attn: Mr. Devin Huyghebaert
Publisher Tax ID	EU826007151
Total	0.00 CAD
Terms and Conditions	

TERMS AND CONDITIONS

This copyrighted material is owned by or exclusively licensed to John Wiley & Sons, Inc. or one of its group companies (each a"Wiley Company") or handled on behalf of a society with which a Wiley Company has exclusive publishing rights in relation to a particular work (collectively "WILEY"). By clicking "accept" in connection with completing this licensing transaction, you agree that the following terms and conditions apply to this transaction (along with the billing and payment terms and conditions established by the Copyright Clearance Center Inc., ("CCC's Billing and Payment terms and conditions"), at the time that you opened your RightsLink account (these are available at any time at http://myaccount.copyright.com).

Terms and Conditions

- The materials you have requested permission to reproduce or reuse (the "Wiley Materials") are protected by copyright.

- You are hereby granted a personal, non-exclusive, non-sub licensable (on a stand-alone basis), non-transferable, worldwide, limited license to reproduce the Wiley Materials for the purpose specified in the licensing process. This license, **and any CONTENT (PDF or image file) purchased as part of your order,** is for a one-time use only and limited to any maximum distribution number specified in the license. The first instance of republication or reuse granted by this license must be completed within two years of the date of the grant of this license (although copies prepared before the end date may be distributed thereafter). The Wiley Materials shall not be used in any other manner or for any other purpose, beyond what is granted in the license. Permission is granted subject to an appropriate acknowledgement given to the author, title of the material/book/journal and the publisher. You shall also duplicate the copyright notice that appears in the Wiley publication in your use of the Wiley Material. Permission is also granted on the understanding that nowhere in the text is a previously published source acknowledged for all or part of this Wiley Material. Any third party content is expressly excluded from this permission.

- With respect to the Wiley Materials, all rights are reserved. Except as expressly granted by the terms of the license, no part of the Wiley Materials may be copied, modified, adapted (except for minor reformatting required by the new Publication), translated, reproduced, transferred or distributed, in any form or by any means, and no derivative works may be made based on the Wiley Materials without the prior permission of the respective copyright owner.**For STM Signatory Publishers clearing permission**